Longwall mining-induced fracture characterisation based on seismic monitoring

Author:
Wang, Shuyu

Publication Date:
2023

DOI:
https://doi.org/10.26190/unsworks/25039

Longwall mining-induced fracture characterisation based on seismic monitoring

Shuyu Wang

A thesis in fulfilment of the requirements for the degree of

Doctor of Philosophy

School of Minerals and Energy Resources Engineering
Faculty of Engineering

January 2023

Originality, Copyright and Authenticity Statements

ORIGINALITY STATEMENT

☑ I hereby declare that this submission is my own work and to the best of my knowledge it contains no materials previously published or written by another person, or substantial proportions of material which have been accepted for the award of any other degree or diploma at UNSW or any other educational institution, except where due acknowledgement is made in the thesis. Any contribution made to the research by others, with whom I have worked at UNSW or elsewhere, is explicitly acknowledged in the thesis. I also declare that the intellectual content of this thesis is the product of my own work, except to the extent that assistance from others in the project's design and conception or in style, presentation and linguistic expression is acknowledged.

COPYRIGHT STATEMENT

☑ I hereby grant the University of New South Wales or its agents a non-exclusive licence to archive and to make available (including to members of the public) my thesis or dissertation in whole or part in the University libraries in all forms of media, now or here after known. I acknowledge that I retain all intellectual property rights which subsist in my thesis or dissertation, such as copyright and patent rights, subject to applicable law. I also retain the right to use all or part of my thesis or dissertation in future works (such as articles or books).

For any substantial portions of copyright material used in this thesis, written permission for use has been obtained, or the copyright material is removed from the final public version of the thesis.

AUTHENTICITY STATEMENT

☑ I certify that the Library deposit digital copy is a direct equivalent of the final officially approved version of my thesis.

Inclusion of Publication Statement

UNSW is supportive of candidates publishing their research results during their candidature as detailed in the UNSW Thesis Examination Procedure.

Publications can be used in the candidate's thesis in lieu of a Chapter provided:

- The candidate contributed **greater than 50%** of the content in the publication and are the "primary author", i.e. they were responsible primarily for the planning, execution and preparation of the work for publication.
- The candidate has obtained approval to include the publication in their thesis in lieu of a Chapter from their Supervisor and Postgraduate Coordinator.
- The publication is not subject to any obligations or contractual agreements with a third party that would constrain its inclusion in the thesis.

☑ The candidate has declared that **their thesis has publications - either published or submitted for publication - incorporated into it in lieu of a Chapter/s. Details of these publications are provided below.**.

Publication Details #1

Full Title:	Quantitative assessment of the spatio-temporal correlations of seismicevents induced by longwall coal mining
Authors:	Shuyu Wang, Guangyao Si, Changbin Wang, Wu Cai, Binglei Li, Joung Oh,Ismet Canbulat
Journal or Book Name:	Journal of Rock Mechanics andGeotechnical Engineering
Volume/Page Numbers:	
Date Accepted/Published:	
Status:	published
The Candidate's Contribution to the Work:	Main data processing and writing
Location of the work in the thesis and/or how the work is incorporated in the thesis:	Chapter 4

Publication Details #2

Full Title:	Using uniaxial seismic monitoring data to interpret the distribution of longwall mining-induced fractures
Authors:	Shuyu Wang, Guangyao Si
Journal or Book Name:	Rock Mechanics and Rock Engineering
Volume/Page Numbers:	
Date Accepted/Published:	
Status:	submitted
The Candidate's Contribution to the Work:	Main data processing and writing
Location of the work in the thesis and/or how the work is incorporated in the thesis:	Chapter 3.2-3.3, Chapter 5.1-5.2

Candidate's Declaration

I confirm that where I have used a publication in lieu of a chapter, the listed publication(s) above meet(s) the requirements to be included in the thesis. I also declare that I have complied with the Thesis Examination Procedure.

Abstract:

Despite several technological advancements, mining-induced fractures are still critical for the safety of underground coal mines. Rocking fracturing as a natural response to mining activities can pose a potential hazard to mine operators, equipment, and infrastructures. The fractures occur not only around the working face that can be visually measured but also above and in front of the working face and where geological structures are affected by mining activities. Therefore, it is of importance to detect and investigate the properties of mining-induced fractures. Mining-induced seismicity has been generated due to rock fracturing during progressive mining activities and can provide critical fracture information. Currently, the application of using seismic monitoring to characterise fractures has remained relatively challenged in mining because mining-induced fractures are initiated by stress change and strata movement after mineral extraction. Compared to seismic monitoring in the oil and gas industry, the fractures and seismic responses may show different characteristics. Therefore, seismic monitoring in mines lacks a comprehensive investigation of received seismic signals to the properties of induced fractures and the effect on mine workings by these fractures. Additionally, constraints such as the quality of seismic signals and the deficiency of correlation analysis of seismic events in underground mining pose great challenges in using seismic data for hazard prediction.

This thesis aims to address these challenges in using seismic monitoring to understand and characterise mining-induced fractures by (1) calculating fracture properties related to seismic source location, magnitude and mechanism based on uniaxial seismic data, (2) spatial and temporal correlation analysis of seismic events, and (3) inspecting fracture distributions and simulation of the fractured zone in longwall coal mines. Firstly, since cheap and easily removable uniaxial geophones close to production areas are preferable in coal mines, a novel method to use uniaxial signal and moment tensor inversion to generate synthetic triaxial waves is designed for a comprehensive description of the fracture properties, including location, radius, aperture and orientation. Secondly, to apply seismic data for advanced analysis, such as rockburst prediction and caving assessment, the correlation of seismic events is proved to be quantitatively assessable, and their correlations may vary throughout the mineral extraction process. The spatial and temporal correlation of seismic event energy is quantitatively analysed using various statistical methods, including autocorrelation function (ACF), semivariogram and Moran's I

analysis. In addition, based on the integrated spatial-temporal (ST) correlation assessment, seismic events are further classified into seven clusters to assess the correlations within individual clusters. Finally, several source parameters such as seismic moment (M_0), seismic source radius (R), fracture aperture (τ), failure type and fracture orientation were used to characterise fractures induced by longwall mining. This thesis also presents the fracture patterns induced caused progressive longwall mining for the first time. Besides, a discrete element method (DEM) model with seismic-derived fractures is generated and proves the impact of mining-induced fractures on altering stress conditions during mineral extraction. In addition, with the analysis of the seismic source mechanism and a synthetic triaxial method, a discrete fracture network (DFN) is generated from monitored seismic events to restore complete induced fractures. Overall, the outcomes of this study lead to a comprehensive assessment of mining-induced fracture properties based on real-time seismic monitoring, demonstrating its significant potential for hazard prediction and improving the safety of resource recovery.

Acknowledgements

This thesis could not have been written without the assistance of a number of people, to whom I am extremely indebted.

Firstly, I would like to acknowledge UNSW University International Postgraduate Award (UIPA) Scholarship for the financial support. It has been an honour to be the recipient of this Scholarship.

I would like to also thank my supervisors Dr Guangyao Si, Dr Joung Oh and Professor Ismet Canbulat for their encouragement, support, and understanding on every step of the way of my research during the past four years. Especially, Dr Guangyao Si, who I would I wish to express my deepest appreciation to, invited me to pursue a PhD at UNSW School of Minerals and Energy Resources Engineering (MERE) when I was bewildered at the summer of 2018 and continuously guide me from a beginner of research. His vast expertise in the mining industry has assisted me in conceiving novel ideas and his patience and invaluable assistance helped me run things smoothly and deliver results on time. I would also like to acknowledge Dr Wu Cai for his invaluable assistance with my research.

It is also important that I acknowledge here the love and encouragement of my family. My parents have always supported me in all of my endeavours, giving me fully understanding of staying Australia for three years since the travel obstacle during COVID-19 and continuing to motivate me to complete my PhD although they miss me so much.

I am grateful to my partner, Yanqiu Tian, as well as our lovely Persian, Cheese, who have been by my side throughout this PhD, living every single minute of it. Thank you.

Last but not least, it was a pleasure to associate with other doctors and candidates at the MERE school. I'd like to thank Dr Changbin Wang, Dr Sarvesh Singh, Dr. Yueyi Pan, Dr Jiachao Ge, Dr Yingzhi Cui, Mr Shitao Liu, Mr Feng Zhang, Mr Xing Zhang, Mr Zizhuo Xiang, Mr Xu Li and Mr Mingwei Chen for stimulating conversations, sleepless nights, and all the fun we've had over the past four years. Also, I gratefully acknowledge my friends externally for their emotional support, Mr Kan Liu, Mr Dubang Liu, Mr Chengyu Wu, Ms Qian Kang, thank you all for your support and input, without which this achievement would not have been possible.

Many thanks for everyone’s support.

Table of Content

List of Figures

List of Tables

List of Symbols

a	the range of influence
c_0	the autocovariance in lag 0
C, C'	the fitting coefficient for the Gaussian function
c_k	the autocovariance
E	energy of seismic events
Ec	cumulative daily energy.
$\mathrm{G}(x)$	fitting functions.
MI	Moran's I value
I_B	Bartlett's limit.
k	lag
N	the total number of seismic events
V_s	the semivariance
μ	the mean of the total studied data points
w_{ij}	an element of a matrix of spatial weights
x_i/x_j	the i_{th}/j_{th} seismic datum
Z	the standardised Moran's I
θ	the scale of fluctuation
f_0	corner frequency
M_0	seismic moment
M_L	Richter magnitude
R	Source radius
τ	source aperture
A	amplitude attenuation
A_0	seismic wave amplitude at the source location
D	distance between the source and the sensor
l	wavelength
Q	rock quality factor
v	wave velocity
f	dominant frequency
Fi	waveform picking function
A_j	amplitude

E_{m1}, E_{m2}	error used in Grid Search algorithm
$\mathbf{M}$	the moment tensor
M	the norm of **M**
M_1, M_2, M_3	the eigenvalues of the moment tensor
G	Green's function
$S(t)$	source time function
u_k	amplitude measured on sensor
k , u_k^0	corrected amplitude
S_k	Sensor polarity
G_{s_k}	geometrical spreading
P_k	anelastic attenuation
F_k	free-surface amplification
C_{w_k}	coupling weight of the receiver
Δu(t)	the magnitude of dislocation
γ	tensile angle
$\hat{f}$	slip vector
$\hat{n}$	normal vector of the fault plane
$\boldsymbol{u}^P$	P wave displacement
μ	Lame constant
A	area of the fault segment
ρ	density,
$\hat{\boldsymbol{r}}$	direction of radiation
V_P	P wave velocity
$\boldsymbol{S}$	source dislocation tensor
β_0	S wave velocity
K_c	a constant that depends on the source model
E	elastic modulus
ν	Poisson's ratio
$tr(M)$	trace component of the diagonalised moment tensor matrix
r	distance between source and receiver
$W_{V\ rms_{peak}}$	amplitude of the peak signal
E	radiated energy

m_c	magnitude of completeness
σ_1	maximum principal stress
σ_2	intermediate principal stresses
σ_3	minimum principal stress
k_n	normal joint stiffness
k_s	shear joint stiffness
K, G	bulk and shear moduli
b	average block size

list of abbreviations

ACF	autocorrelation function
ST	spatial-temporal
DEM	discrete element method
DFN	discrete fracture network
SOF	scale of fluctuation
RMS	root mean square
SNR	signal-to-noise ratio
LTCC	Longwall Top Coal Caving
LW	Longwall
ASC	Applied Seismology Consulting
SOF	scale of fluctuation
DC	double couple
ISO	isotropic components
CLVD	compensated linear vector dipole

Chapter 1. Introduction

This chapter explores the context and complexities of deep-level longwall coal mining, a procedure laden with difficulties such as probable rock failure, increased gas emissions, and changing stress conditions. The research reported here is intended to address these issues by improving seismic monitoring and thereby improving our understanding of mining-induced stress and cracks. This understanding is critical for the creation of risk-mitigation measures, which will ultimately improve the safety and productivity of coal mining operations. The research goals are grouped into three major goals. The first is the creation of a seismic source mechanism-based analysis method, which will provide a more in-depth understanding of seismic activity sources and their relationship to the mining process. The second goal is to develop a method for analysing seismic parameter spatial and temporal correlation. This will give information on seismic activity patterns and their relevance to mining operations. The fourth and most important goal is to comprehend the distribution of mining-induced fractures. This will be accomplished by developing a computational model of these fractures that will allow us to forecast their behaviour and devise effective management techniques. The research aims to assure the safety, sustainability, and productivity of coal mining operations through these collaborative efforts, thereby contributing to the development of safer and more efficient mining practises.

1.1. Background

In recent years, the demand for coal resources has skyrocketed due to the increased social and economic needs of nations, particularly in developing nations (e.g., China, India, and Indonesia). As surface mineral reserves become depleted due to increased demand, operators are gradually transitioning to underground mining. However, the depth of mining and the scope of extracted orebodies continue to grow. Mining at greater depths under high-stress conditions causes a variety of problems, including falling rocks, roof collapses, roadway deformations, ground movements, and rock bursts, which raise serious health and safety concerns as well as costly production delays (Fujii and Ishijima 1991; Ranjith et al. 2017; Zhao et al. 2021).

To efficiently extract coal resources, longwall mining is a highly productive underground mining method that is normally applied. In longwall mining, a relatively long mining face (typically in the range of 100 m to 300 m but maybe longer) is created by driving a preparation roadway at right angles between two entry roadways that form the sides of the longwall block. Once the longwall face equipment has been installed, coal can be extracted along the full length of the face in slices of a given width. The modern longwall face is supported by hydraulically powered supports, and these supports are progressively moved across to support the newly extracted face as slices are taken, allowing the section where the coal had previously been excavated and supported to collapse. The resource recovery ratio of longwall mining has been very high in recent years- in theory, 100% of the block of coal can be extracted, though, in practice, there is always some coal left in the goaf (Brady 1995). In addition, when longwall operates in a safe and efficient manner, coal is mined in a systematic, relatively continuous, and repetitive process, which is ideal for strata control and associated mining hazard management.

The excavation of large volumes of mineral resources at depth and the resulting redistribution of stress can result in fracture initiation, propagation, and rock mass movement along pre-existing fracture planes. This is one of the most significant challenges associated with sustainable mining in longwall operations. Mining-induced fractures can interact with a pre-existing discrete fracture network and flow channels that connect to a nearby gassy coal seam or high-pressure aquifer, posing a serious threat to coal production faces in the event of a gas release or water inrush. Reliable prevention and management of mining-induced gas (water) inflows and reservoir (aquifer) interference are significant emerging issues for the mining industry. The Australian coal mining industry is subject to unprecedented public and political scrutiny, necessitating unprecedented environmental responsibility. Where significant aquifers, surface water, or flooded workings are involved, the lack of robust and reliable analysis tools may have a substantial impact on the industry's ability to obtain mining approval and licences (Adhikary and Guo 2014).

In addition, rock failure as a natural response to mining activities can pose a potential hazard to mine operators, equipment, and infrastructures. These processes are usually accompanied by the generation of seismic waves known as mining-induced seismicity, which have been reported in underground mines worldwide (Li et al. 2007). As Figure 1-1 shows, within the mined area of a longwall panel, gas or water can migrate into the workings through the destressed area and high-flow fracture channels. Thus, understanding mining-induced fractures are important to prevent water inrush, protect shallow aquifers, and guide gas drainage designs. It has been documented that rock failure processes are associated with detectable seismic signals (Xiao et al. 2016; Cai et al. 2019; Cao et al. 2020). As Figure 1-1 shows, each seismic event recorded by geophones indicates rock failure at a certain location, and the associated seismic wave emissions may convey the source information of that fracture.

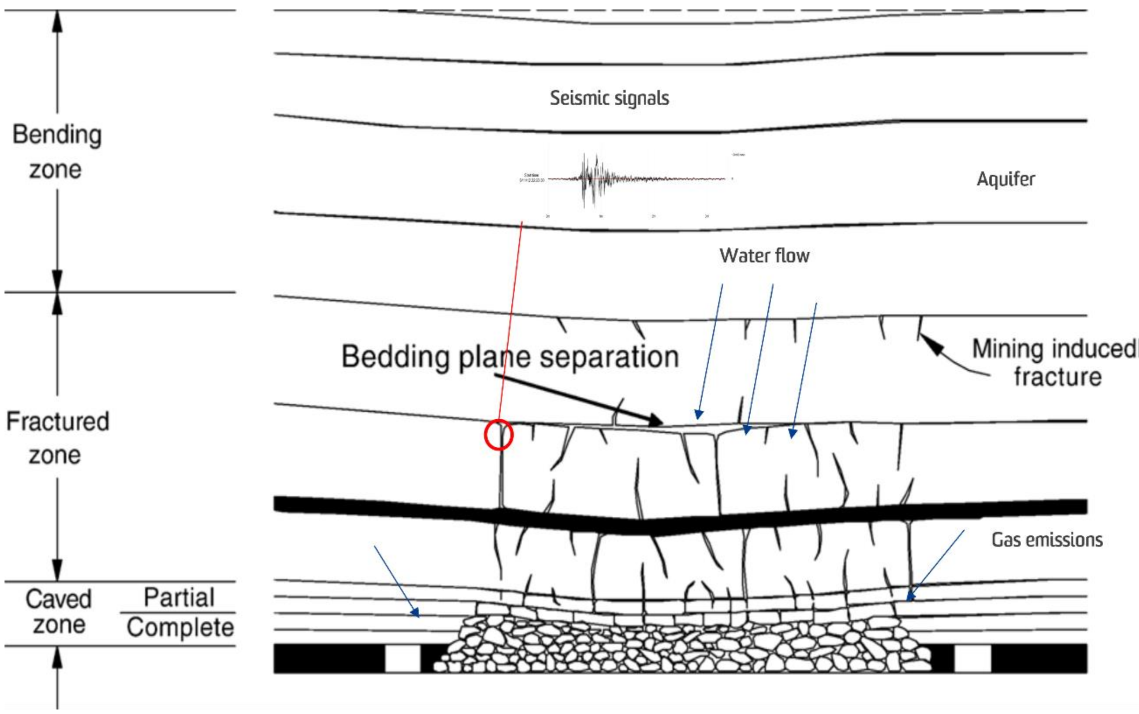

Figure 1-1 Schematic diagram of fracture induced by longwall mining and generated seismicity

In a large picture, mining-induced seismicity, as the response of rock mass to continuous mineral extraction, can represent either the initiation and propagation of new fractures or the slippage of pre-existing weak planes in rock mass induced by stress redistribution during mining (Lei et al. 2014). Mining-induced seismic events, which correspond to the sudden release of elastic strain energy in the rock mass, can be caused by fault slip due to the interaction of tectonic stresses and mining-induced stresses away from mine openings or the sudden failure of rock masses due to stress concentration near the mining area.

Mining-induced seismicity is usually controlled by the mining depth, mining speed, excavation geometry and geological discontinuities. Also, one or the combination of the above factors would lead to different seismic behaviours (Guha 2000). Correspondingly, the inversion of seismic data collected at mine sites can reflect the characteristics of the above parameters to some extent (Bosch et al. 2010). For instance, the temporal variation of geomechanical properties of rock material can be inferred by seismic data (Zhao et al.

2018). A clustering of seismic events could indicate local rock instability or/and substantial stress changes (Mendecki et al. 1999). Therefore, seismic monitoring has been widely used to optimise rock failure-related engineering designs (hydraulic fracturing in unconventional gas recovery) (Schultz et al. 2020a) and predict potential rock failure and the induced seismic hazards (coal/rock bursts and gas outburst) (Zhao et al. 2018). Coal bursts or rock bursts are a particular case of seismic events induced by mining activities that cause injury to the workforce or damage to underground workings. As a result, all rock bursts are essentially seismic events, but not all mining-induced seismic events would trigger rock bursts (Dmowska and Saltzman 2001).

The energy released from a seismic event is radiated as seismic waves. Seismic waves are essentially oscillations due to elastic deformations, which propagate through the Earth and can be recorded by seismic sensors and data acquisition systems. The seismic moment and seismic energy released by these sources may cover a tremendous range of magnitudes with various degrees of ground shaking intensities and associated damage. The seismic energy, magnitude, their mutual relationships as well as the determination of seismic source mechanisms are critical in seismic data analysis. In order to accurately calculate these seismic parameters, it is recommended to a large number of valid triaxial seismic wave signals.

When monitoring seismicity in underground coal mines, both the uniaxial sensors and triaxial sensors can be installed near a longwall panel to monitor seismic waves generated during coal extraction. Uniaxial sensors only record the amplitude information of seismic waves along the installation direction, while triaxial sensors can record the other two seismic amplitudes perpendicular to the installation direction. The processing of triaxial seismic trace data will be more accurate and more convenient, given the S wave and source vector can be easily determined. However, for most mines, triaxial sensors are much more expensive and inflexible compared with uniaxial sensors. In general, triaxial sensors are permanently cemented in the host rock, while uniaxial sensors can be easily relocated. Thus, seismic data analysis methods introduced in previous investigations normally require high-quality triaxial seismic signals to calculate credible fracture parameters(Li et al. 2007; Leśniak and Isakow 2009; Si et al. 2015). This can be achieved in metalliferous mines with permanent triaxial geophones but is difficult in coal mines since the rapid material extraction rate requires frequent relocation of geophones. In coal mines, cheap and easily removable uniaxial geophones close to production areas are preferable. This increases the difficulty of using seismic data from coal mines to obtain accurate source mechanism and clustering analysis, especially in Chinese mines where uniaxial geophones are dominant.

Mining-induced seismicity has also been found to be internally correlated in both time and space domains as a result of rock fracturing during progressive mining activities. Based on the distribution of seismic events, seismic monitoring may contribute to predicting mining-induced seismic hazards. Mining-induced seismicity does not distribute uniformly in space or time. In the space domain, most of the explosive types of seismic events caused by mining activities are energetically weak. In contrast, events with high energy commonly occur in tectonic regions and are presumably caused by the interaction between tectonic stresses and mining-induced stresses (Stec 2007). While in the time domain, the seismic events tend to form nests, swarms, and sequences (Gibowicz 2009). Previous research indicates seismic hazards are related to high-energy events near mine openings (Leśniak and Isakow 2009; Cai et al. 2019). A direct relationship between seismicity and gas emission rate has been reported by (Si et al. 2015), which can be used to provide early warning for uncontrolled gas emissions. Fault slip and seismic activities can be numerically simulated to comprehensively explore seismicity induced by mine extraction (Cao et al. 2018a). Thus, understanding the temporal and spatial correlation of mining-induced seismic events is an essential step in using seismic data for further advanced seismic analysis, such as rock burst prediction and caving assessment.

However, there are no clear methods for carrying out this critical work. Input parameters for seismic hazard prediction, such as the time frame of historical data and effective prediction distance, are selected based on site-specific experience with no statistical or physical explanation. The only way to increase the accuracy of present seismic prediction algorithms is to determine the spatial and temporal correlations of mining-induced seismicity. The temporal and spatial correlation of seismic event energy obtained from a sample mine is quantitatively evaluated in this work using a number of statistical approaches, including the autocorrelation function (ACF), semivariogram, and Moran's I analysis. The examination of spatial-temporal (ST) correlations and cluster-based correlations is also noteworthy in this study. Seismic event correlations are quantitatively quantifiable, and their correlations can change during the mineral extraction process.

In recent years, motivated by improving coal mining safety, reducing fugitive gas emissions, and capturing clean energy, it is significantly important to improve the understanding of the rock failure process during coal extraction and fluid transport in mining-induced fractures. Previous research shows that the water flow in coal seam floors can be numerically simulated with the help of mining-induced fracture evolution (Lu and Wang 2015a). And rock failure and mining-induced fractures can be simulated by coupling the interrelation of stress and damages (Tang 2002). However, integrating induced seismic data is a more efficient and more reliable way of understanding fracturing activities at the coal mining process. Therefore, this thesis provides a systematic investigation of understanding the relationship between progressive rock failure and seismicity evolution induced by mining, particularly under the background of underground longwall coal mining.

1.2. Motivation

Since their introduction in the 1970s to the coal mining industries of the United Kingdom and West Germany, geophysical methods have been utilised in coal mines around the globe. There is a vast array of applications in both surface and underground mining. Applications include coal seam mapping and geological fault detection, lithological mapping, geotechnical evaluation, assessment of the rock mass response to mining, void detection, location of trapped miners, and guidance of drills and mining equipment. In addition to a wide array of techniques, which includes geophysical borehole logging, potential field methods, seismic reflection (2D and 3D), resistivity, electromagnetics, and seismic monitoring using active and passive sources, there is a wide range of techniques that can be employed. Consequently, mining-induced seismicity monitoring is essentially a geophysical technology. Apart from geophysics, geomechanical, geological, and reservoir engineering knowledge are all required for the advanced processing and interpretation of induced seismic data.

Seismic event locations and magnitudes provide valuable information about the spatial extension of fracture zones (Wang et al. 2016), and the inversion of seismic moment tensors can provide extra information about the specific dynamics of rock fracturing processes (Gibowicz and Kijko 1994a; Sellers et al. 2003; Ma et al. 2019). The identified hypocentres may also reveal failure planes or other underlying structures that control the distribution of seismic events (Young et al. 1992).

The inversion of seismic source mechanisms as a typical seismic analysis method is a promising method for the mining industry to understand rock fracturing behaviour during resource extraction. By conducting seismic moment tensor inversion, discrete seismic events can be connected/clustered based on the physical mechanism at their source, such as the event failure mechanism, principal strain axes, and potential failure plane orientations (Young et al. 1992; Shearer 1999; Gibowicz 2009b; Zhao et al. 2018). Evaluating event failure mechanisms is crucial for understanding the fractures induced by progressive resource extraction in underground mines. Results on the failure plane orientation can also help describe the spatial distribution of mining-induced fractures and generate a probabilistic fracture network (Maxwell et al. 2010; Zhao et al. 2019).

This thesis targets to have a comprehensive understanding of longwall mining-induced fractures and triggered stress change based on seismic monitoring. To achieve this, three main aspects are going to be investigated in this research:

- Above all, the fracture information to be determined by seismic data includes multi-attributes of source location, released energy, fracture orientation, fracture radius and fracture aperture. As discussed in Section 1.1, these parameters cannot be achieved by uniaxial seismic signals based on current approaches that are developed for triaxial seismic signals. Therefore, developing a comprehensive method of processing uniaxial seismic signals from raw waveforms to back-calculate fracture properties is required and will be explored in this thesis. Thus, this thesis focuses on developing a novel method to use uniaxial signals, radiation patterns, and moment tensor inversion to generate synthetic triaxial waves and then determine fracture geometries and distributions induced by longwall coal mining. This approach is demonstrated by analysing uniaxial data recorded in a case study coal mine in China.

- Because fracturing operations include crack opening, sliding, and propagation, different fracture types can create distinct seismic waves. Understanding mining-induced fractures necessitates the development of internal correlations of mining-induced seismic data, which can, to some extent, represent parent fracture information. Mining-induced seismicity has been discovered to be internally correlated in both time and space domains during progressive coal extraction activities, and understanding the temporal and spatial correlation of mining-induced seismic events is a necessary step before using seismic data for further analysis, such as rock burst prediction and caving assessment. There are, however, no recognised ways to carry out this crucial work. In the spatial, temporal, and spatial-temporal domains, correlation analysis is an appropriate option. It is critical to determine which aspects are connected and which are not based on the fractures' spatial and temporal information. Furthermore, input parameters used for seismic hazard prediction, such as the time frame of historical seismic data and effective prediction distance, are calculated based on site-specific experience without statistical or physical backing. As a result, the accuracy of present seismic prediction systems is severely limited, which can only be addressed by quantifying the spatial and temporal correlations of mining-induced seismicity.

- More importantly, seismic source parameters, such as seismic moment (M_0) and seismic source radius (R), can be used to characterise fracture patterns induced by longwall mining, such as failure type, fracture aperture (τ), fracture length and fracture orientation. Thus, based on seismic data collected from a study site, this thesis also presents the fracture patterns induced by progressive longwall mining. The distribution of seismic-derived fractures can be inferred and assessed together with the geomechanical response and longwall advance rate during coal extraction. Afterwards, to better understand the relationship between the derived fractures and longwall mining, a numerical modelling approach has been proposed to simulate the longwall caving process with the derived fractures based on field seismic monitoring data. It has been proved in this thesis that the modelling results can be significantly different once considering seismic-derived fractures.

1.3. Research problems, aims and objectives

Coal mining is extending to deeper and deeper levels, facing ever-increasing gas content and much higher in-situ stress in production districts. This ever-increasing challenge of potential rock failure and gas emission in coal mining is caused by the significant alteration of stress during coal extraction. The primary limitation of applying longwall mining systems to recover coal resources in a safe, sustainable and productive manner comes from a throughout understanding of mining-induced stress and fractures, which can be potentially achieved by seismic monitoring.

The success of the longwall mining process is critically dependent on the behaviour of rock failure above and below the mining seam, as well as gas-water two-phase transport around the working area. Therefore, this thesis was systematically designed to optimise the use of seismic monitoring and interrogate seismic data obtained in underground coal mines by:

- Improving the understanding of seismic source information and fracture patterns induced by longwall mining.
- Quantitative analysing of the correlations of processed seismic data induced by longwall mining.
- Establishing the relationship between fractures and seismicity evolution during the progressive rock failure caused by longwall mining.

The aim of this thesis includes:

AIM 1 – Develop a seismic source mechanism-based source parameter analysis method from uniaxial or triaxial traces of seismic waveforms.

1.a) Investigate seismic monitoring procedures in underground mines.

1.b) Investigate the information conveyed from seismic signals.

1.c) Explore new methods for triggering, filtering, and processing seismic signals.

AIM 2 – Develop an approach to analyse the spatial and temporal correlation of seismic parameters, which will benefit further fracture information analysis

2.a) Develop a workflow for the quantitative correlation analysis of seismic data in the temporal and spatial domains separately.

2.b) Propose an approach to conduct spatial-temporal (ST) correlation analysis at the same time.

2.c) Develop a clustering method and analysis the correlation of seismic data before and after clustering.

AIM 3 – Develop a comprehensive understanding of longwall mining-induced fracture distribution by seismic source parameter and mechanism analysis and then use that fracture information to build a numerical model based on a case study mine.

3.a) Develop an approach to interpret fracture distribution from seismic data.

3.b) Analysis the mining-induced fractures and generate numerical models based on the interpreted fracture data.

3.c) Model simulation based on observed fracture distribution.

1.4. Thesis structure

The structure of the thesis follows a logical progression of research in order to achieve the objectives stated in Section 1.3. Figure 1-1 displays the general structure of the thesis. First, a comprehensive review of the current state of knowledge regarding seismic monitoring in underground mining applications is conducted to identify research gaps and formulate objectives. The remaining chapters then address specific groups of objectives. All chapters, with the exception of Chapters 1 and 6, are either published or submitted for publication and serve as replacements for individual chapters.

The content of each chapter is described in Figure 1-1 shown below:

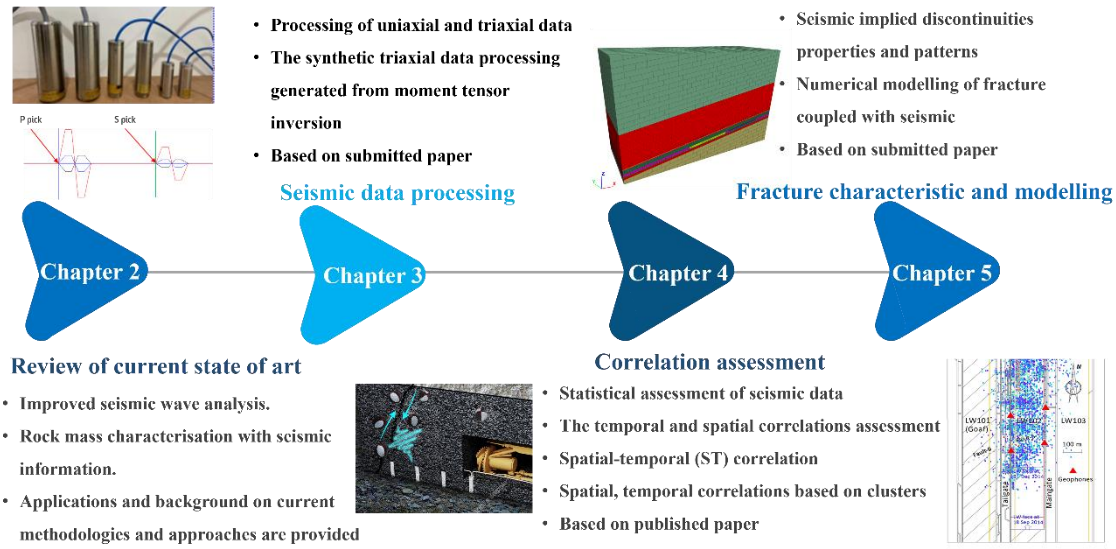

Figure 1-2 The content of this thesis

Chapter 1 – Introduction

This chapter provides background on (1) the need for seismic monitoring in underground mines to facilitate routine inspection, (2) an overview of the research problem, (3) the relevance of improving current seismic monitoring analysis methods for large-scale mine analysis, and (4) aims and objectives for the thesis.

Chapter 2 – A review of seismic monitoring for underground mining applications

This chapter examines the current state-of-the-art seismic monitoring in critical underground mining applications. The main areas reviewed after a thorough literature review, followed by insights on existing challenges and scope for future work.

The main research gaps identified from the literature review are addressed in subsequent body chapters.

Chapter 3 –Processing of uniaxial and triaxial seismic data

This chapter consists of three sections which are described below:

Section 3.1 – A preliminary investigation of seismic signal acquisition and filtering

Section 3.2 – The uniaxial seismic data processing, seismic event location and source mechanism determination.

Section 3.3 – The synthetic triaxial data processing generated from uniaxial seismic signal

Moreover, a discussion is provided on possible applications of synthetic triaxial data in underground mines.

Chapter 4 – Statistical assessment of the correlation of mining-induced seismic events

Section 4.1 - Statistical methods applied to analysing seismic correlations in the time and space domains

Section 4.2 – Quantitative assessment of the temporal and spatial correlations of seismic events induced by longwall coal mining.

Section 4.3 – Propose a clustering method and then apply the spatial and temporal correlations analysis on clustered seismic events

Chapter 5 – Seismic-derived fractures during longwall mining and their integration into numerical modelling

This chapter is split into three sections and focuses on seismic-derived fracture properties.

Section 5.1 – Fracture properties determination from seismic parameters and moment tensor inversion

Section 5.2 – Interpretation of fracture distribution and model generation based on calculated fracture properties

Section 5.3 – Numerical modelling of fracture distribution inferred from seismic events during the coal extraction process

Chapter 6 – Conclusions and recommendations for future work

Chapter 6 summarises the conclusions drawn from each chapter to enable seismic monitoring to ensure mine safety and improve mine planning by accurate and comprehensive distributions of mining-induced fractures in underground mines. The chapter also provides insights on further development required to facilitate the wider applicability of seismic monitoring.

Note: Since the main body chapters are based on three publications, the introduction, literature review and conclusion part of each chapter will be used directly in those chapters. Hence, some amount of overlap may be encountered in the introduction and literature review sections of individual chapters.

1.5. Research publications and presentations

I. Si G, Cai W, **Wang S**, Li X. Prediction of Relatively High-Energy Seismic Events Using Spatial–Temporal Parametrisation of Mining-Induced Seismicity. *Rock Mech Rock Eng.* July 2020. doi:10.1007/s00603-020-02210-3

II. **Wang, S.**, Si, G., Wang, C., Cai, W., Li, B., Oh, J. and Canbulat, I., 2022. Quantitative assessment of the spatio-temporal correlations of seismic events induced by longwall coal mining. *Journal of Rock Mechanics and Geotechnical Engineering.* Apr 2022. doi:10.1016/j.jrmge.2022.04.002

III. **Wang S**, Si G, 'Using uniaxial seismic monitoring data to interpret the distribution of longwall mining-induced fractures' (submitted to RMRE)

Chapter 2. Literature review

This chapter presents a review of available literature covering seismic monitoring technology and applications in mines, geomechanical factors affecting seismic events, and numerical modelling work related to mining-induced seismicity. The objective of this review is to present the background knowledge for the investigation of mining-induced seismicity.

2.1. Basic technics involved in longwall mining seismic monitoring

The seismic monitoring system installed in underground mines and other underground engineering applications consists of sensors, data acquisition, data storage and transmission, data processing and visualisation, as well as real-time response. Seismic monitoring is not a new technology in the mining industry. It has primary applications in caving assessment and rock burst management (Zhu et al. 2017). Over the years, seismic monitoring has been developed as a real-time, remote, and non-invasive approach to detecting underground rock failure processes.

The seismic processing techniques were initially applied to the study of earthquake-generated seismic waves. It is logical to expect that the physical and mathematical relationships created to describe and evaluate earthquakes should also apply to mine-induced seismic activity. Mendecki et al., (1997) noted that the physical rules driving centimetre-scale and kilometre-scale deformation are nearly equivalent, implying that seismology has a degree of scale independence. This means that the seismology theory can be applied to phenomena ranging from acoustic emission in laboratory rock cracking to earthquakes in geological faults. The mine seismicity can be detected at scales on both large-scale and laboratory rock failure.

There are two types of seismic waves: the surface wave and the body wave. The surface wave is the wave that travels along the earth's surface or the boundary between two distinctly different rock strata. Since seismic monitoring in longwall mining is often conducted at deep subsurface, and sensors are not situated at the surface of any strata, this thesis will only discuss the body wave, i.e., the wave that travels through the interior of the rocks. P-waves (or compressional waves) and S-waves (or shear waves) are two types of body waves (Shearer 1999). Additionally, P-waves are known as longitudinal or dilatational waves, and S-waves known as transverse waves that do not affect the material's volume. In a P-wave, the particles move in the direction of propagation, but in an S-wave, the particles move in the opposite direction. Usually, the speed of the P-wave is higher than the S-wave, and the S-wave cannot pass-through fluid material while P-wave can.

As described in Chapter 1, the seismic event is a phenomenon that releases detectable seismic waves with a sudden, inelastic deformation of a given rock volume. The radiation of seismic waves also radiates the energy and releases stress at the source. Different seismic events have different tremor amplitudes and frequencies, which depend on the stiffness and stress state of the rock, the amplitude and the magnitude of the seismic source, and the rate at which the rock deforms during fracturing (Mendecki 1996). Seismic monitoring systems can only measure the part of deformation and strain related to recorded seismic waves. When many seismic events across a specific space are recorded and analysed, it is possible to quantify changes in deformation and stress states within that space. The stress and stress change caused by seismic activity are distinct (Mendecki et al. 1999). In a given space volume, generally, the seismic deformation is proportional to the seismic moment, and the stress is proportional to the ratio of seismic energy to seismic moment. Except the seismic moment and seismic energy, several basic parameters also help to describe the seismic events: the occurring time; the event location; the magnitude; the corner frequency, the stress drops and the source mechanism. Other parameters like seismic radius and apertures are calculated based on the above basic parameters. Listed below are some key parameters and pertinent studies.

Typically, the first attributes to be established are the event origin's triggering time and location. Regardless of the size or duration of an event, the source location can be inferred from the arrival time (Shearer 1999). The travel time of seismic waves can then be inverted using various approaches to determine the event location. These methods will be contained in Chapter 3. Measuring both P- and S-waves allows for calculating a more precise location. The event can be readily mislocated if only P-wave arrival time data are supplied. In addition, a bad sensor network may result in significant location errors. Adding a second station on the opposite side of the event or measuring both P- and S-wave arrival time could improve the event’s location. The time difference between P- and S-wave arrival time can be utilised to calculate the distance between the source and receiver at each station.

The seismic moment, M_0, is the most dependable seismic intensity metric applicable to mining seismic occurrences (Gibowicz and Kijko 1994b; Sen et al. 2013; Eyre and van der Baan 2015). Seismic waveform data are frequently used to estimate the seismic moment, which involves complicated math. Slippage on an internal discontinuity in a rock mass is linked to seismic activity. To understand how seismic waves are created and how the radiated energy relates to the source, the physical properties of the source must be analysed in order to construct a mechanical model representing the physical process of fracture. The point-source approximation was used in the first mathematical description of the source mechanism, which is valid provided the observation locations are positioned at a sufficient distance from the source and the wavelengths are significant (Udías and Buforn 2017). The source is represented by a system of body forces operating at a place in this technique; these forces are referred to as similar forces since they must produce fracture.

Moment tensor is a generalisation of forces that can act at a point in an elastic material. Despite being an idealisation, it has been proven to be a valuable approximation for modelling distant seismic reactions for tiny sources relative to the seismic wavelength (Shearer 1999). Since the moment tensor is symmetric, it can be diagonalised. Its eigenvalues and eigenvectors can be determined and further subdivided into an isotropic and a deviatoric component. The sum of the eigenvalues describes the source's volume change (Fletcher and McGarr 2005; Linzer 2005; Cesca et al. 2012).

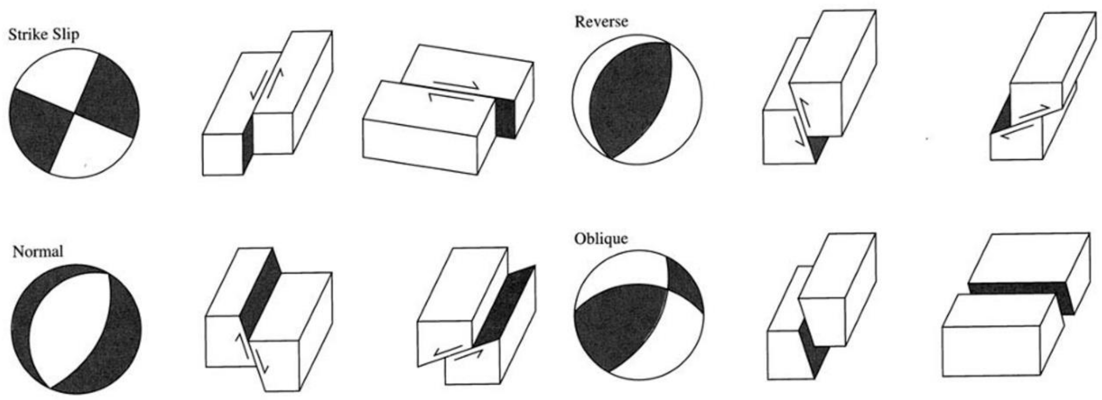

Figure 2-1 Four typical focal spheres and their corresponding fault geometries (Shearer 1999)

The most prevalent way to determine a seismic event focal mechanism is to observe the first motion of the P-wave. It has the benefit of requiring only the vertical component to be recorded, and it is easy to recognise on the seismic signal at the same time as the arrival time is selected. The first motion of the P-wave at a receiver defines whether the wave left the source in a compressional (upward) or dilatational (downward) quadrant (Shearer 1999). The result is plotted on a focus sphere as a point. If enough points are plotted, it is possible to divide the focal sphere into compressional and dilatational quadrants and represent two orthogonal planes that define the focal mechanism. Figure 2-1 depicts three distinct focal mechanisms and their respective fault planes. The focus sphere is an effective means of demonstrating various focal tools. The compressional quadrant is darkened, creating the appearance of a beach ball for the focus sphere. In these types, normal and reverse faulting can be distinguished by noting whether the centre is black or white. The centre of normal faulting is white, while the centre of reverse faulting is black.

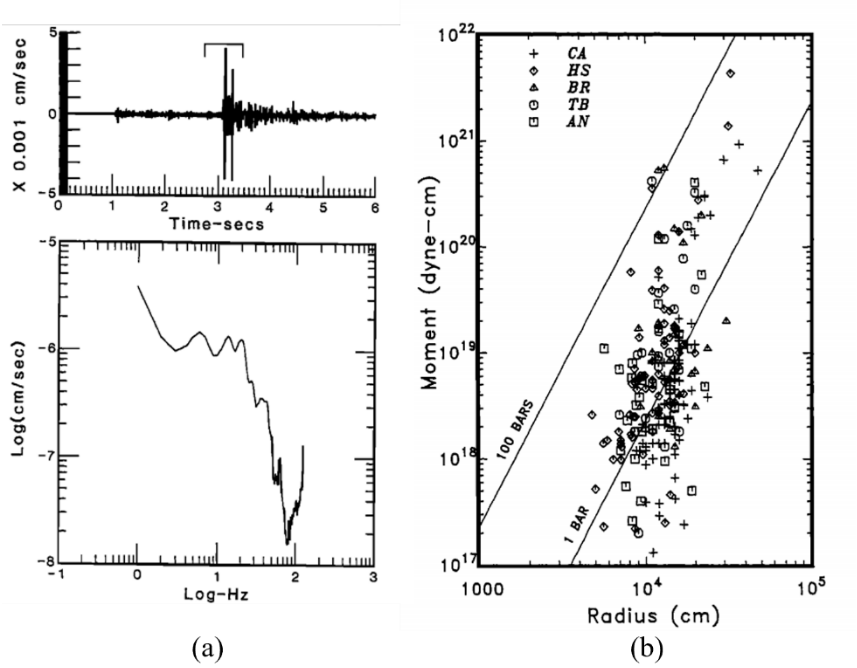

Figure 2-2 An example of (a) velocity seismogram and frequency spectrum and (b) seismic moment as a function of source radius by (Fletcher et al. 1986)

The corner frequency, f_0, of a seismic event qis the dominating frequency emitted from the source; it is associated with the seismic moment and stress drop (Mendecki et al. 1999). Figure 2-2a depicts a velocity seismogram and the matching frequency spectrum for the S-wave. Lower frequencies contain information on strain changes produced by seismicity, while higher frequencies contain information regarding stress changes. The radius of seismic source is found to be inversely proportional to f_0 (Brune 1970; Duncan and Eisner 2010; Glazer 2018). Figure 2-2b depicts the seismic moment as a function of the source radius, defined by the range of continuous decrease (Fletcher et al. 1986). Over four orders of magnitude in the seismic moment, the source radius for these occurrences is roughly consistent. This apparent consistency results in a strong relationship between stress drop and seismic moment (McGarr 1984).

Shearer (1999) defines stress drop as the average stress difference across a fault before and after a seismic event occurs. Stress drop is the estimated stress that accurately depicts stress variation during fault slippage (Gibowicz and Kijko 1994b). Seismic data can be used to calculate the dynamic stress drop (or effective stress), which is the difference between the initial shear stress and kinetic friction on the fault. There are numerous ways to determine the stress drop, some of which involve using ground velocity and acceleration information. The static stress decrease can be estimated using the magnitude and radius of the seismic moment. The seismic radius can be calculated utilising corner frequency, as shown in Chapter 3. Stress reductions can vary significantly between events. The range stress drop in mine seismicity is 0.01 MPa to 10 MPa (Gibowicz and Kijko 1994b).

Seismic energy represents the total elastic energy it emits during an event (Gibowicz and Kijko 1994b). In analysing seismic hazards, seismic energy is more straightforward than seismic moment in describing the potential damage that one seismic event can cause to artificial structures. Seismic energy is often used to measure the magnitude of seismic occurrences in mines (Gibowicz and Lasocki 2001). Typically, for the mining-induced seismic events, the energy flux was estimated based on the peak velocity, the dominant period, and the duration of the body-wave arrivals. The connection between magnitude and seismic energy was then proposed, typically as a linear relationship between magnitude and logarithm of energy (Gibowicz and Kijko 1994b). If the magnitudes of seismic occurrences are assumed to be independent random variables with equal distributions, as depicted in Figure 2-3, the frequency-magnitude relationship follows the Gutenberg-Richter relation. The seismic events that deviate from this distribution should undergo a magnitude of completeness analysis (Rydelek and Sacks 1989; Woessner and Wiemer 2005). Correlated with Figure 2-2, seismic moment and the energy parameter in the Gutenberg-Richter relation of also share a common theme, representing the energy involved in seismic activity.

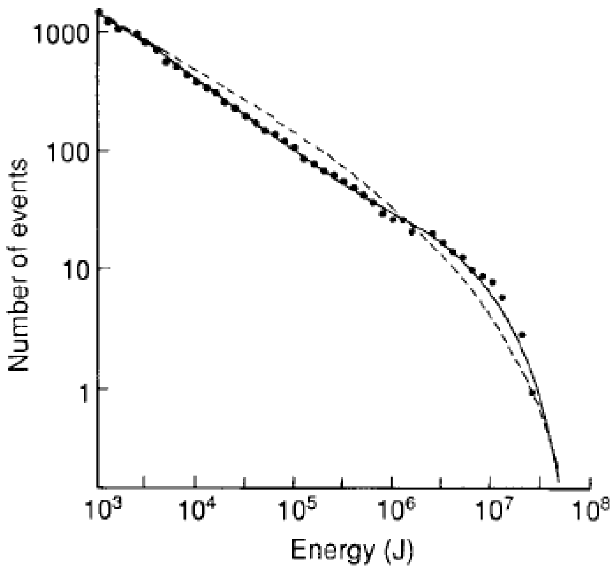

Figure 2-3 Sample case of frequency-energy distribution and a Gutenberg-Richter relation dashed curve by Głowacka and Kijko 1989)

There are numerous distinct magnitude scales for seismic occurrences (Gutenberg and Richter 2010; Udías and Buforn 2017). The magnitude defines the quantity of energy released and is independent of the generating method. The seismic energy is proportional to the square of the amplitude; hence the magnitude is proportional to the energy's logarithm. Since amplitude is simple to measure, it is the most widely used of all magnitude scales (Shearer 1999). The amplitude is calculated for a single frequency, which defines the magnitude as seismic energy radiated over a set of narrow frequency band (Shearer 1999). To account for this, the most used magnitude scale is the local or Richter magnitude, represented by M_L, which is defined as the logarithm of the highest amplitude measured by a conventional Wood-Anderson seismograph at a distance of 100 km. The definition is based on the premise that the ratio of the most significant amplitudes at two given distances is independent of azimuth and the same for all considered seismicity (Gibowicz and Kijko 1994b). The advantage of the Richter scale is that it may be used as a reference for future magnitude scales.

Mining seismic systems report maximum magnitudes between 3 and 5 and minimum magnitudes between -4 and 3 (Mendecki et al. 1999). The expected conner frequencies of all seismic events in the volume to be monitored specify the range of frequencies that must be recorded for processing to be helpful. The spectrum where the majority of energy is emitted partially depends on the magnitude of the seismicity. Low-frequency waves dominate a significant event, i.e., frequency lowers with rising energy magnitude, whereas high frequency decays more quickly with increasing distance from the event's epicentre (Jaeger 1979). It has been demonstrated that mining-induced seismic events release seismic energy ranging from micro-seismic events of 10-5 J to massive rock shocks of 109 J (Jaeger 1979). The corresponding frequency ranges from less than 1 Hz to more than 10 kHz. The coverage area and sensitivity of seismic sensors determine the sensor type and layout of a seismic network. Two types of sensors span from 1 Hz to 10 kHz frequencies: microdetectors and piezoelectric accelerometers (Mendecki et al. 1999).

A standard workflow of seismic processing is listed in Figure 2-4. Firstly, the orientation of the three component geophone data and velocity model is calibrated by check shots (or perforation shots). After that, the noise is suppressed by filtering the raw waves with a defined time-frequency to enhance the signal-to-noise ratio. Subsequently, the events are triggered to identify the signals that belong to the event. The detected events can be located using the ray or full complete form methods based on the velocity model and onset time. The double difference method can future minimise the influence of uncertain velocity model on the event location. The source mechanism can also be derived by moment tensor inversion if data acquisition coverage is large, and the shear wave arrival time is precise.

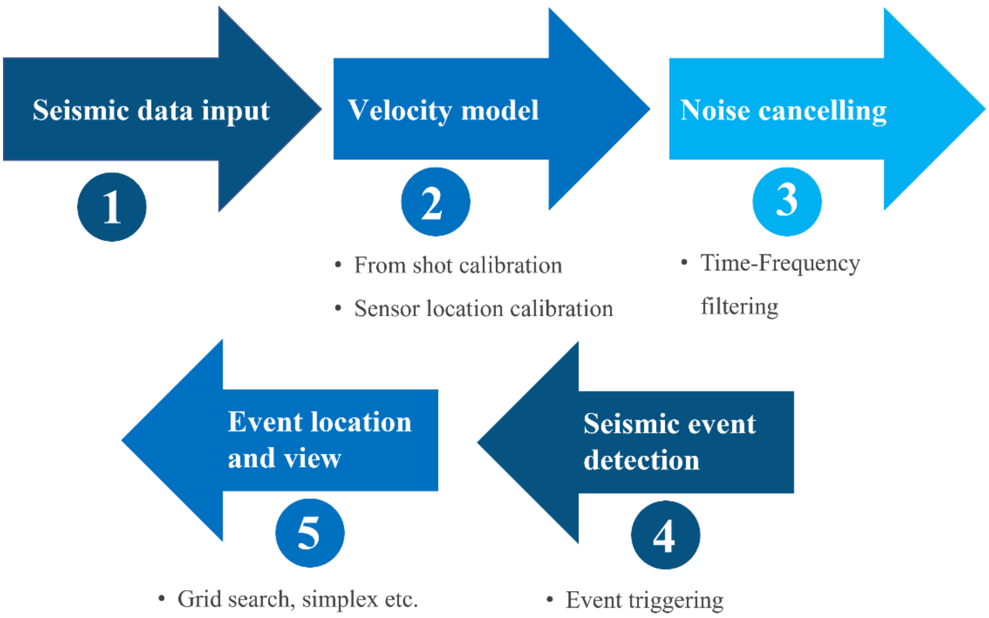

Figure 2-4 A standard workflow of micro-seismic processing

2.2. Seismicity applied in mines

The application of geophysics in coal mining can be dated back to the 1970s and originated primarily in Great Britain and West Germany. At that time, the majority of coal mines in these counties were underground. They were digging deeper, and it was becoming increasingly difficult to extract coal. Priority was given to the maintenance of mine output, and delays caused by unforeseen geological faults posed significant difficulties (Madariaga 1976; Potvin et al. 2010; Cai et al. 2021a).

Seismic monitoring in mines permits numerical evaluation of field observations. In mines, seismic monitoring is used to quantify seismicity exposure and to direct actions to prevent or reduce dynamic mining hazards. Mendecki et al. (1999)established the five objectives for measuring the seismic reaction of the rock mass after mining. The first is to locate probable rock bursts associated with moderate or large seismic events and to help prospective rescue efforts. Second, it aids in the validation of assumptions and parameters used in mine design and numerical modelling in order to improve design layouts, mining sequencing, and support procedures. Real-time seismic monitoring also helps to identify changes in seismic parameters over time and space in order to direct control measures such as the timing and placement of destressing blasts, the suspension or resumption of mining in each area, and the management of seismic exposure, among other things. The other goal is to detect unplanned or substantial changes in seismic parameter behaviour or to recognise trends that might lead to workplace instabilities. This would help in the control of any dynamic rock ejection incidents. The final goal is to improve the efficacy of the mine planning and monitoring procedures. Even if there is little damage, seismic back-analysis of huge instability is critical. To make mining safer and more productive, it is also required to examine seismic rock mass behaviour in relation to pillars, backfill, alternative mining layouts, procedures, and excavation rates.

The information gathered by the seismic sensors is concealed within seismic waves. To extract information for use in mine processing, the seismology techniques have been applied. This section will first describe seismic monitoring procedure applied in mine field in general, followed by an explanation of the seismological parameters used to describe seismicity.

There are numerous sensors available for seismic monitoring, including surface sensors and downhole sensors. At a minimal cost, the surface sensors are positioned with compact spacing and good coverage. However, the signal-to-noise ratio (SNR) is low due to the large distance from the subsurface events and the noise contamination near the surface (Duncan and Eisner 2010). The selection of downhole sensors for a seismic network relies on the required coverage area and the system's sensitivity. The frequency range from 1 Hz to 10 kHz is covered by small geophones and piezoelectric accelerometers (Mendecki et al. 1999). Geophones are suited for sparse networks, such as regional monitoring of multiple mining activities. The geophones can capture low frequencies at great distances, and it is unlikely that a significant event will occur close enough to multiple sensors to induce signal clipping. In dense networks, piezoelectric accelerometers are suitable. Since high frequencies are sensitive to distance, they attenuate rapidly. These accelerometers are useful for monitoring the entire mine. Both types of sensors should be installed in boreholes that extend beyond the fractured rock surrounding an excavation. The sensor should be grouted into the hole to ensure a strong connection to the rock. The grout should have the same acoustic impedance (density times propagation velocity) as the surrounding rock (Mendecki et al. 1999). To avoid trapping acoustic energy, the hole must be entirely filled around the sensor. Additionally, the sensors must be mounted with a specified orientation. Knowledge of the sensor's orientation is also beneficial for the localisation of events and the accurate estimation of the moment tensor.

In addition, seismic monitoring systems consist of a network of geophones that measure the acoustic waveforms created by rock fractures at the individual geophone locations. With the digitisation of geophone monitoring systems, data are automatically uploaded for access by engineers, and large-scale patterns can be evaluated (de la Vergne 2003). The utility of geophones is contingent on the accuracy of the estimated seismic velocities and the precision of the acoustic waveform measurement. When identifying the location of the centre, accuracy is often within a few metres. Nonetheless, more precise results can be attained by deploying a robust seismic network of geophones.

Implementing a monitoring network requires defining the network's spatial formation, volume, and configuration in order to reduce error. The distance to the event and the structural geometry between the event and the geophones should be considered while planning the geophones' spatial arrangement. In order to identify many waveforms from a single event, geophones should be configured at a variety of distances surrounding the event. The size of the monitoring network is determined by the number of sensors employed. The volume of the network will vary based on the identified critical structures or stops. The seismic sensor setup might be uniaxial or triaxial. Triaxial arrangements can evaluate the event's size, seismic energy, and seismic moment, although uniaxial geophones are more precise in locating the event's source. Uniaxial sensors are superior for mine coverage, while triaxial sensors are superior for post-processing seismic data. Triaxial sensors consist of three uniaxial sensors positioned orthogonally. The fundamental role of uniaxial and triaxial sensors is distinct since uniaxial sensors pinpoint the precise location of event sources, whereas triaxial sensors determine the seismic source parameters. Although uniaxial sensors are less expensive, a proper balance between triaxial and uniaxial sensors is required for a complete record of seismic wave energy, which leads to precision in source parameters and mechanism, more accurate S-wave detection, and an optimum seismic array. As a rule of thumb, one triaxial sensor is required for every three uniaxial sensors.

The induced seismicity signals collected by the sensors contain both shear and compression waves. Based on the distance between the sensors and the treatment well, the frequency typically ranges from a few Hz to thousands of Hz. As the distance from the shot rises, both the noise and the high-frequency component of the signal decrease, resulting in the shot signal being scarcely detectable by surface monitoring sensors. Ideal seismic monitoring systems transmit data in real-time to the operator (or processing centre). Monitoring seismic activity is a real-time, non-invasive, and remote method for detecting underground collapse processes. In certain instances, the limitations of the field conditions make real-time transmission difficult. Therefore, the data are stored on a disc and analysed later. Despite this, it is worthwhile to investigate the recorded seismic data after a lengthy time period. The seismic processing procedure for both circumstances is comparable; the saved data can be analysed more thoroughly to construct a processing system for investigating real-time data.

With the sensor received signal, fracture parameters, including location, radius, aperture and fracture orientation, as triggered by longwall mining operations, should be appropriately calculated using seismic data. Since seismic data collected from uniaxial geophones cannot provide intact displacement information at the sensor location, the energy and magnitude of the seismic source calculated by uniaxial data will not be complete. Thus, seismic data analysis methods introduced in previous investigations normally require high-quality triaxial seismic signals to calculate credible fracture parameters (Li et al. 2007; Leśniak and Isakow 2009; Si et al. 2015). As Figure 2-5 shows, characterising the source parameters such as M_0, R, τ, failure type and fracture orientation were used to characterise fractures induced by longwall mining. This can be achieved in metalliferous mines with permanent triaxial geophones but is difficult in coal mines since the rapid material extraction rate requires frequent relocation of geophones. In coal mines, cheap and easily removable uniaxial geophones close to production areas are preferable. This increases the difficulty of using seismic data from coal mines to obtain accurate source mechanism data for calculation and clustering analysis, especially in Chinese mines where uniaxial geophones are dominant. While in this thesis, the required parameters can be interpreted by the source mechanism derived complete triaxial signal.

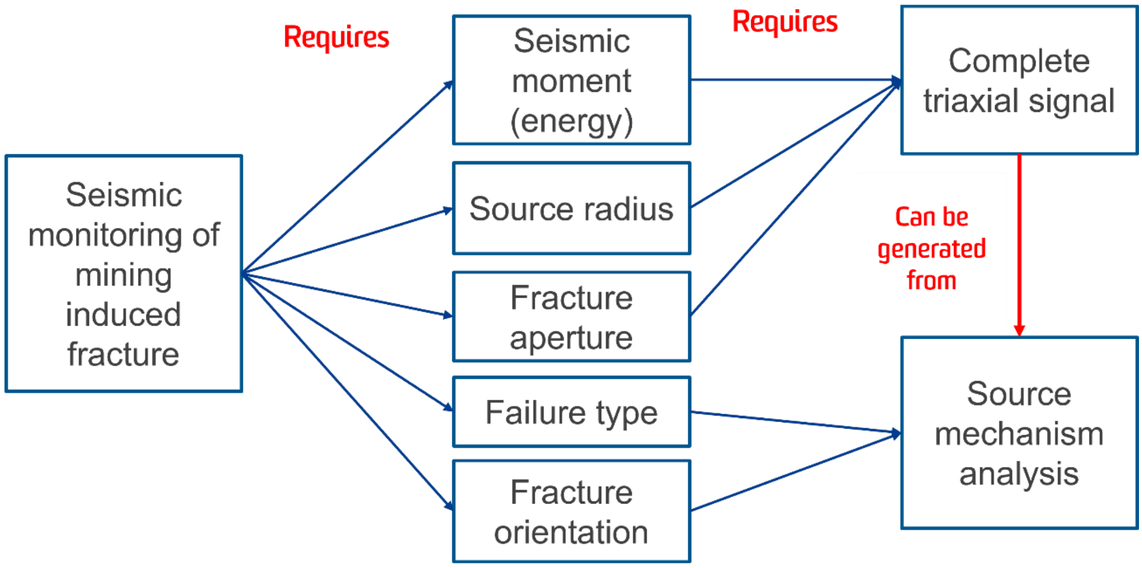

Figure 2-5 basic logic of applying seismic processing to help with fracture information

From recent studies of mining-induced seismicity, two broad types of mine tremors are observed almost universally: (Gibowicz and Kijko 1994b). One type of seismicity is directly connected with mining operations, associated with fractures forming at stope faces. This is the one that has usually been a concern. Another type is the seismicity associated with the movement of major geologic discontinuities. The magnitude of mining-induced seismicity of the first type is between low to medium. The number is directly proportional to mining activity, which can be measured by the excavation rate.

The seismicity will usually happen within 100m near the mining face and weak zones. When the stress induced by mining activity exceeds the shear strength of the material, the rock will be ruptured, which might trigger rock bursts and other disasters. The rock failure process is a natural response to mining activities and is associated with seismic events. It poses a potential hazard to mine operators, equipment, and infrastructures. Based on the distribution of seismic events, seismic monitoring may contribute to predicting mining-induced seismic hazards. Mining-induced seismicity does not distribute uniformly in space or time. In the space domain, most of the explosive types of seismic events caused by mining activities are energetically weak. In contrast, events with high energy commonly occur in tectonic regions and are presumably caused by the interaction between tectonic stresses and mining-induced stresses (Stec 2007). While in the time domain, the seismic events tend to form nests, swarms, and sequences (Gibowicz 2009a). Previous research indicates that seismic hazards are mostly related to high-energy events near mine openings (Leśniak and Isakow 2009; Cai et al. 2019). A direct relationship between seismicity and gas emission rate has been reported by (Si et al. 2015), which can be used to provide early warning for uncontrolled gas emissions. Fault slip and seismic activities can be numerically simulated to comprehensively explore seismicity induced by mine extraction (Cao et al. 2018a).

The difficulty of using a large amount of seismic data collected from mining operations for prediction purposes lies in the lack of understanding of the internal correlation between seismic events, as mining-induced seismicity is not a random process (Gibowicz 2009a), but has a high correlation with mining activities both spatially and temporally (Arabasz et al. 2005). Invalid prediction results or misleading data interpretation can be derived if the correlation is not well-understood. For instance, during seismic data analysis, questions need to be addressed beforehand, such as how much past data (time window) is required to predict future events and the maximum distance that can be effectively predicted with confidence (grid size). The time window and grid size are essential parameters for investigating spatial and temporal evolutions of seismic events. An undersized time window may not be enough to reflect the general pattern of seismic events. An oversized time window may include unnecessary noisy data that reduce prediction accuracy (Kijko and Funk 1996). Also, a too-large grid may significantly reduce the resolution/accuracy of seismic hazard prediction in space (Kisilevich et al. 2010). A too-small grid can increase computational time and cause overfitting issues. Therefore, the determination of time window and grid size for the temporal and spatial prediction of seismic hazard, respectively, remains a significant challenge using historical seismic data. In order to determine the appropriate time window and grid size, a correlation assessment of seismic data would be required in both the time and space domains.

The correlation analysis of mining-induced seismicity, including its randomness, stationary, and memoryless, would provide an understanding of the past seismic data (Bischoff et al. 2010); (González et al. 2016). However, there has been no attempt to assess the correlation of mining-induced seismicity quantitively so far. This paper focuses on filling this research gap by applying three different methods to various types of seismic data:

- The autocorrelation function (ACF) calculates the correlation with a delayed copy of the data itself, and equidistant data is required.
- The semivariogram is used to calculate the degree of correlation as a function of distance or time step.
- The Moran's I describes the correlation extended in a specific time window, commonly used for a cross-comparison and correlation threshold assessment.

These quantitative correlation assessment approaches can be applied to any parameters of mining-induced seismicity, including spatial location, onset time, energy, source radius, apparent stress, etc. This thesis will focus on radiated energy, which represents the total elastic energy radiated by mining activities and better reflects the influence on artificial structures compared to the magnitude and other parameters (Gibowicz and Kijko 1994a).

Furthermore, many researchers proposed that seismic events can be divided into clusters due to the spatially distinct rock mass failure processes associated with temporally dependent mining activities (Gibowicz 1986; Leśniak and Isakow 2009; Woodward et al. 2018). The seismic events from different clusters may be independent, whereas events within one cluster are internally correlated (Kijko and Funk 1996). During a mining process, the overall correlation of the entire seismic dataset may be different from the correlation within individual clusters because the cluster-based data can be recognised as being related to a specific area or time. Thus, it is necessary to re-assess correlation characteristics within each cluster and between clusters after seismic data is clustered.

Instead of seismic energy used in correlation analysis, the seismic source mechanism inversion as a typical seismic analysis method, is also essential for the mining industry to understand rock fracturing behaviour during resource extraction. By conducting seismic moment tensor inversion, the seismic observations of a discrete seismic event can be connected to the physical mechanism at its sources, such as the event failure mechanism, principal strain axes, and potential failure plane orientations (Young et al. 1992; Shearer 1999; Gibowicz 2009; Zhao et al. 2018). Evaluating event failure mechanisms is crucial for understanding the fractures induced by progressive resource extraction in underground mines. The seismic event represents either the initiation and propagation of new fractures or the slippage of pre-existing weak planes in rock mass as a response to mining activities (Lei et al. 2014). Results on the failure plane orientation can also help describe the spatial distribution of mining-induced fractures and generate a probabilistic fracture network (Maxwell et al. 2010; Zhao et al. 2019).

In a pioneering work recently published to solve the problem of the impact of rock failure mechanism on the mine field, seismic imagining has been applied for downhole monitoring especially to image fracture network deformation (Maxwell 2010). A fracture network model defined by seismic data should contain information on the geometric properties of individual fractures, such as location, orientation, size and aperture, which can be obtained by advanced seismic signal processing and data analysis. Seismic events triggered during fracture initiation or reactivation are widely used to infer induced fracture network models that involve large-scale rock failure, such as hydraulic fracturing in unconventional reservoir recovery (Dershowitz et al. 2010; Cipolla et al. 2011; Sayers and den Boer 2012; Zhao et al. 2014; Carpenter 2017). Each seismic event can be regarded as a fractured opening (or sliding) in a tensile (or shear) mode, and each failure occurring on a new or pre-existing fracture plane with a specific geometry and radiated energy can be seen as part of the induced fracture network. Hence, the geometry and complexity of fractures can be determined by analysing seismic event patterns and estimating the stimulated volume during the generation of microfractures (Rogers et al. 2010; Zhang et al. 2019; Schultz et al. 2020a). Therefore, similarly, seismic event distributions during mineral extraction can be used to reconstruct the induced fracture network. Note that the failure mechanism of hydraulic fracturing in the oil and gas industry is mostly driven by the pore pressure change caused by fluid injection, but mining-induced fractures are initiated by stress change and strata movement after mineral extraction. This suggests that mining-induced fractures and seismic responses may show different characteristics.

There are other methods involved in seismic processing has the potential to help this thesis topic as well. Many researchers have also developed other methods for passive seismic emission tomography. Duncan and others have proposed a method for increasing the resolution of the amplitude selection by determining the vertical distribution as measured by parasitic sources. Surface monitoring methods have also been developed to stimulate fracturing (Abbott et al. 2007; Barker 2009). As a rule, a set of vertical telephones is placed along the spokes of a wheel centred on the head of a treatment well.

Duncan and Eisner (2010) investigated the details of the collection, processing, and migration of this technology.

A fracture network model defined by seismic data should contain information on the geometric properties of individual fractures, such as location, orientation, size and aperture, which can be obtained by advanced seismic signal processing and data analysis. Seismic events triggered during fracture initiation or reactivation are widely used to infer induced fracture network models that involve large-scale rock failure, such as hydraulic fracturing in unconventional reservoir recovery (Dershowitz et al. 2010; Cipolla et al. 2011; Sayers and den Boer 2012; Carpenter 2017; Zhao et al. 2019). Each seismic event can be regarded as a fractured opening (or sliding) in a tensile (or shear) mode, and each failure occurring on a new or pre-existing fracture plane with a specific geometry and radiated energy can be seen as part of the induced fracture network. Hence, the geometry and complexity of fractures can be determined by analysing seismic event patterns and estimating the stimulated volume during the generation of microfractures (Rogers et al. 2010; Zhang et al. 2019; Schultz et al. 2020b). Therefore, similarly, seismic event distributions during mineral extraction can be used to reconstruct the induced fracture network. Note that the failure mechanism of hydraulic fracturing in the oil and gas industry is mostly driven by the pore pressure change caused by fluid injection, but mining-induced fractures are initiated by stress change and strata movement after mineral extraction. This suggests that mining-induced fractures and seismic responses may show different characteristics. Therefore, this paper mainly focuses on the inversion of fractures induced by longwall mining, especially the coupling with the solutions of rock failure mechanism and fracture geometry based on seismic moment tensors.

In recent years, understanding the fundamental mechanisms and processes of rock failure and fluid transport in mining-induced fractures is significant and has a vital role in the safety of coal extraction above gassy seams or confined aquifers. It is investigated that mining-induced fracture evolution and water flow in coal seam floor above a confined aquifer by numerical simulation (Lu and Wang 2015a).

Seismic techniques have developed as a crucial tool for monitoring fluid processes at the scale of a reservoir. Seismic activity in a subsurface reservoir may be caused by the brittle deformation of reservoir rocks resulting from the fluid injection. The capacity to locate the sites of seismic events enables the tracking of fluid movement and investigation of the reservoir's stress level. Seismic monitoring applications have included seismic mapping activity caused during a programme of cyclic steam stimulation (McGillivray 2005) or CO2 sequestration (White 2012) , as well as monitoring and characterisation of hydraulic fracturing (Nolen-Hoeksema et al.; Sasaki and Kaieda 2002; Rutledge and Phillips 2003). In many instances, the primary goals of seismic monitoring are to detect and precisely pinpoint all seismic activity above a specified magnitude threshold. Typically, this is achieved by utilising techniques derived from earthquake seismology, whose procedures are extensively documented in the literature. Beyond such first-order issues regarding the location and distribution of seismic activity, various earthquake-related approaches can be used to define seismic occurrences in greater detail, assuming appropriate data quality. This may involve spectral analysis for determining rupture size and stress drop, moment-tensor inversion, and alterations to the Coulomb stress field. This tutorial's objective is to provide a quick summary of selected techniques for characterising seismic sources. Although the background theory is established from the standpoint of earthquake seismology, the approaches outlined are intrinsically scalable and extensively relevant to reservoir-scale seismic monitoring.

Moreover, mining-induced seismicity is a persistent issue in the majority of mines. Large overburden pressure and tectonic pressures exert strain on subterranean rock and coal strata. The sequence of mining excavation perturbs the original stress field, which may stimulate the creation or re-opening and migration of microfractures around and beyond excavation openings, manifesting as seismic activity (Cao et al. 2018b). Hazzard and Young (2004) described a method for extracting quantitative seismic source information from events generated by a particle flow code (PFC) model with low numerical damping. These techniques might be applied to any current PFC model in order to extract seismic data. The algorithms function in both 2D and 3D, and it was demonstrated that the PFC models in both dimensions create realistic locations, magnitudes, and mechanisms.

2.3. The recent works related to seismic.

The purpose of this thesis is to interpret the induced fracture using the seismic monitoring method. This method has been used in the petroleum industry and hard rock mines. The reproducibility of phenomena, such as fault initiation and development, elastic rebound, uplift or seismic activities, etc., offers an attractive supplement to physical model tests in both geological and geomechanical problems.

During the past decades, significant progress has been made in the development of induced seismicity monitoring for related human activities. Hydraulic fracturing (HF) and induced seismicity monitoring are operating procedures for the safe and effective production of oil and gas from unconventional resources, particularly shales (Li et al. 2018). HF is a technique that is used for extracting petroleum resources from impermeable host rocks. In this process, fluid injected under high pressure causes fractures to propagate. One concern is HF-induced seismicity since fluids driven under high pressure also have the potential to reactivate faults. Therefore, great effort has been made to provide the geometry of fractures, stimulated volume, geomechanical models of the relationship between seismicity and HF, the spatial-temporal distribution and source mechanisms of seismic events (Schultz et al. 2020b). Figure 2-6 presents an example of petroleum development of the Wufeng-Longmaxi Formations, exceptional increases in earthquake rates in the Zhaotong and Changning shale gas fields (Chen et al. 2017; Lei et al. 2017). The location of seismicity is shown alongside focal mechanisms of larger magnitude events is shown in the figure. The cause of an abnormal earthquake as the overpressure-driven reactivation of pre-existing faults is investigated using seismic monitoring technology in this research. It indicates that careful monitoring of induced seismicity is essential for safe and effective shale gas exploitation.

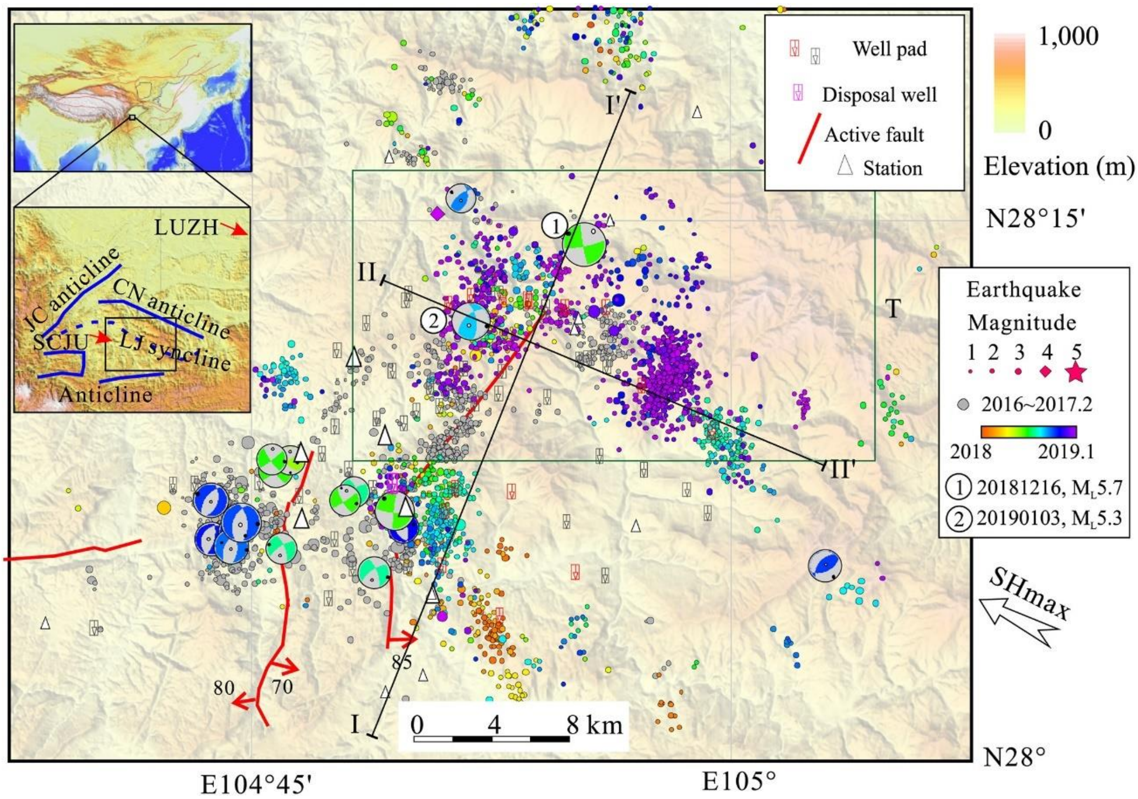

Figure 2-6 China's Sichuan Basin, depicting HF wells and earthquakes near Changning shale gas block. Relocations of earthquakes are depicted alongside focal mechanisms of larger events (beach balls), stimulated HF pads (red polygons), pads (red polygons), producing HF wells (black polygons), disposal wells (pink polygons), faults (red lines), and recording stations (triangles). Figure reproduced from (Lei et al. 2017)

Seismicity in underground coal mines, on the other hand, also requires the comprehensive fracture invitation, and this method has great potential to be applied in the longwall coal mine. However, different from hydraulic fractures, the mechanism applies to generate fractures, and seismicity is other than fluid injection. Experiments have been conducted to show that coal is an elastic, brittle- plastic material with strain-weakening behaviour (Wang et al. 2013). The stress-strain curves show the typical behaviour of coal with increasing strength and effective confining stress. An initial non-linear portion of the curve is caused by the closing of the pre-existing cleats in the coal and followed by a linear elastic response at intermediate stresses. A final non-linear portion develops due to pre-rupture cracking. The fracture generated in the mine is a result of stress condition change. There are two mechanisms causing seismic events. One type of rock failure results from the dynamic loads imposed by fault-slip events, and the other type results from the failure of the rock mass itself (Gill et al. 1993). Sometimes there is a third type defined, which is a combination of the two mechanisms and is referred to as pillar burst. A review is made to simply investigate the type of underlying mechanism that caused the seismic event. Table 2-1 presents examples of case studies classifying the underlying mechanism involved in seismic events.

Table 2-1 Classification according to the underlying mechanism

The underlying mechanism causing seismic event	
Instantaneous slip on an existing geological discontinuity	(Gill et al. 1993)
	(Kaiser and Maloney 1997)
	(Lei et al. 2021)
	(Pine et al. 2006)
	(Cai et al. 2021b)
Instantaneous fracturing of highly stressed rock	(Kleczek and Zorychta 2022)
	(Bischoff et al. 2010)
	(Lu and Wang 2015b)
	(Arabasz et al. 1997)
Both	(Brummer et al. 1990)
	(Yi and Kaiser 1993)
	(Bischoff et al. 2010)

Despite the fact that different mechanisms occurred in the mining process, researchers already make an effort in hard rock mines. The failure process and the failure mechanism of a rock mass during transforming from open pit mining to underground mining in the Shirengou iron mine site is investigated by seismic processing (Zhao et al. 2017). Idea results were obtained with high efficiency from seismic monitoring and moment tensor analysis. However, their studies' limitations include the rock type, the assumption of a double-couple source model and a relatively low efficient classification method. In my research, I would like to apply the article's Hybrid MTI analysis approach to a working longwall mining face. The rock mass fracture processes are explored, including fracture orientations, fracture scales, and implemented planes. Figure 2-7 depicts three fracture zones and four fitting planes, as well as the slip tendency analysis. It demonstrates that the rock mass of the pit bottom and the top of the goaf are vulnerable to additional damage. The failure type of rock mass during the transition from open-pit to underground mining is mostly shear failure and tensile failure, which are generally concentrated in the ceiling of the goaf. This means that seismic monitoring and moment tensor inversion may effectively evaluate rock failure processes and mechanisms.

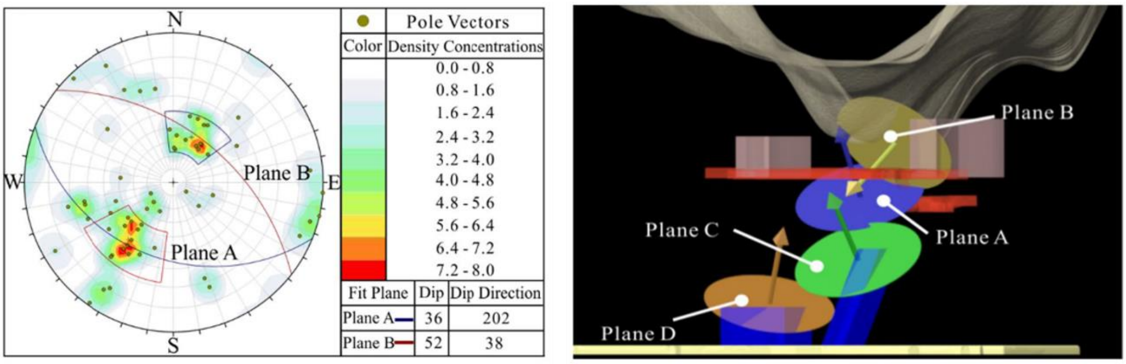

(a) (b)

Figure 2-7 Azimuth statistics for fracture planes. (a) The stereographic projection of the fracture planes. (b) The schematic diagram of the four fitting planes (Zhao et al. 2017)

Except for the source mechanism, the source radiation pattern more directly presents theoretical and observational results of the source displacement or velocity at the occurrence of the vibration of the source tremor. Within a shear-tensile failure, the radiation pattern is governed by two additional parameters: tensile angle α and Poisson's ratio ν (Kwiatek and Ben-Zion 2013), as can be seen in Figure 2-8. It is assumed that the shape of a tensile motion is like a pulse with no displacement at the end, and the tensile angle concept is used to describe the angle between the unit slip vector and unit fault normal. The tensile angle is measured between the vector along the slip direction projected on the fault plane and the actual direction of the fault movement, which is positive for fracture opening and negative for closing motions. With the help of the radiation pattern, the radiated seismic energy is estimated accurately in complex station network conditions. Other than seismic energy, the radiation pattern has the potential to improve the understanding of the motion of the seismic source, and this will be discussed in this thesis.

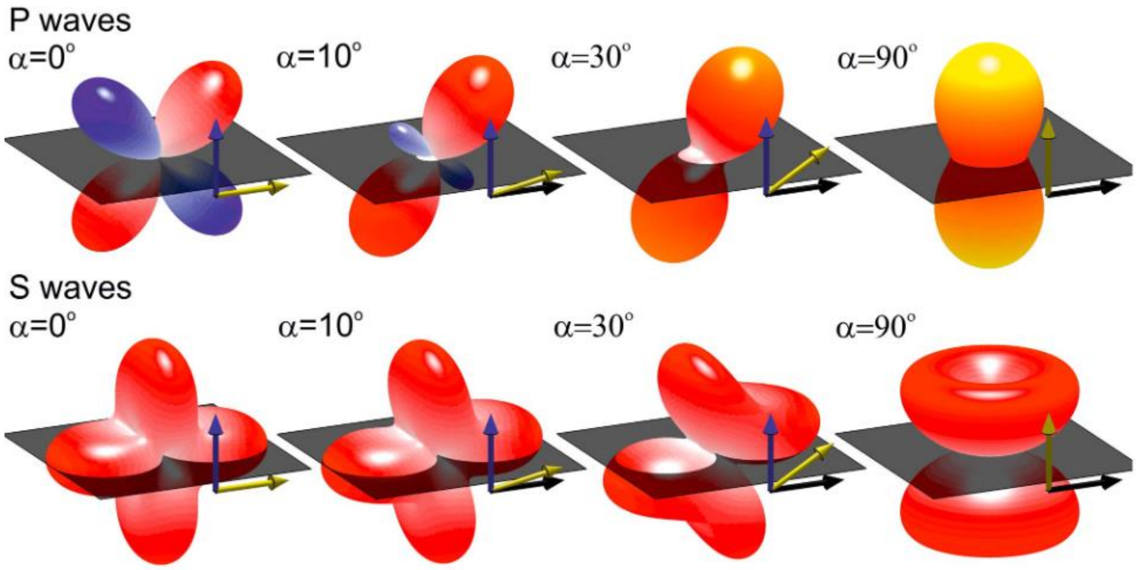

Figure 2-8 Influence of the tensile angle on the shape of the radiation pattern of (top)P and (bottom) S Waves assuming Poisson's ratio 0.25 as a function of the tensile angle. (Kwiatek and Ben-Zion 2013)

The seismic radiated energy also helps to understand the distribution of seismic events and the relevance within it, then develop the characteristic and prediction method of the onset of HE seismic events induced by mining (Si et al. 2020). Figure 2-9 presents the relevance and the cluster trend of seismic events around one high-energy seismic event using principal component analysis (PCA) and kernel density estimation. It represents that the high-energy events have a strong correlation with the clusters of past seismic events, i.e., high-energy events are not isolated and, therefore, can be predicted if the development of event clustering has been characterised early enough.

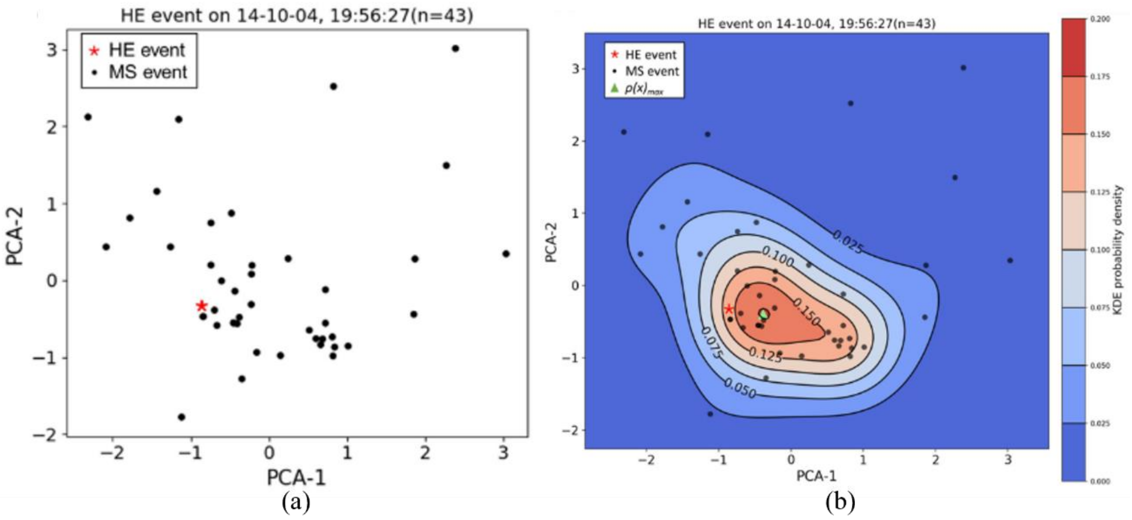

Figure 2-9 Clustering of seismic events before the high energy (HE) event A: a 2D PCA transformation, and b probability density function obtained from the kernel density estimation (Si et al. 2020)

In order to have a more specific understanding of the correlation within the seismic data, the semivariogram function (SVF) as a geo-statistics method and autocorrelation function (ACF) from random field theory and time series analysis is applied to seven soundings of well logging at a location in Hayti, Pemiscot County, Missouri as Figure 2-10 shows (Onyejekwe et al. 2016). The scale of fluctuation (SOF) is also used to quantitively determine the spatial variability of geotechnical parameters in this research. The SOF calculated from SVF was mostly higher than that computed using the ACF based on the data analysis in his research.

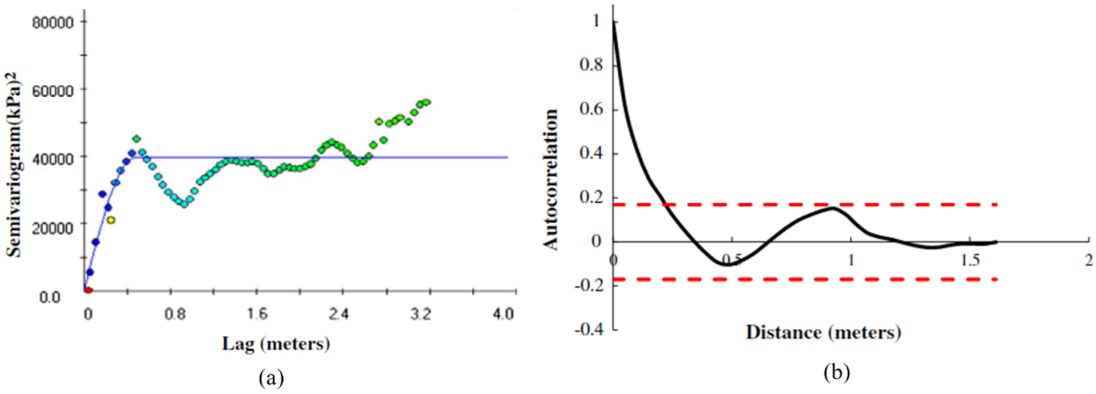

Figure 2-10 a) Semivariogram Plot and (b) Autocorrelation Plot (Onyejekwe et al. 2016)

The correlation assessment of seismic data improves the understanding of fault initiation and development, elastic rebound, uplift or seismic activities, which offers an attractive supplement to physical model tests in both geological and geomechanical problems. It has been shown that the rock failure process analysis can model geological processes and rock engineering problems (Tang 2002). FLAC 3D, as a finite difference element method software, is suitable for simulating the 3D model related to the mining process.

Cao et al. (2018b) use the built-in DFN facility inFLAC3D to create a discrete fracture model (Figure 2-11a) following a power law size distribution distributed throughout a 3D continuum model in a probabilistic way to account for the stochastic nature of seismicity. The DFN-based modelling approach developed was adopted to simulate the evolution of seismicity induced by the progressive face advance in a longwall top coal caving panel at Coal Mine Velenje, Slovenia. The model results indicate that the power law fracture size distribution can be used to model longwall-mining-induced seismicity. Cai et al. (2021b) apply the 3D model in Figure 2-11b to validate the mechanisms of fault reactivation and its induced coal burst based on the superposition of static and dynamic stresses, which include two kinds of fault reactivations from mining-induced quasi-static stress

(FRMSS)-dominated and seismic-based dynamic stress (FRSDS)-dominated. Yasitli and Unver (2005) present 3D modelling work of the top-coal-caving mechanism by using the finite difference code FLAC 3D at the M3 longwall panel of the Omerler Underground Mine located at Tuncbilek Turkey (Figure 2-11c). A special pre-fracture blasting strategy just sufficient enough to form cracks in the top coal is suggested by means of comparing with the results of numerical modelling.

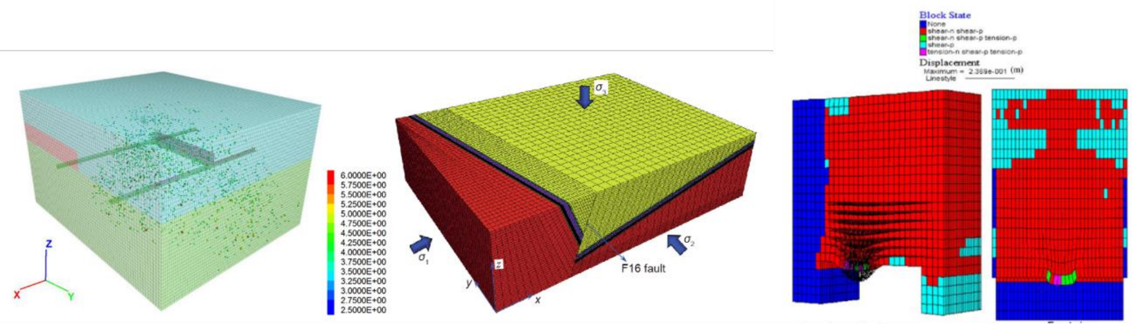

Figure 2-11 (a) Three-dimensional distribution of mining-induced seismicity and the released energy at LTCC panel K.-50/C during coal production. (Cao et al. 2018b) (b) Numerical modelling for the No. 25 mining district of Yuejin Coal Mine. (Cai et al. 2021b) and (c) State of failure in top coal during caving after pre-fracture blasting. (Yasitli and Unver 2005)

On the other hand, Discrete element modelling is a more proper way of directly modelling the fracture behaviour based on the construction model but consumes a lot of computation (Lei et al. 2017). As shown in Figure 2-12a and b, Harthong et al. (2012) studied the influence of fracture network properties on the mechanical behaviour of fractured rocks by integrating 3D fractal DFNs into a bonded-particle model associated with the smooth joint contact treatment. Pine et al. (2006) apply the combined similar model to tackle the geomechanical problems for various engineering applications, as shown in Figure 2-12c. It illustrates that the presence of natural fractures may dominate the strength of slender pillars but have a reduced influence on wider pillars.

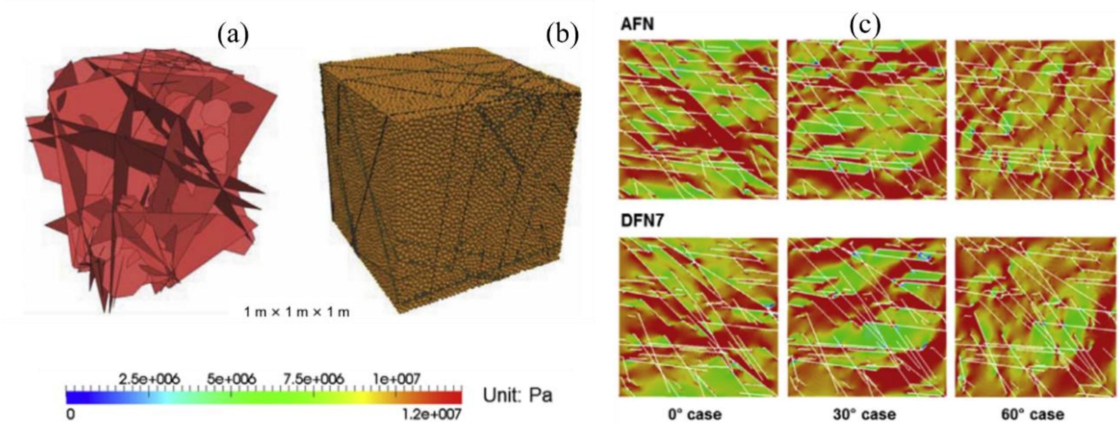

Figure 2-12 Integration of (a) a fractal DFN into (b) the YADE bonded-particle model (BPM) for mechanical modelling of fractured rocks. (Harthong et al. 2012) (c) Heterogeneous distribution of local maximum principal stresses in fractured rocks. (Lei et al. 2017)

Figure 2-13 depicts another application of the discrete element approach. It created a discontinued modelling technique to explore Longwall Top Coal Caving behaviours, including stress distribution, coal and rock failures, top coal caving, and roof strata rupture, as well as the influence of overburden movement on top coal caving (Le et al. 2018). Figure 2-13 shows an example of a state of failure in the top coal before its first caving. As can be seen, the top coal failed in both intact blocks and discontinuities. The mechanism of the first caving of top coal, in this case, can be attributed to stress caving

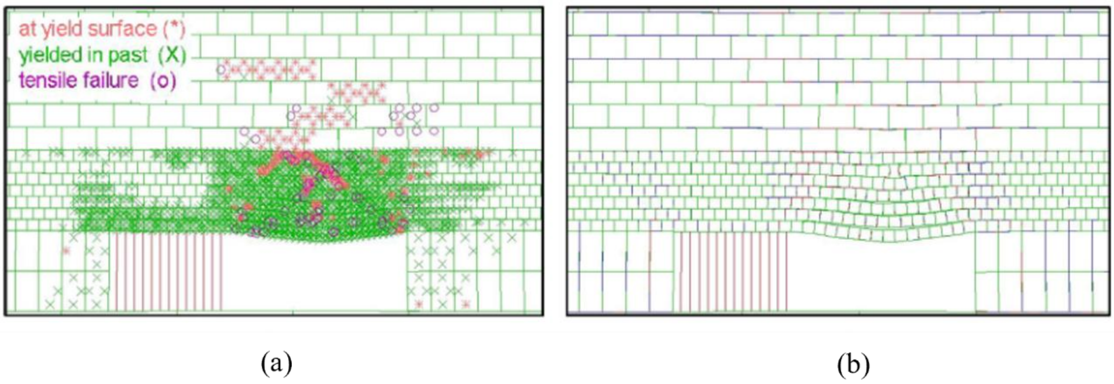

Figure 2-13 Failure in top coal before the first caving. (a) Block failure and (b) discontinuity failure (Le et al. 2018).

2.4. *Summary*

This literature study is not meant to address all aspects of seismicity; rather, it will focus on fundamental concepts and vocabulary. The literature review will also provide background information for the identification of significant parameters to be explored in the Licentiate Thesis cases.

During the recovery of Mineral resources, instabilities in underground mines may arise from natural factors, including geological settings anomalies, structural discontinuities, fracture patterns and lithology changes in the rock mass. Therefore, the importance of seismic monitoring in the rock mass around the longwall mine cannot be underestimated. The review first introduces a comprehensive procedure of seismic processing and the involved challenges. According to the review, it shows a possibility to understand the seismic signal from the site of the source behaviour, which helps resume seismic signal information from incomplete seismic signals. Then seismic monitoring application in mines is introduced, which covers most of the techniques involved in this thesis. In the third section of this chapter, the cases are detailed and introduced at each aim of this thesis introduced in Chapter 1. Each case has challenges that will be addressed in this thesis and finally form a comprehensive seismic processing method to investigate fracture behaviour in longwall mining.

The conclusion from this literature review is that the aspects that should be investigated for mining induced fractures in longwall mining are source mechanism, seismic energy and magnitude, spatial and temporal correlations, fracture location, orientation and size.

Chapter 3. Processing of uniaxial and triaxial seismic data

This chapter investigates the induced seismic wave processing procedure, which generally includes the waveform pre-processing, seismic event location, energy and seismic source mechanism calculation. A novel method of generating synthetic triaxial waveforms from uniaxial seismic sensors has been proposed.

First, the preliminary processing of mining-induced seismic signals is shown in Section 3.1 based on the data received from a case study underground coal mine. The parameters related to the location and source mechanism of seismic events are then calculated in Section 3.2. In order to simultaneously investigate the parameters related to seismic source mechanism and energy magnitude at a specific event location, a new approach to generate synthetic triaxial waves from uniaxial signals is proposed in Section 3.3. This is achieved by using the source information and radiation pattern obtained in Section 3.2. Additionally, as a demonstration of the proposed method, seismic data obtained from the case study mine were analysed and shown in Section 3.3.

Seismic wave signals were received from the Yuejin coal mine, which was operated by Yima Coal Mining Group in the west of Henan Province, China. Longwall (LW) 110 in this mine with comprehensive seismic monitoring data was selected as the case study panel. The panel was about 800-830 m deep with significantly high in-situ stress. The panel retreat started in May 2011 and was completed in October 2012, which only mined about 570 m (about 1.2 m per day) over the 16 months monitoring period due to the high coal burst risk. LW110 was adjacent to the mined goaf in the north, and the F16 reverse fault in the south, and solid unmined coal in the east and west (Cai et al. 2018). The panel was 865 m long and 191 m wide. The thickness of the target coal seam ranged from 8.4 m to 13.2 m (about 11.5 m on average) with a moderate dipping angle of 12°. Longwall top coal caving was applied in this panel, which may also increase the coal burst risk (Li et al. 2018). During the retreating period, the panel was exposed to frequent seismic hazards, which induced more than ten coal bursts. This chapter is based on a submitted paper III.

Chapter 3 is oriented to address Aim 1, which focuses on developing a seismic source mechanism-based parameter analysis method from uniaxial or triaxial seismic traces.

3.1. *Uniaxial seismic signal acquisition and processing*

A 16-channel "ARAMIS M/E" seismic monitoring system developed by EMAG (Poland) was installed to record seismic signals from April 2011. More information about the monitoring system can be found in Cai et al. (2018). The "ARAMIS M/E" seismic monitoring system is designed to collect raw data from its sensor array in the form of electrical signals. These signals show movement produced by seismic activity. A succession of processing stages are used to make sense of these signals. The raw data is converted using an Analog-to-Digital Converter (ADC) as the initial stage in this procedure. This gadget converts analogue electrical signals into digital data that a computer can process. Following the ADC conversion, the data is de-noise processed. This stage is critical in reducing the impact of noise from diverse sources and so improving the clarity and dependability of the seismic data. The next step is to adjust for instrument responses. This is required to account for the system's sensors' distinctive properties and potential biases. The accuracy of data interpretation is increased by accounting for these issues. Following that, the data is processed through a series of stages, including Fourier Transformations. This mathematical method converts time-domain signals to frequency-domain data. This transformation is critical for distinguishing between different types of seismic waves because it allows for the separation and analysis of the various frequency components within the seismic data. The procedure concludes with the analysis and interpretation of the produced data. This is frequently accomplished through the use of computer algorithms, such as triggering mechanisms and visualisation tools. These techniques aid in the identification and isolation of specific signals indicative of seismic events.

The seismic dataset during the retreating period contains 4,725 seismic events, and each seismic event has seismograms detected by 4 to 16 sensors. The sampling rate (i.e., the number of samples acquired per second) of the sensors is 200 Hz. Four of the 16 sensors, S13, S14, S15, and S16, are installed in the two longwall entries for the LW110 panel. Since only uniaxial sensors are used in the Yima coal mine, it provides the advantage that these four sensors can be easily relocated during mining. As Figure 3-1 shows, S13 and S14 sensors are installed at the maingate, which relocated five times during progressive coal extraction in this panel. The sensors at the tailgate, S15 and S16, also relocated eight times since the rock is more unstable. The sensor would be relocated when the working face approached close to the sensor's current location. Since all 16 sensors are located around several different longwall and development workings and conduct the monitoring work at the same time, at least four sensors can receive waveform signals from each seismic event, which guarantees the quality of event location.

This study used the commercial seismology software Insite-Geo from Applied Seismology Consulting (ASC) to extract seismic signal information and calculate moment tensors. Since the majority of seismic sensors were installed around the case study longwall panel, the input P wave velocity model was assumed as homogeneous with a velocity of 4,000 m/s as an average value based on Cai et al. (2014). Using this velocity model, the collapsing grid search algorithm was implemented to locate seismic events.

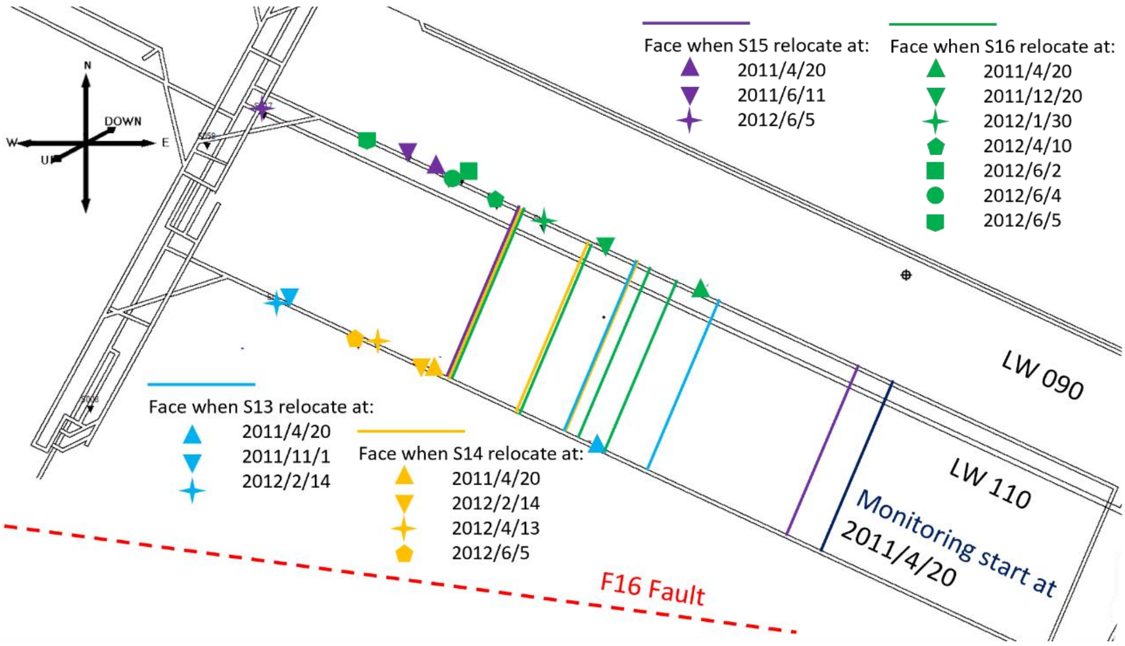

Figure 3-1 Distribution of seismic sensors and their relocation time during the mining of LW110, the coloured lines also show the face positions when those sensors were relocated.

3.1.1. Seismic wave attenuation

Since seismic waves would not travel through a perfectly elastic medium, rocks as the transport media are causing dissipation of energy while seismic waves propagate through them. This also results in the decay of the amplitude of seismic waves. Attenuation is related to velocity dispersion. To calculate the difference between the source displacement and the displacement recorded by seismic sensors, the attenuation of seismic waves was considered. The amplitude attenuation through inhomogeneous media is calculated as (Aki and Richards 1980):

$$A = A_0 e^{\left(-\frac{\pi D}{l Q}\right)} \tag{3.1}$$

where D is the distance between the source and the sensor, A_0 is the seismic wave amplitude at the source location, and l is the wavelength of the radiated P wave. Attenuation is measured by a dimensionless number known as the rock quality factor Q. Q is defined as the ratio of stored energy to dispersed energy, which is related to the physical state of the rock. It measures the relative energy loss per oscillation cycle. Q increases when the density and the velocity of rock material increase. In this study, P waves were assumed to be transported in a homogeneous media; thus, a constant Q was applied. The rock quality factor Q is selected as 200 in the following study for the case study coal mine, which is an average value of unsaturated mudstone. Since the abutment stress is about 50-200 m in front of the mined zone (Cai et al. 2018), according to Equation 3.1, the amplitude attenuated about 15% of the original amplitude.

3.1.2. Signal filtering

Except considering the attenuation of seismic waves, the raw seismic waves need to be filtered before any signal processing. The signal frequency received by sensors is in a wide range, which depends on the geological condition, mining depth, distance to sensors, etc. When the distances between geophones and seismic sources are relatively short, there is minor interference to the signals. The dominant wavelength of seismic waves is given by:

$$\lambda = \frac{v}{f} \tag{3.2}$$

where v is wave velocity and f is the dominant frequency. A graph of wavelength as a function of velocity for various frequencies is plotted in Figure 3-2. The seismic wave velocity in the case study mine is assumed at about 4000 m/s. In addition, typical seismic wavelengths range from 100 m to 250 m and generally increase with depth. Therefore, the dominant frequency of seismic signals typically varies between 40 Hz and 16 Hz and decreases with depth.

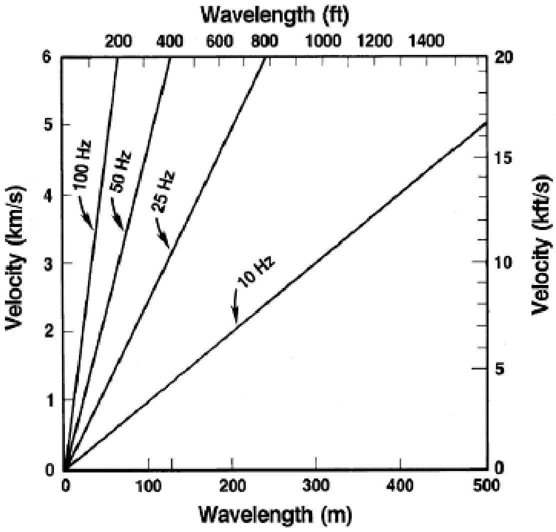

Figure 3-2 The wavelength graph as a function of velocity for various frequency values (Sheriff 1976)

To analyse seismic signals in the frequency domain, the fast Fourier transform (FFT) can convert a signal from its original domain (often time or space) to a representation in the frequency domain and vice versa. The FFT is obtained by decomposing a sequence of values into components of different frequencies. After calculation, the frequency spectra can be displayed and used to determine the main frequency range that is of interest.

There are generally two kinds of frequency distributions of seismic signals. One of them is the seismic events triggered by the mining-induced fractures around the longwall panel. Such an example is the seismic event A that occurred at 07:22:36 on 23/07/2011, as shown in Figure 3-3. Since the sampling rate of the ARAMIS seismic monitoring system is 500 Hz, the duration of the signal recorded is 3.2s in total. According to the FFT result in Figure 3-4, the dominant frequency of seismic event A is about 127 Hz.

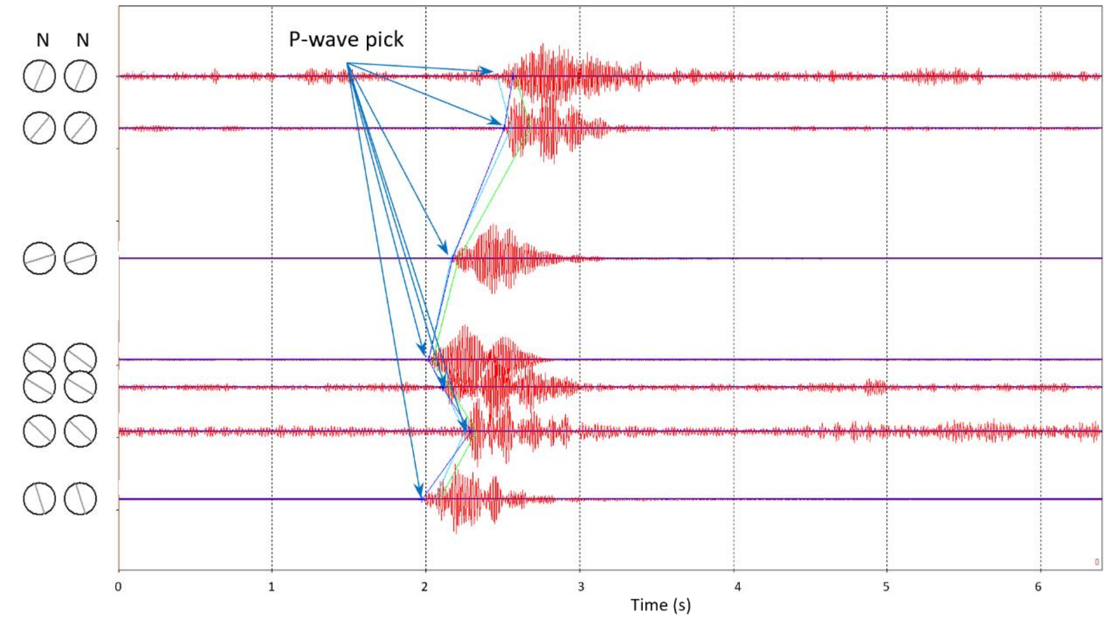

Figure 3-3 Samples of uniaxial seismic signals with the pick of P wave arrival time.

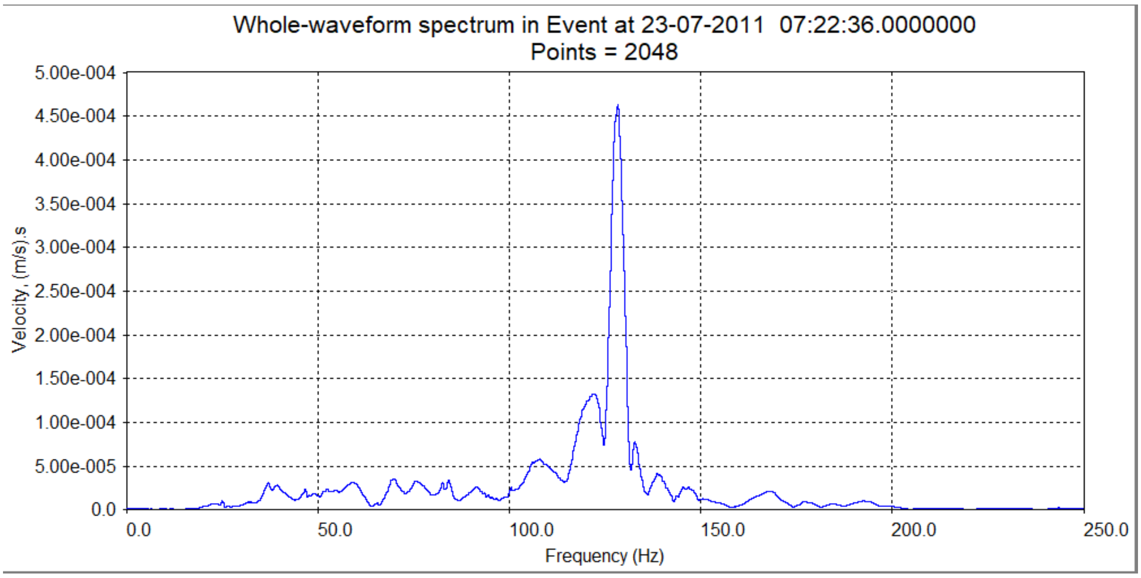

Figure 3-4 FFT result of the seismic event A at 23/07/2011

The other kind of seismic signal has a low dominant frequency, which can be detected as rock failure events that occur far away from the panel. These events have a low dominant frequency. The signal duration of these events is normally very long, and the amplitude is small compared to other near-panel events. Figures 3-5 and 3-6 show that event B, which occurred on 19/08/2011, is located far away from the current panel using the lowpass filtering. It could be induced by other workings or fractures triggered by regional stress change. Therefore, the seismic event of this kind is excluded from this study.

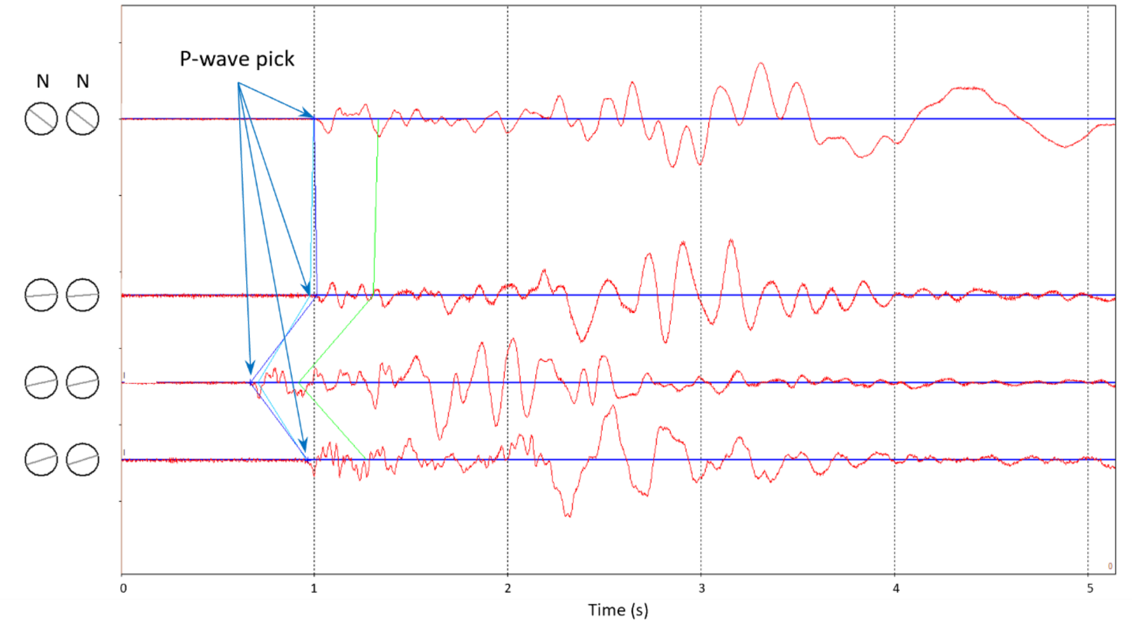

Figure 3-5 Uniaxial seismic signals of Event B on 19/08/2011 with the pick of P wave arrival time.

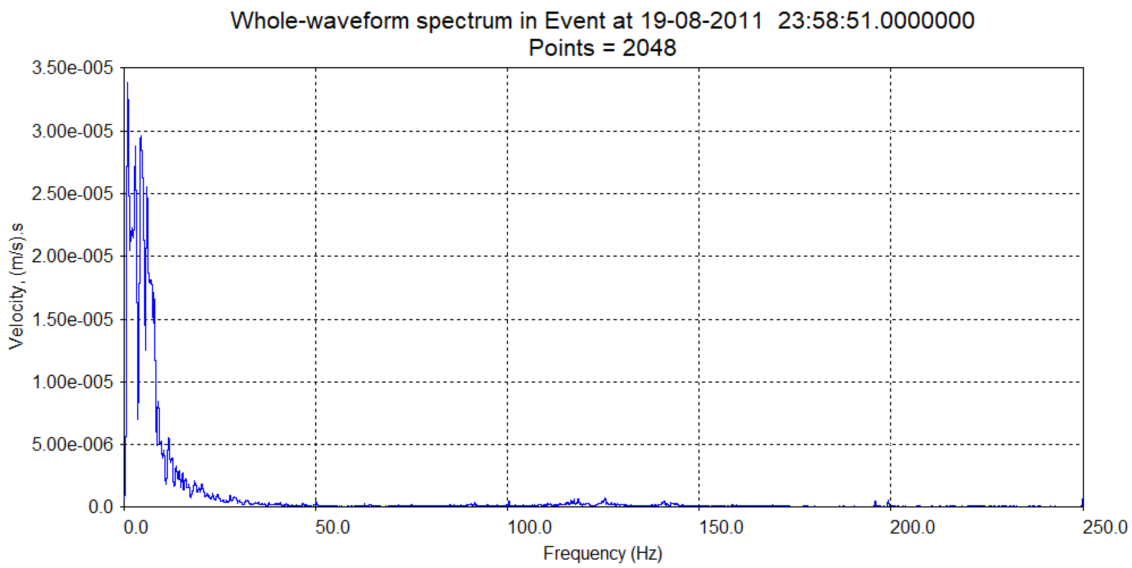

Figure 3-6 FFT result of Event B at 19/08/2011

Because the low amplitude seismic signals are sensitive to background noise, researchers have proposed several filtering methods to filter these weak signals, such as the Hilbert–Huang transform (HHT) method (Huang and Wu 2008) and wavelet-packet threshold filtering method (Donoho 1995). This thesis applied the band-pass filtering method to filter weak signals because seismic traces received typically contain some low-frequency and high-frequency ambient noise. To eliminate the influence of these artefacts during integration or differentiation, the received uniaxial seismic waveforms were bandpass filtered with the lower frequency cap of 30 Hz and upper-frequency cap of 150 Hz.

3.1.3. *Signal picking*

After filtering, the quality of seismic signals has been improved remarkably. The P-wave arrival time can be easily recognised. The ratio of the average amplitude in the front window and back window (as shown in Figure 3-7a) of a seismic trace was used to pick the P-wave arrival time. During the background noise period (before the arrival of P-waves), the amplitude ratio is close to zero. When the sensor receives ground vibration, the amplitude ratio will increase suddenly, and the arrival time can be characterised by this change. Using this method, the signal-to-noise (SNR) ratio of the filtered waveforms was significantly enhanced.

The root mean square (RMS) algorithms can be used to optimise the picking of P-wave arrival time. Firstly, this algorithm calculates a picking function using a moving window approach. At each waveform data point *i,* two windows are generated: a front window and a back window. The value F_i is calculated by:

$$F_i = \frac{\sum_{j=i+1}^{i+NF} A_j^2}{\sum_{j=i-1}^{i-NB} A_j^2} \tag{3.3}$$

where A_j is the amplitude, NF is the length of the front window in data points, NB is the length of the back window in data points. The F_i function represents a difference in the energy contained in the front window compared to the back window. Peaks occur in the function where waveform signals suddenly increase in amplitude relative to the data behind them. These peaks can then be used to estimate the arrival time of different phases. The P-wave arrival can often be picked with high confidence as it emerges from just a background noise level. S-wave arrivals often emerge out of the P-wave coda (higher amplitude than the background noise) and so tend to have more uncertainty in their picking.

Take Event A in Section 3.1.2 as an example. It is known that this event is caused by mining activities, and it was detected by seven different sensors in Figure 3-1. The amplitude of each signal varies to a large degree as a result of various hypocentre distances and wave attenuation introduced in Section 3.1.1. The P-pick result is shown in Table 3-1 Wave pick information of Event A at 23/07/2011Table 3-1. The SNR is also calculated for each sensor, and the large SNR suggests a high-quality seismic signal and always with relatively high amplitude.

Table 3-1 Wave pick information of Event A at 23/07/2011

Sensor ID	North	East	Down	P-pick	Theoretical P-wave pick time	Theoretical S-wave pick time	SNR
5	41464.633	80507.063	193.026	1.212	1.21	1.318	4.71
10	41452.213	80866.742	196.031	1.256	1.256	1.386	11.1
12	40620.658	80545.382	324.809	1.08	1.078	1.132	193.4
13	40601.791	79856.486	446	1.002	1.006	1.03	53.1
14	40682.036	79684.164	453.461	1.054	1.054	1.096	9.44
15	40938.318	79524.142	411.962	1.124	1.116	1.186	4.42
16	40760.941	79959.275	412.933	0.992	1.008	1.03	493.7

Figure 3-7a shows the seismic signal with the highest SNR from Sensor 16 for Event A. The P-wave pick time is at the first rise of the RMS from Equation 3.3, which is calculated by the amplitude from the front and back windows. To ensure the clear trend of the RMS curve, the front window is usually larger than the back window. Since the signal is uniaxial and the FFT shows a multi-peak in Figure 3-7b, the S-wave arrival is relatively hard to pick from RMS. In addition, without the polarization direction from the triaxial signal, the S-wave pick can only be calculated, and this will be introduced in Section 3.1.4.

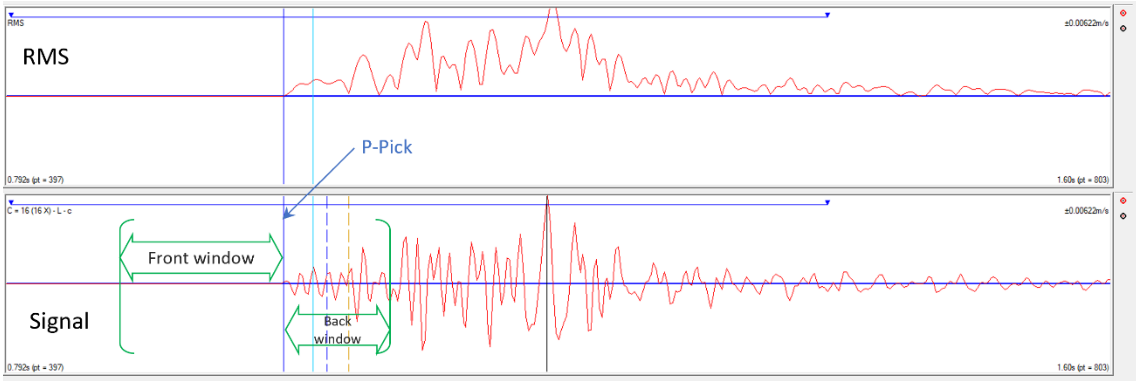

(a)

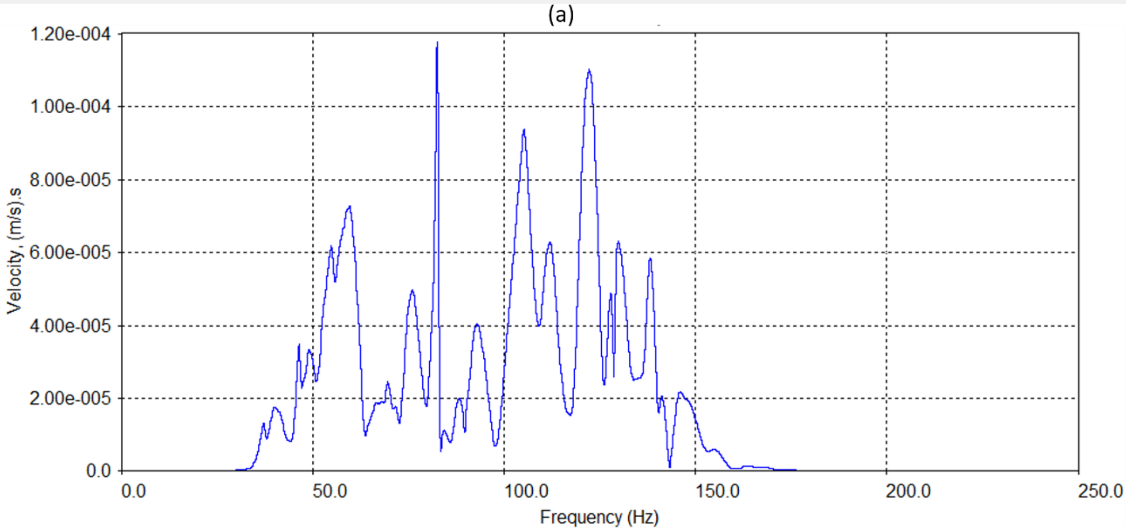

(b)

Figure 3-7 (a) Raw seismic signal and (b) frequency received by Sensor 16 as an example of wave picking for Event A at 23/07/2011

Similar to Event A, the pick information of Event B in Section 3.1.2 on 19/08/2011 is shown in Table 3-2. Four sensors around the longwall panel detected this event. Each wave is picked at the P-wave arrival. These four sensors are not installed around LW 110, which means the mining activities from LW 110 did not trigger this seismic event. The SNR is also calculated for each sensor and compared to Event A. The SNR is very low since the average amplitude of this event is two orders (1%) lower than the amplitude of Event A.

Table 3-2 Wave pick information of Event A at 19/08/2011

sensor ID	North	East	Down	P-pick	Theoretical P-wave pick time	Theoretical S-wave pick time	SNR
1	43360.54	80226.084	170.5	1.01	1.006	2.27	18.5
8	41184.08	79645.399	328.609	1.01	0.992	2.238	6.65
11	41003.91	80767.61	249.729	0.684	0.708	1.672	13
13	40601.79	79856.486	446	0.946	0.94	2.136	8.95

Figure 3-8a shows the seismic signal with the highest SNR from Sensor 16 for Event B. The FFT shows a single peak of this signal in Figure 3-8b. The frequency indicates this is a typical earthquake-like event that is not induced by the working of the study longwall panel.

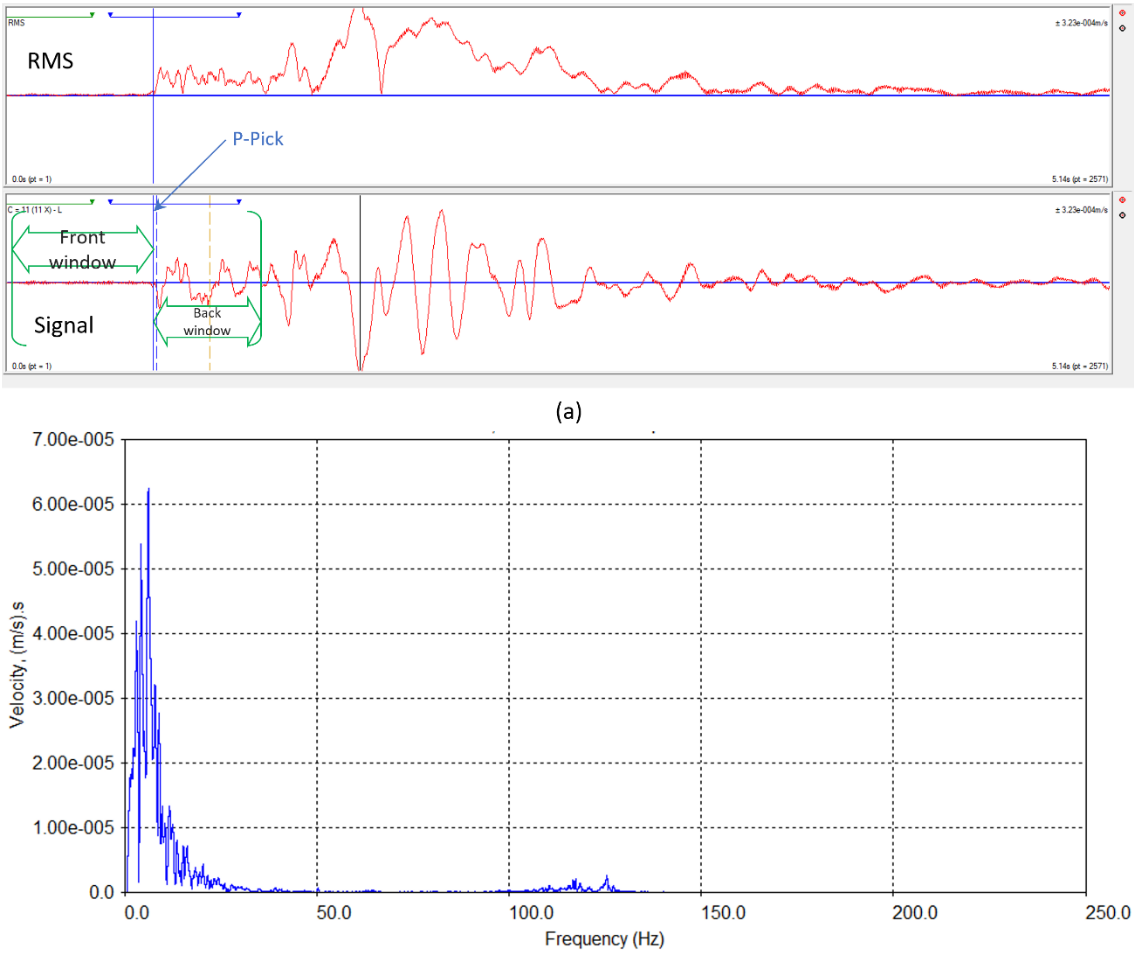

Figure 3-8 (a) Raw seismic signal and (b) frequency received by Sensor 11 as an example of wave picking for Event B at 19/08/2011

3.1.4. Seismic event location

This research employs a collapsing grid search algorithm with a single-velocity model. The basic method applied to decrease the location error is called the Downhill Simplex algorithm. This method is an iterative procedure that searches the error space for a minimum value (Nelder and Mead 1965; Press and Allen 1995). The method employs a geometric shape called a simplex. Each vertex of this three-dimensional tetrahedron is defined by its spatial coordinates (x, y, z). At each vertex, the error space is computed. For the subsequent iteration, the simplex is then instructed to move or deflate. The simplex explores the error space until it reaches a minimal. The algorithm calculates an error value for each arrival time (P or S-wave) on each sensor by summing the travel-time residuals across the array. The error space at the specified location in space is then the average of these arrival error values.

The collapsing grid search algorithm, instead, searches a three-dimensional space between the measured travel times chosen for each receiver and the theoretical travel times calculated based on the ray path and velocity model. This method is notoriously difficult to implement since the algorithm must search each 3D position. The search can cause lengthy computations in some cases within a large space.

The InSite software by Applied Seismology Consulting Ltd introduced a collapsing strategy to improve the search procedure of the above method to reduce computation (ASC 2022). In this instance, the initial course grid is searched for the position with the smallest error, E_{m1}. The algorithm then assumes that this local minimum is spatially close to the global minimum and generates a smaller and finer grid (a collapsed grid) around this location. The minimum misfit within this grid is then identified as E_{m2}, and a second collapsed grid is established. The algorithm continues until a specific location resolution is obtained. Figure 3-9 shows a collapsed cell dimension with respect to the not collapsed cell at the ratio that is used in all location processing in this thesis. The new collapsed grid consists of 64 not collapsed cells (4x4x4).

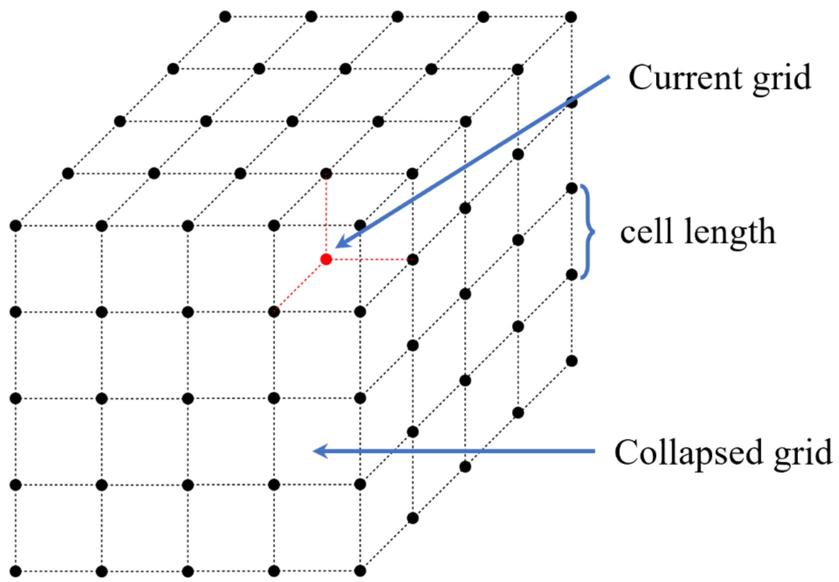

Figure 3-9 Definition of a collapsed grid volume, idea inspired by (ASC 2022)

The location of the event can be calculated based on this method. The advantage of this method, despite the extensive computations, is that the algorithm assumes that the deepest minimum it discovers within a particular grid is not a local minim located some distance from the required global minim. Larger collapsed grids result in a greater number of collapsing loops and, consequently, longer computations. The location vector for Event A is listed in Table 3-3, and its relative location within the panel is presented in Figure 3-10. The event is above the longwall panel and ahead of the current working face, which is the area of active rock failure with energy release.

Table 3-3 Location-related properties of Event A at 23/07/2011

Date	**Time**	**North**	**East**	**Down**	**SNR**
23/07/2011	7:22:36	40449.570	80055.087	462.751	69.980
Signal properties					
sensor ID	Sensor event Distance	Sensor event Azimuth	Sensor event Plunge	Theoretical P-wave pick time	Theoretical S-wave pick time
5	1143.410	204.002	13.644	1.210	1.318
10	1317.276	218.991	11.682	1.256	1.386
12	537.297	250.764	14.876	1.078	1.132
13	250.787	127.469	3.830	1.006	1.030
14	437.847	122.076	1.216	1.054	1.096
15	723.434	132.630	4.026	1.116	1.186
16	329.566	162.896	8.694	1.008	1.030

Within Table 3-3, the distances between the event and each sensor are also demonstrated, as well as the azimuth and plunge. As known from Section 3.1.1, the distance has a directly proportional relationship with the signal amplitude, and the amplitude affects the SNR of each seismic signal. Therefore, compared with Table 3-1, the large SNR generally has a low travel distance. In addition, the theoretical P and S wave pick time can be calculated with the event location, and the assumed P/S wave velocity. The theoretical P-wave pick time can be used to verify the manually picked arrival time, and the theoretical S-wave pick can be used in further processing.

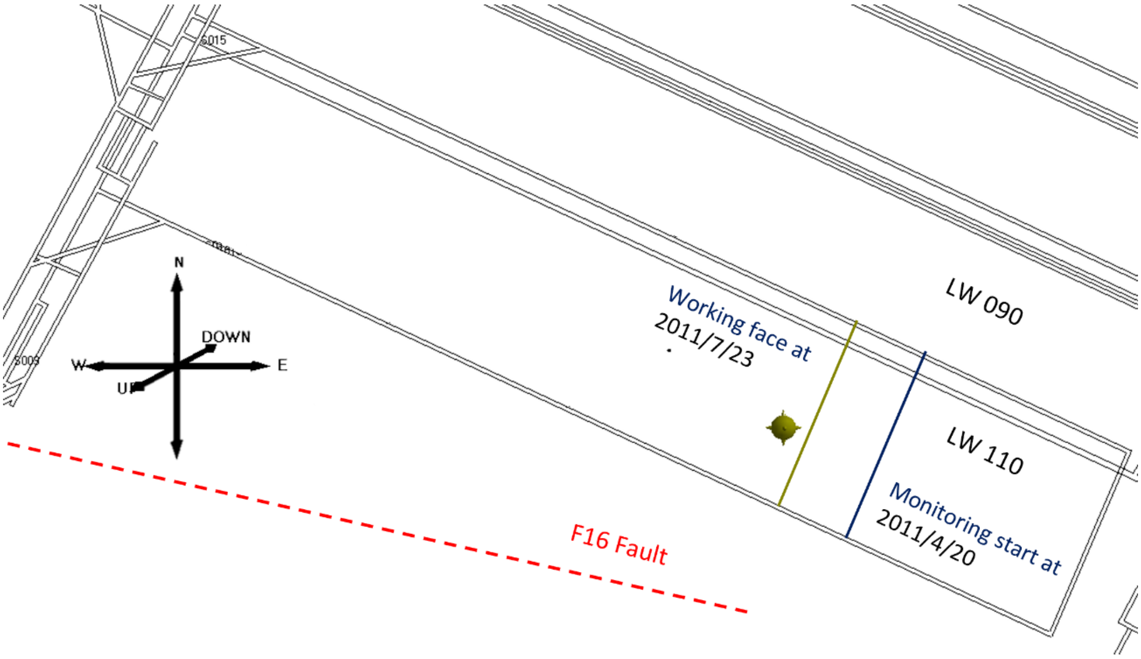

Figure 3-10 Location of Event A at 23/07/2011

Since in Section 3.1.2, Event B is defined as a large seismic activity far away from the study panel, its location can only be calculated with a grid that is over 1000 m far from the panel. The location vector is listed in Table 3-4. The consistency of the manually P-wave pick time and the theoretical P-wave pick time justify the reliability of the calculated location, and the event is over 3000 m away from the working face, which also verified that this event is caused by the reactivation of a large tectonic structure far from the longwall panel.

Table 3-4 Location-related properties of Event B at 19/08/2011

Date	**Time**	**North**	**East**	**Down**	**SNR**
23/07/2011	7:22:36	41130.7	83500.6	271.553	11.300
Signal properties					
Sensor ID	Sensor event Distance	Sensor event Azimuth	Sensor event Plunge	Theoretical P-wave pick time	Theoretical S-wave pick time
1	5049.653	119.548	2.561	1.006	2.270
8	4986.464	93.584	-3.144	0.992	2.238
11	3854.157	91.952	-2.894	0.708	1.672
13	4781.845	86.740	-4.689	0.940	2.136

3.1.5. Source mechanism calculation

Seismic moment tensor inversion is used to study the source mechanism of a seismic event, which can imply the failure type, seismic moment, and the potential orientation of mining-induced fractures. The moment tensor matrix is used to solve the magnitude of seismic events, fracture types and orientations, which allows us to understand the fracturing behaviour and evolving stress field (Baig and Urbancic, 2010). In a general form, the moment tensor (**M**) can be described by a matrix of nine force couples (Aki and Richards 1980):

$$\mathbf{M} = \begin{bmatrix} M_{xx} & M_{xy} & M_{xz} \\ M_{yx} & M_{yy} & M_{yz} \\ M_{zx} & M_{zy} & M_{zz} \end{bmatrix} \tag{3.4}$$

where the M_{ij} indicates the strength of the stress measured along the vertical and horizontal axis of the x, y, and z directions (Figure 3-11). The seismic moment tensor is a symmetrical tensor consisting of six components (Eyre and van der Baan 2015), which can be decomposed into three different components: double couple (DC), isotropic components (ISO) and compensated linear vector dipole (CLVD). The DC component is the off-diagonal element (M_{xy}, M_{xz}, M_{yz}) to avoid rotation. The ISO component is the diagonal elements (M_{xx}, M_{yy}, M_{zz}) to describe volumetric changes. If the volumetric change is zero, the moment tensor decomposition also contains the CLVD component when one of the diagonal elements is compensated by others, and the summation of the three diagonal elements is zero. The CLVD and ISO components play an important role in elucidating the underlying rock failure mechanism, as they imply the volumetric change of rock mass in response to mining stress. The moment tensor can be decomposed as (Vavryčuk 2015):

$$\mathbf{M} = M(C_{ISO}E_{ISO} + C_{DC}E_{DC} + C_{CLVD}E_{CLVD}) \tag{3.5}$$

where M is the norm of **M** and represents a scalar seismic moment for a general seismic source. E_{ISO}, E_{DC}, and E_{CLVD} are the base tensor for the ISO, DC and CLVD component, respectively. C_{ISO}, C_{DC}, and C_{CLVD} control the relative strengths of ISO, DC and CLVD, respectively, and they can be calculated by:

$$\begin{bmatrix} C_{ISO} \\ C_{DC} \\ C_{CLVD} \end{bmatrix} = \frac{1}{M}\begin{bmatrix} M_{ISO} \\ M_{DC} \\ M_{CLVD} \end{bmatrix} = \frac{1}{M}\begin{bmatrix} \frac{1}{3}(M_1 + M_2 + M_3) \\ \frac{2}{3}(M_1 + M_3 - 2M_2) \\ \frac{1}{2}(M_1 - M_3 - |M_1 + M_3 - 2M_2|) \end{bmatrix} \tag{3.6}$$

Here M_1, M_2, and M_3 are the eigenvalues of the moment tensor with the eigenvectors which are related to the fracture plane orientation and its sliding direction.

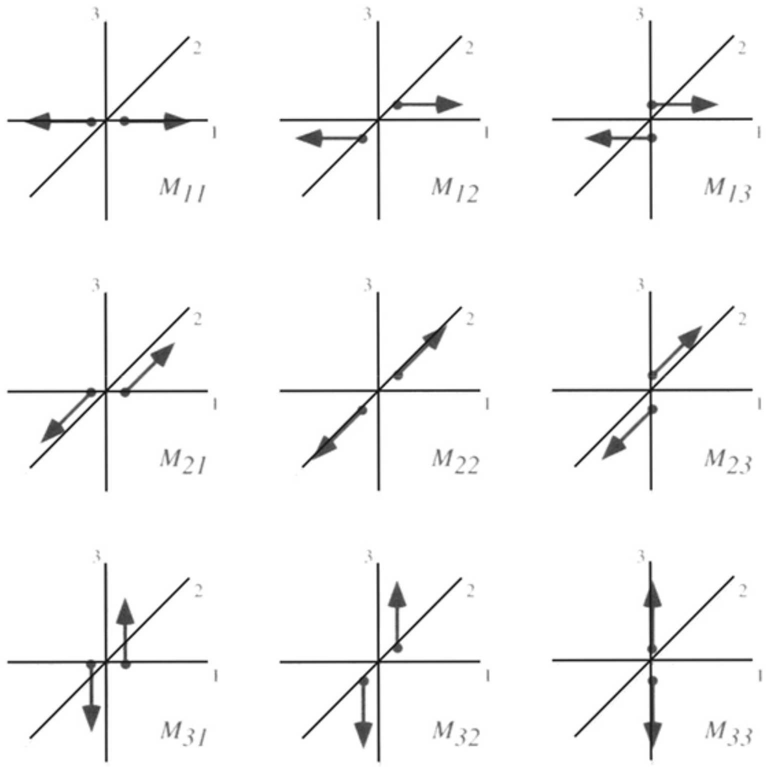

Figure 3-11 Moment-tensor elements, represented as force couples (Shearer 1999)

To solve the moment tensor, the displacement *d* received by sensors can be expressed by Green's function (*G*), moment tensor (*M*) and source time function (*S*(*t*)) (Zerva 1988):

$$d(x,t) = G * M * S(t) \tag{3.7}$$

where *x* is the location of the geophone sensor and *t* is the time. To solve the moment tensor matrix, it is required to display the full amplitude of the phase P and S waves in the focus sphere around the source. The first motion of a seismic wave (i.e., the P wave in this paper) or the combination of the first motion and S/P amplitude ratio is commonly used in seismology to determine source mechanisms. For a seismic event enclosed by sensors from different azimuths, the first motion of the P wave can be used to invert the source radiation pattern. Upward and downward first motions represent the compressional and dilatational source moment, respectively (Wang et al. 2016).

The Green's function takes into account the radiation pattern of the source, the propagation effects along the path, and the response effects of the receiver. By assuming that the receivers are in the far field and that the propagation medium is homogeneous and isotropic, these can be simplified. G contains the P-wave radiation components, which can be easily calculated from the known locations of the source and receiver (de Natale and Zollo 1989).

The source-sensor distance *r* can be calculated from Section 3.1.4, each amplitude in the vector *u* is first corrected for path and sensor effects using:

$$u_k^0 = S_k \cdot P_k \cdot F_k \cdot \frac{1}{C_{w_k}} \cdot G_{s_k} \cdot u_k \tag{3.8}$$

Where u_k is the amplitude measured on sensor *k* and u_k^0 is the corrected amplitude. The S_k is the Sensor polarity. G_{s_k} is the geometrical spreading. The P_k is anelastic attenuation. F_k is free-surface amplification. Take a simplified $F_k = 1$ in this research because the sensor is grouted into the medium and there is no free surface (Aki and Richards 1980). C_{w_k} is the coupling weight of the receiver. In this study, the C_{w_k} remains at 1.

Using Singular Value Decomposition (Stump and Johnson 1977), the matrix G can then be inverted, and the vector M can be calculated. The MT decomposition provides an analysis of the source mechanism's type and orientation (Pettitt 1998).

To completely resolve the six independent elements, the complete amplitudes of at least two non-planar linear matrices must be determined. Consequently, the sensor array must be widely dispersed and positioned on separate planes (Trifu and Shumila 2002). In other words, a high signal-to-noise ratio and adequate sensor coverage are required around a seismic event. Seismic events that occur outside the sensor's enclosed area or with a low energy release are difficult to analyse. This paper assumes that the mine's sensor distribution is adequate. Due to accuracy concerns, seismic events with very low energy that are detected by fewer than six sensors will not be analysed.

Alternately, beach-ball diagrams are frequently used to depict this source type. In the early days of earthquake seismology, it was common to practise to deduce the focal mechanism from P-wave first-motion data. These diagrams illustrate a lower-hemispheric projection of P-wave first motion data, separating the lower focal hemisphere into regions with compressional and dilatational first motion. This presentation of seismic source mechanisms produces the classic beach-ball patterns that characterise numerous types of events, such as strike-slip, normal faulting, and normal faulting (Figure 3-12).

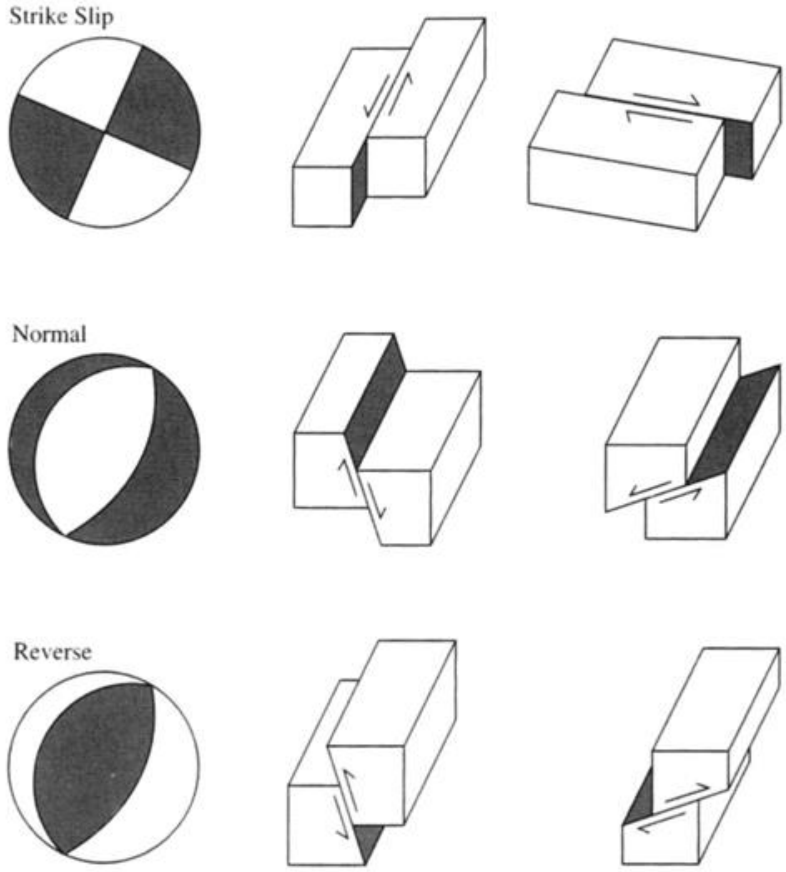

Figure 3-12 P-wave radiation pattern by beach ball diagrams for different types of faults. (Shearer 1999)

The source mechanism of Event A and the component of the moment tensor are summarised in Table 3-5. The ISO, DC and CLVD components determined this event as a result of a tensile failure.

Table 3-5 Moment tensor-related properties of Event A at 23/07/2011

Date	Time	North	East	Down	Moment Tensor (Euclidean):		
23/07/2011	7:22:36	40449.570	80055.087	462.751	-0.026	-0.0279	-0.1606
%ISO	**%DC**	**%CLVD**	**T-Value**	**K-Value**		-0.022	-0.1561
-42.68	-0.34	-56.99	0.99	-0.33			-0.9471

The beach ball as a view representation of the moment tensor is also plotted in Figure 3-13a. The beach ball is a graphic symbol that indicates the type of slip that occurs during seismicity: strike-slip, normal, thrust (reverse), or some combination. It also shows the orientation of the fault that slipped. The 2-dimensional focal mechanism circle is the projection of the fault orientation and slip on the lower half of a sphere surrounding the seismic source. In this case, the shadow area is the outward displacement, and the white area is the inward displacement. The direction of displacement at each direction can be implied from the beach ball as well. In addition, the Hudson T-K plot can represent the source mechanism more clearly in a special coordinate (Hudson 1984).

From the T-K plot in Figure 3-13b, the event is located close to the T=+1 zone, which indicates that this event is caused by compression near the excavated zone.

In addition to the previously listed parameters, fracture toughness and filler material properties have a substantial impact on seismic monitoring outcomes. The degree of fracture toughness, for example, can influence the sort of failure that occurs. Shear failures are more prone to happen when the toughness is high. When toughness is low, the result is more likely to be tensile failures. The properties of the filler substance utilised are also important. Softer filler materials are more likely to cause shear failures. Harder materials, on the other hand, are more likely to cause tensile failures. These variables have a direct impact on seismic wave propagation and subsequent data interpretation. This emphasises the significance of these elements in seismic monitoring and emphasises the necessity for additional investigation in future studies. Understanding how these elements influence seismic monitoring can lead to more accurate data interpretation and, as a result, more successful seismic monitoring tactics.

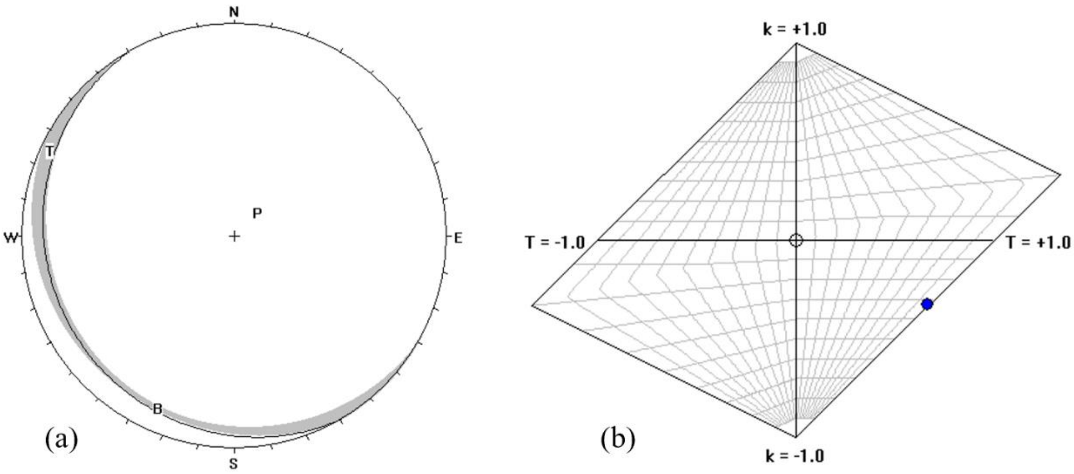

Figure 3-13 (a)Beach ball and (b)T-K plot of Event A at 23/07/2011

3.2. Field seismic data analysis and radiation pattern determination

In the study coal mine, 4,024 seismic event data from 17,202 seismic signals were received by geophones. Each signal contains information on a single seismicity caused by material extraction. The results from all these seismic data are presented and analysed in the following sections.

3.2.1. Location and source mechanism

The location of seismic events can be calculated using the collapse grid search method introduced in Section 3.1.4. The distribution of seismic events is shown in Figure 3-14. A few events are located around the F16 fault. Also, it has a trend that intensive seismic activities were reported at the tailgate side (LW 090) of the panel, near the goaf zone, which suggests that frequent fracture generation and propagation occurred in the rock mass around the tailgate.

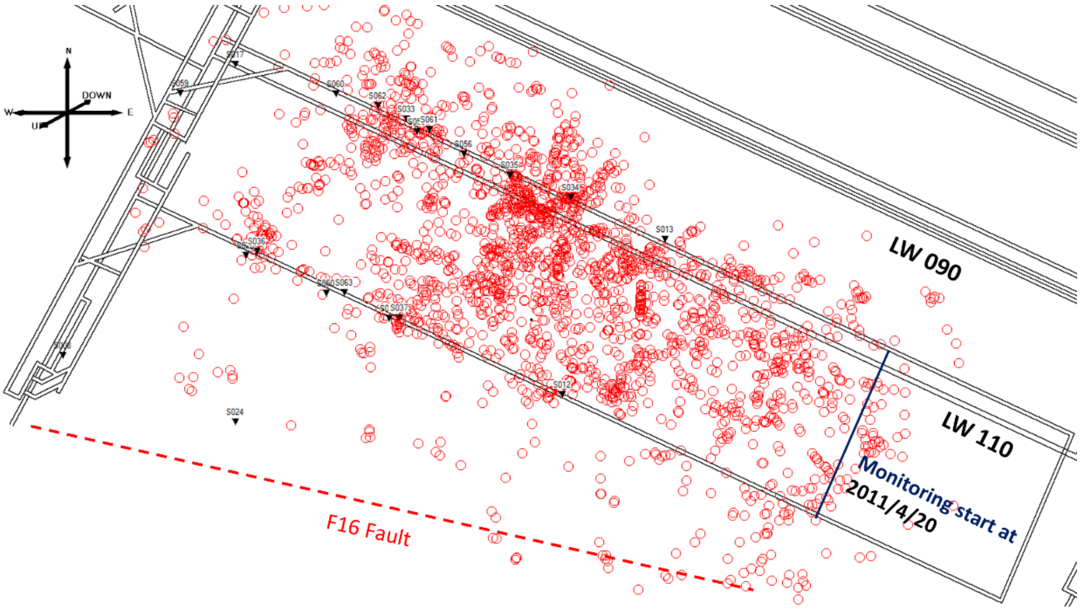

Figure 3-14 Distribution of all recorded seismic events induced by LW 110

Seismic moment tensor inversion was performed on 2,807 seismic events recorded in LW110, the other events are not satisfied for a proper moment tensor inversion since these events were not received by at least six uniaxial sensor or cannot have six clear signals enough to pick six arrival times. Using six or more sensors to identify the same seismic event may result in a buildup of monitoring mistakes. However, there are a number of solutions that can be used to address this issue in future research. One of these ways is to calibrate sensors on a regular basis. We can fix any systematic inaccuracies that may emerge over time by keeping the sensors at their peak performance and precision. Another useful option is the use of redundancy and sensor fusion techniques. Multiple sensors are used to monitor the same parameter with redundancy. This allows for more precise readings because the likelihood of all sensors malfunctioning at the same time is low. Sensor fusion, on the other hand, entails combining input from various sensors to make more thorough computations that can also improve accuracy. Kalman filters and other mathematical error correcting techniques can also be used. These strategies are utilised for mistake prediction and correction, which helps to reduce the risk of error accumulation even further. As a result, it is critical to consider these considerations while determining the optimal way to reducing monitoring errors.

The results are shown in beach balls in Figure 3-15. Figure 3-15 indicates that seismic events near the panel are mainly tensile failure with sub-horizontal fracture planes, which can be explained by the low energy of the explosive type of seismic events induced by roof buckling after stress relief. At the south side of the longwall panel in Figure 3-15, the F16 reverse fault presenting at about 50 m to 200 m away from the longwall panel has changed the seismic failure mechanism. In contrast with the predominant tensile failure in the near-panel region, the events near the F16 reverse fault are mostly shear failures. The high energy events that occurred in the tectonic regions (i.e., near the fault) are presumably caused by the interaction between tectonic stresses and mining-induced stresses. The longwall face retreated from the southeast to the northwest, which is consistent with the occurrence of seismic events (the green colour indicates old events while the red colour indicates new events in chronological order). As shown in Figure 3-15, since the tailgate is next to the mined goaf, there are clearly more events near the tailgate than the maingate. The beach balls near the fault also indicate a reverse faulting mechanism with the minimum principal stress in the vertical direction (Vavryčuk 2015). This is consistent with the site condition of a minimum vertical principal stress of 20.5 MPa and maximum horizontal principal stress of 29 MPa (Cai et al. 2014).

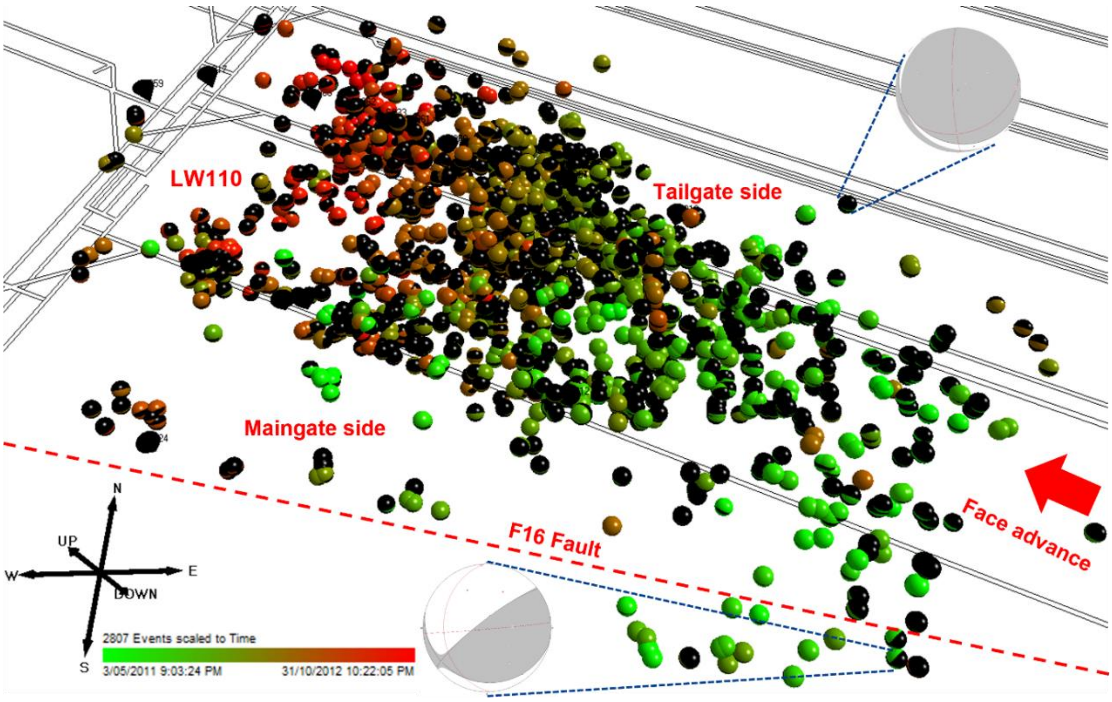

Figure 3-15 Source mechanism of seismic events recorded in LW110 shown in beach balls. The colour of each beach ball shows the onset time per seismic event (green indicates old events, and red indicates new events in chronological order).

The result of moment tensor inversion in LW110 can be further presented in the Hudson T-K plot, which is a special coordinate projection to visualise source types of various seismic moment tensors (Hudson 1984). T and K values in the plot represent the decomposition of the moment tensor into a deviatoric (shear) and an isotropic (volumetric) component, respectively. As shown in Figure 3-16, seismic events in the pure DC domain will have T=0 and K=0, while T=±1 indicates a pure tensile. The explosion (T=0, K=+1) and implosion (T=0, K=-1) are barely observed in mining-induced seismicity. Thus, the explosion/implosion component (K value) of most mining-induced seismicity is also low. Figure 3-16 shows a clustering trend of seismic events in the T-K plot. The tensile failures concentrate in the two blue ovals, and the shear failures concentrate in the green oval. It demonstrates that most seismic events in LW110 were triggered by tensile failure, and only a small proportion was caused by shearing.

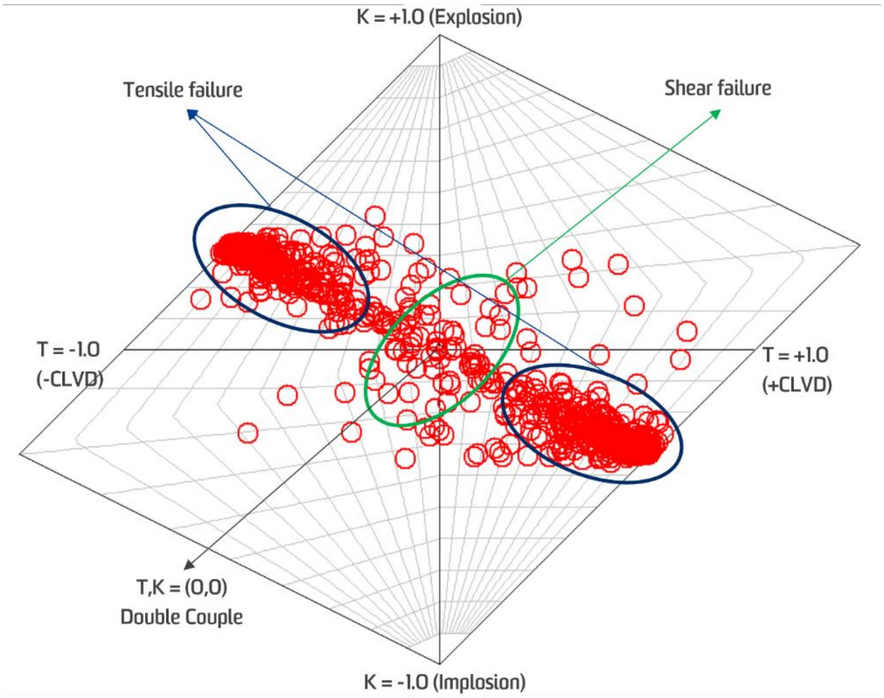

Figure 3-16 T-K plot for the seismic events recorded in LW110 (each event was represented by one red circle). T and K represent the decomposition of the moment tensor into a deviatoric (shear) and an isotropic (volumetric) component, respectively.

3.2.2. Fault plane solution

Since the moment tensor inversion result indicates two potential fault planes and normal vectors, structure analysis is then conducted to determine the preferential orientation of the seismic events. Since seismicity tends to occur along one or more sets of pre-existing subparallel joints in rock, we can obtain the fault plane solutions (the orientation of the fractures) with the help of the three-point method (Fehler et al. 1987). In this study, as shown in Figure 3-17, for a seismic event at location X, the moment tensor inversion provides two fault plane solutions, Fault Plane 1 (FP1) and Fault Plane 2 (FP2). Points Y and Z are two events around X, which are assumed to be triggered along the same plane of X (the red plane in Figure 3-17). Therefore, the fault plane solution for X would be FP1, given the smaller angle difference with the red plane compared to FP2. To determine the orientation of mining-induced fractures, the three-point method is applied to back-calculate the preferential fracture orientation within a cloud of events by fitting every group of three events with one potential failure plane, resulting in a total of C_n^3 planes (a n-combination of a set of three points, n is the total number of nearest points to Point X, including itself). Considering the location accuracy and the extent of the fracture zone, the events fitted in each plane can be constrained spatially within a particular range (100 m in this research) (Collins et al. 2002). The obtained fracture network can then be displayed in a stereonet, and areas with a high-density of fracture plane poles in the stereonet indicate the preferential orientation of mining-induced fractures.

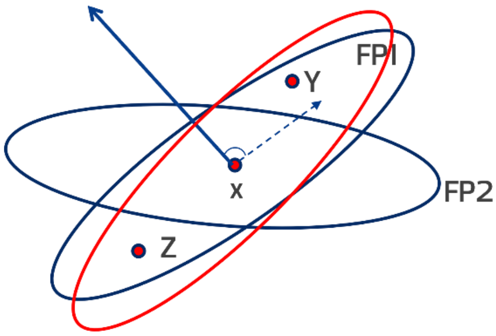

Figure 3-17 Schematic of the three-point method used in the structural analysis, with three seismic events at Points X, Y and Z and two potential fault planes FP1 and FP2 for Point X.

3.2.3. Radiation pattern

The radiation pattern of seismic waves needs to be determined to further investigate the displacement of the seismic source based on the source mechanism and the fault plane solution. The radiation pattern characterises the source movement along all directions in space. It is controlled by the seismic wave type (P/S), source mechanism, azimuth of observation, and take-off angle. For a shear faulting, its radiation pattern for a given take-off angle and azimuth can be determined by the strike, dip, and slip rake along the fault plane, according to Boore and Boatwright (1984).

In this study, the radiation pattern method developed by (Ou, 2008) is adopted as a shear-tensile source model to demonstrate the radiation pattern of a seismic event. Within a shear-tensile failure, the radiation pattern is governed by two additional parameters: tensile angle γ and Poisson's ratio ν (Kwiatek and Ben-Zion 2013). It is assumed that the shape of a tensile motion is like a pulse with no displacement at the end, and the tensile angle concept is used to describe the angle between the unit slip vector and unit fault normal. The tensile angle is measured between the vector along the slip direction projected on the fault plane and the actual direction of the fault movement, which is positive for fracture opening and negative for closing motions (Figure 3-18). Note that although it is termed as the 'tensile angle', it can also represent a shear failure in the fracture when the tensile angle γ = 0°, the radiation from the shear-tensile source model corresponds to the classic pure shear source. When γ = 90°, the radiation corresponds to the pure tensile opening.

Aki and Richards (1980) assumed that for non-homogeneous source material in homogeneous propagation media, the radiated pattern coefficient can describe the relative displacement of the source. To investigate the radiation pattern of P waves for a tensile-shear fault dislocated in a certain direction, the displacement vector function is written as:

$$\Delta\boldsymbol{u}(t) = \Delta u(t)\left(\sin\gamma\,\hat{n} + \cos\gamma\,\hat{f}\right) \tag{3.9}$$

where Δu(t) is the magnitude of dislocation, γ is the tensile angle, $\hat{f}$ is the slip vector and $\hat{n}$ is the normal vector of the fault plane. The P wave displacement ($\boldsymbol{u}^P$) for a tensile fault segment dislocated in a direction is written as (Ou 2008):

$$\boldsymbol{u}^P = \frac{\mu A \Delta u\left(\hat{\boldsymbol{r}}^{\boldsymbol{T}}\boldsymbol{S}\hat{\boldsymbol{r}}\right)}{4\pi\rho {V_P}^3 r}\hat{\boldsymbol{r}} \tag{3.10}$$

where μ is the Lame constant, A is the area of the fault segment, ρ is density, $\hat{\boldsymbol{r}}$ is the direction of radiation, V_P is the P wave velocity, and $\boldsymbol{S}$ is called the source dislocation tensor. The detailed explanation of $\boldsymbol{S}$ can be found in (Ou, 2008). As long as the strike, dip, rake of the fracture plane and the tensile angle are available, the radiation pattern at the source can be calculated. The calculation of the direction of the fracture plane is shown in Sections 3.2.1 and 3.2.2. Since the component of the seismic moment can be written as $M_{ij} = \mu A r$, the tensile angle can be calculated based on the proportion of the DC component and the ISO+CLVD component.

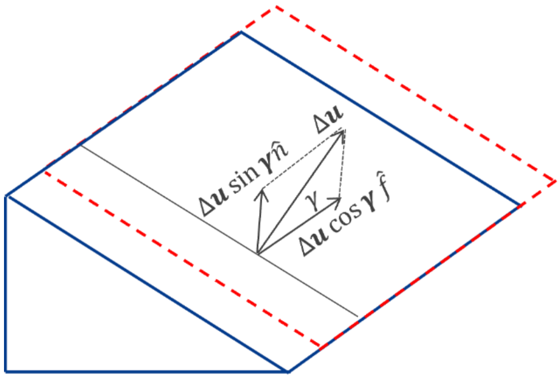

Figure 3-18 An example of a tensile-shear fault segment, and the displacement vector (Δu), the unit slip vector (f̂), and the unit fault normal (n̂).

3.2.4. *Source parameter estimation*

Seismic source parameters considered in this study include seismic moment, moment magnitude, source radius, and the aperture change of induced fractures. The source dimension is usually expressed as the radius of the fracture plane and is related to the corner frequency of the seismic wave, which can be calculated as (Brune, 1970; Duncan and Eisner, 2010; Glazer, 2016):

$$R = \frac{K_c \beta_0}{2\pi f_c} \tag{3.11}$$

where R is the source radius, β_0 is the S wave velocity in the vicinity of the source, and K_c is a constant that depends on the source model. In this paper, P waves are used to solve the corner frequency f_c, so K_c is set as 1.32 based on (Madariaga, 1976).

After the diagonalisation of the moment tensor, it can be expressed in the principal axis coordinate as follows:

$$\mathrm{M} = \begin{bmatrix} M_1 & 0 & 0 \\ 0 & M_2 & 0 \\ 0 & 0 & M_3 \end{bmatrix} = us \begin{bmatrix} (\lambda+\mu)\hat{n}\hat{v}+\mu & 0 & 0 \\ 0 & \lambda\hat{n}\hat{v} & 0 \\ 0 & 0 & (\lambda+\mu)\hat{n}\hat{v}-\mu \end{bmatrix} \tag{3.12}$$

where u is the displacement in the direction of motion for fractures as derived by seismic data, s is the surface area of the fracture, and $\hat{n}$ and $\hat{v}$ are the normal and motion direction of the fracture, respectively. λ and μ are Lame constants defined as:

$$\lambda = \frac{E\nu}{(1+\nu)(1-2\nu)} \tag{3.13}$$

$$\mu = \frac{E}{2(1+\nu)} \tag{3.14}$$

where E is the elastic modulus and ν is Poisson's ratio. The fracture aperture change τ deduced from the focal mechanism can be obtained as (Zhao et al. 2019):

$$\tau = u \times \cos\theta = \frac{4\pi f_c^2 \times \cos\theta \times tr(M)}{K_c^2 \beta_0^2 \times (3\lambda + 2\nu)\hat{n}\hat{v}} \tag{3.15}$$

where θ is the angle between $\boldsymbol{n}$ and $\boldsymbol{v}$, which can be obtained by using moment tensor inversion, and $tr(M)$ is the trace component of the diagonalised moment tensor matrix.

3.2.5. Local magnitude and b-value

The instrument magnitude is calculated for every instrument using,

$$M_I = A \cdot log10\left(r \cdot W_{V\ rms_{peak}}\right) + B \tag{3.16}$$

where r is the distance between source and receiver. A single instrument magnitude for the event is calculated by averaging the magnitudes of the instruments used at the source location. $W_{V\ rms_{peak}}$ is the amplitude of the peak signal (DC to peak) on the RMS Velocity Waveform. A and B are constants configured by the user. A is 1 and B is 0 for the purpose of this calculation. The magnitude is determined regardless of the number of channels present in the instrument. This calculation therefore maximises the use of the array's available data.

With the local magnitude, the b-value can be calculated. Despite it is not the seismic moment magnitude, the instrument magnitude can also reflect the trend of b-value variation. The b-value is the slope of a log-normal distribution of passive seismic event sizes, namely the number of events versus their magnitudes. The b-value is defined by the Gutenberg–Richter law (Gutenberg and Richter 1956), which expresses the relationship between the magnitude and total number of seismic in any given region and period of larger than that magnitude:

$$N = 10^{a-bM} \tag{3.17}$$

where, *N* is the number of event that the magnitude large than *M*.

The b-value is often used to describe the nature of seismic event distributions in time domain. Initially, it was believed that b-values could be used as a predictor of large-magnitude event, but more commonly it has been used to describe the stress and fracture state of rock mass. Figure 3-19 illustrates the computed b-values from the cumulative frequency-magnitude relationship for LW 110. Figure 3-20 shows the temporal variation of the b-value measured for the LW 110 from 20/04/2011 to 30/10/2012. The blue line shows the rolling average, and it is clear to observe the cyclic trend, indicating several cycles of stress change. The slowly increase of the b-value could be the stress build-up or strain softening, and the slow drop can be seen as the strain hardening (Main et al. 1989).

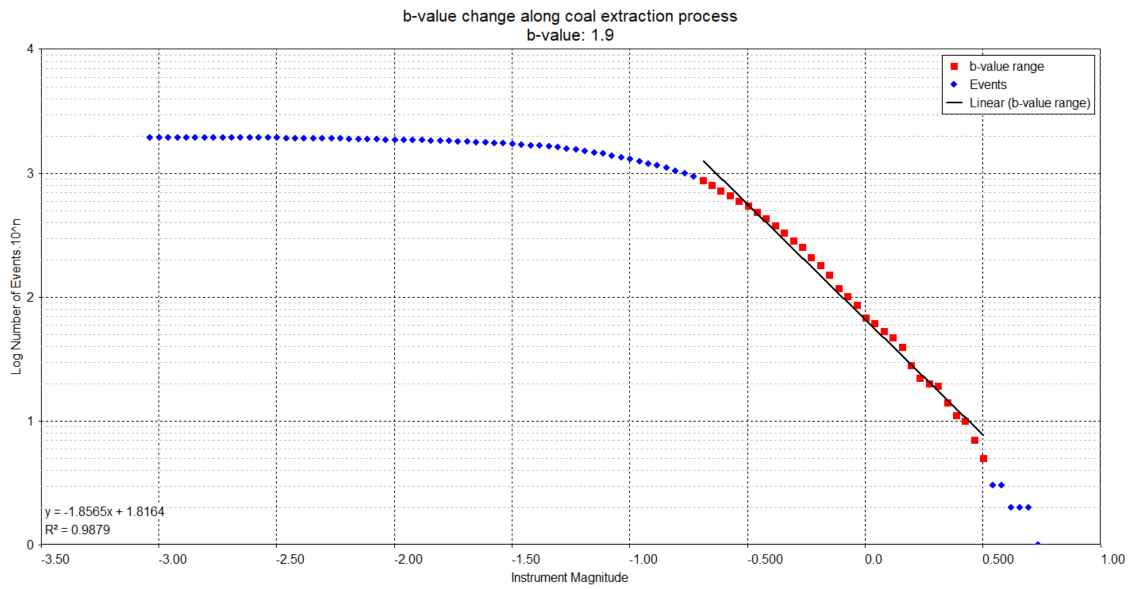

Figure 3-19 b-value of seismic data using instrument magnitude

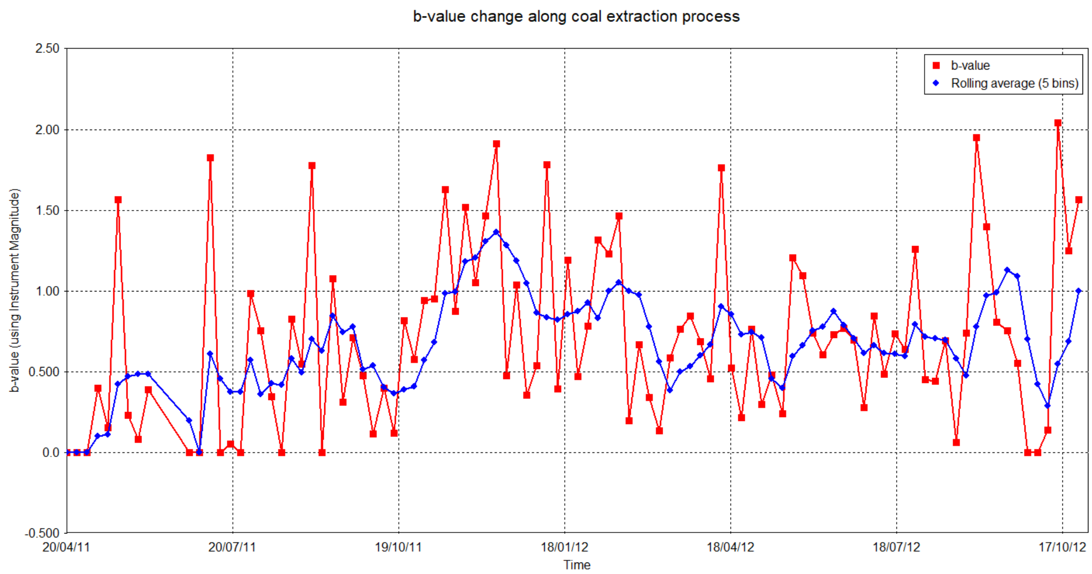

Figure 3-20 b-value change along the coal extraction process

3.3. *synthetic triaxial data processing generated from the uniaxial signal*

With the help of the fault plane solution (Section 3.2.2) and radiation pattern (Section 3.2.3), the displacement at the source location at each wave propagation direction can be easily determined. Along with the assumed seismic wave attenuation (Section 3.1.1), the 3D displacement at the sensor location caused by seismicity can be calculated. This allows us to generate a synthetic triaxial wave as the signal received at triaxial sensors.

To this end, it is necessary to first calculate the seismic source mechanism, which can provide more explicit information on the source plane. After determining the source mechanism, a synthetic triaxial wave can be generated based on the wave attenuation and the relative location between the source and sensors. To be more specific, the following steps are performed to develop and validate synthetic triaxial waves:

1. Assume a specific source mechanism that can be obtained using uniaxial seismic data, as shown in Figure 3-21a. There are eight sensors randomly distributed in space enclosing the event, 100–300 m away from the event hypocentre.
2. Calculate the radiation pattern from the assumed source mechanism to solve the 3D displacement at the sensor location (Figure 3-21b).
3. Use all eight sensors to record synthetic triaxial seismograms released from the radiation pattern in Step 2, as shown in Figure 3-21c, where the blue vertical line indicates the P-wave pick.
4. Back calculate the source mechanism (Figure 3-21d) based on the synthetic triaxial signal, and then compare the obtained source mechanism with the original input in Step 1.

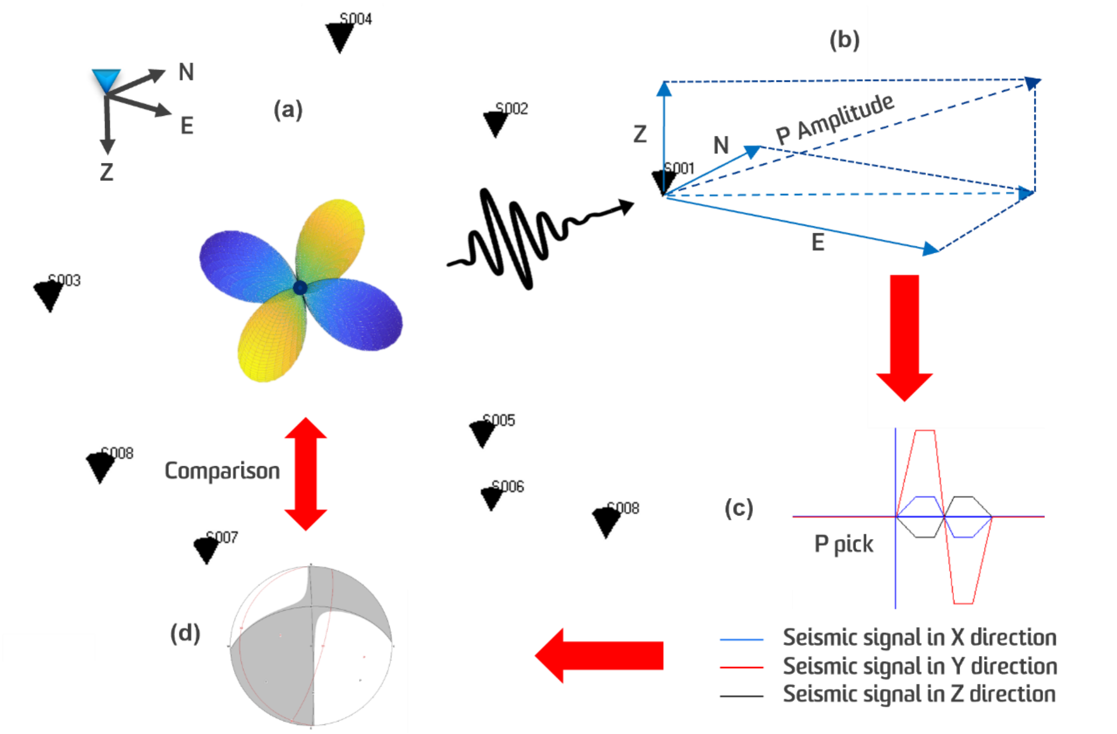

Figure 3-21 An example of synthetic triaxial wave validation: (a) generation of a radiation pattern based on the assumed input parameters, (b) the displacement calculation at the sensor location, (c) synthetic triaxial waves generation for each sensor, and (d) invert the moment tensor, draw the beach ball, and solve the fault plane to compare with the initial radiation pattern.

Two more factors need to be considered to complete the synthetic triaxial wave: the fault plane and the slip vector. In the shear-tensile failure model (see Section 3.1.5), the radiation pattern is affected by the strike and dip of the fracture plane, the rake of the slip vector, the tensile angle and Poisson's ratio (Aki and Richards 1980). Six different validation tests were conducted using different tensile angles (0°, 15°, 30°, 45°, 60°, and 90°). Figure 3-22 shows examples of a beach ball and its radiation pattern for the six different tensile angles. As P wave is used to invert the moment tensor in this study, only the P wave radiation pattern is presented. The other parameters are set as: amplitude = 10^{-4} m, Poisson's ratio = 0.4, dip direction = 120°, dip = 30°, and rake = 60°. Although constant values were used for strike, dip and rake in this study, they can still generate universal results given sensors are randomly distributed and their positions relative to the failure source are also random, without the need to vary these values in different tests.

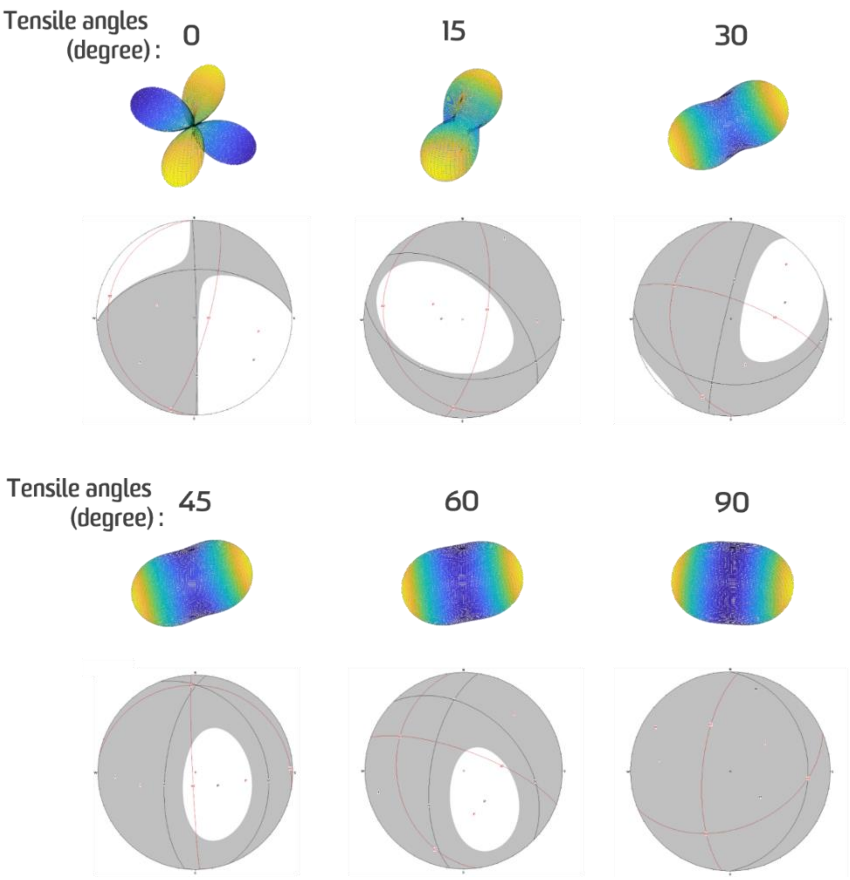

Figure 3-22 Radiation patterns and associated beach balls for the tensile angles of 0°, 15°, 30°, 45°, 60°, and 90°.

The comparison between the initial radiation pattern (ground truth) and the inverted beach ball is shown in Figure 3-23, which suggests that the discrepancies are generally below 30 degrees. It indicates that the source mechanism generated by the synthetic triaxial signal can roughly restore the original source information. One possible reason for the discrepancy is that the radiation pattern does not actually consider the explosive component. The variation of the DC component of the source mechanism shows a linear declining trend with the tensile angle increasing (see

Figure 3-23). It suggests that the source mechanism of the synthetic triaxial signal can represent the true failure type, as DC represents the shear mechanism and lower tensile angle means more shearing (Section 3.1.5).

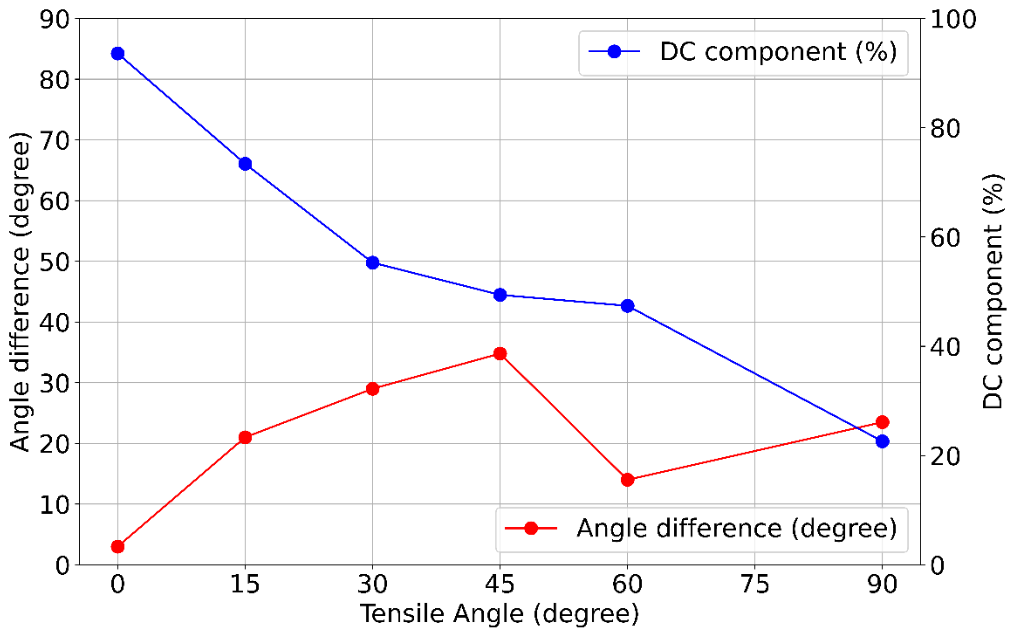

Figure 3-23 Discrepancy between the true fracture plane and the source mechanism inverted fracture plane, and the variation of the DC component in the source mechanism with the increase of tensile angle.

In the following study, the method of calculating the seismic parameter and generating an explicit mining-induced fracture network from the uniaxial seismic data includes seismogram processing, event location, moment tensor inversion and source parameter estimation. The workflow of generating a mining-induced fracture network is described in Figure 3-24.

The uniaxial seismic waves are first obtained from a case study site. The P wave arrival time is picked on the uniaxial seismic data and the event location process is completed based on the P arrival pick. Using at least six P waves after picking, seismic moment tensors can be inverted as introduced in Section 3.1.5 using the first motion of seismograms (step ① in Figure 3-24). By applying the fault plane solution from Section 3.2.2, the most-likely fracture plane can be determined. Then the radiation pattern can be inferred (step ② Figure 3-24). Building on the required parameters calculated from moment tensor inversion and radiation pattern as introduced in Section 3.3, a triaxial seismic signal is generated by synthesising the P wave amplitudes in all three orthogonal directions (step ③ in Figure 3-24). Steps ② and ③ describe the overall synthetic triaxial generation process in Figure 3-21. This process includes the steps from (a) to (d) but does not include a comparison between (d) and (a). The validation of the synthetic triaxial can be found in Section 3.3. To generate the mining-induced fracture network, the processing and analysing of synthetic triaxial seismic waves, including calculation of the M_0, seismic source radius R and fracture aperture change τ, are executed as introduced in Section 3.3 (step 4 in Figure 3-24). With a comprehensive and quantitative identification of each seismic-related fracture, the induced fracture network along the longwall panel can be determined.

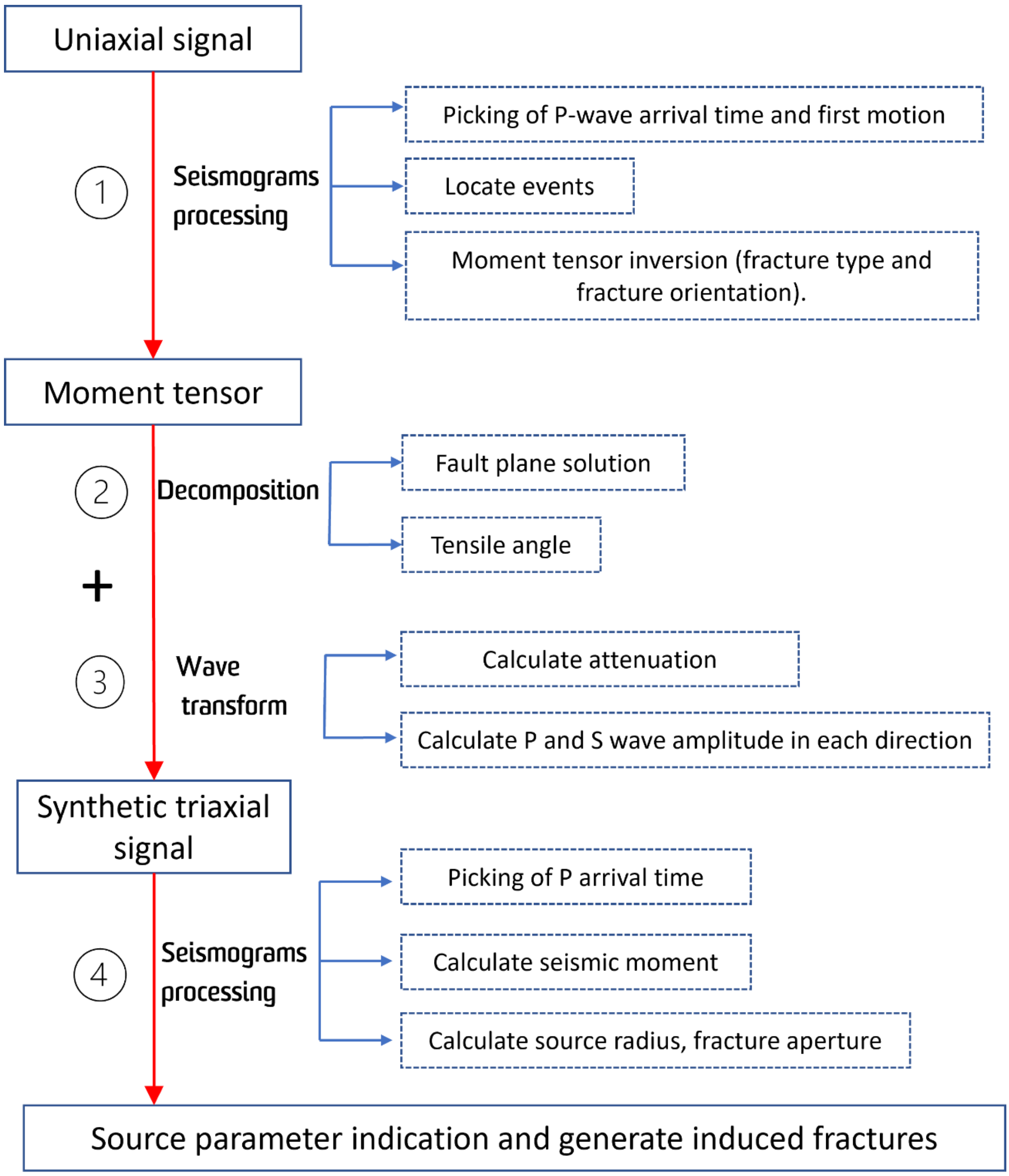

Figure 3-24 A comprehensive workflow to determine mining-induced fracture network based on uniaxial seismic data.

3.4. Conclusions

This study developed a novel approach using uniaxial seismic data to derive synthetic triaxial waves from calculating source parameters by using seismic wave processing methods, including failure mechanism, fracture orientation, fracture radius and aperture.

Seismic monitoring data collected from the Yima underground coal mine in China was processed to verify the feasibility of the proposed method.

The seismic moment tensor inversion was applied to each uniaxial seismic event, and the source failure type was analysed. The failure type was then used to determine the source radiation pattern. The uniaxial signal can be extrapolated to a synthetic triaxial wave with the help of failure plane solution analysis and radiation pattern. This method has been validated by a simple one-period waveform. The differences between the fracture orientation calculated by the synthetic triaxial wave and the initial hypothesis (ground truth angle) are generally less than 30 degrees. The source mechanism derived by the synthetic wave can basically restore the initial hypothesis.

It should be highlighted that in deriving synthetic triaxial waves from uniaxial seismic data, it is critical to ensure that the synthetic process is not influenced by differences in data acquisition, processing, and interpretation methods between the new and old systems. This could include investigating [sensor sensitivity and resolution, noise handling, and any mathematical or statistical comparison that compensates for differences in computing models used. It is also worth noting that additional tests, simulations, or triaxial field seismic monitoring data will be required in the future work of this research.

Taking the Yima coal mine as the case study site, the seismic signal processing, including pre-processing of filtering, frequency domain analysis, wave picks, event locates, and moment tensor inversion, are calculated in detail with the sample seismic waves and seismic events using the proposed uniaxial seismic data analysis method. The b-value is also analysed as an application of the novel synthetic triaxial seismic wave processing method. At last, the flowchart of the integrated seismic signal processing is presented as the preliminary signal process method of the following Chapter 4 and Chapter 5.

Chapter 4. Statistical assessment of mining induced seismic events

This chapter is based on published paper II. The analysis is based on a case study in this paper. Hujiahe Coal Mine is located in the west of Shaanxi province, China. The studied panel, longwall (LW) 102 is about 700 m in depth, 1493 m in length and 180 m in width. The target coal seam has a thickness varying from 13 m to 22.50 m, and the maximum dip angle is 9°. A fully mechanised longwall top coal caving method is adopted, with 3.50 m mined by a shearer and the remaining coal at the top extracted by gravity caving. The coal seam is sequentially overlaid with a 5.95 m thick sandy mudstone layer, a 23.70 m thick siltstone, a 4.65 m thick mudstone, and a 4.80 m thick siltstone.

The 16-channel “ARAMIS M/E” seismic monitoring system developed by EMAG in Poland was installed in the mine in September 2013. For more information about this monitoring system, please refer to Cai et al. (2018). The pre-process of the raw analog seismic signal used in the 16-channel “ARAMIS M/E” seismic monitoring system is the same process that already introduced in Section 3.1. LW102 started to retreat in May 2014 and was completed in July 2015. Although the seismic monitoring system was installed before the start of the panel, due to the calibration delay in the early stage, the system was only available to record reliable seismic activities in the panel from September 2014. Therefore, seismic data from September to July 2015, a total of 293 days, were used for the spatial and temporal correlation analysis in this research.

In this thesis, the seismic dataset contains 14,024 seismic events, and each seismic event is a 5-dimensional array including the 3D spatial location (longitude, latitude, and depth), onset time and recorded seismic energy. Due to the lower accuracy and variance compared to the longitude and latitude, the depth of each seismic event is not considered in this research.

The distribution of cumulative radiated energy and the number of seismic events for one day and their evolution over time (Figure 4-1.a) and space (Figure 4-1.b and c) can be expressed. Over a period of time, the relationship between the number of events (N) and cumulative energy (Log(E)) within individual production days is unclear. A notable example is a comparison between Period 1 and 2 in Figure 4-1(a), a high number of seismic events with low energy level could be observed in Period 1, while in Period 2 only a few high radiated energy events along the main fracture occurs, which results in the maintenance of high cumulative energy but decrease of the event number. A similar pattern can be observed in the space domain as well, as presented in Figure 4-1(b). The conclusion can be drawn from Figure 4-1 that the distribution of seismic events and the energy level can vary significantly in space and time, and this leads to the significance of exploring the correlations based on event location, onset time and radiated energy.

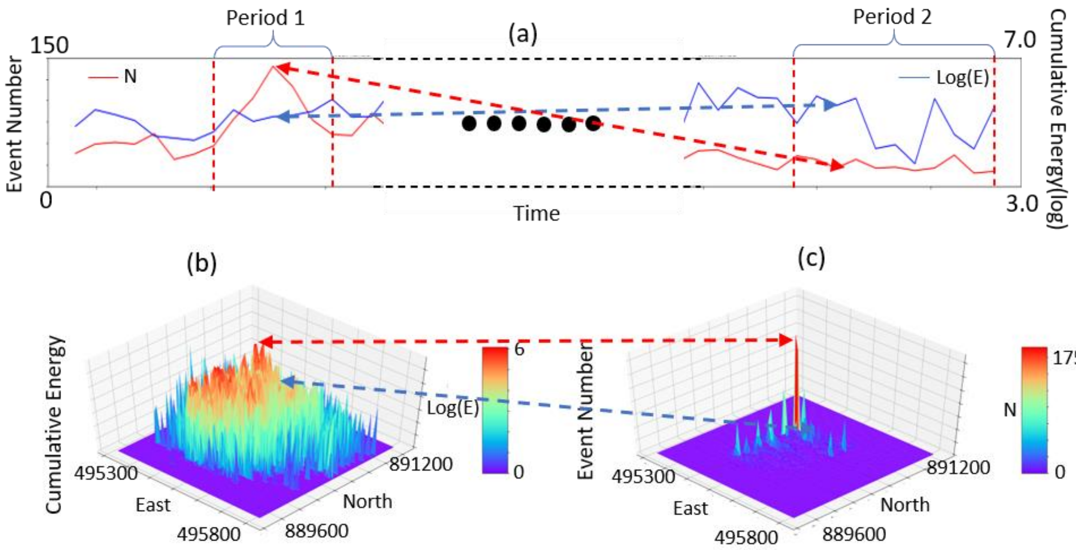

Figure 4-1 (a) time correlation (b)(c) spatial correlation of energy and number of seismic data

Figure 4-2a shows the probability density of seismic events occurring time, while Figure 4-2b and c shows the probability density of longitude and latitude. Figure 4-2d presents a contour map of spatial event density, and the longwall panel is drawn as the red dashed line. Excluding the depth and seismic energy, the distribution of the original seismic event shows both clustering and discrete characteristics in times (Figure 4-2a) and space (Figure 4-2b).

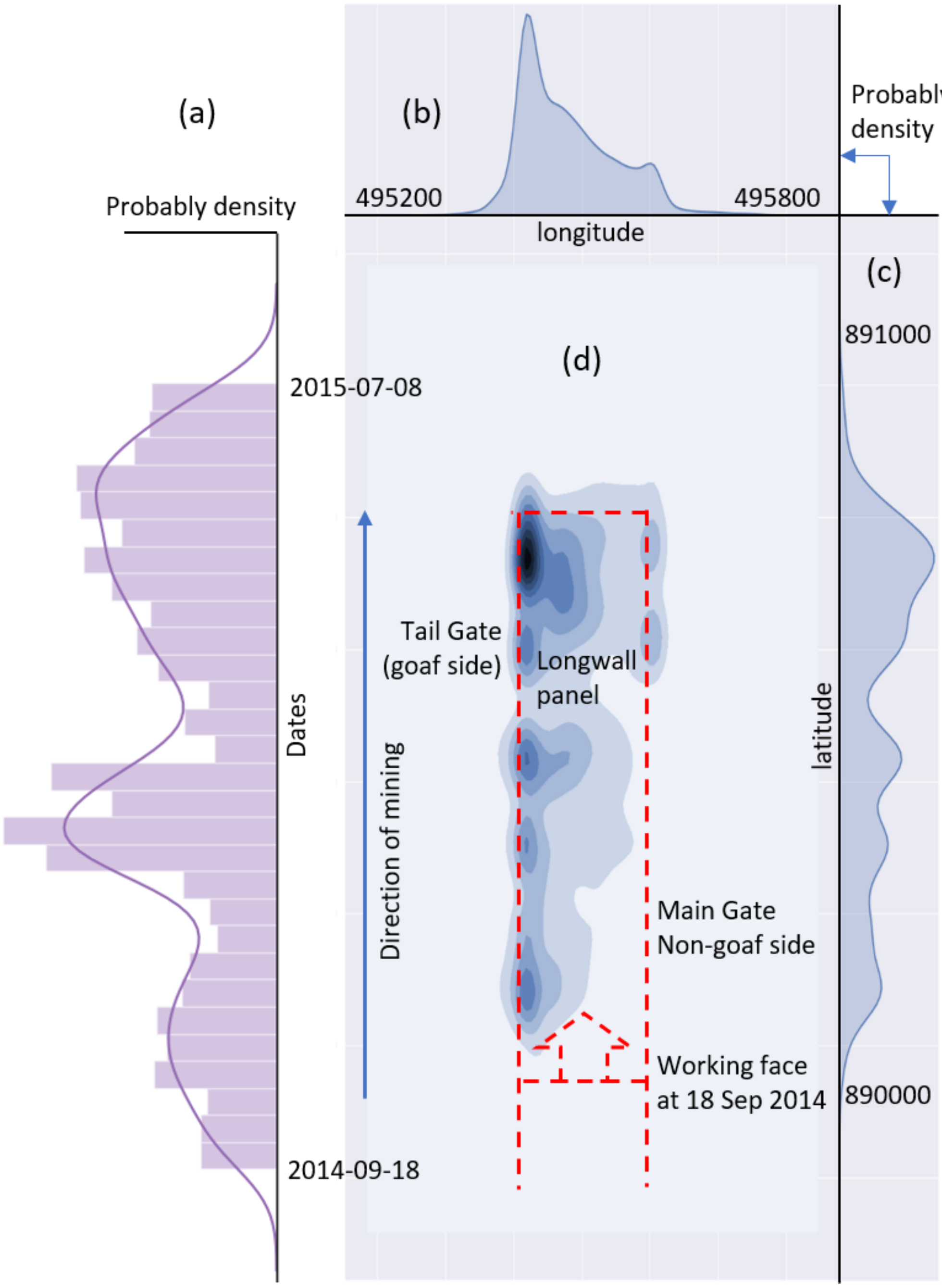

Figure 4-2 Overview of the space and time distribution of all seismic data including probability density of (a) seismic events occurring time, probability density of (b) longitude and (c) latitude, (d)contour map of spatial event density.

The initially collected radiated energy (*E*) data from geophones can be calculated in the scale of *log10(E)*, which has been widely used in seismology research. The probability density function of the energy distribution in local magnitude is shown in Figure 4-3, the energy level is ranged from about +1.0 to +7.0, and this has the significant consistency with the observation from (Fujii and Ishijima 1991). In seismology, the detection capacity of the seismic sensor depends on the density and distribution of geophones, the recording characteristics, and the attenuation in rock. Similar to the completeness magnitude(Gutenberg and Richter 1956), the completeness energy level can be defined as the lowest energy level at which 100% of the seismic events in a space-time volume are detected. To ensure the completeness of the seismic data array during the study period, the magnitude of completeness (m_c) is applied to determine the lowest energy magnitude of seismic events that the seismic monitoring system can fully detect. Only seismic events with energy magnitudes larger than m_c are regarded as complete and used for further analysis. Figure 4-3 shows the probability density function of recorded seismic events over the monitoring period in LW102, where the m_c is found to be at log E=2.3. According to the assumption, a completeness energy level, denoted by log E>2.3, is the lowest energy level at which all seismic events within the monitoring domain may be detected. This threshold is critical since it determines the monitoring system's sensitivity, ensuring that no seismic events are missed due to being below the detection limit. Thus, a total of 8024 seismic events with log E>2.3 are selected for the temporal and spatial correlation analysis.

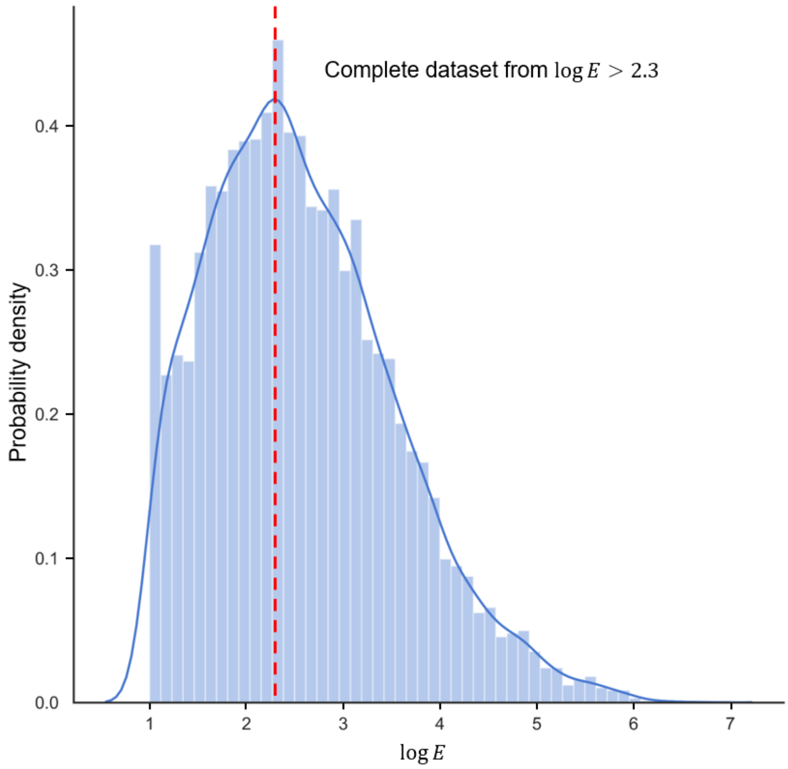

Figure 4-3 Probability density plot of log E for all recorded seismic events.

Figure 4-4a shows the spatial distribution of the selected seismic events in LW102. A large number of events with higher energy magnitudes are located around Fault 5-6. Also, in Figure 4-4b, the contour map of seismic event probability density indicates that intensive seismic activities were reported at the tailgate side of the panel due to the nearby goaf zone.

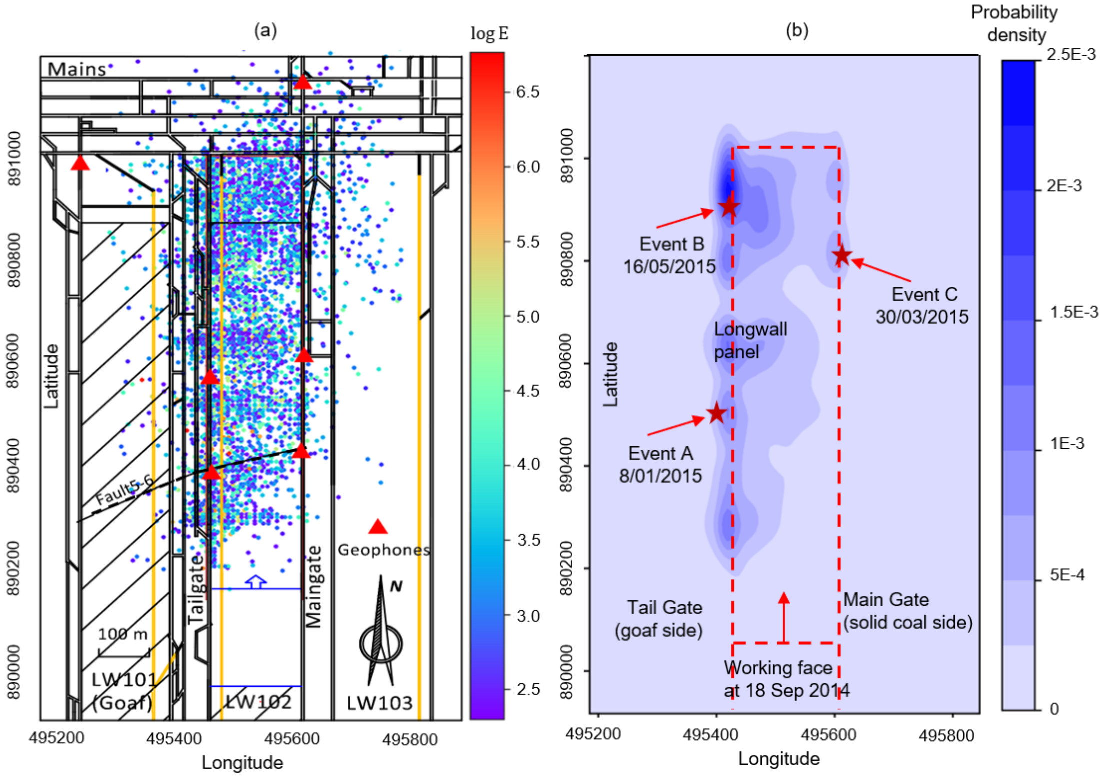

Figure 4-4 (a) Spatial distribution of seismic events (colour represent log E), longwall layout and geophone stations, (b) the probability density distribution of seismic events in a horizontal plane. The red dashed line shows the longwall panel, and Event A, B and C are three typical event locations, which will be discussed in following sections.

Besides the overall figure to show all seismic events recorded over the monitoring period, the monthly evolution of seismic events is shown in Figure 4-5.

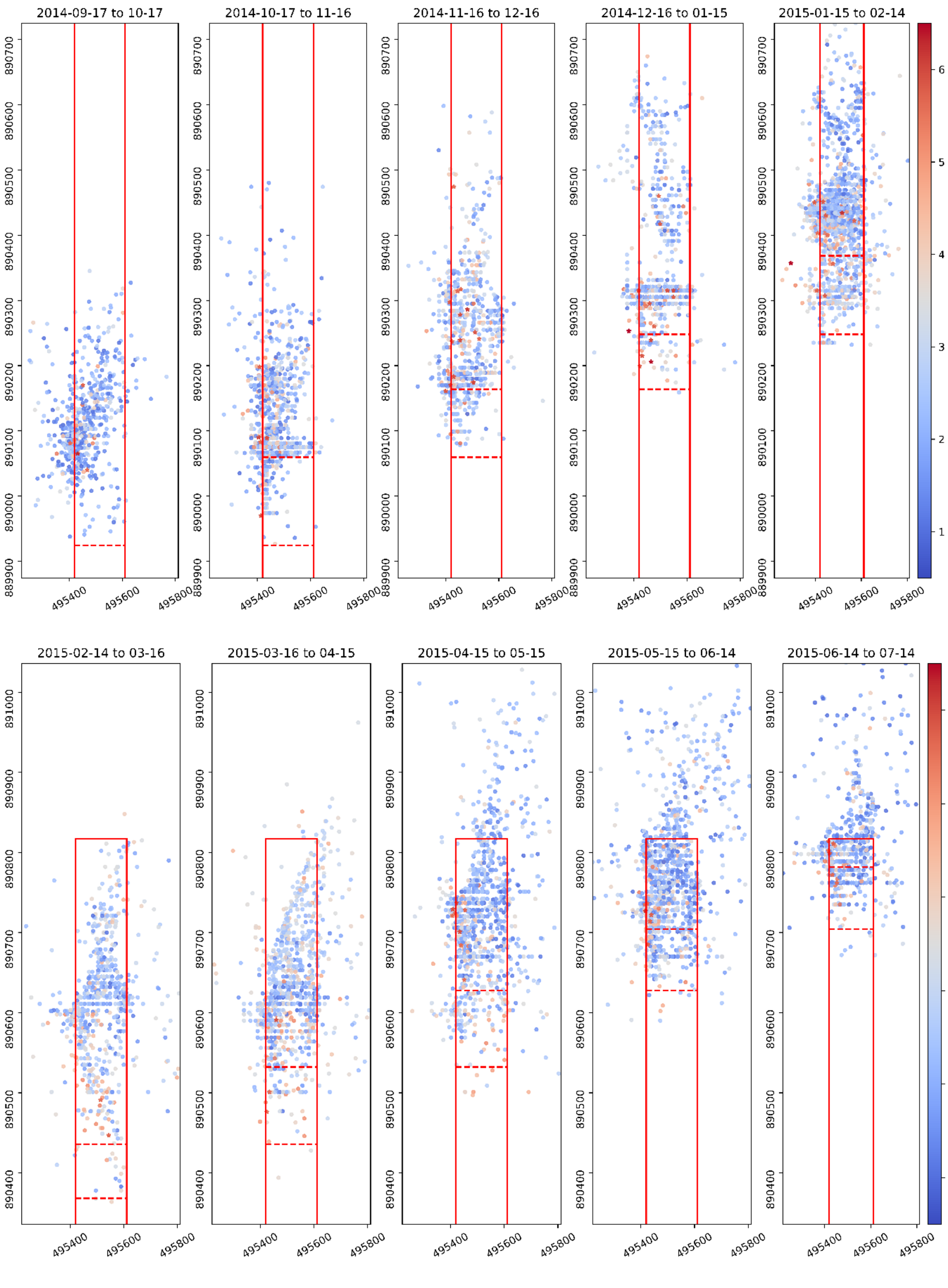

Figure 4-5 Monthly evolution of seismic events spatial distribution in LW110 over the monitoring period. The two dashed lines in each figure indicate the start and the end of the working face over the specified period.

4.1. Stationary test for time series data

The property of stationary process test is of the essence in time series analysis, for implementing that whether the results of empirical analysis maintain appropriate robustness with the change of input parameters. A stationary time series is one whose properties do not depend on the time at which the series is observed. Thus, time series with trends, or with seasonality, are not stationary. The trend and seasonality will affect the value of the time series at different times. In general, a stationary time series will have constant statistical properties such as mean, variance, autocorrelation, etc.

In order to test whether a time series data is stationary, the Augmented Dickey Fuller Test (ADF) is a unique 'Unit Root Test', it is testing if $\phi = 0$ in this model of the data:

$$y_t = \alpha + \beta t + \phi y_{t-1} + e_t \tag{4.1}$$

Which can be written as:

$$\Delta y_t = y_t - y_{t-1} = \alpha + \beta t + \gamma y_{t-1} + e_t \tag{4.2}$$

where y_t is the time-serial data. It is written this way so we can do a linear regression of Δy_t against y_{t-1} and t and test if γ is different from 0. If $\gamma = 0$, then we have a random walk process. If not and $-1 < \gamma + 1 < 1$then we have a stationary process.

The ADF test allows for higher-order autoregressive processes by including Δy_{t-p} in the model. But the test is still if $\gamma = 0$. The null hypothesis for ADF tests is that the data are non-stationary. Rejecting the null hypothesis requires a p-value of less than 0.05 (or smaller).

Table 4-1 ADF test result

ADF test	1%	5%	10%	test value	accept/reject	conclusion
discrete time serial data	-3.4311	-2.8618	-2.5669	-15.0519	reject	stationary
daily event number	-3.4531	-2.8715	-2.5721	-4.111167	reject	stationary
cumulative daily event energy	-3.4532	-2.8716	-2.5721	-5.784185	reject	stationary

Table 4-1 provides the result of ADF test. It illustrates that for all of the three data series (discrete-time serial data, daily event number and daily cumulative event energy) that this paper is going to study, they all meet the condition of rejecting the hypothesis, which, on other words, can be recognized as stationary data. Further correlation analysis of these three time-series data can be ubiquity, and the correlation pattern would not change with the different period or data format used in the research.

4.2. *Statistical methods applied on seismic parameters in time and space domain*

The difficulty of using a large amount of seismic data collected from mining operations for prediction purposes lies in the lack of understanding of the internal correlation between seismic events, as mining-induced seismicity is not a random process (Gibowicz 2009) but has a high correlation with mining activities both spatially and temporally (Arabasz et al. 2005). Invalid prediction results or misleading data interpretation can be derived if the correlation is not well-understood. For instance, during seismic data analysis, questions need to be addressed beforehand, such as how much past data (time window) are required to predict future events and the maximum distance that can be effectively predicted with confidence (grid size). The time window and grid size are essential parameters for investigating spatial and temporal evolutions of seismic events. An undersized time window may not be enough to reflect the general pattern of seismic events. An oversized time window may include unnecessary noisy data that reduce prediction accuracy (Kijko and Funk 1996). Also, a too-large grid may significantly reduce the resolution/accuracy of seismic hazard prediction in space (Kisilevich et al. 2010). A too-small grid can increase computational time and cause overfitting issues. Therefore, the determination of time window and grid size for the temporal and spatial prediction of seismic hazard, respectively, remains a significant challenge using historical seismic data. In order to determine the appropriate time window and grid size, a correlation assessment on seismic data would be required in both the time and space domain.

The correlation analysis of mining-induced seismicity, including its randomness, stationary, and memoryless, would provide an understanding of the past seismic data (Bischoff et al. 2010; González et al. 2016); However, there is no attempt to assess the correlation of mining-induced seismicity quantitively so far. This paper focuses on filling this research gap by applying three different methods to various types of seismic data:

- Autocorrelation function (ACF) calculates the correlation with a delayed copy of the data itself, and equidistant data is required.

- Semivariogram is used to calculate the degree of correlation as a function of distance or time step.
- Moran's I describes the correlation extended in a specific time window, commonly used for a cross-comparison and correlation threshold assessment.

These quantitative correlation assessment approaches can be applied to any parameters of mining-induced seismicity, including spatial location, onset time, energy, source radius, apparent stress, etc. This paper will focus on radiated energy, which represents the total elastic energy radiated by mining activities and is better reflecting the influence on artificial structures compared to the magnitude and other parameters (Gibowicz and Kijko 1994).

Furthermore, many researchers proposed that seismic events can be divided into clusters due to the spatially distinct rock mass failure processes associated with the temporally dependent mining activities (Gibowicz 1986; Leśniak and Isakow 2009; Woodward et al. 2018). The seismic events from different clusters may be independent, whereas events within one cluster are internally correlated (Kijko and Funk 1996). During a mining process, the overall correlation of the entire seismic dataset may be different from the correlation within individual clusters because the cluster-based data can be recognised as being related to a specific area or time. Thus, it is necessary to re-assess correlation characteristics within each cluster and between clusters after seismic data being clustered.

The natural response of rock failure to mining activities is related to seismic occurrences, which can pose a risk to mine operators, equipment, and infrastructure. Because of rock fracture during progressive mining activities, mining-induced seismicity has been demonstrated to be intrinsically associated in both the time and space domains. Understanding the temporal and spatial correlation of mining-induced seismic events is a prerequisite for using seismic data for other purposes, such as rock burst prediction and caving assessment. There are, however, no recognised ways to carry out this crucial work. Input parameters for seismic hazard prediction, such as the time frame of prior data and effective prediction distance, are selected based on site-specific experience with no statistical or physical justification. As a result, the accuracy of present seismic prediction systems is severely limited, which can only be addressed by quantifying the spatial and temporal correlations of mining-induced seismicity. The temporal and spatial correlation of seismic event energy obtained from a sample mine is quantitatively evaluated in this work, utilising several statistical approaches such as Autocorrelation Function (ACF), semivariogram, and Moran's I analysis. Furthermore, seismic events are further divided into seven clusters based on the integrated Spatial-Temporal (ST) correlation evaluation in order to analyse the correlations within particular clusters. The correlations of seismic events are determined to be quantitatively assessable, and their correlations may fluctuate during the mineral extraction process.

Seismic monitoring data collected Hujiahe coal mine is used in this study. Firstly, the correlative period and correlative distance of seismic data are calculated by the ACF and semivariogram function, respectively. The Moran's I is used to evaluate the extent of the correlation and temporal variability. Using the results obtained from the above methods, a spatial-temporal (ST) integrated analysis is conducted to examine the seismic correlation in time and space simultaneously. Finally, seismic events are divided into multiple clusters to investigate the local correlation within individual clusters.

4.2.1. Autocorrelation function (ACF)

In this paper, the *ACF* is used to analyse time-series data of seismic energy. This method normally requires the same time interval between data points (an evenly spaced dataset). A gridding process is required to pre-process the unevenly spaced seismic data onset time. Therefore, the raw seismic energy data recorded with uneven time interval are calculated as cumulative daily energy, which has the same time interval. Assuming k is the lag in the time domain, the temporal variability of two seismic data points with a time difference of k can be calculated based on the autocovariance c_k and the autocorrelation ACF_k. The autocovariance c_k is the covariance of the two seismic data x_i and x_{i+k} at the time *i* and *i+k*, respectively (Equation 4.3):

$$c_k = \frac{\sum_{i=1}^{N}(x_i - \mu)(x_{i+k} - \mu)}{N} \tag{4.3}$$

Where *N* and μ are the number and the mean of the total studied data points, respectively. For an array of seismic data with lag *k*, its *ACF* is defined in Equation 4.4:

$$ACF_k = \frac{c_k}{c_0} = \frac{\sum_{i=1}^{N-k}(x_i - \mu)\,(x_{i+k} - \mu)}{\sum_{i=1}^{N}(x_i - \mu)^2} \tag{4.4}$$

where c_0 is the autocovariance when *k=0*, which is the self-covariance of x_i. ACF_k ranges from -1 to 1, and it shows the variation of seismic data correlation along with *k*. A typical ACF plot is shown in Figure 4-6a. ACF_k equals 1 when k is 0, and it shows a downward trend with the increase of k. The seismic data array is regarded as correlated until the ACF_k falls below Bartlett's limit (I_B), which is expressed as Equation 4.5 (Jaksa et al. 1999):

$$I_B = \pm \frac{1.96}{\sqrt{N}} \tag{4.5}$$

The range of k before ACF_k reaching Bartlett's limit is called the correlative period. The highest correlative period of seismic data is presented when ACF_k reaches the upper limit of I_B, and the corresponding time lag is called the scale of fluctuation (SOF). For the lag larger than the SOF, it is considered that seismic data presents no correlation. Apart from the correlative period calculated using ACF, SOF can also be used to represent correlative distance, which is calculated using Semivariogram (Onyejekwe et al. 2016).

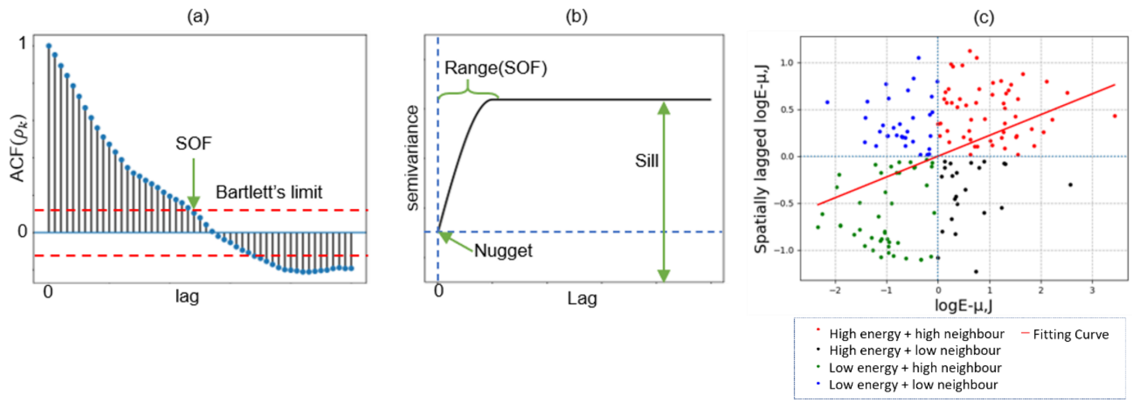

Figure 4-6 An example plots of (a) ACF, (b) semivariogram, and (c) Moran's I

4.2.2. Semivariogram function

In order to quantitively evaluate the correlation of the unevenly spaced seismic data, semivariogram function is used here. Semivariogram is a graph showing the variation of semivariance with different lags. For a given lag k in the time or space domain, the semivariance Vs of a seismic data array is calculated as introduced by (Clark, 1979):

$$V_s = \frac{\sum_{i=1}^{N(k)} (x_i - x_{i+k})^2}{2N(k)} \tag{4.6}$$

In Equation 4.6, *N(k)* is the number of data pairs separated by lag k. x_i represents the i^{th} seismic datum, and x_{i+k} represents the paired seismic datum of x_i with a spatial or temporal interval of k. Semivariogram is the curve of the semivariance results at different lags fitted by selected mathematical models. A typical semivariogram is shown in Figure 4-6b; the semivariance of the data array increases along with the lag increase until a maximum is reached at a certain lag; the increasing of the semivariances indicates the decline of autocorrelation. Three parameters are used to characterise the correlation of a semivariogram:

a) Nugget, the semivariance when k=0.

b) Sill, the maximum semivariance of the data array.

c) Range, i.e. SOF, the critical lag length for the semivariance to reach the sill.

In a semivariogram, a lower nugget and sill indicate a higher correlation. A lower SOF suggests the faster attenuation of correlation along with the lag increase. The calculation of SOF varies slightly between different mathematical models. Table 4-2 lists three fitting models used in this research to calculate SOF.

Table 4-2 Mathematical models available for semivariogram fitting

Model	Fitting Function	SOF, θ
Gaussian	$\mathrm{G}(x) = C\left(1 - e^{\frac{-k^2}{a^2}}\right) + C'$	$\theta = \pi^{0.5}a$
Spherical	$\mathrm{G}(x) = C\left(\frac{3k}{2a} - \frac{k^3}{2a^3}\right) + C' \quad k < a$ $\mathrm{G}(x) = C + C' \quad k > a$	$\theta = \frac{3}{4}a$
Exponential	$\mathrm{G}(x) = C\left(1 - e^{\frac{-k}{a}}\right) + C'$	$\theta = 2a$

Note: a, C, C' are fitting parameters.

4.2.3. Moran's I

Moran's I (MI) is an index to describe the spatial similarity of a dataset. (Tiefelsdorf and Boots, 1995) suggest that Moran's I is proved to be flexible for investigating the characteristics of the distribution and correlations for distinct spatial data. For a seismic data array with N seismic events, its MI is defined in Equation 4.7 (Tiefelsdorf and Boots 1995):

$$MI = \frac{N}{\sum_i \sum_j w_{ij}} \frac{\sum_j w_{ij}(x_i - \bar{x})(x_j - \bar{x})}{\sum_i (x_i - \bar{x})} \tag{4.7}$$

Where $\bar{x}$ is the mean of the seismic data array. x_i and x_j are the seismic data of events i and j. w_{ij} is a matrix of spatial weights. In this equation, spatial weights are calculated based on the inverse distance weighting of k-nearest points (ten points are selected in this paper).

MI can also be calculated graphically using Moran's I scatter plot shown in Fig.1c. In this figure, the horizontal axis is $(x_i - \overline{x})$. The vertical axis shows the difference between the average of the above ten nearest seismic data (x_i) and $\bar{x}$. MI is then calculated as the linearly fitted line slope for all data points across the origin, which is shown as the red line. As the calculation of the slope in this figure is essentially the same as Equation 4.7, identical *MI* results will be achieved using this graphic method or Equation 4.7. In Figure 4-6c, the four quadrants demonstrate different correlation conditions of seismic events. The first quadrant indicates high energy seismic events are clustered with high energy neighbouring events, and the third quadrant indicates low energy seismic events are clustered with low energy neighbours. Seismic events in the second and fourth quadrants show low energy events are sitting close to high energy neighbours and high energy events are close to low energy neighbours, respectively.

4.3. *Quantitative assessment of the temporal correlations of seismic events induced by longwall coal mining*

In this section, both ACF and Semivariogram are used to investigate the temporal correlation of the seismic data in LW102. ACF is used to assess the temporal correlation of an evenly spaced seismic data array (cumulative daily seismic energy). Semivariogram is used to investigate the temporal correlation of non-evenly spaced seismic data (seismic energy per event). The SOF in the time domain (SOF-time) is determined for both ACF and Semivariogram to quantify the correlative period of the seismic data.

4.3.1. *Autocorrelation functions (ACF)*

As mentioned in Section 2.1, the ACF analysis is applied to the evenly spaced data with the same interval. The raw seismic events are pre-processed into daily cumulative data. A total of 293 data points representing the cumulative energy within 293 monitoring days are applied to calculate ACF_k, where x is substituted by $\log E_c$, and E_c is the cumulative daily energy. The Bartlett's limit is calculated.

Figure 4-7 is the ACF results of cumulative daily seismic energy in LW102 with different lags. In this figure, the I_B is ±0.1145 shown as the red dashed lines, and the SOF-time is calculated as six days, which indicates a relatively strong correlation of cumulative daily energy in six days. In other words, the future daily seismic energy in LW102 is likely to be dependent on the recorded seismic energy in the past six days. It will be independent with any data beyond that period. The ACF of daily seismic energy drops to 0.44 when the lag is only one day, which shows the increase of randomness.

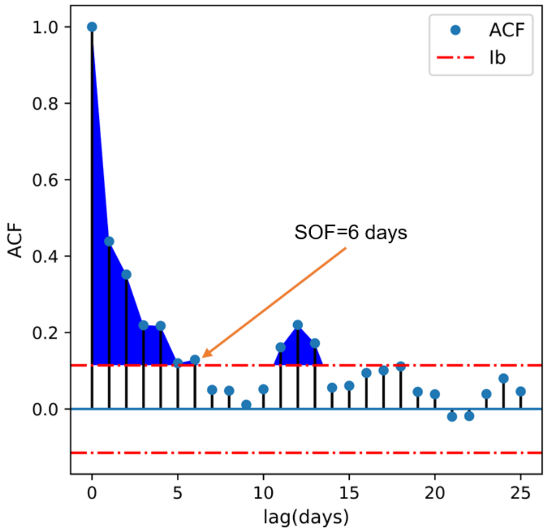

Figure 4-7 ACF plot for cumulative daily energy.

Besides, the value of cumulative daily energy is also affected by the number of events that occurred during the day and face advance distance on that day. Therefore, the daily average energy and energy per meter of face advance are also applied in the ACF analysis. The average daily energy can be calculated as $\log\frac{E_c}{N}$, and the N is the number of seismic events that occurred on that day. The average energy per metre can be calculated as $\log\frac{E_c}{F}$, where F is the face advance distance on that day.

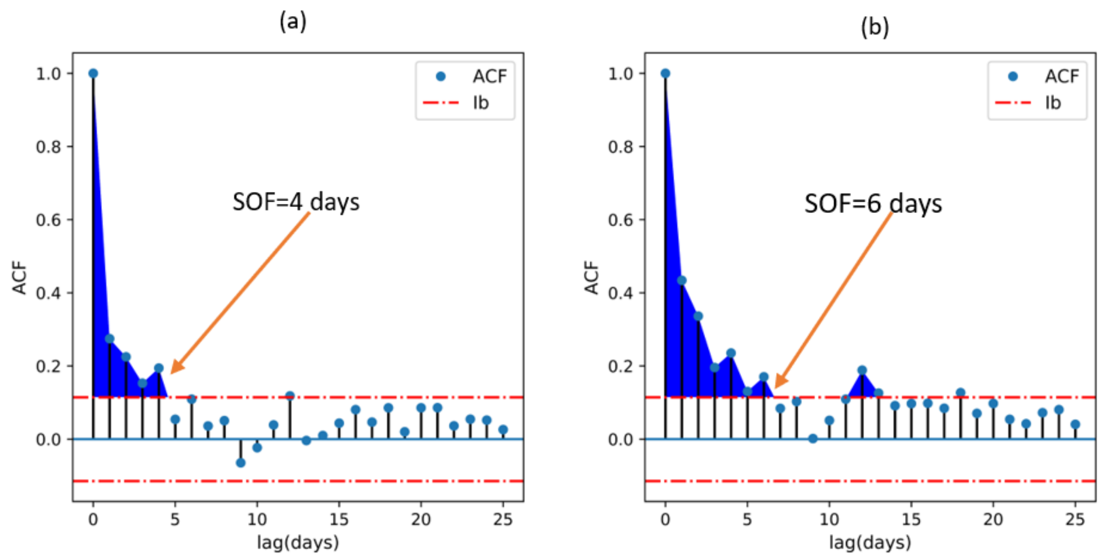

Figure 4-8 ACF plot for (a) the average daily energy and (b) the average energy per metre of face advance.

The ACF values of the above two parameters are presented in Figure 4-8. The SOF-time of average daily energy decreases to four days, and the SOF-time of average energy per metre remains at six days compared to Figure 4-7. The similar SOF-time calculated from Figure 4-7and Figure 4-8 indicates that the number of events and the face advance rate only have a marginal effect on the autocorrelation of cumulative energy. One possible reason could be that $\log\left(\frac{E_c}{N}\right)$ is equal to $\log(E_c) - \log(N)$, and comparing with Ec, the value of N is much smaller in orders of magnitude. The same reason also applies to the face advance rate F. In other words, if one seismic event has a very high energy release in a typical production day, it will significantly increase the average value and decrease the correlation of cumulative energy.

Therefore, the correlation of cumulative energy analysed via ACF provides an approach to quantitively assess the correlation of seismic event energy. The event number and face rate can also be considered and analysed. But the result is sensitive to high energy events. The method in this chapter is suitable for a zone with similar size of fractures that can trigger seismic events with comparable energy levels.

Apart from the daily cumulative seismic energy, the daily seismic event number can also be analysed via ACF. Figure 4-9 shows the ACF results of the daily event number. It indicates that the SOF-time of the daily event number is 26 days, given the I_B at ±0.1145, representing a strong correlation of daily seismic event number within 26 days. Also, the ACF of the daily event number is larger than 0.5 when the lag is lower than four days. It indicates that the daily event number is significantly influenced by those event numbers recorded in the past four days. Due to the strong correlation in the low lag of seismic event number, seismic event number prediction would yield more reliable results than that of cumulative energy.

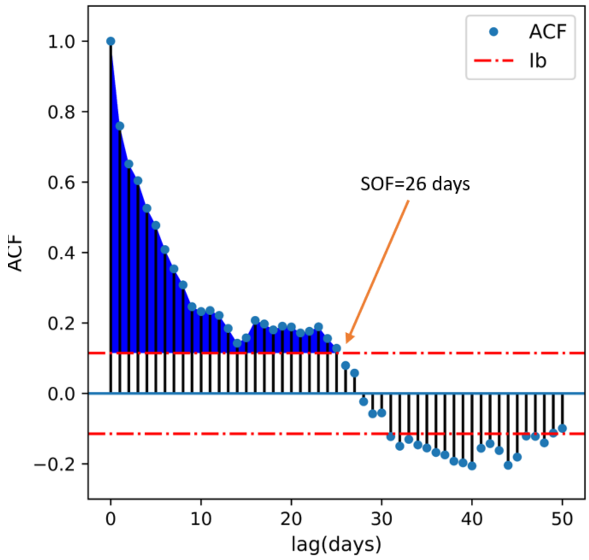

Figure 4-9 ACF plot for daily event number.

4.3.2. *Semivariogram function*

(1). Overall semivariogram evaluation

Unlike ACF dealing with evenly spaced seismic data (cumulative daily energy), the semivariogram function is applied to assess the temporal correlation of the unevenly spaced seismic data, such as the onset time of individual seismic events. The algorithm of this method can be referred to as Section 2.2. The semivariances of seismic energy based on time lag are calculated and presented in Figure 4-10 as red circles. To obtain the semivariogram function, a goodness-of-fit test is conducted to select the best-fit model from three mathematical models, i.e., Gaussian, spherical, and exponential. The fitting performance of each model is evaluated by Root-Mean-Square (RMS) and R-square. These results are summarised in Table 4-3, indicating that the exponential model best fits the semivariances of the studied seismic data because of the lowest RMS and the highest R-square. It should be noted that the exponential fitting is the best-fit model when analysing the temporal correlation using all seismic energy data. The best-fit model may vary depending on the type and amount of seismic data inputted in this method.

Table 4-3 Comparison of three fitting models for the temporal semivariogram of seismic energy.

	RMS	*R-square*
Gaussian	0.00642483	0.362562
Spherical	0.00641485	0.364542
Exponential	0.00635507	0.37633

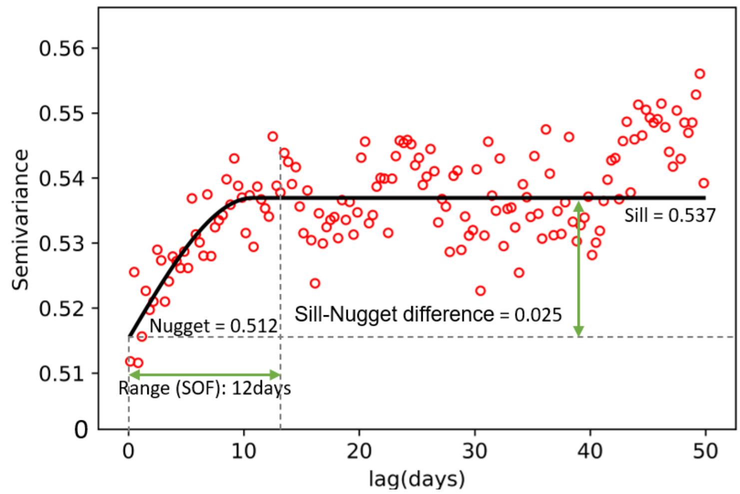

Figure 4-10 Semivariogram of seismic energy, the red circles are the semivariance value at each time lag, and they are fitted by the exponential function as presented in the black curve.

The black line in Figure 4-10 shows the semivariogram of the seismic energy of the studied events in LW102. The SOF-time of about 12 days indicates that the seismic energy of individual events is becoming less correlated along with the lag increase within 12 days. The difference between the sill and nugget is 0.025, which is significantly lower than the nugget, which implies a rapid decline of the correlation and high variability of seismic energy in a short time range.

It should be noted that the SOF-time of 12 days correlative period is calculated based on the unevenly spaced seismic energy data. In comparison, the SOF-time of six days correlative period obtained by ACF is based on the daily cumulative seismic energy data. Compared with the semivariogram method, ACF requires pre-processing unevenly spaced seismic energy as cumulative daily energy, which may introduce an artificial effect or bias to the correlation analysis. Thus, it is believed that SOF-time calculated by the semivariogram function can better reflect the correlation nature of raw seismic data. An application of the 12 days SOF-time will be presented in Section 5.2.

(2). The maximum correlation period determined by semivariances

The SOF-time calculated by semivariogram is the average correlative period of all seismic energy data in the study period, which means that if the correlative period of partial data is assessed, the result could fluctuate around 12 days. Besides the average correlative period of the overall data, the maximum correlative period is critical to be evaluated. This could be achieved by the semivariances calculation based on all the seismic data with a time difference smaller than the lag *k*, rather than using the paired seismic data x_{i+k} in Eq.4.

This specific semivariance is called the cumulative semivariance, which represents the evolution of semivariance along with the increasing of input data. Figure 4-11 shows the cumulative semivariance of the studied seismic data (marked as red crosses), which increases rapidly at the beginning and then flattens. The first-order derivative of the cumulative semivariance (marked as blue dots) is also calculated. The derivative has a gradual downward trend and tends to reach the elbow point when lag *k* is at around 40 days. The slop drops to around 0 for the first time at this elbow point. It suggests that 40 days is the maximum correlative period of studied seismic energy data. The reason is that when lag *k* is larger than 40 days, most of the first-order derivative is close to 0 due to the slow increase of the cumulative semivariance. It means that semivariance considering the data within 40 days will not be much different from the semivariance considering more than 40 days. Therefore, the correlation analysis of seismic data within 40 continuous days can capture the general correlation characteristics over that period.

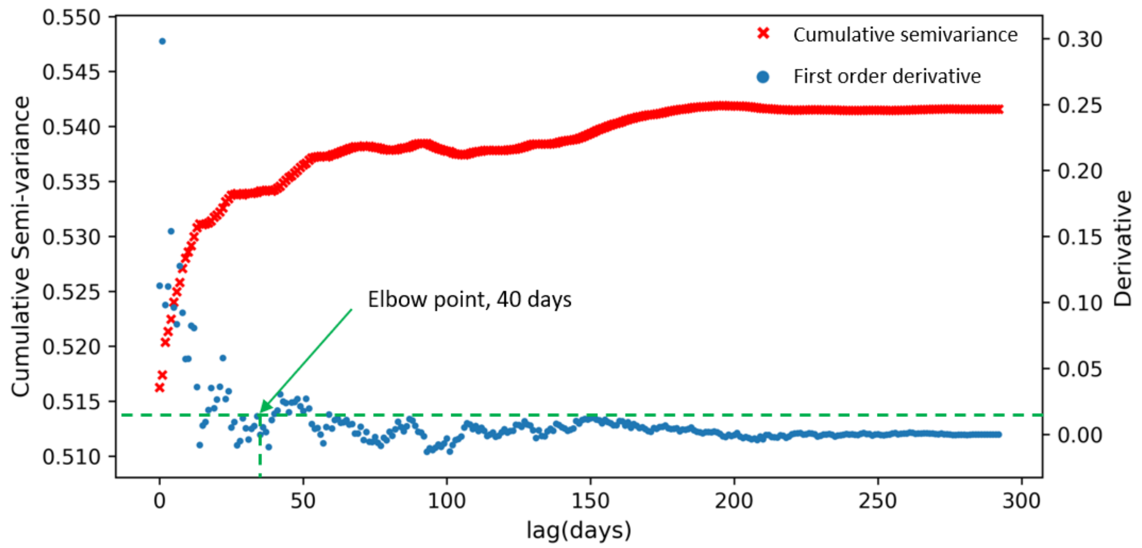

Figure 4-11 cumulative semivariance (marked as red cross) and its first-order derivative (marked as blue dot), the green arrow noted the elbow point. The green dashed line represents its lag of 40 days and cumulative semivariance of 0.514.

(3). The evolution of seismic data correlation in the time domain

Besides the average correlative period and the maximum correlative period, an attempt has been made to analyse the evolution of the temporal correlation of the studied seismic data over the ten months of the monitoring period, the semivariogram function is used to assess the correlation of seismic data recorded within sequential periods. A moving time window based on the maximum correlative period is defined here, which can sequentially select seismic data within that time window. The moving window is large enough to capture the inherent correlation of seismic data within the selected period. Still, it should not be too large to ensure enough sequential periods to reflect the temporal variation of seismic data correlation.

According to the maximum correlative period calculated above, semivariogram analysis can be applied to every moving time window with 40 days of seismic data. The moving step is set as one day. The SOF-time, nugget and sill are sequentially calculated by the best-fit from Gaussian, exponential and spherical models for each time window. The variations of SOF-time selected by the best-fit and its RMS are shown in Figure 4-12. It should be noted that the trend of how SOF changes at a different time is more critical than the exact magnitude of SOF because of the variability of fitting quality in each period. As expected, the temporal correlation of seismic energy is not a constant value but varies with time. The trend of the correlative period evolution shows a periodic distribution during the whole process of the coal extraction, and it tends to form seven peaks with different sizes. It should also be noted that before March 2015, the SOF shows a significant variance with a relatively high RMS, indicating the low quality of the semivariogram fitting. After March 2015, a more reliable SOF can be derived due to the lower RMS.

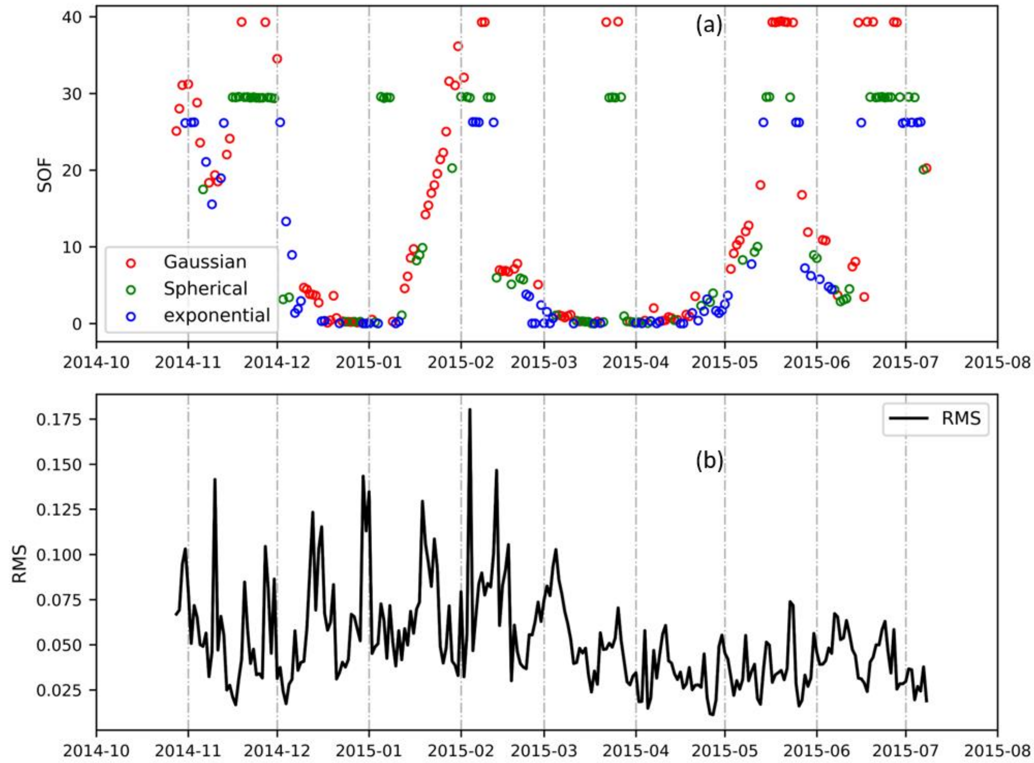

Figure 4-12 (a) The evolution of SOF-time in each time window calculated by semivariogram using the best-fit method from Gaussian, Spherical and Exponential models. (b) the RMS of semivariogram fitting in each time window

4.4. *Quantitative assessment of the spatial correlations of seismic events induced by longwall coal mining*

Moran's I and the Semivariogram are used to investigate the spatial correlation characteristics of the seismic energy. The degree of spatial dependence between seismic events is quantified. Only the horizontal locations of the studied seismic events are used here due to the location errors in the vertical direction of seismic data recorded in tabulate coal deposits. The SOF in the space domain (SOF-space) is determined based on semivariogram to quantify the correlative area of the seismic data.

4.4.1. *Moran's I*

Moran's I is applied to assess the extent of spatial correlation and identify a strong spatial correlation period based on a moving time window method. As mentioned in the previous section, the correlative period of the studied seismic data is about 12 days, which is the average SOF-time of unevenly spaced seismic energy data calculated in Section 4.3. Therefore, the time window of Moran's I calculation is set as 12 days. The reason for not using the maximum correlative period is that MI does not require the moving time window to be large enough to reflect the general correlation characteristics over a long period. The variation of the spatial correlation is more critical in this section. Also, since the analysis should be based on randomisation assumption and conduct null hypothesis testing, the MI results are further standardised as the *Z*-value using Eq.6. A P-value less than 5% is considered significant (reject the null hypothesis), suggesting seismic events are spatially autocorrelated on the global scale.

$$Z = \frac{MI - E(MI)}{\sqrt{var(MI)}} \tag{4.8}$$

Figure 4-13 shows the plot of *MI* and *Z* for seismic events recorded over the monitoring period. The MI value is calculated by both the mathematic equation and the graphic method mentioned in Section 4.2. These two methods show identical MI values. The evolution of MI value indicates various correlation degrees of seismic events in space when LW102 is retreating. Except for one date below the confidence limit, most of the Z values are higher than the 5% confidence interval limit, indicating seismic energy are spatially correlated at various degrees, which supports the concept of seismic event prediction in space.

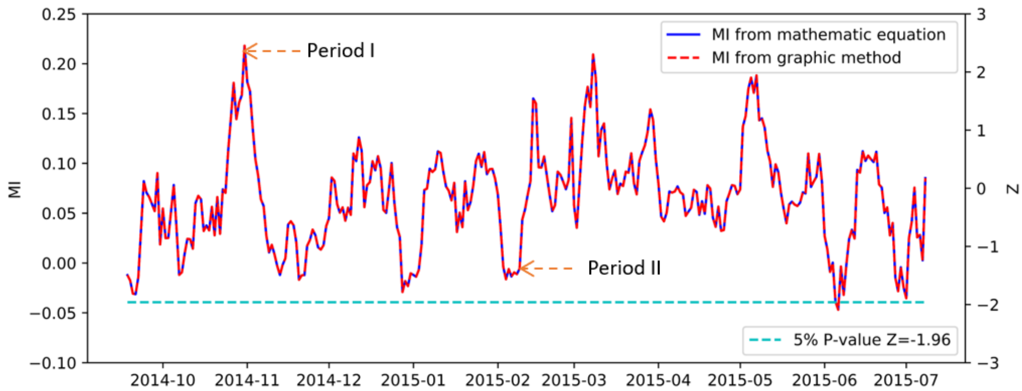

Figure 4-13 MI values calculated from two different methods (in the left axis) and Z value (in the right axis) over the monitoring period, a 5% P-Value of Z is drawn as the blue dashed line.

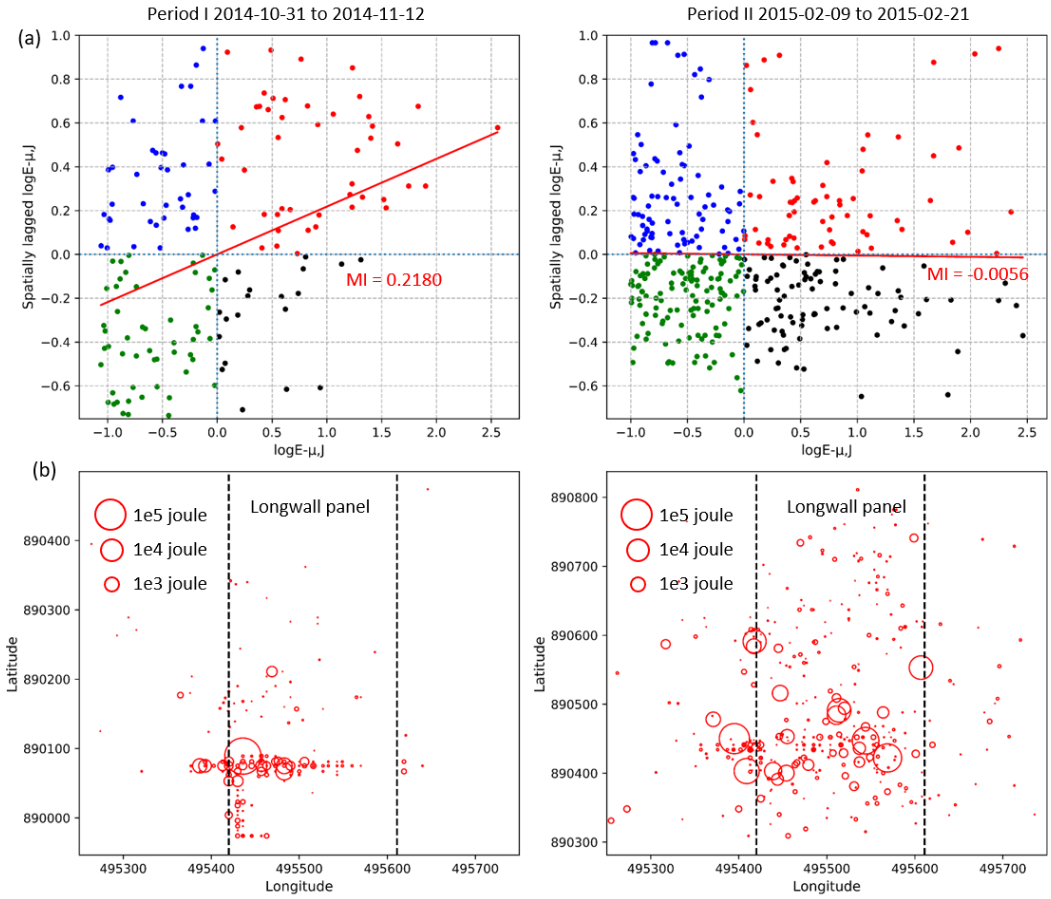

Figure 4-14 (a) Typical Moran's I calculated using the graphic method, and the red line is the linear fitting; MI value is the slope of the red line, (b) the spatial distribution plots of seismic events for Period I and II, size of the circle indicates the seismic

To examine the spatial energy distribution when different *MI* value is detected, the seismic event distributions at two typical periods (Period I and Period II) with *MI*>0 and *MI*=0, respectively, are presented in Figure 4-14. Figure 4-14a shows the scatter plot of *MI* values calculated using the graphic method for Period I and Period II. Figure 4-14b illustrates the spatial energy distributions of the seismic events at these two periods. According to this figure, from 31 October 2014 to 12 November 2014 (Period I), the *MI* reaches the maximum of the entire monitoring period. The seismic events have a clear trend of high energy events clustered together in space, and so as the low energy events. From 09 February 2015 to 21 February 2015 (Period II), *MI* is close to 0, which means no spatial correlation of seismic energy among these events. By visually inspecting the plot of the seismic event distribution in Period II in Figure 4-14b, the same conclusion can be achieved: the high energy events and low energy events are distributed randomly in this 2D horizontal space.

4.4.2. 2D spatial semivariogram

In order to obtain the correlative distance (radius), the method used here to measure the correlation from point to point is the 2D spatial semivariogram, which can quantify the degree of spatial dependence between samples in a specific orientation and assess the degree of attribute's continuity. The algorithm of the semivariogram can be referred to as Section 4.2.

In Equation 4.6, x_i indicates the i^{th} seismic event energy and lag k represents the radius of the searching circle in the calculation of spatial semivariogram. Table 4-4 shows the evaluation results of three fitting methods and the best-fit method is the exponential function. Figure 4-15 presents the spatial semivariogram plot for the LW102 working face, in which the calculated semivariance is shown in red circles and the fitted exponential model in black curve. The correlative distance is defined as the SOF-space, which is 23m in this case. The released energy of a seismic event has a gradually decreasing correlation along with the increase of the distance from its hypocentre within 23 m radius, and no correlation presents beyond this radius. The difference between the sill and nugget is 0.127, which is relatively higher than the temporal semivariogram but still much smaller than the nugget and sill. It implies a rapid decline of the correlation and high variability of seismic energy in a short distance.

Table 4-4 Comparison of three fitting models for the spatial semivariogram of seismic energy.

	RMS	*R*-square
Gaussian	0.018912	0.615597
Spherical	0.017715	0.662701
Exponential	0.017561	0.668547

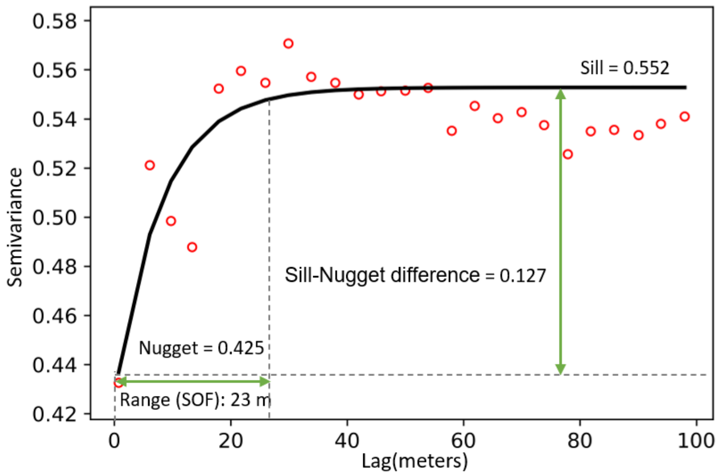

Figure 4-15 Spatial variogram plot for seismic energy over the monitoring period. The red circles are the semivariance. They are fitted by the exponential function as presented in the black curve.

4.5. *Spatial-temporal correlation assessment using reference seismic events.*

To simultaneously investigate the spatial and temporal (ST) correlation around a reference location and time registered by the occurrence of a reference seismic event in LW102, the distance and time difference between the reference event and other seismic events need to be considered together. The calculation of distance only considers longitude and latitude coordinates for the same reason mentioned in Section 3. Three seismic events were selected as the reference events in this research. These selected seismic events all have relatively high energy and located close to the longwall panel because the high energy events in the coal extraction process always represent a large formation of discontinuities and massive energy release. It is worth noting that the method proposed in this section could be used in any reference events with a specific onset time and location. The selected Event A has the seismic energy of 2.6 MJ, which is located around Fault 5-6. Event B is located near the tailgate (goaf side) with seismic energy of 1.4 MJ. Event C is a seismic event with an energy of 280 kJ located near the maingate (solid coal side). The location of these three events, as well as their occurring time, are highlighted in Figure 4-4.

Based on Event A, B and C, the time difference and distance between all other events and the reference events are calculated, which are shown as scatter plots in Figure 4-16a. The y-axis shows the Euclidean distance difference, while the x-axis shows the time difference. Based on the data in Figure 4-16a, to calculate the semivariogram for both time and distance simultaneously, a unity-based normalisation needs to be applied to these two parameters. The maximum distance is taken as 800m, and the maximum time difference is taken as 300 days. The corresponding semivariogram is calculated and presented in Figure 4-16b, following the method introduced in Section 4.2. Herein, the property x_i represents event energy, and lag k is a unity-based normalisation of the time difference and distance. The exponential function is used because it is proved in Section 4.3 as the best-fit method when dealing with all studied seismic data. The lag k in the semivariogram plots in Figure 4-16b contains the information conveyed in both the time and space domain.

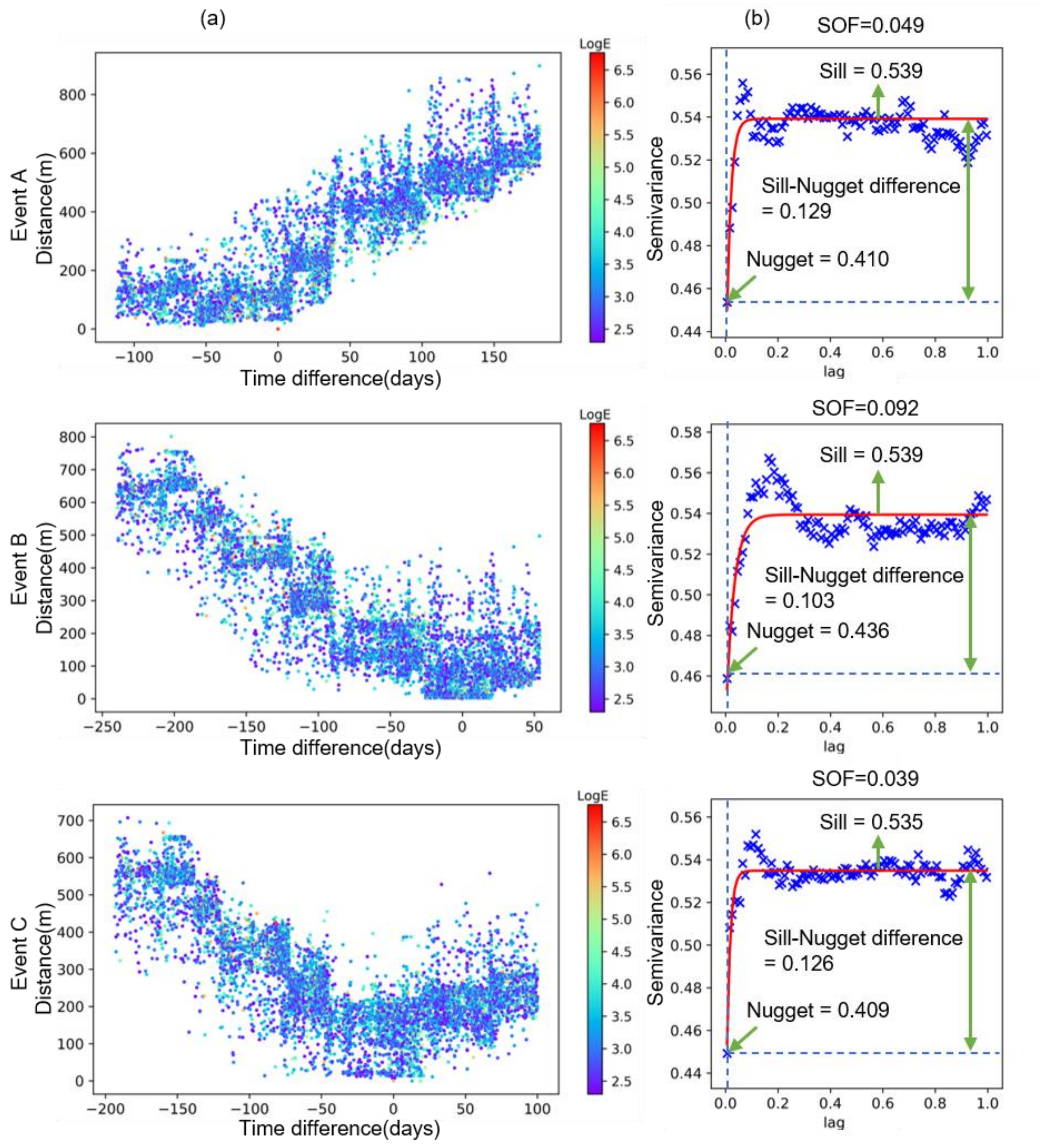

Figure 4-16 (a) 2D distribution of time difference and distance between reference events and all other seismic events (b) semivariograms for the three reference events.

The distance-time difference plots in Figure 4-16a show that a linear relationship between distance and time difference can be observed for the reference events. The semivariogram plots in Figure 4-16b all show an upward trend before levelling off. The parameters of the three semivariogram plots are also similar, with nugget at around 0.4 and sill at 0.54. The similarity of the nugget and sill for all three reference events indicates that the extent of ST correlation close to or far from the reference events is similar and less affected by the specific location or onset time of the reference events.

Based on the semivariogram plot, the SOF of time difference and distance can be obtained by inverting the process of the unity-based normalisation. The SOF-time for the three reference events A, B, and C are 2, 4, and 2 days, respectively, and the SOF-space are 4.9, 9.2 and 3.9 m, respectively. Compared to the SOF-time of 12 days in Section 5.1.2 and SOF-space of 23 m in Section 4.3, the SOF obtained by ST correlation analysis is much smaller in both the time and space domain. This is because it is less likely to have seismic events with strong temporal and spatial correlation at the same time.

The ST correlation gives relatively stable correlation results when assessing the correlation characteristics around three reference events. The nugget and sill are very similar, and the SOF only has a marginal difference. This conclusion seems to be the opposite of the conclusion that the correlation is variational in the time and space domain, as discussed before. But in fact, the temporal and spatial correlation assessments are designed to detect the overall correlation trend. In contrast, ST correlation chooses three reference points and assesses the correlation by taking the three points as a basis. The correlation near the reference points (nugget) and the correlation far from the reference points (sill) are purely based on the location and onset time of three reference events. The three points all have relatively high energy, which indicates that they might be induced by the slipping of pre-existing fractures. Besides, the three locations all have a similar event density, energy distribution, and even seismicity source mechanism.

4.5.1. Discussion on the impact of energy uncertainty.

We appreciate that, as a basic parameter to assess the interactions among seismic events, seismic energy can be very uncertain. This is highly related to the network configuration and coverage concerning the orientation of the tectonic structures that radiate the energy during seismic rupture. To investigate how energy uncertainty may affect the correlation analysis results and whether bias would be introduced if seismic input data contain inherent uncertainties, a 50% variation was added to the seismic energy data (each energy is changed into a random value within ±50% of its original value, following a Gaussian distribution). Figure 4-17 presents the correlation results calculated using the proposed three methods. Figure 4-17 a and b show that the seismic events with and without energy uncertainty have very similar ACF values and almost identical SOF-time from ACF. Figure 4-17c and d indicate that a slight difference of sill and nugget is shown when considering energy uncertainty. The change of SOF-time is less than 1 day, and thus the SOF-time from the semivariogram remains the same value. Figure 4-17e and f also indicate a very similar MI value. The results in Figure 4-17 demonstrate the energy uncertainty of seismic events will cause limited impact on the correlation results.

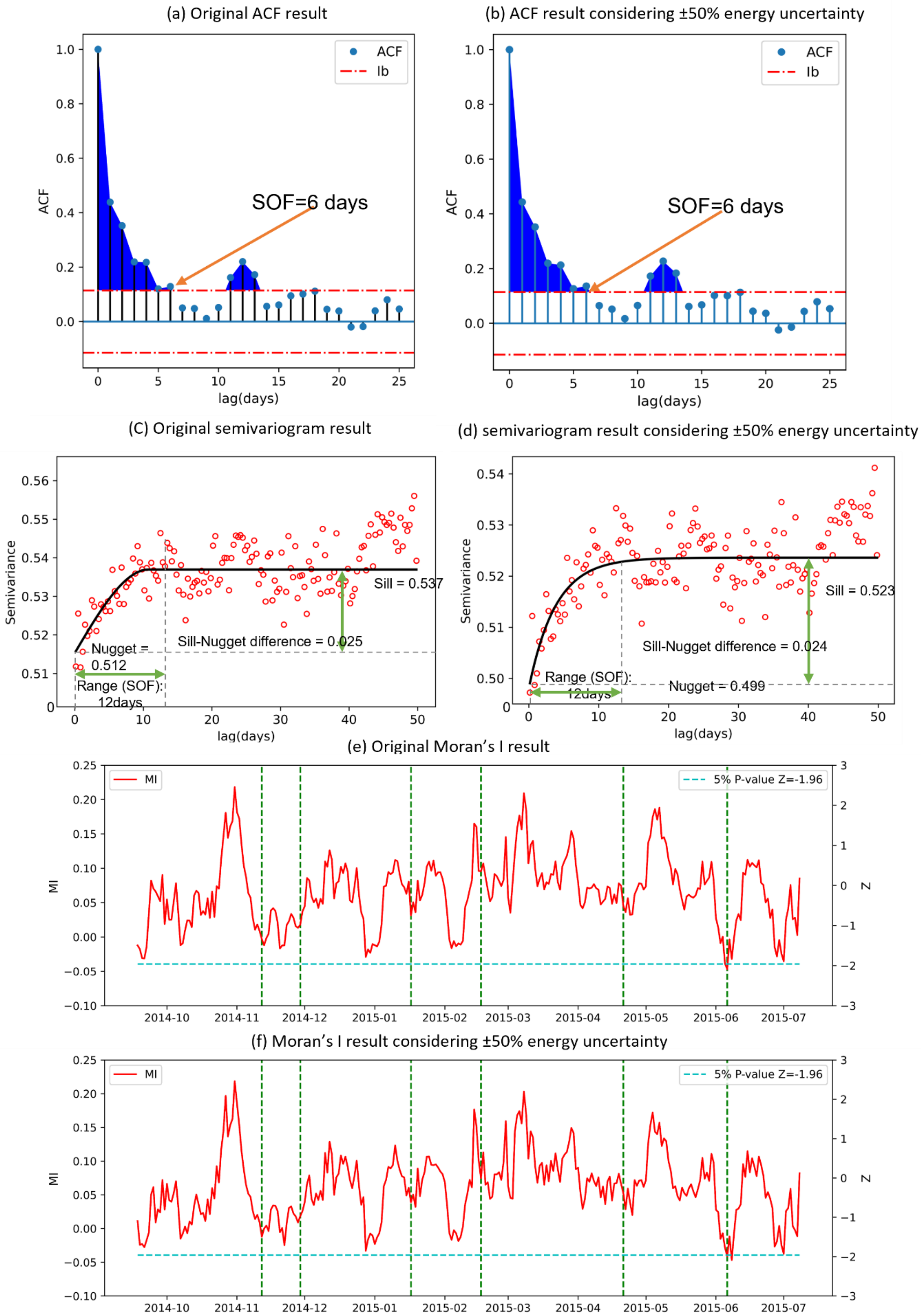

Figure 4-17 Correlation analysis results using the ACF method on (a) raw seismic energy data and (b) seismic energy considering uncertainty; the semivariogram method on (c) raw seismic energy data and (d) seismic energy considering uncertainty; the Moran's I method

4.6. *Clusters methods and spatial, temporal correlations based on clusters*

4.6.1. Spatial-temporal cluster based on face advances.

The spatial and temporal correlation analysis in Section 5 demonstrates the overall correlation of all seismic events in LW102. However, as seismic events from similar sources are more likely to be clustered in time and space, the correlation result of seismic events in one cluster may be interfered by events in other clusters. A seismic event in a cluster commonly presents a significant correlation with other seismic events in that cluster but shows independence to the evens that belong to other clusters (Kijko and Sciocatti, 1995). To remove the interference between different seismic event clusters and explore the correlation within individual clusters, a spatial-temporal based clustering method is used.

According to the data of LW102 face position at each production date, the distances of individual seismic events to the longwall face at the time of being recorded can be calculated (hereafter referred to as face-event distance). Figure 4-18 shows the boxplot of face-event distances on each production date over the monitoring period in LW102. In this figure, each box shows the face-event distance distribution within the day. The coloured box ranges from the 25th percentile and 75th percentile, and the transverse line within the box indicates the median of the face-event distance.

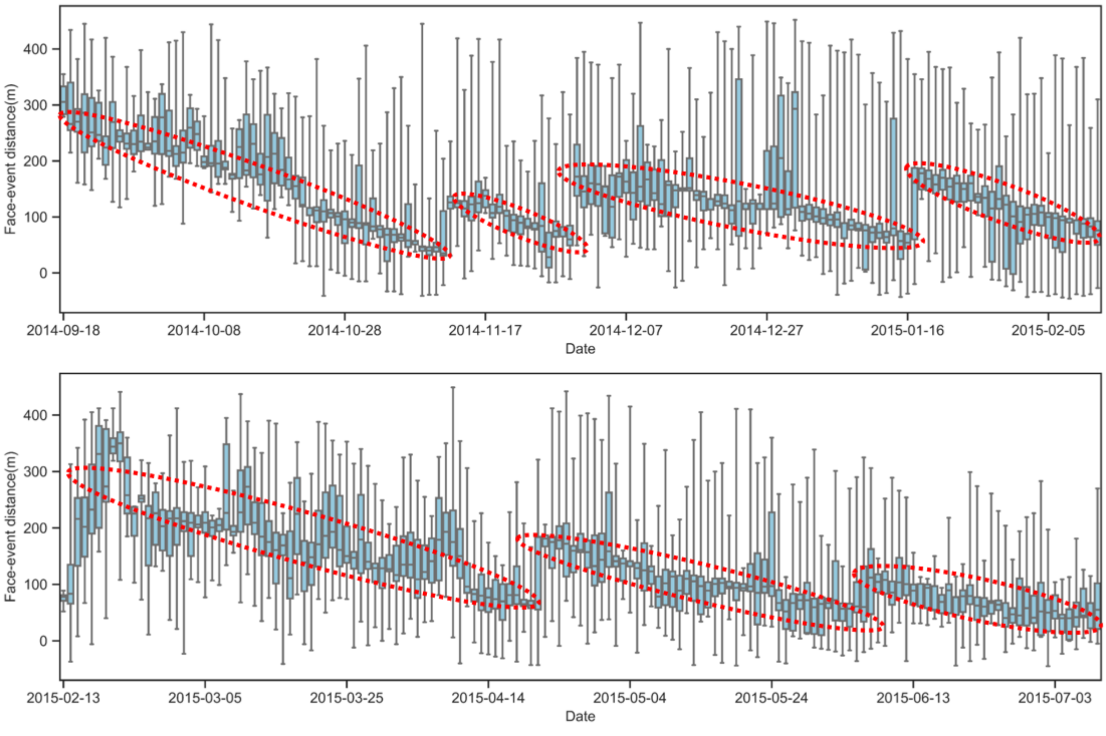

Figure 4-18 Boxplot of face-event distance distribution in each day versus the date, red circle indicates the range of clusters.

Figure 4-18 shows that seismic events generally first presented at around 200-300 m ahead of the face, and as the progressive advance of the face, the face-event distance reduced to about 50 m. This trend repeated seven times over the monitoring period, representing the cyclical change of mining-induced stress, which forms the basis of clustering. Therefore, 7 clusters of seismic events are determined based on the cyclical tendency of the median face-event distance in Figure 4-18. The identified clusters are listed in Table 4-5, and the spatial distribution of seismic events in seven clusters can be seen in Figure 4-19.

Table 4-5 The details of seven clusters of seismic events.

Cluster #	Start time	End time	Number of seismic events with log $E > +2.3$
1	18-Sep-14	12-Nov-14	952
2	13-Nov-14	29-Nov-14	402
3	30-Nov-14	17-Jan-15	1395
4	18-Jan-15	17-Feb-15	1436
5	18-Feb-15	21-Apr-15	1568
6	22-Apr-15	6-Jun-15	1716
7	7-Jun-15	8-Jul-15	751

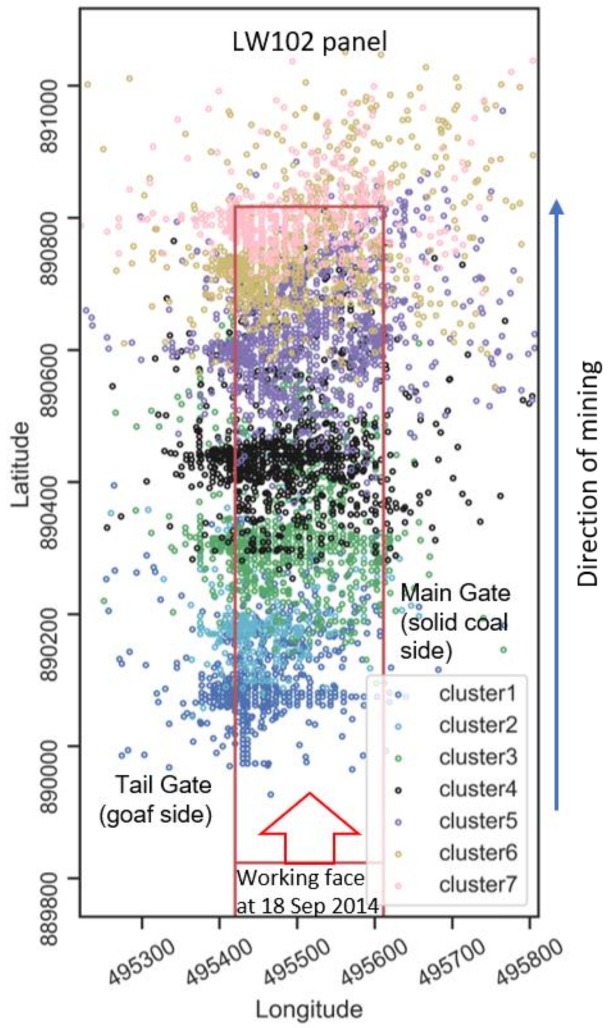

Figure 4-19 Spatial distribution of seismic events in different clusters in LW102

4.6.2. Temporal correlation assessment of seismic events within individual clusters

Based on the clustering result in Section 4.5, temporal correlations within individual clusters can be explored using both ACF and the semivariogram function similar to the procedure in Section 5.1. Figure 4-20 shows the ACF of the identified seven seismic clusters. According to this figure, for most of the seismic clusters, the SOF-time of cumulative daily energy is 2-4 days, respectively. Furthermore, a lower SOF-time of cumulative daily energy is presented when investigating the ACF in clustered data. The reason could be that in the plot of ACF like Fig.1a, at a specific lag *k*, the ACF value for total seismic data is approximately the average of the ACF values for individual clusters. Therefore, for the ACF of each cluster, the ACF value with smaller *k* tends to be lower. The SOF-time only depends on the first point when the ACF value is lower than Bartlett's limit. Therefore, if the ACF value at a small k in one of the clusters is occasionally lower than Bartlett's limit, the SOF-time for this cluster would be low.

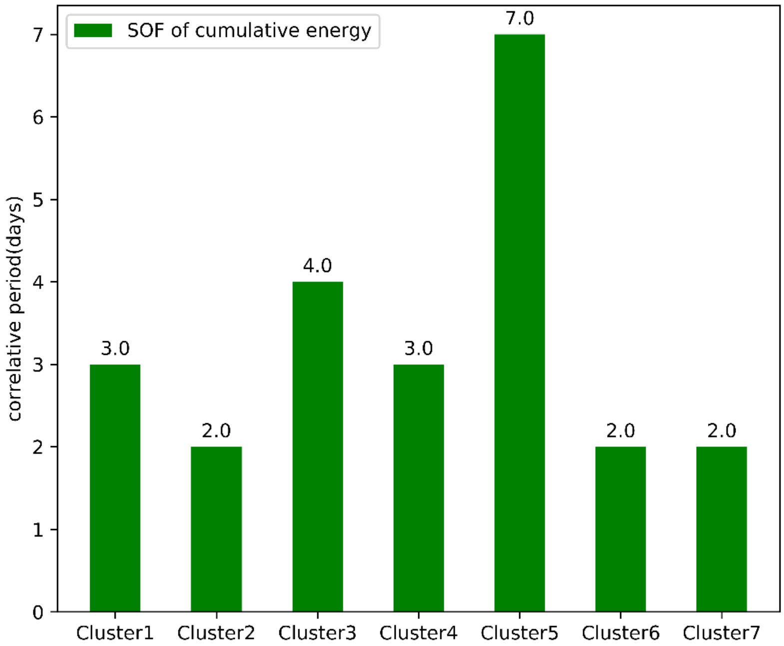

Figure 4-20 SOF-time result of each cluster calculated by ACF using the cumulative daily energy.

Figure 4-21 shows the semivariogram result of the identified seismic clusters. Exponential fitting is used as determined in Section 4.3. According to Figure 4-21, seismic clusters show different fitting curves and parameters, indicating various correlations between clusters. The SOF-time, nugget and sill of the seismic event energy for each cluster are summarised in Figure 4-22. Compared to the SOF-time using cumulative daily energy, a higher SOF-time is presented when using the non-evenly spaced seismic energy data. It suggests that converting the non-evenly spaced seismic energy data to the cumulative daily energy data may weaken its temporal correlation.

As discussed in Section 4.2, in order to compare the correlation between clusters, the SOF-time is not the only assessment measure; the nugget and the sill can also reflect vital information. A relatively strong correlation cluster should have a large difference between sill and nugget with an appropriate SOF-time. In addition, the small nugget indicates a strong correlation of the events within a short period, and the small sill indicates a strong correlation of the events with a large time difference.

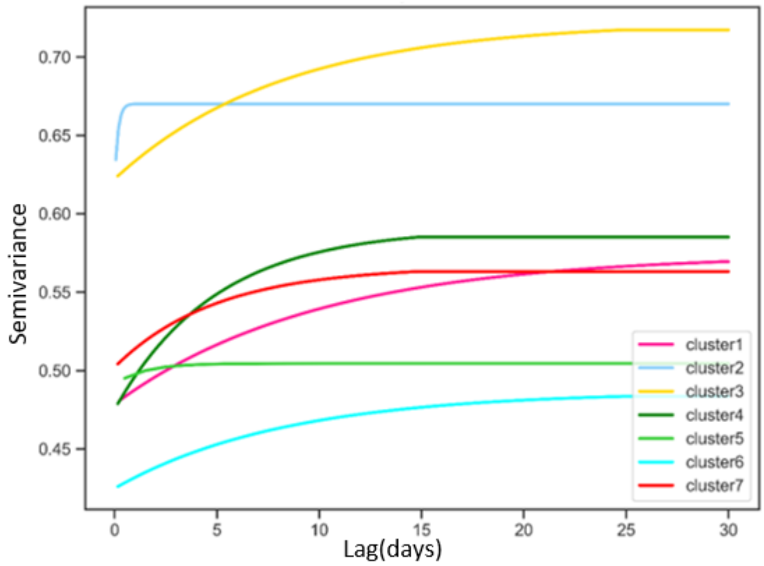

Figure 4-21 Semivariogram plot for each cluster

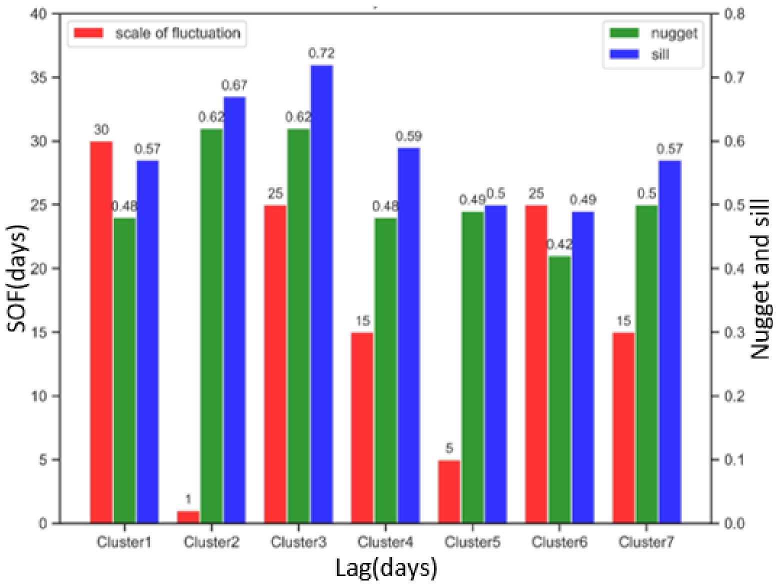

Figure 4-22 SOF-time, nugget, and sill for each cluster

4.6.3. *Spatial correlation assessment of seismic events within clusters*

Apart from the temporal correlation, the spatial correlation can also be investigated based on the identified clusters. The spatial correlation of different seismic clusters can be represented by the evolution of Moran's I over the monitoring period. Figure 4-23a shows the Moran's I result of seismic data in LW102 during the monitoring period, separated by different clusters. For most clusters, such as Clusters 1, 3, 5, 6, and 7, there will be one or more peaks of MI located in the middle of each cluster period, and MI values at the start and end of the cluster are lower than the peak value. It illustrates the concentration and transfer of the high-density seismic activity area from one cluster to another as a response to progressive coal extraction in the longwall face. The reason could be that the seismic events tend to assemble in the centre of clusters. Still, with the advance of the longwall face, the seismic events transfer from one centre to another, which positively increase the randomness of the event location and decreases the MI value. Furthermore, the peak value, the range of MI, and the evolutionary process show different patterns among the identified seven seismic clusters, which is mainly because of the varying spatial correlation of seismic events during the panel retreating.

To investigate the MI characteristics within one cluster, three typical MI at the start, the highest MI and the end of Cluster 5 are used for analysis. Usually, the transformation of seismic events between clusters leads to a relatively low MI value. However, at the start of Cluster 5, MI may present a higher value if the events are concentrated in more than one centre. Also, in Figure 4-23b and Figure 4-23d, the semivariogram at the start shows a higher nugget and a lower SOF-space, indicating a low spatial correlation and a low radius of the correlative area. In contrast, in Figure 4-23c, the peak MI point presented a lower nugget and higher SOF-space due to a large and concentrated seismic events area. Due to limited seismic data available within each week, discrete semivariance points and poor semivariogram fitting were encountered. This may introduce an error in the correlative radius estimation. Therefore, a certain amount of data that can be used in semivariogram analysis should be required.

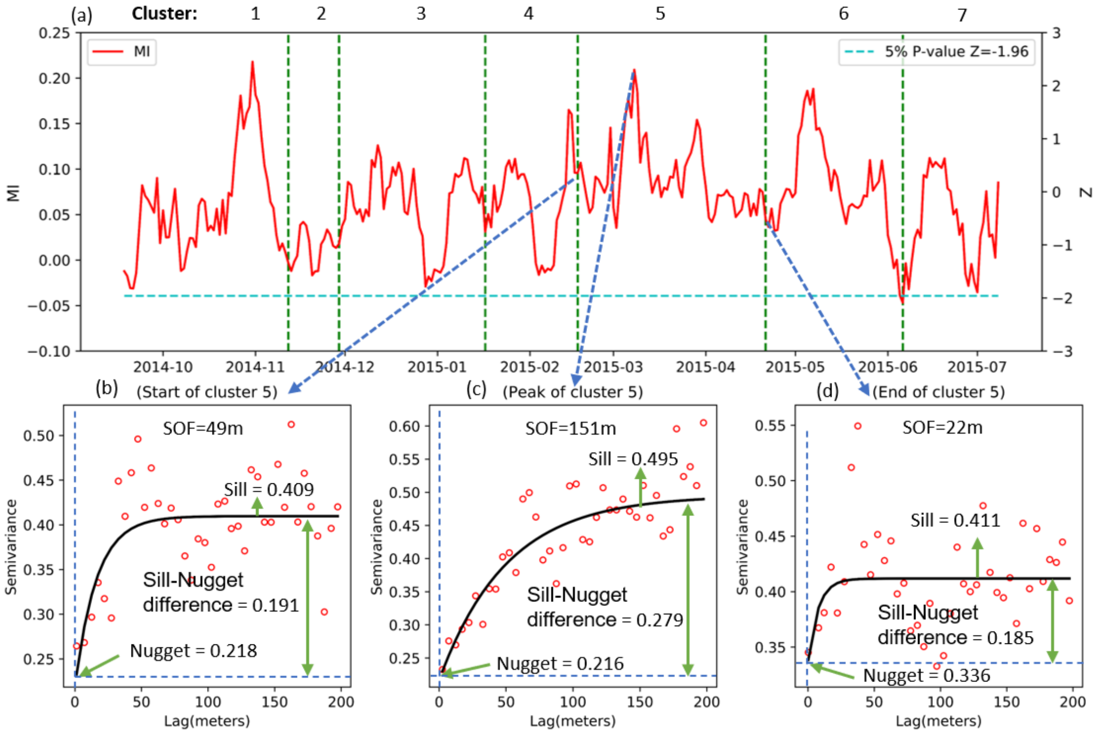

Figure 4-23 (a)Moran's I separated by clusters of seismic events and semivariogram for the (b) start, (c) peak and (d) end of Cluster 5.

4.7. Discussions

In Section 4.3, the temporal correlations for both unevenly spaced and cumulative data are investigated. The unevenly spaced seismic data are cumulated based on days in order to implement ACF to investigate the SOF. The unit of cumulation is a critical parameter that will primarily affect the correlation accuracy if not defined appropriately. Due to a working circle of 8 hours in the study mine site, and to guarantee enough samples in each cumulative unit, the unit of cumulation is set as one day as a multiple of 8 hours. The SOF is calculated based on ACF appropriately in Section 4.3, while it is relatively different from the SOF calculated for unevenly spaced data using semivariograms in Section 4.3. One reason could be a difference in the input data, while the other reason might be the limitation of the sample number after temporal cumulation based on one day. The cumulation has the advantage of smoothing the seismic data in the time domain but may also hide the short-term correlation behaviour inherited on that day.

In the temporal correlation of the SOF evolution in Section 4.3, the selection of a moving time window is critical. A too-short moving time window will not reflect the real correlative period. A too-long moving time window will decrease the variance and increase the chance that the data being affected by noise within each time window. 40

days moving time window is selected to calculate the variation of SOF along the total period in Section 4.3. In this variation distribution, the trend of how SOF changes a different times is more critical than the exact value of SOF. The reason is that the SOF value will be affected by the length of the moving time window, no matter if it is the best moving time window, but an appropriate moving time window will present the most apparent trend of the SOF variation.

Similar to SOF changes over time in Section 4.3, the Spatial SOF could be variational along with different locations and the range of study area. The whole space can be separated into grids and calculate SOF based on spatial semivariogram. The grid size will be critical, as well. A too-large grid size will increase the chance that the data being affected by noise. In contrast, a too-small grid size will limit the number in calculating the correlation and decrease the reliability of the result of the correlation. Meanwhile, due to an aggregation of the most seismic events and randomness of high energy events, the spatial correlation calculated by grids will have a large difference with nearby grids. Therefore, the correlation evolution analysis in the space domain for seismic-like data is still a challenge.

In Section 4.5, the ST correlation gives a relatively stable correlation property when calculating the correlation around three typical points. The nugget and sill are very similar, and the SOF has some differences. This conclusion seems to be the opposite of the conclusion that the correlation is variational in the time and space domain discussed before. But in fact, the temporal and spatial correlation assessment detects the overall trend of correlation. In contrast, ST correlation chooses three typical points and assesses the correlation by taking the three points as a basis. The correlation near the reference points (nugget) and the correlation far from the reference points (sill) are based on the three points. The three points all have relatively high energy, which indicates that they might be induced by the slipping of pre-existing fractures. They are indeed located in the major centre of one cluster. The similar nugget and sill value might result in the major cluster centre. There is a concentrated fractured zone, no matter if there is a natural fault. The three locations all have a similar event density, energy distribution, and even seismicity source mechanism. And the different SOF values might reflect the difference in the fractured zone size and the different stages of fractures that most of the events are in.

4.8. *Conclusions*

In this study, quantitative approaches were applied for temporal, spatial and spatial-temporal correlation analysis of a set of seismic data in the longwall mining process.

ACF was used to evaluate the correlation of evenly spaced seismic data and in combination with semivariogram, whereby the temporal correlation of unevenly spaced seismic energy was also assessed. The SOF-time is applied to represent the period that a notable correlation of seismic data shows within. The SOF-time is calculated as six days for cumulative daily energy and 12 days for unevenly spaced seismic energy data, representing a potential reference period that seismic events within this period can contribute to further evaluation and prediction. A semivariances assessment detects the maximum correlative period as 40 days, and the temporal correlation within this period can represent a universal correlation of a period larger than 40 days. With the maximum correlative period as a moving time window and on account of the long-term mining operation and the variability of the temporal correlation in different mining stages, the evolution of the temporal correlation is determined.

The spatial correlation of the seismic data was estimated using Moran's I. Based on the Z value, most of the monitoring periods present a strong spatial correlation. To determine the radius of the correlative area (SOF-space), the spatial semivariogram assessment was applied. The seismic data shows a strong spatial correlation within 23 metres area, which can be explained as the seismic response to mining abutment stress or a set of localised discontinuities. The correlative period and distance scale can be used as the critical input parameters for seismic/rock burst hazard prediction, seismic attributes inversion, and mining-induced fracture characterisation.

The spatial-temporal correlation has been assessed by investigating the distance and time difference with respect to three reference points. The quantitative assessment shows similarity on all three points and can be explained by the fracture behaviour during coal extraction. The proposed method introduced in Sections 5 and 6 improved the understanding of correlation for various purposes and multiple data types. It provides a rational approach to quantitatively assess the seismic data correlations in longwall mining.

To assess the spatial and temporal correlation between different clusters, clear clustering characteristics have been observed by investigating distance distribution to working face versus time distributions. Within each cluster, the evaluation of correlation can have variable patterns. More parameters, such as nuggets and sills, must be applied when assessing the correlation between or within clusters. The investigation of correlations within clusters provides an understanding of the correlation within a specific period of mine activities or an area of rock mass discontinuities. The SOF-time and SOF-space of each cluster offer references to select a more accurate time window and grid size for other seismic data-driven prediction tasks. The ACF value, MI value, the nugget and sill in the semivariogram all contribute to evaluating the reliability of the SOF.

Chapter 5. Seismic-derived fractures during longwall mining and their integration into numerical modelling

The case study mine is the same site used in Chapter 3, which is Yuejin coal mine, operated by Yima Coal Mining Group, in the west of Henan Province, China. Longwall (LW) 110 in this mine with comprehensive seismic monitoring data was selected as the case study panel. The extraction of LW 110 applied the Longwall Top Coal Caving (LTCC) mining method. The detailed panel information can be found in Chapter 3. The pre-process of the raw analog seismic signal used in the 16-channel "ARAMIS M/E" seismic monitoring system is the same process that already introduced in Section 3.1.

This study used the commercial seismology software Insite-Geo from Applied Seismology Consulting (ASC) to extract seismic signal information and calculate moment tensors. Since the majority of seismic sensors were installed around the case study longwall panel, the input P wave velocity model was assumed as homogeneous with the velocity of 4,000 m/s as an average value (Cai et al., 2014). Based on this single-velocity model, the collapsing grid search algorithm was implemented to locate seismic events. To eliminate the influence of artefacts during the integration and differentiation, the received uniaxial seismic waveforms were bandpass filtered with the cap frequency of 150 Hz. The ratio of the average amplitude in the front window and back window (as shown in Figure 5-1) was used to pick the P wave arrival time. During the background noise period, the amplitude ratio is close to zero. When the sensor receives seismic signals, the amplitude ratio will have a sudden increase, and the arrival time can be picked up by this change. Using this method, the signal-to-noise ratio of the filtered waveform was significantly enhanced. An example of the synthetic waveform pick-up is shown in Figure 5-1. The seismic event is picked up by six different sensors, and each sensor received three seismic signals that indicate the displacement at the sensor location in x, y, and z directions, as Figure 5-1 shows. In this research, the x direction is set as east–west, the y direction is set as north–south, and the z direction is the depth. Since the original uniaxial sensor is cemented on the floor, the original received uniaxial seismic signal is the signal in the z direction only.

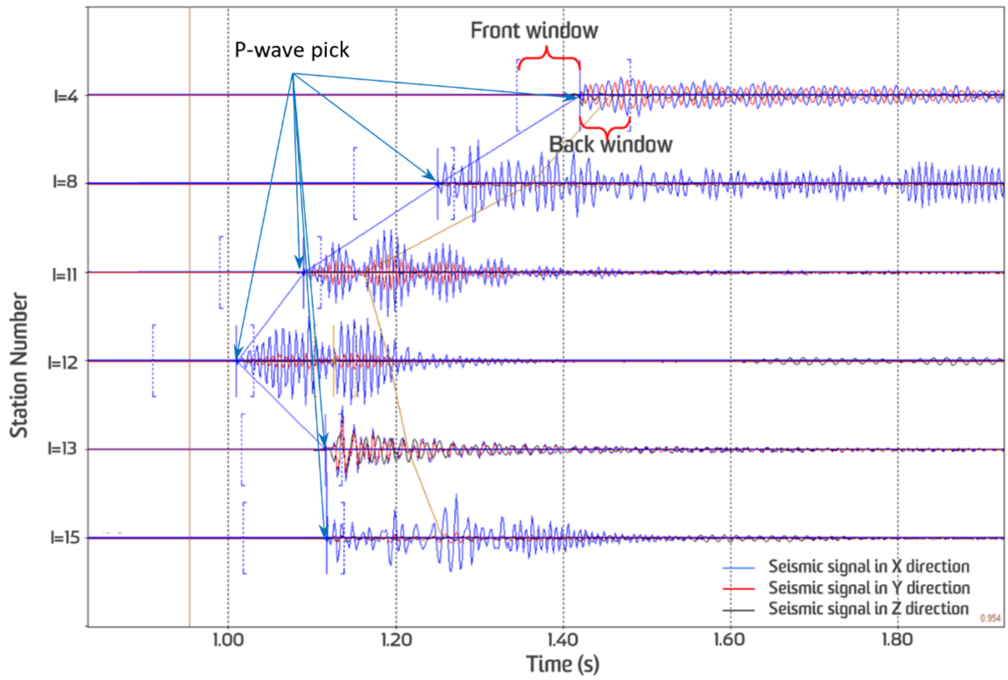

Figure 5-1 An example of synthetic triaxial seismograms and its P wave pick-up.

5.1. *Fracture properties determination from seismic parameters and moment tensor inversion*

Seismic source parameters considered in this study include seismic moment, moment magnitude, source radius, and the aperture change of induced fractures. The source dimension is usually expressed as the radius of the fracture plane and is related to the corner frequency of the seismic wave, which can be calculated as (Brune 1970; Duncan and Eisner 2010; Glazer 2016):

$$R = \frac{K_c \beta_0}{2\pi f_c} \tag{5.1}$$

where R is the source radius, β_0 is the S wave velocity in the vicinity of the source, and K_c is a constant that depends on the source model. In this paper, P waves are used to solve the corner frequency f_c, so K_c is set as 1.32 based on (Madariaga, 1976).

After the diagonalisation of the moment tensor, it can be expressed in the principal axis coordinate as follows:

$$\mathrm{M} = \begin{bmatrix} M_1 & 0 & 0 \\ 0 & M_2 & 0 \\ 0 & 0 & M_3 \end{bmatrix} = us \begin{bmatrix} (\lambda + \mu)\hat{n}\hat{v} + \mu & 0 & 0 \\ 0 & \lambda\hat{n}\hat{v} & 0 \\ 0 & 0 & (\lambda + \mu)\hat{n}\hat{v} - \mu \end{bmatrix} \tag{5.2}$$

where u is the displacement in the direction of motion for fractures as derived by seismic data, s is the surface area of the fracture, and $\hat{n}$ and $\hat{v}$ are the normal and motion direction of the fracture, respectively. λ and μ are Lame constants defined as:

$$\lambda = \frac{Ev}{(1+v)(1-2v)} \tag{5.3}$$

$$\mu = \frac{E}{2(1+v)} \tag{5.4}$$

where E is the elastic modulus and v is Poisson's ratio. The fracture aperture change τ deduced from the focal mechanism can be obtained as (Zhao et al. 2019):

$$\tau = u \times \cos\theta = \frac{4\pi f_c^2 \times \cos\theta \times tr(M)}{K_c^2 \beta_0^2 \times (3\lambda + 2v)\hat{n}\hat{v}} \tag{5.5}$$

where θ is the angle between $\boldsymbol{n}$ and $\boldsymbol{v}$, which can be obtained by using moment tensor inversion, and $tr(M)$ is the trace component of the diagonalised moment tensor matrix. To apply the Equation 5.5, some basic assumptions are required: first, the failure type of the seismic induced fracture need to be shear-tensile; and the rock material is impermeable, inert and incompressible.

Using the synthetic triaxial signal generated from shear or tensile events, M_0, R and τ can be calculated based on the empirical equations in Chapter 3. The spatial distribution of seismic events used for this analysis is shown in Figure 5-2. A few events are located around the F16 fault. Also, the contour map of the seismic event probability density indicates that intensive seismic activities were reported at the tailgate side of the panel, near the goaf zone, which suggests that frequent fracture generation and propagation occurred in the rock mass around the tailgate.

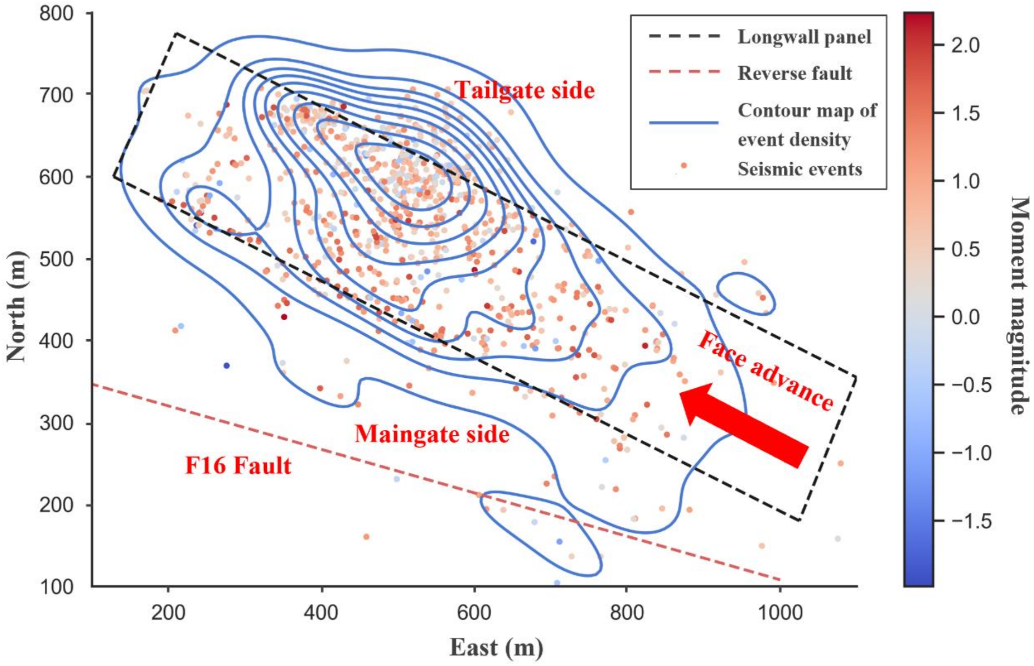

Figure 5-2 2D spatial distribution of seismic events in LW110 that are used for this analysis. The blue lines are the kernel density contours, the colour bar indicates the moment magnitude, and the red line denotes the reverse fault.

The source parameters of the seismic events were calculated based on synthetic triaxial signals. Figure 5-3 shows the density distribution of seismic moment magnitude, fracture source radius, and fracture aperture (in the logarithm scale). The moment magnitude ranges from -2 to 2.3, the fracture radius ranges from 7 m to 17.6 m, and the aperture ranges from 0 m to 0.023 m, with most of them between 0.01 mm to 1 mm. Note that the aperture here is only taken as the aperture change. As shown in Figure 5-3a, the moment magnitude has a normal distribution as a result of incomplete recording of low-energy seismic events due to sensor sensitivity. For fracture radius in Figure 5-3b, it also follows a similar distribution but with a long tail. Some events showed an apparent higher radius than others, which might be the seismic events generated by the interaction of material extraction and tectonic activities. Since the aperture tends to have a directly proportional relationship with the source radius, certain events also have much larger apertures as Figure 5-3c shows. Most mining-induced fractures are less than 1 mm wide while a few events with high seismic moments can have aperture change of 1–2 cm.

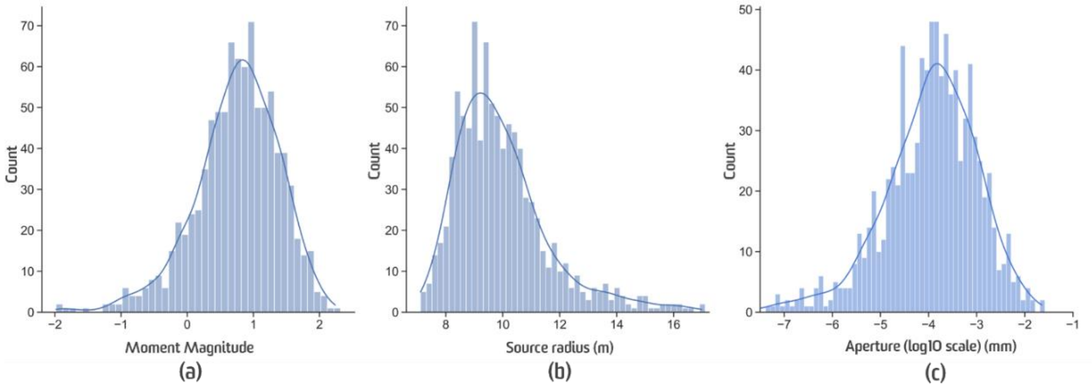

Figure 5-3 Density distribution of (a) seismic moment magnitude, (b) mining-induced fracture radius and (c) aperture.

As introduced in Section 2.1, seismic events can be classified by different failure types according to the moment tensor inversion. The failure type can be characterised as the DC majored (shear failure) and non-DC majored (tensile failure). To investigate the distribution of shear failure and tensile failure conveyed by seismic data, the probability density distributions of M_0, R and τ as clustered by different failure types are shown in Figure 5-4. In general, the seismic events of two different failure types show similar density distributions. Theoretically, shear failure should have a higher seismic energy release compared to tensile failure.

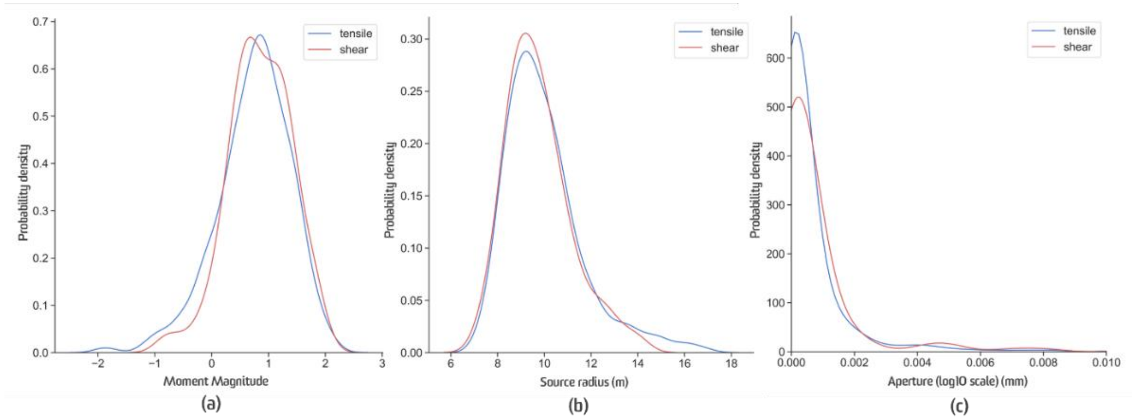

Figure 5-4 Probability density plot of (a) moment magnitude and (b) source radius and (c) seismic induced aperture of mining-induced fractures as classified by different failure types.

On the other hand, the shear failure with large energy release is related to the interaction of mining activities with geological structures. To further investigate the spatial distribution of shear failure and tensile failure related to the F16 reverse fault, Figure 5-5 cross-plots the moment magnitudes of seismic events with different failure types and their distances to the reverse fault F16 in LW110. It shows that the distance to the reverse fault does affect the energy magnitude of mining-induced seismic events, especially the shear type failure. When approaching the reverse fault, the moment magnitude of shear-type events increases with a steeper slope than the tensile-type events.

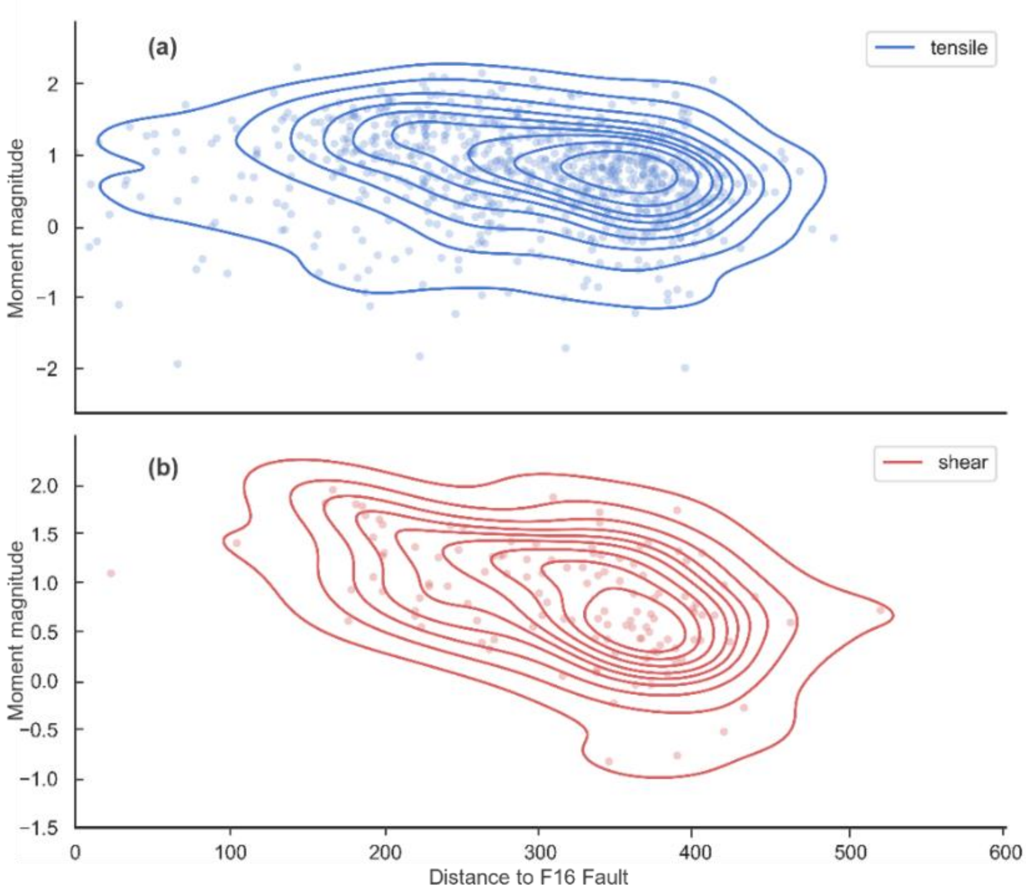

Figure 5-5 Correlation between moment magnitudes of seismic events and their distances to the F16 fault for (a) tensile failure and (b) shear failure.

The other condition that affects the distribution of seismic events and the induced fractures is the relative location of the goaf area. The goaf area is noted in Figure 5-2, and from these two figures, the seismic events present a cluster trend near the goaf area. Besides, the M_0, R and τ can also reflect different conditions on the goaf side and the solid side. In Figure 5-6, the parameter X at the x-axis represents the location along the working face (from the first hydraulic support to the last). The X=0 is the middle of the working face. Thus, the length of the face is from -100 m to 100 m on the x-axis, as the red dashed line shows. The X<-100 m area is the solid coal side, and the X>100 m area is the goaf side. From Figure 5-6 a and c, the moment magnitude and the aperture at the goaf side are slightly lower than the solid side for both shear and tensile failures, which is due to more frequent seismic activities on the tailgate side. Although the total energy release of rock fracturing would be larger on the tailgate side, the magnitude of each seismic event is lower, with a more frequent fracture activity and smaller fracture size. On the other hand, the radius in Figure 5-6b shows a low peak in the centre of the not mined area compared to the tunnel area for both failure types. The average size of each single fracture is wider near the tunnel than the not mined area.

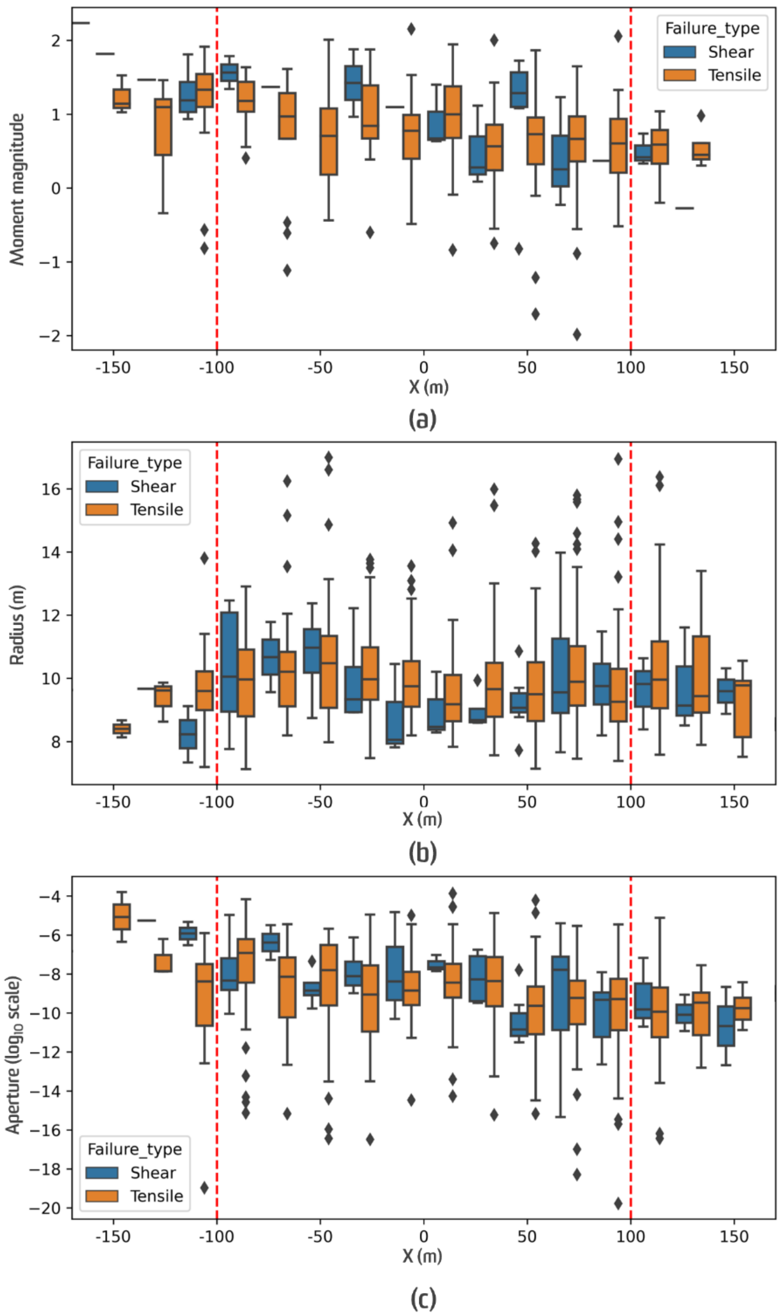

Figure 5-6 The box plot of (a) moment magnitude, (b) source radius and (c) aperture change in the logarithm scale as classified by different failure types. The red dashed line shows the edge of the longwall panel.

5.2. *Interpretation of fracture distribution and model generation based on calculated fracture properties.*

This section is going to analysis fracture plane orientation and the mining-induced fracture network model derived from seismic data. the orientation is given by the method of fault plane solution which decides the fault plane from two potential fracture planes from moment mechanism resolution.

Since the moment tensor inversion result indicates two potential fault planes and normal vectors, structure analysis is then conducted to determine the preferential orientation of the seismic events. Since seismicity tends to occur along one or more sets of pre-existing subparallel joints in rock, we can obtain the fault plane solutions (the orientation of the fractures) with the help of a three-point method (Fehler et al. 1987). In this study, as shown in Figure 5-7, for each seismic event X, the moment tensor inversion provides two fault plane solutions, Fault Plane 1 (FP1) and Fault Plane 2 (FP2). Points Y and Z are two events around X, which are assumed to be triggered along the same plane of X (the red plane in Figure 5-7). Therefore, the fault plane solution for X would be FP1 given the smaller angle difference with the red plane, compared to FP2. To determine the orientation of mining-induced fractures, the three-point method is applied to back-calculate the preferential fracture orientation within a cloud of events by fitting every group of three events with one potential failure plane, resulting in a total of C_n^3 planes (a n-combination of a set of three points, n is the total number of nearest points to Point X including itself). Considering the location accuracy and the extent of the fracture zone, the events fitted in each plane can be constrained spatially within a particular range (100 m in this research) (Collins et al. 2002). The obtained fracture network can then be displayed in a stereonet, and areas with high-density fracture poles in the stereonet indicate the preferential orientation of mining-induced fractures.

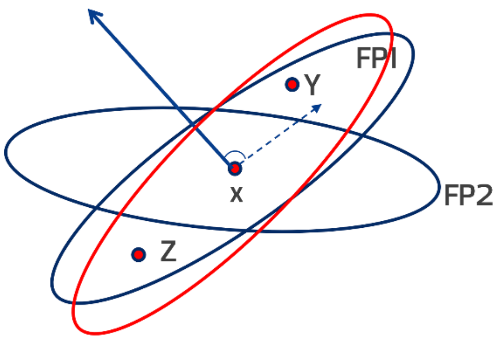

Figure 5-7 Schematic of the three-point method used in the structural analysis, with three seismic events at Points X, Y and Z and two potential fault planes FP1 and FP2 for Point X.

The distribution of the seismic events reflects the shape of mining-induced fractures. First, the cross-sectional view (facing the longwall retreat direction) of the spatial relationship between seismic events and the longwall panel is shown in Figure 5-8. Most seismic events are located about 10–30 m above the longwall panel, which is within the thick mudstone layer. The densest clustered area of seismic events is ~20 m above the longwall panel, which is mainly caused by the top coal caving operation. Since the rock will be more vulnerable near the goaf side (tailgate), more seismic events are concentrated near that side.

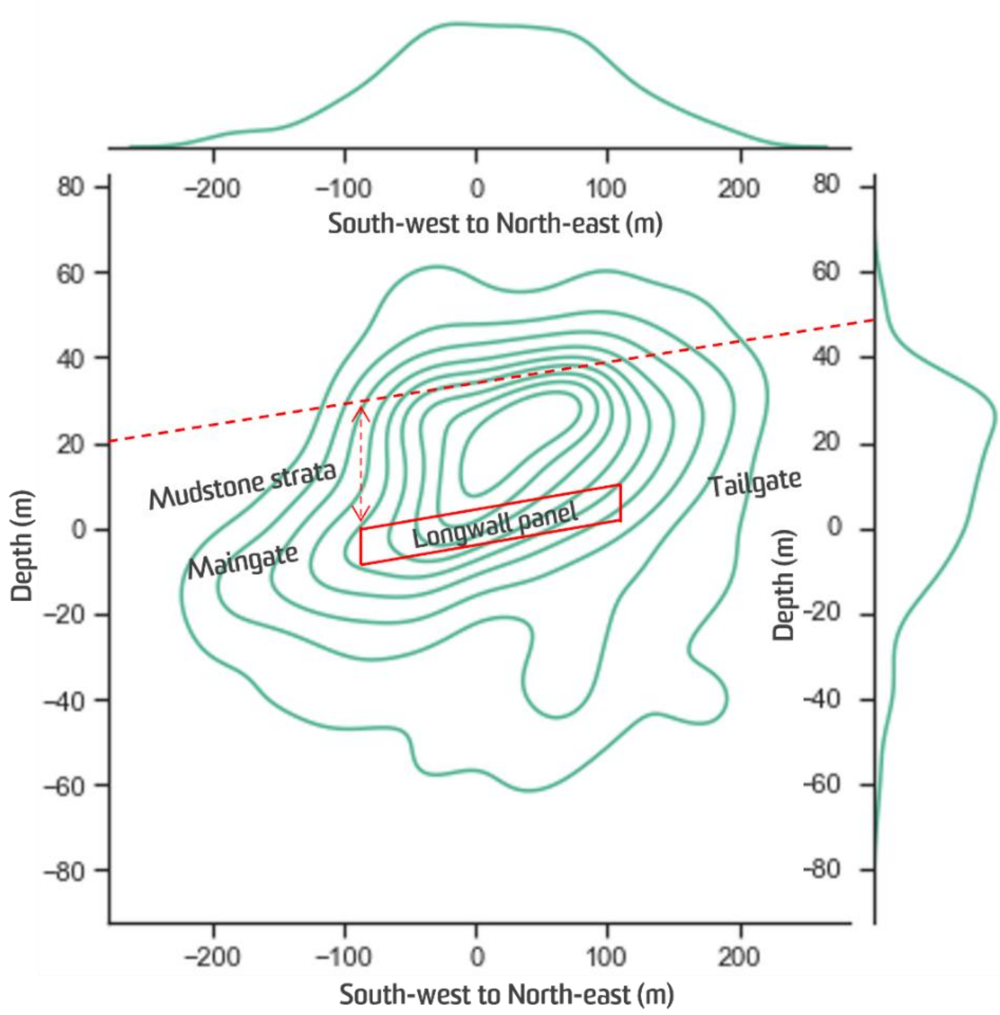

Figure 5-8 The probability density plot of seismic events: a cross-sectional view along the face retreat direction.

The orientation of mining-induced fractures can also be calculated from the moment tensor decomposition as Section 3.1 shows. From two potential sets of fracture planes, the most likely fault plane orientation can be solved by the three-point method. Considering the location error and fracture slip, the preferred fault plane direction is determined based on every set of three seismic events within the total of 2,807 events.

The obtained pole (the normal vector) distribution of fracture planes is displayed in the stereonet, and the high-density area indicates the overall preferential orientation of mining-induced fractures (Figure 5-9a).

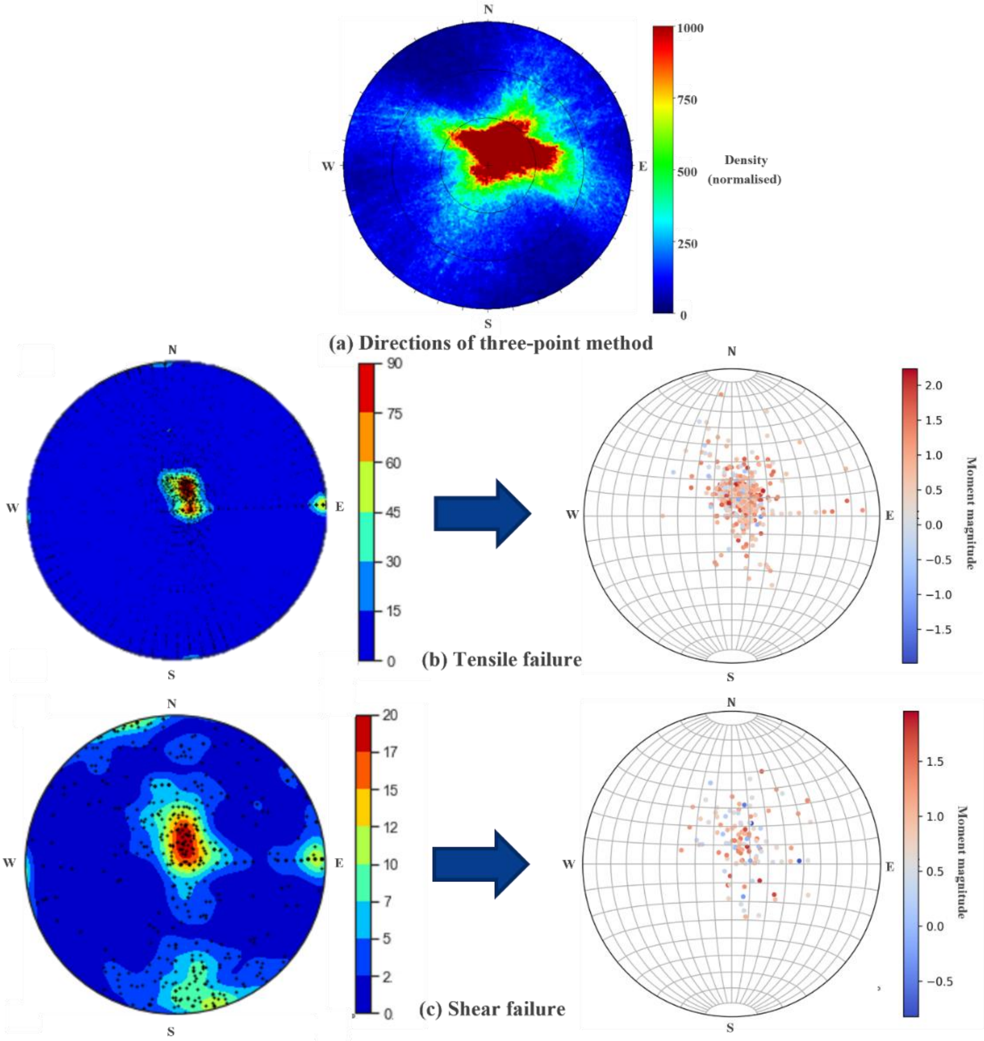

Figure 5-9 (a) Density distribution of the poles of mining-induced fractures determined by the three-point method in a stereonet. The stereographic projection of the pole density of raw fracture planes (left) and fracture planes (right) determined by the three-poi

The fault plane solutions for the tensile and shear failure are shown in Figure 5-9b and Figure 5-9c, respectively. The left figures show the pole distribution of all potential fracture planes, while the right figures show the pole distribution after applying the three-point method for structural analysis. It is also interesting to observe that tensile fractures are clustered in low dipping angles (<10°), representing near-horizontal fracture planes, and the dip direction is towards NNE. On the other hand, shear fractures are sparser, with dipping angles being less than 40 degrees. The dip direction for the majority of shear fractures is also NNE, and the secondary dip direction is towards NW. The northernfacing dip direction is believed to be caused by the combined effect of the longwall mining direction (moving into NW) and the previously mined area (goaf) in the NE direction of LW 110.

With the distribution of moment magnitude classified by failure types in Figure 5-9b and Figure 5-9c, the fracture orientation of both failure types does not show a clear relationship with the moment magnitude. The high magnitude events are distributed evenly, which indicates that there is not a clear geological structure or structure set with a dominating dip direction and dip angle.

The spatial distribution of fractures induced by longwall mining is presented in Figure 5-10. Each fracture is represented by a disk. The radius of the disk is the source radius. The average aperture change of all fractures was 0.001 m, which is too small to be correctly presented and thus is not shown. The distributions of the tensile failure and the shear failure are visualised separately in Figure 5-10.

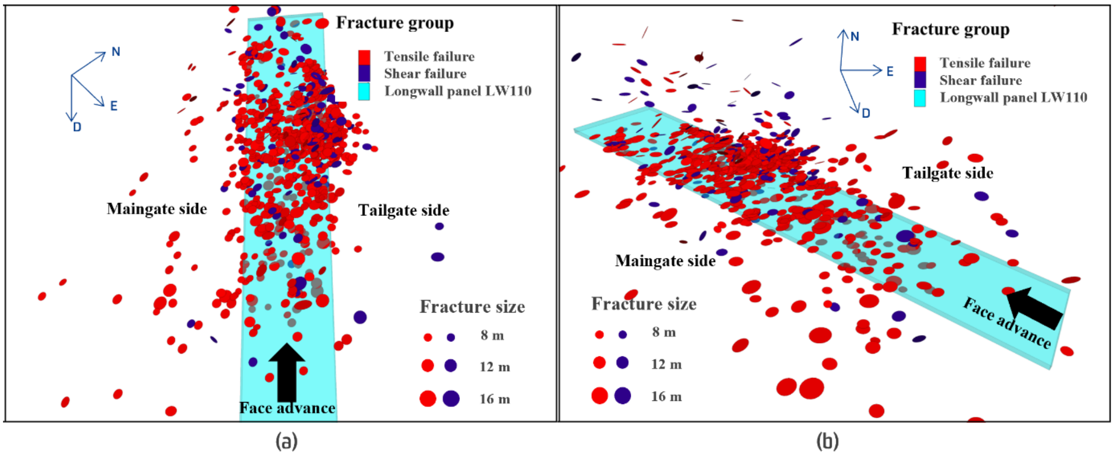

Figure 5-10 Fracture distribution induced by the coal extraction process in LW110 from May 2011 to October 2012, as coloured by the shear failure and tensile failure. It is presented as overview (a) and side view (b).

To investigate the relationship of fracture orientations with the goaf area, the probability density plots of dip direction and dip angle along the face-line (X as defined in Figure 5-7) are plotted in Figure 5-11. In Figure 5-11a, most events have a dip direction of 100–300 degrees, the red dashed line is the dip direction of the longwall panel, which is about 204 degrees, and the dip direction of the seismic event shows a symmetrical pattern at the centre of about 204 degrees. The dip direction at the tailgate side has more variation than the maingate side. There are two other clusters that concentrate on the goaf side, which have about ±50 degrees variation from the longwall panel dip direction. In Figure 5-11b, the dip angle of the seismic events shows a similar pattern with the dip direction, and the highest density area is about 12 degrees which is close to the dip angle of the longwall panel. The dip angle of seismic events also varies more on the tailgate side.

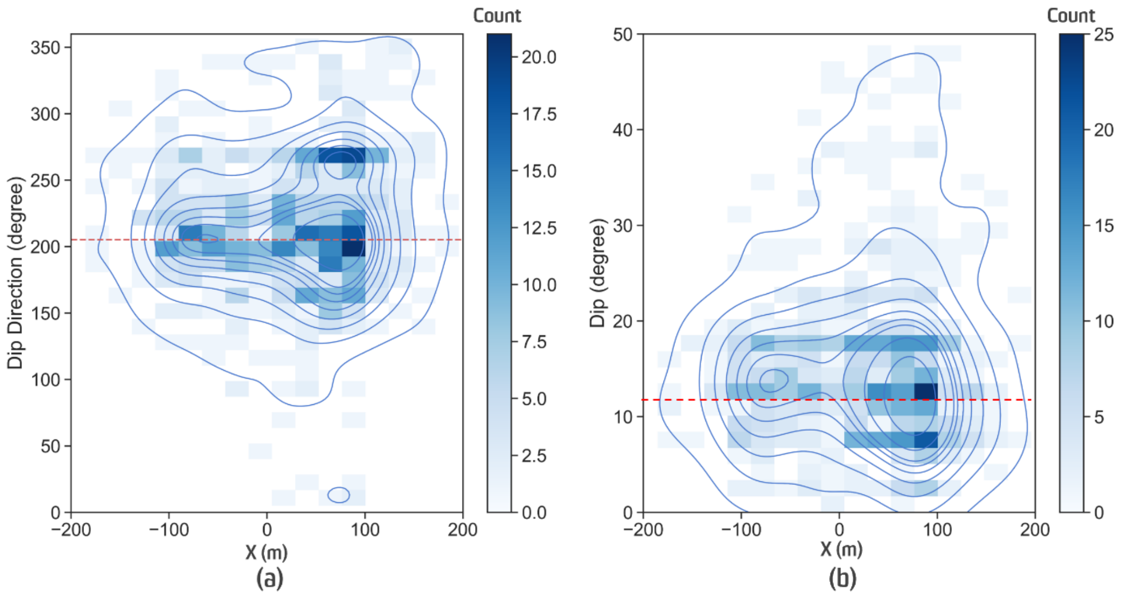

Figure 5-11 The probability density plots of (a) dip direction and (b) dip angle of seismic events across the face-line. The red dashed line shows the dip direction and dip angle of the longwall panel.

The difference of the failure type also presents different fracture geometries. As shown in Figure 5-12 a and b, the dip direction and dip angle of shear-type events are more widely distributed (higher variance) compared with the tensile-type events. The average dip angle of tensile-type events is slightly lower than that of shear-type events, suggesting that tensile failure fault planes are closer to the horizontal direction, the same as reported in Section 4.1.

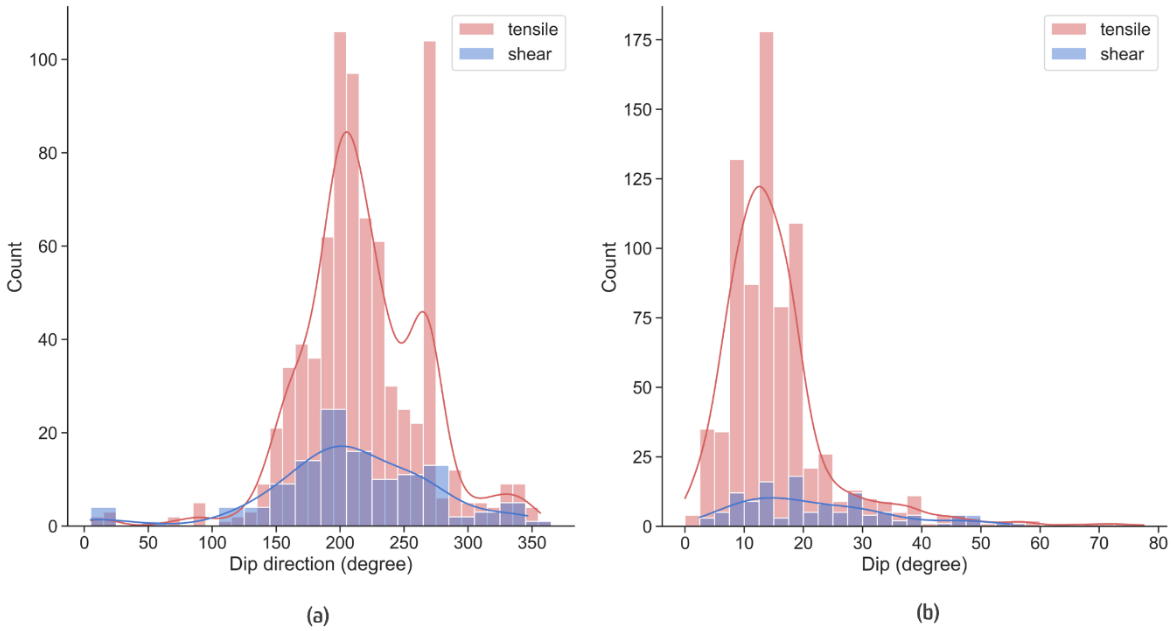

Figure 5-12 Probability density plots of the (a) dip direction and (b) dip angle of mining-induced fractures as classified by tensile and shear failure types.

5.3. *Numerical modelling of fracture displacement coupled with seismic events during the mine extraction process*

With the seismic-derived fractures analysed in Sections 5.1 and 5.2, the spatial distribution of fractures induced by longwall mining along with their fracture size, fracture orientation and aperture change can be characterised around the longwall panel. In order to comprehensively analyse the effect of the induced fractures on the rock properties around the longwall panel during progressive coal extraction, a number of numerical models have been developed based on the seismic events recorded at the study mine.

Seismic event selection was made according to the b-value calculated in Section 3.2. As shown in Figure 5-13a, the red line is the b-value calculated based on instrument magnitude within every five days of time interval, and the blue line indicates the rolling average of every five b-values nearby. A cyclical increase and decrease in the b-value can be observed over the life span of this longwall. The b-value increase can be seen as the strain softening or elastic stress build-up, and the b-value drop may indicate strain hardening or dynamic failure (Main et al. 1989). According to Figure 5-13b, the start and the end of the monitoring period with a low number of seismic events are excluded in this analysis, and thus the overall mining period of LW 110 can be roughly divided into four cycles to be used for the following numerical modelling tasks, as the green lines shown in Figure 5-13a. Each cycle contains a b-value increase and a b-value drop.

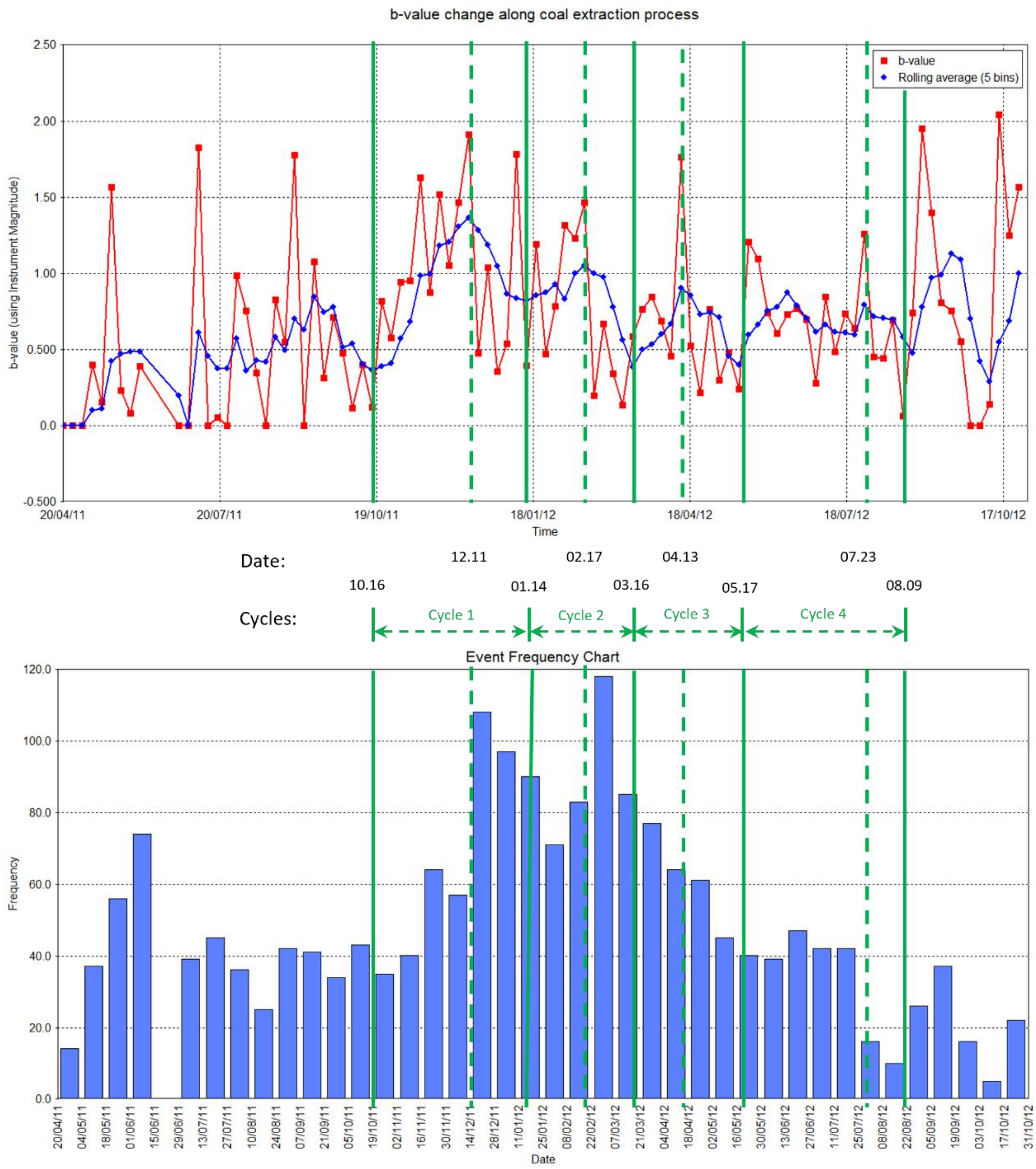

Figure 5-13 Evolution of (a) b-value and (b) seismic event frequency (number of events) during the monitoring period.

The date period and face advance distance of each cycle are shown in Table 5-1. The spatial location of seismic events and corresponding cycle position can be seen in Figure 5-14. The corresponding face-line position at the start of seismic monitoring is indicated by the solid red line in Figure 5-14, and the selected four cycles are at the middle to the end segment of the longwall panel. The upper side of LW 110 is the tailgate, as introduced earlier in Chapter 5, and the F16 reverse fault is located next to the maingate side of LW 110, as the green dashed line shows. Seismic events are concentrated at the tailgate side.

A similar conclusion can be drawn from Figure 5-14: in the space domain, the four cycles are also located in the area where the seismic events are generally concentrated. From the conclusions of Chapter 4, the seismic events involved in these four cycles are both spatial and temporal correlated. The b-value variation can be used as the basis for the clustering analysis of seismic events. Therefore, the correlation analysis applied to the evens in four different cycles separately will yield different results, and the simulation of coal excavation all together in one go or by multiple sequential steps will show different phenomena. Also, in order to eliminate the model instability and convergency issues caused by large-scale excavation, the simulation in this project is designed to cover the four b-value cycles, with a total of eight sequential excavation steps on the numerical model to be proposed in the following section.

Table 5-1 Date of Cycles 1-4 and their face advance distances

	Start date	Peak b-value date	End date	Face advance distance (m)
Cycle 1	16/10/2011	11/12/2011	14/01/2012	96.7
Cycle 2	14/01/2012	17/02/2012	16/03/2012	67.4
Cycle 3	16/03/2012	13/04/2012	17/05/2012	71.8
Cycle 4	17/05/2012	23/07/2012	9/08/2012	66.8

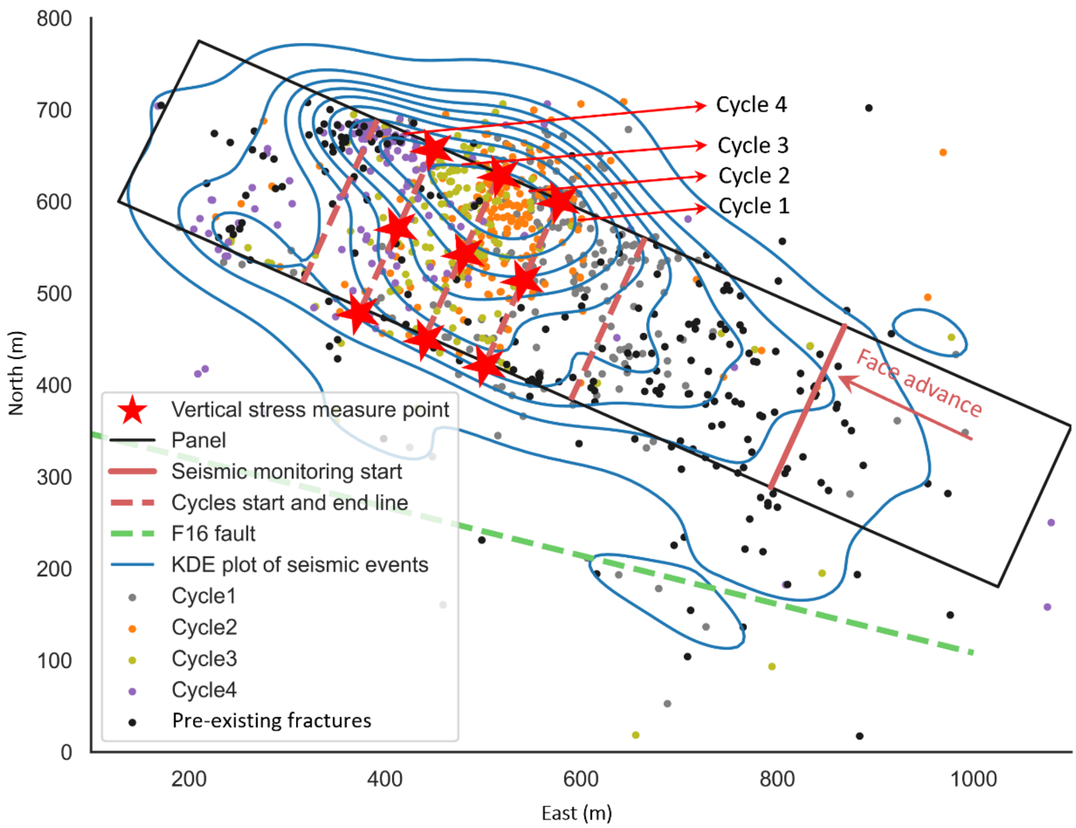

Figure 5-14 Spatial location of Cycle 1-4. The green dashed line indicates the F16 fault, and the red solid lines indicate the face location when the seismic monitoring started. Five red dashed lines outline the face advance ranges during the four cycles. The red star indicates nine vertical stress measurement points in the following numerical simulation. Seismic events were clustered into four cycles and others. The density probability of all seismic events estimated by KDE is shown in the blue line contour.

5.3.1. *Model development*

A 3DEC numerical model was developed by simplifying the mining layout at the Yuejin Coal Mine, China. The model workflow is shown in Figure 5-15. A numerical model is first created following the stratigraphy and geometry of the study longwall panel with extensive seismic monitoring. The model is large enough to simulate longwall panel excavation during the abovementioned Cycles 1-4. In this research, the fault and rock-solid are modelled using the discrete element method. The seismic-derived DFN is used to segment the model as well as an intermediate structure between discrete elements. The rock properties, mechanical properties of the fault, and in-situ stress are then set and input into the model based on previous research (Wang et al. 2020; Cai et al. 2021b). Afterwards, since the study mine contains multiple panels and the target panel, LW 110, was at the edge and scheduled to be mined last, the adjacent longwall panel had already been extracted and was simulated as goaf. By doing so, the model has been restored to its original state before the mining operation starts at the LW 110 panel. Therefore, the displacement for rock and fractures are reset to zero to complete initialization before the simulation runs.

During simulating the excavation process of LW 110, at each excavation step, the relevant seismic-derived fractures for that step are activated in the model step by step (eight excavation steps for four cycles in total), and the coal material is extracted at once during each excavation step. The relevant fractures contain the spatial and temporal information recorded over that specific excavation step. As shown in Figure 5-14, some events (denoted as Pre-existing fractures) occurred within the area where the working face passed but before the earliest cycle started. They are chosen from all seismic event in LW 110 panel and occurs before the Cycle 1 started within the target area and spatially occurred within the target area. These seismic events are inputted into the model before adding in any mining-induced fractures from Cycle 1-4. After each step of coal extraction, the stress distribution and fracture information around the mining area are recorded and updated in the model. The model result of stress distribution is then compared with the same simulation without considering and simulating seismic-derived fractures. Meanwhile, the fracture information is also analysed and compared with the result of seismic monitoring.

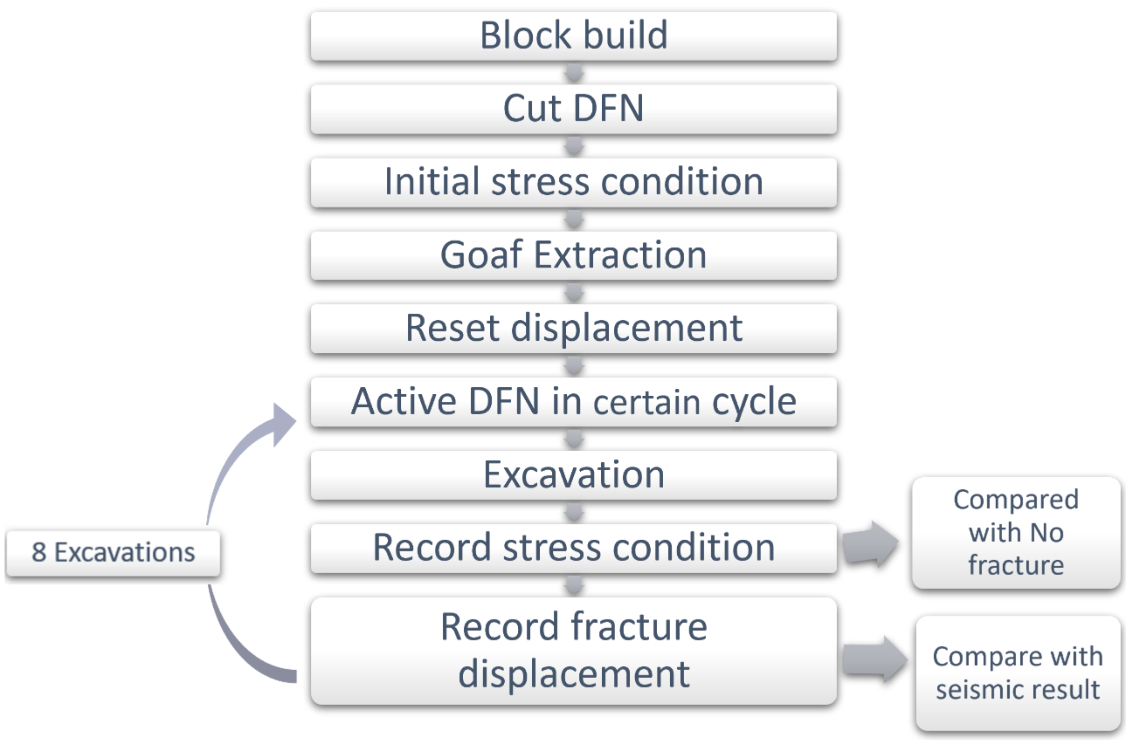

Figure 5-15 Workflow of the simulation process. The first five steps in the flowchart are only required for the model set-up, and the loop covers an iterative process to be executed within each excavation step

The LW 110 panel is 200 m wide and fairly deep at about 800-830 m underground. The coal seam thickness is about 10 m with a maximum dip angle of 12°. The seam is overlain successively by 18 m thick mudstone, 2 m thick coal layer, 4 m thick sandy mudstone, and underlain by 4 m thick mudstone as described in Figure 5-16. The interbedding layers are mainly mudstone. Another thin coal seam (about 2 m) is located at 28 m above the mining level and the strata above the thin coal are mainly sandy mudstone and sandstone. The fully mechanized top coal caving method was used to recover the total 10 m height of the panel.

Primarily, the numerical model developed contains 95,756 grids with a geometry of 800 m×500 m×300 m (in the order of X, Y, and Z axes). The model's upper boundary is 400 meters higher than the working face, which is about two times the size of the face width to avoid the boundary effect. The width of the simulated longwall panel is fixed at 200 m and at 800 m deep. This gives the panel width-to-depth ratio of 0.25, which falls in the subcritical mining category.

The target panel, LW 110 has an adjacent panel (LW 090), which is extracted before the start of mining LW 110. As Figure 5-16 shows, LW 090 is located at the top-right side of LW 110. In this research, solid rock layers are simulated by grids with a brick shape. The grid size of rock layers is the smallest in the surrounding area of the longwall panel and gradually increases towards the model boundary. The smallest grid size is 6 m×6 m×3 m, while the largest is 40 m×40 m×20 m (in the order of x, y, and z axes). The longwall face retreat direction is along the y-axis.

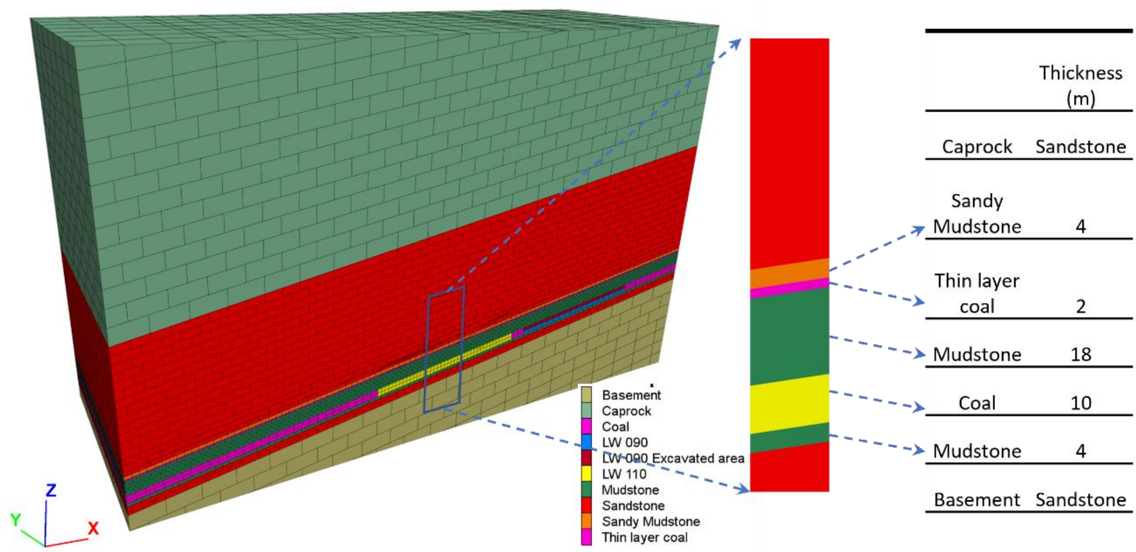

Figure 5-16 Model configuration based on the field geological condition, the thickness and lithology of each strata layer are shown in the table at the right side.

According to the simulation workflow, the in-situ stress condition is then applied to the model. The stress measurement locations at the mine site were in the main haulage roadway, which is too far away from the modelling area. Therefore, the in-situ stress is applied according to Cai et al. (2020), in which a FLAC3D model was developed to simulate regional stress distribution and later verified by in-situ stress measurement. Therefore, the same stress condition is applied in this model: σ_1=28.9 MPa, σ_2=23.9 MPa and σ_3 =20.5 MPa. The minimum principal stress (σ_3) is in the vertical direction (z axis), and the maximum (σ_1) and intermediate (σ_2) principal stresses are in the horizontal direction along x and y axes, respectively.

The boundary condition of the model is that: the bottom boundary is fixed, (velocity = 0) and roller boundary (i.e., displacement in the vertical direction is allowed, and the horizontal direction is fixed) is applied onto the four sidewalls (Chaulya et al. 1999).

After model initialization, the contour plot of the vertical in-situ stress at the model front view (cross-section of the x-z plane) is shown in Figure 5-17. To better eliminate the artificial effects caused by small-size elements, the stress contour plot is shown in the volumetric average of each element. As presented, despite a dipping stratum, the vertical stress roughly follows the 0.025 MPa per metre gradient. The plot indicates about a 0.75 MPa difference between the highest and lowest vertical stress within the longwall panel, as a result of the dipping angle and 30 m elevation difference across the panel. Despite the stress distribution looks discontinuous in Figure 5-17, the structure is expected to be continuous. The discontinuity is a result of the bedding plane and does not reflect the actual physical conditions.

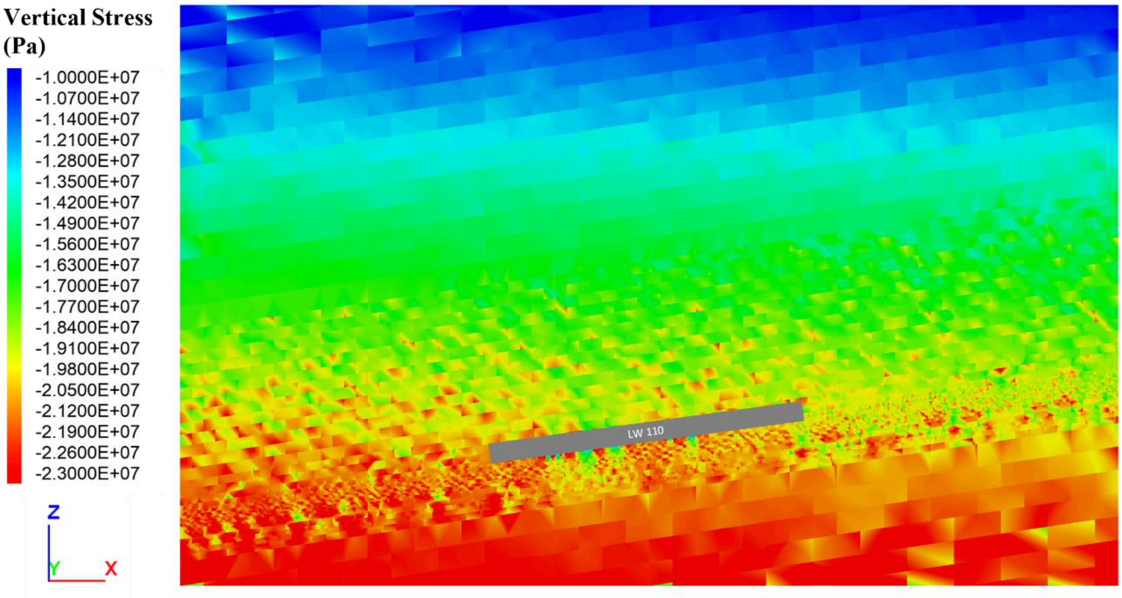

Figure 5-17 Contour plot of the vertical stress distribution for the modelled area. The figure shows the front view (cross-section of the x-z plane) of the panel with face moving along the y-axis, and the location of LW 110 is shown in the middle.

5.3.2. *Material and seismic-derived fracture properties*

The physical properties and thickness of the coal and coal measure rocks were determined based on field geological and experimental investigations (Cai et al. 2020b). The properties of all layers introduced in this research are summarised in Table 5-2. The density of the coal layer is at about 1,300 kg.m^{-3}, and the mudstone and sandstone have a density of 2,200 kg.m^{-3} and 2,700 kg.m^{-3}, respectively.

Table 5-2 Mechanical properties of each layer used in the numerical model

Lithology	Density (kg.m^{-3})	Young's modulus (GPa)	Poisson's ratio
Cap rock/Basement	2700	8.9	0.19
Sandy Mudstone	2600	7.7	0.18
Mudstone	2200	6.64	0.17

Coal	1300	5.87	0.17
Sandstone	2700	8.9	0.19

Since this research will mainly focus on the performance of the fractures, the rock blocks are defined as elastic material. Therefore, the joint between rock block elements is defined as elasto-plastic and follows the Mohr-Coulomb failure criteria. The Mohr-Coulomb failure criterion is determining the point of failure in materials like soil and rock. It works on the principle that failure occurs when the shear stress on a plane surpasses the shear strength of the material. This strength is a function of normal stress, defined by cohesion and internal friction angle. In terms of stress-strain, the model assumes an elastic-perfectly plastic response. Deformation is elastic until reaching the yield point, defined by the Mohr-Coulomb criterion, then becomes plastic with no further stress increase. Since the mechanical properties of all joints are difficult to be directly measured, they can only be determined by trials and errors to match with field observations. The calibrated results are reported by Cai et al. (2020) which used cohesion = 2.0 MPa and friction angle = 30° for joint planes.

An additional property to be determined is the ratio between the normal (k_n) and shear joint stiffness (k_s). From the perspective of calculation efficiency, that the stiffness of the blocks and joints are of the same order of magnitude. Therefore, based on information in the previous research, it was selected that (Gao and Stead 2014):

$$0.1 < \frac{K + \frac{4}{3}G}{bk_n} < 1 \tag{5.6}$$

where b is the average block size, and K and G are the bulk and shear moduli of the blocks, respectively. With these considerations, there is a single elastic micro-parameter that is independent. The model's macro-deformability was then matched by rescaling the micro-elastic properties. After obtaining k_n, the relationship of k_n and k_s is also summarised by (Li et al. 2022). The results shown in Figure 5-18 as well as the Equation 5.6, suggest that for weak bedding planes, especially infilled with claystone, the normal stiffness can be set as 4 - 40 GPa/m. Based on mostly used value in Australian and worldwide benchmark, the ratio between normal and shear stiffness (k_n/k_s) is normally set as 10 (Bandis et al. 1983; Li et al. 2022). The range defined by Equation 5.6 and an average block size of 3 m is shown in the figure as well. Thus, the model selected k_n = 10 GPa/m and k_s = 1 GPa/m.

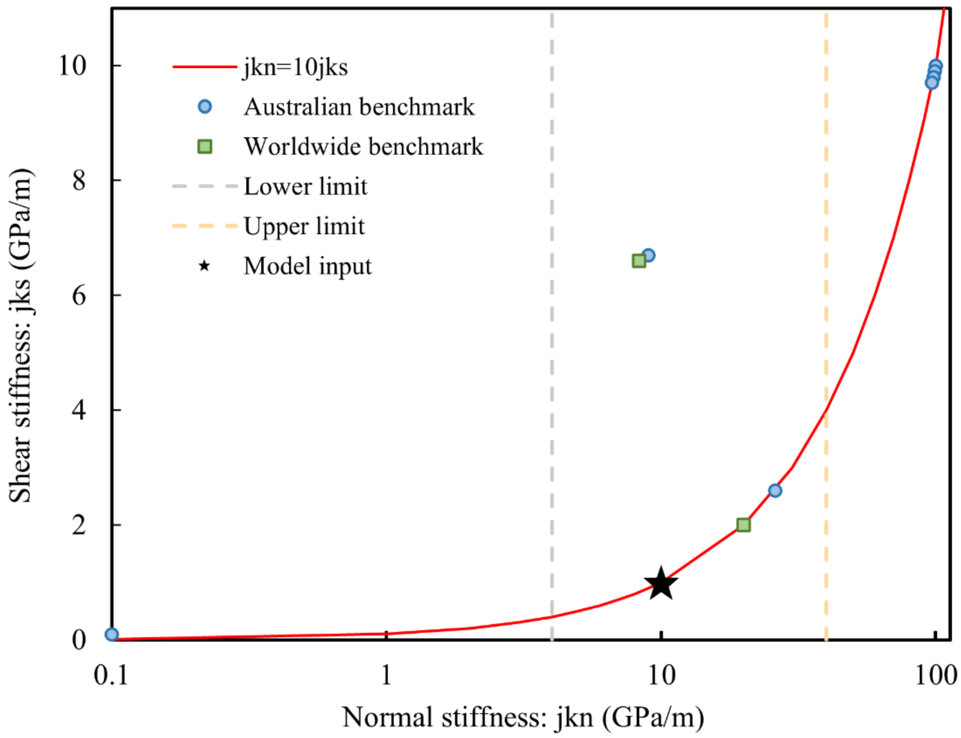

Figure 5-18 The normal and shear stiffness of bedding planes used in previous studies and this research (Li et al. 2022)

Additionally, the seismic-derived fractures will also affect the performance of the model by initiating sliding between rock block elements. The radius of disk-shaped fractures is calculated based on the fracture size shown in Section 5.2 with an initial aperture of zero. Here we assume that the seismic-derived fractures are all generated during coal extraction. As Figure 5-19 shows, each seismic-derived fracture is implemented in the model by cutting the rock block elements and generating a new joint of the same size, orientation, and location using the fracture information obtained from the seismic data above. In other words, before running the simulation, every fracture was put into the model, but they were initially considered closed due to their high cohesion values. As the simulation progresses, any fractures participating in the process are redefined to be open by setting their cohesiveness to zero. This change makes it easier for fracturing activities to occur within the model. The model effectively reflects the real-world process in which initially stable geological structures become destabilised as a result of mining-induced stress, resulting in fracture formation and propagation. The timing of adding each fracture also align with the onset time of the corresponding seismic event, which is reflected by the eight longwall extraction steps at various face retreat distances in the numerical model.

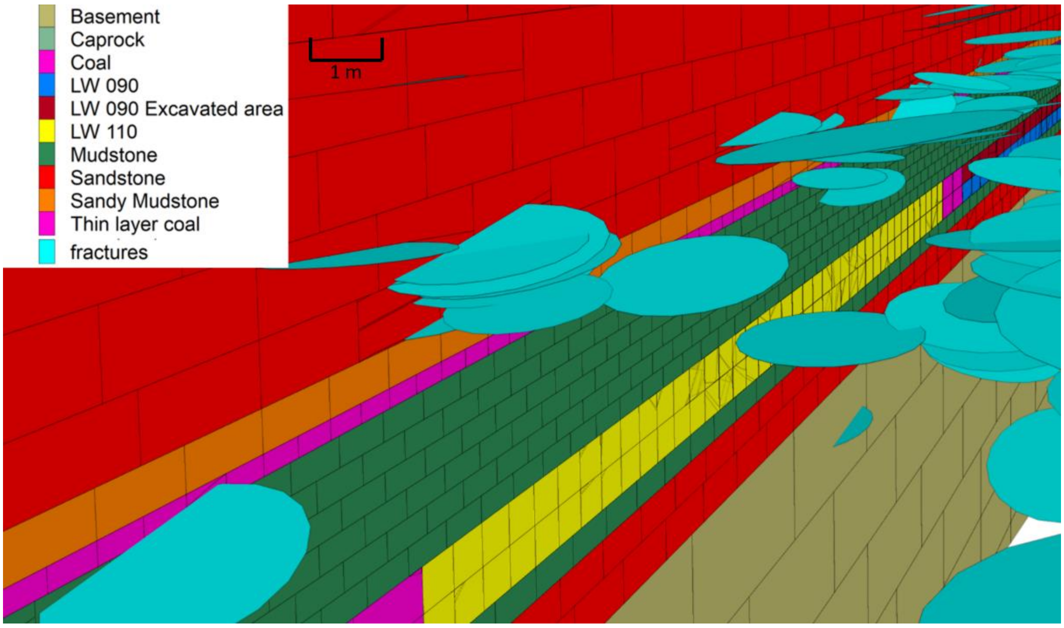

Figure 5-19 Rock block elements intersected by seismic-derived fractures

5.3.3. *Goaf extraction*

Since the modelled area also contains LW 090, which was mined before LW 110, the goaf formed by LW 090 needs to be considered before simulating the extraction of LW110. The physical location of LW 090 is at the top right side of LW 110 as shown in Figure 5-20.

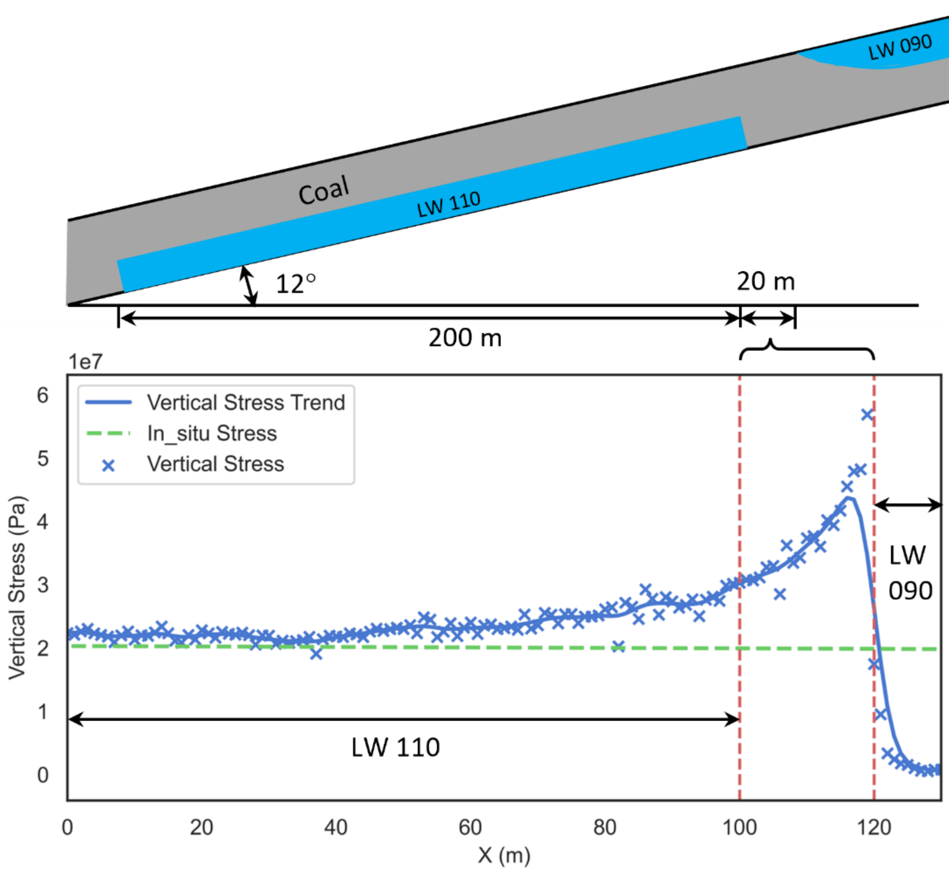

Figure 5-20 Vertical stress profile from LW 110 to LW 090

Figure 5-20 shows the variation of normalized vertical stress along a profile line from LW 110 to LW 090 at a depth of 2 m below the coal seam. It presents the vertical stress trend after extracting LW 090 and before mining LW 110. The stress curve follows the general trend of the stress distribution around a mined zone. Zones of vertical stress exceeding the in-situ overburden stress are known as the abutment zones, and the elevated stresses are known as abutment stresses. After the extraction of LW 090, high magnitude abutment stress appears around the neighbouring longwall panel LW 110. The location in which the elevated vertical stress decrease back to the in-situ stress is about 60 m from the tailgate, which means that about 60 m is affected by the extraction of LW 090. As the mining starts in LW 110, the dramatic decrease of the vertical stress after the face passing over will occur within 60 m from the tailgate. Within this area, the surrounding strata are in a transition state from the compression to extension. This phenomenon will inevitably reduce the inherent stability of the rock strata and induce mining fractures. This also explains that seismic-derived fractures are more active in this area compared to the area that are close to the maingate.

5.3.4. *Mining steps*

After the goaf extraction, the overall displacement of the model was reset to zero. Therefore, in the following analysis, the model would only show new displacements caused by the extraction of LW 110. The extraction of the LW 110 in this simulation extracts the total of 10 m coal at the same time within each step though the extraction of LW 110 applied the (LTCC) mining method as stated above. The actual height of the shields and the coal cut at the working face is 3 m, and the rest of the coal is extracted by gravity caving behind shields. The extraction of total 10 m in simulation is reasonable because that the stress distribution caused by LTCC is in general similar to that caused by conventional longwall mining (Le et al. 2018). The similarity is due to the fact that LTCC uses the conventional longwall method for extracting the lower coal section.

The extraction of the studied area in LW 110 was simulated by four mining cycles as defined earlier (Cycles 1-4 and each cycle has two excavation steps). After each excavation step, the unbalanced force in the model is monitored continuously to check whether equilibrium has been reached. A threshold value of 10^{-4} is set for the ratio of $\frac{Unbalanced\ Force}{Force\ in\ this\ gridpoin}$ to control the completion of each excavation step in the model. If the unbalanced ratio is larger than 10^{-4} and the maximum vertical roof displacement is smaller than the mining height, this solving process continues until the unbalanced ratio becomes less than 10^{-4}, and then, the next excavation step is simulated. Using this unbalanced ratio, about 40,000 to 50,000 calculation timesteps are completed in each excavation step. The ratio variation during the model equilibrium process is shown in Figure 5-21. Cycle 4 takes longer to equilibrium according to the figure, and this may be because at this step the excavation runs through the entire model. In addition, a few fractures generated from Cycle 4 are not considered within the model domain as Figure 5-14 shows, since the induced fractures tend to occur at a certain distance ahead of the longwall face. Thus, the simulation result in Cycle 4 will only be used to show the final model state, and not be compared against the other three cycles hereafter.

The mining-induced fractures considered in this model were pre-defined at the model set-up stage to intersect rock blocks as shown in Section 5.3.3. The cohesion and tension of the fractures at this stage were assigned with an extremely high value (10^7 Pa) to force these fractures to maintain closed. After the initialise of the model (i.e., LW 090 is extracted), the fractures that located within the modelled area but occurred before Cycle 1 starts are reset to be active, i.e., the cohesion and tension of these fractures are re-assigned to zero. This step resumes the mining state that the working face approaches the starting position of Cycle 1. In addition, before simulating each extraction step in Cycles 1-4, the fractures involved in that step are also reset to be active according to the triggering time of these fractures and face positions. Therefore, a total of nine groups of fractures were activated in sequence during the whole simulation process.

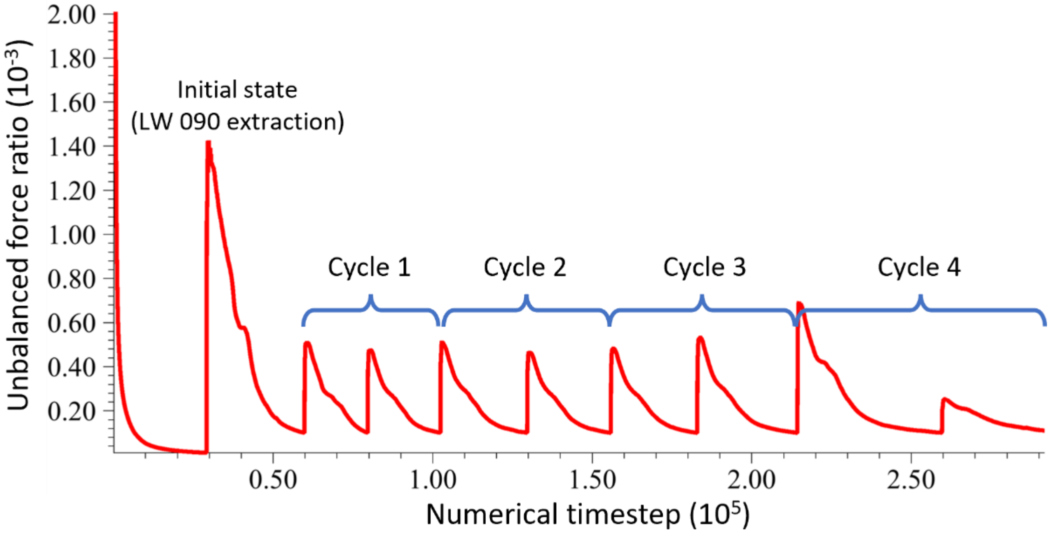

Figure 5-21 The evolution of unbalance force ratio during the equilibrium process for each excavation step in all four cycles

5.3.5. *Stress and displacement caused by progressive mining*

Figure 5-22a shows the displacement contour for a typical excavation step after reaching the model equilibrium. It can be seen that the roof overlying strata in the inclined direction of the goaf will gradually drop with the movement of the mining face. After coal extraction, the direct roof caves in and the old roof collapses, the height of roof caving and fracturing above the goaf expands, and the maximum subsidence of the roof increases gradually (in the blue area, the deeper the colour, the larger is the subsidence). After coal extraction, the floor is in the unloading state, and the floor heave phenomenon can be observed. Compared to the roof collapse, the displacement of the floor is relatively low. At the final excavation step within the study area, the roof subsidence value at the centre of LW 090 reaches 3.2 m, and the roof subsidence value at the centre of LW 110 reaches 4.2 m (as Figure 5-22 presents). The subsidence displacement contour of the overlying strata above the extracted panel shows an inverted trapezoid shape. In addition, the floor at the centre of LW 110 is affected by the unloading of the coal seam, and the amount of floor heave ranges from 0 m to 0.27 m with the advance of the mining face. However, the displacement is not as large as the amount of roof subsidence. Figure 5-23 also presents the subsidence profile from the centre of LW 110 to the model top boundary (a vertical profile line). As this figure shows, the subsidence can be up to 4.2 m and drops sharply within the mudstone area (as annotated by the dashed lines).

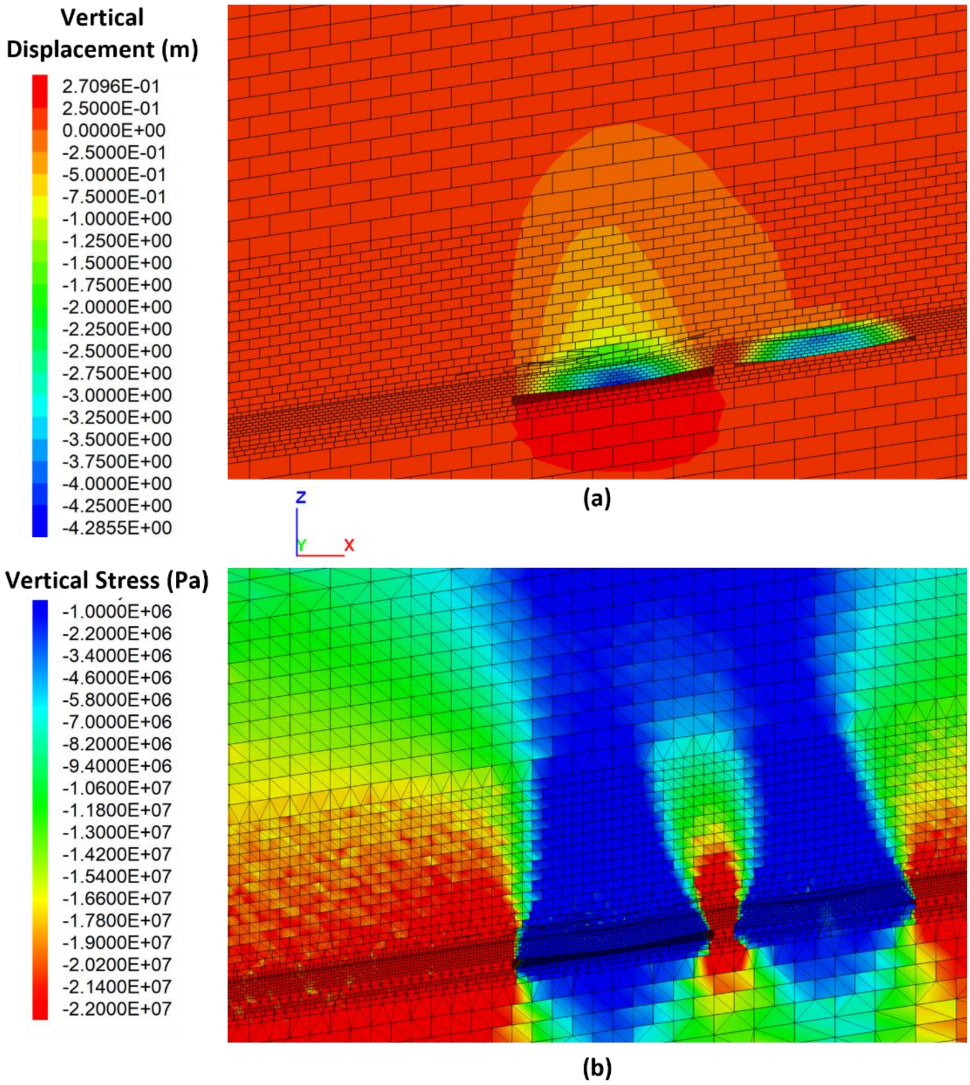

Figure 5-22 The equilibrium state of the model showing the contour of (a) the displacement and (b) the vertical stress at the front view (i.e., the cross-section of x-z plane)

The final modelling result of vertical stress distribution around the panel in the nearby rock formations is shown in Figure 5-22b. As can be seen from the figure, abutment stress can be observed at both the tailgate and maingate sides due to the bending and subsidence of the overlying strata after a large area of the coal seam is mined out. In other words, coal extraction leads to high-stress concentration near the remanent coal pillars. Since the high-stress area caused by LW 090 was superimposed with the abutment stress induced by LW 110, the dynamic mining of LW 110 triggered more fractures at the tailgate side, which is also confirmed by the spatial distribution of microseismic data.

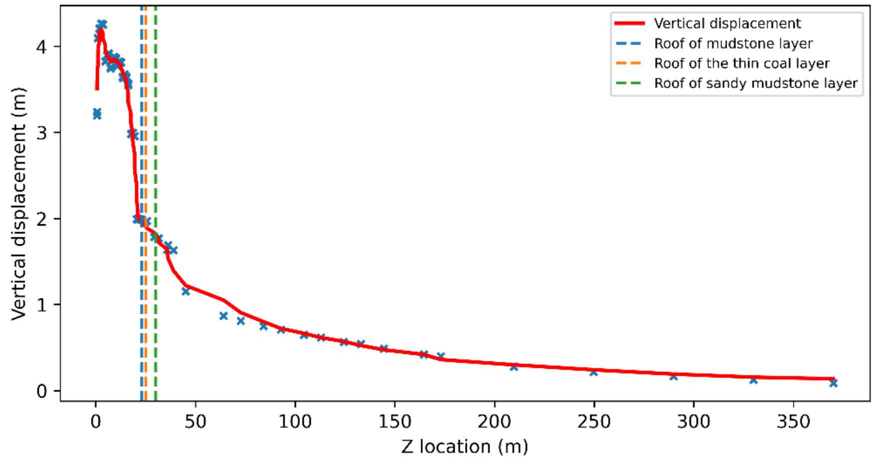

Figure 5-23 Subsidence profile of the roof strata from the centre of the LW 110 panel to the model top boundary

Note that before the modelled coal extraction, the vertical and horizontal stresses denoted the minor and major principal stresses in the in-situ condition, respectively. Due to the extraction, the vertical stress was relieved above and below the mined-out area, whereas it concentrated in the unmined coal (abutment stress). With the face advancing, the area of vertical stress relief and the abutment stress also increased. The horizontal stress, from the start of the extraction, continued to concentrate on the immediate roof and main roof. When the strata failed, the horizontal stress was significantly released; however, it could still be transferred to the broken but not fully caved strata.

The distributions of vertical stresses at different stages of mining in the model are shown in Figure 5-24. As the mining advances, the region of abutment stress keeps moving forward along with the face and its magnitude also increases continuously. This phenomenon can be observed in all three figures in Figure 5-24. Such results indicate that as the extraction advances, the stress redistribution in the floor strata may experience three stages: (i) the origin stress state before mining, (ii) a gradual increase as the mining face approaches, and (iii) a dramatic decrease after the face passing over. The measurement points are 1 m above the seam floor at the middle of the panel (Figure 5-24a), the tailgate (Figure 5-24b) and the maingate (Figure 5-24c). The location of these measurement points seen from the plan view is shown in Figure 5-14. The magnitude and location of abutment stress are displayed at the face advance at the end of Cycles 1-3. The results of Figure 5-24a suggest that the maximum abutment stress was twice the overburden stress and occurred about 6 m ahead of the face after Cycle 1 excavation. After Cycles 2 and 3, the peak abutment stresses are about 1.5 and 1.9 times the pre-mining stress, respectively. Simultaneously, the peak abutment stress reached 10 m and 6 m ahead of the face line. This is because the relief of high horizontal principal stress is significant and may cause a reduction in vertical stress.

Alternatively, at the tailgate and the maingate, the roof stress shows relief after the working face passes by (see Figure 5-24 b and c). The vertical stress can decrease to 0.5 times the initial stress and occur gradually until about 100 m away from the face. An even more significant stress drop occurs at the tailgate side since the tailgate is already in the high-stress area. On the other hand, it shows a very unlikely trend that the vertical stress at the tailgate can resume the in-situ stress state after mining.

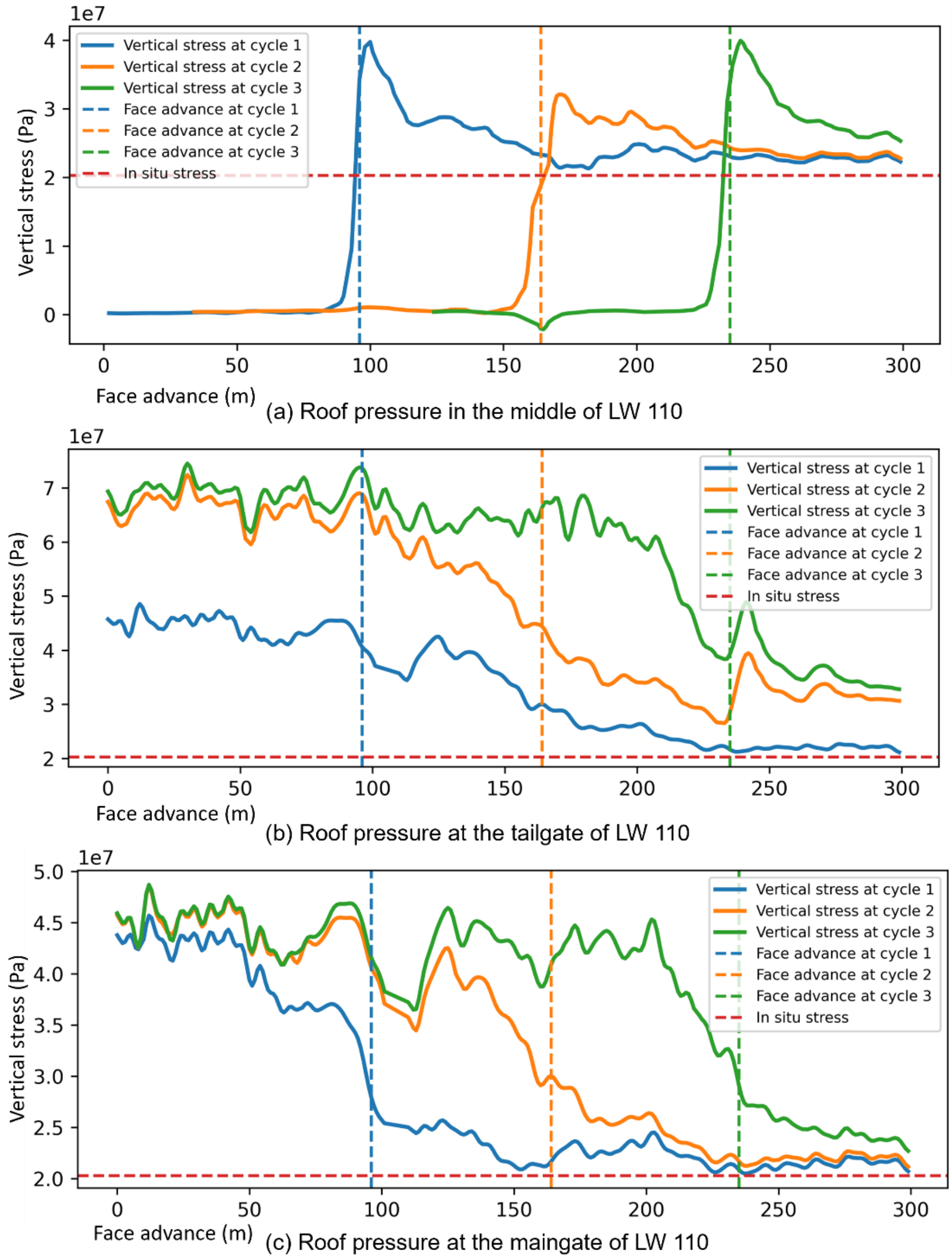

Figure 5-24 Vertical stress changes of the measurement points at (a) the centre of LW 110, (b) the tailgate, and (c) the maingate after the completion of mining Cycles 1-3

5.3.6. *Seismic-derived fracture simulation results*

During mining operations, the abutment stress progresses along with the direction of face advancement, which consequently generates a mostly quasistatic loading on the roof-coal-floor system. Under this loading condition, coal fracturing usually starts at the excavation boundary, where the vertical stress is the post-peak residual stress and transfers gradually to the deeper solid coal along with the coal excavation (Cai et al. 2019). It has also been observed in this research.

The failure state of seismic-derived fractures at the end of the coal extraction is displayed in Figure 5-25. Despite appearing as quadrilaterals due to mesh separation in the simulation, the fractures remain functionally round. This is a visual discrepancy that doesn't impact the simulation's operation or data interpretation. The discontinuities failed in both tension and shear. The discontinuities that have slipped (shear failure) are shown in Figure 5-25a, and those that have opened (tensile failure) are shown in Figure 5-25b. As can be seen from the figure, both slipping and opening fractures were observed in the upper strata. Comparing the shear displacement and the normal displacement in the same colour scale, both the shear and normal displacement occurred at the area above the support, while the shear displacement is obviously larger than the normal displacement. This can be explained in combination with the maximum principal stress distribution and fracture spatial distribution as shown in Figure 5-26, which takes Cycle 2 as an example. From this figure, it can be observed that in a normal mining cycle, the stress is accumulated in the above strata ahead the working face and then released at the fracture locations. Therefore, in the fractures relative far above the panel in the overlaying strata, the confining stress becomes greater, and that causes discontinuities to have a shear displacement. Meanwhile, in the roof strata immediately above the support, the horizontal stress is considerably released. The vertical stress still acts owing to the weight of the overlying strata. A low confining stress is formed in this area and a normal displacement occurred in the fractures along the similar dip as the working face. In this condition, coal mass tend to fail in tension along the vertical joints (Kelly et al. 2002; Gao et al. 2014). It is also noted that the assumption of discontinuities with zero tensile strength and zero cohesion in the simulation process can facilitate the development of the in the model and generate reasonable results.

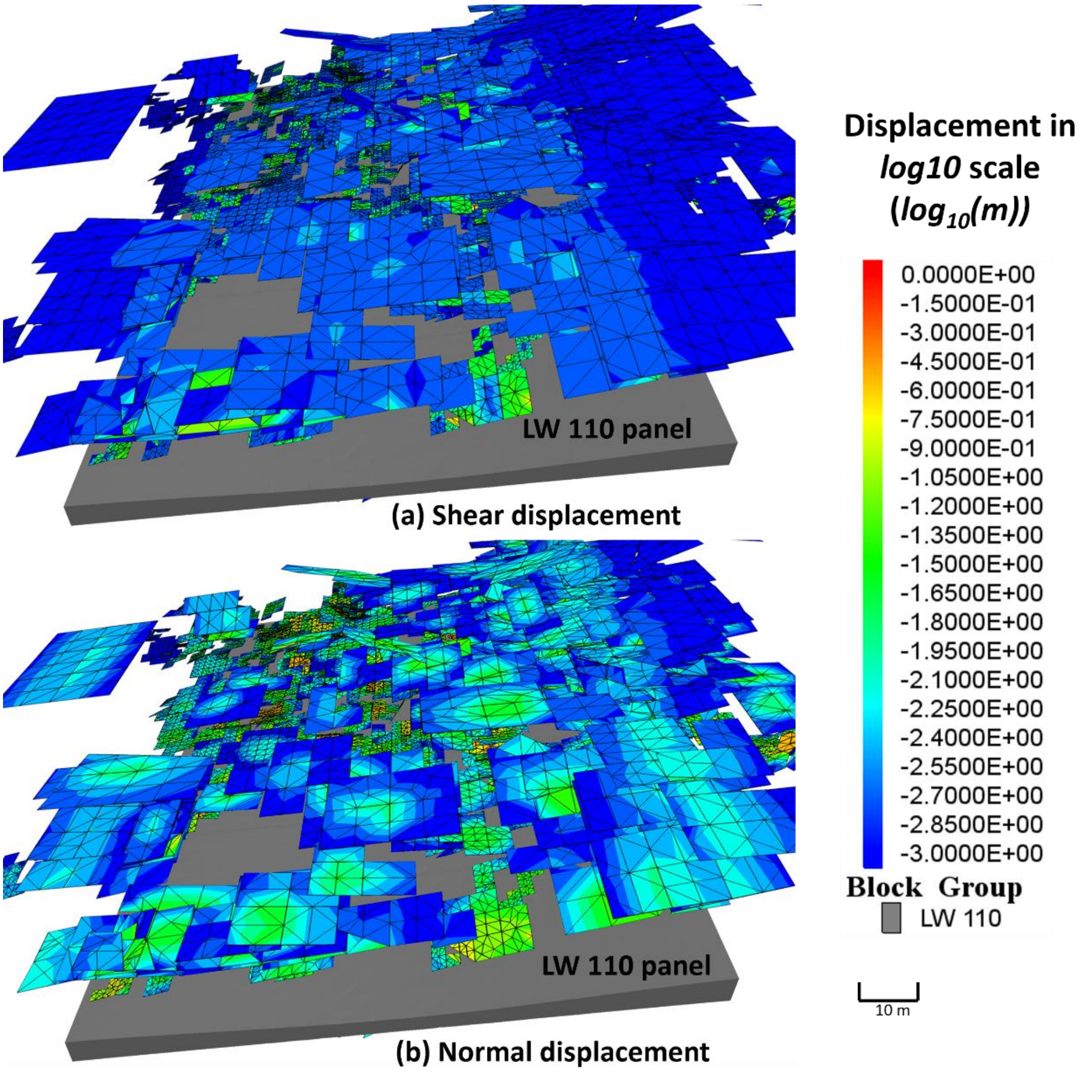

Figure 5-25 The seismic-derived fractures displacement in log10 scale: (a) shear displacement and (b) normal displacement

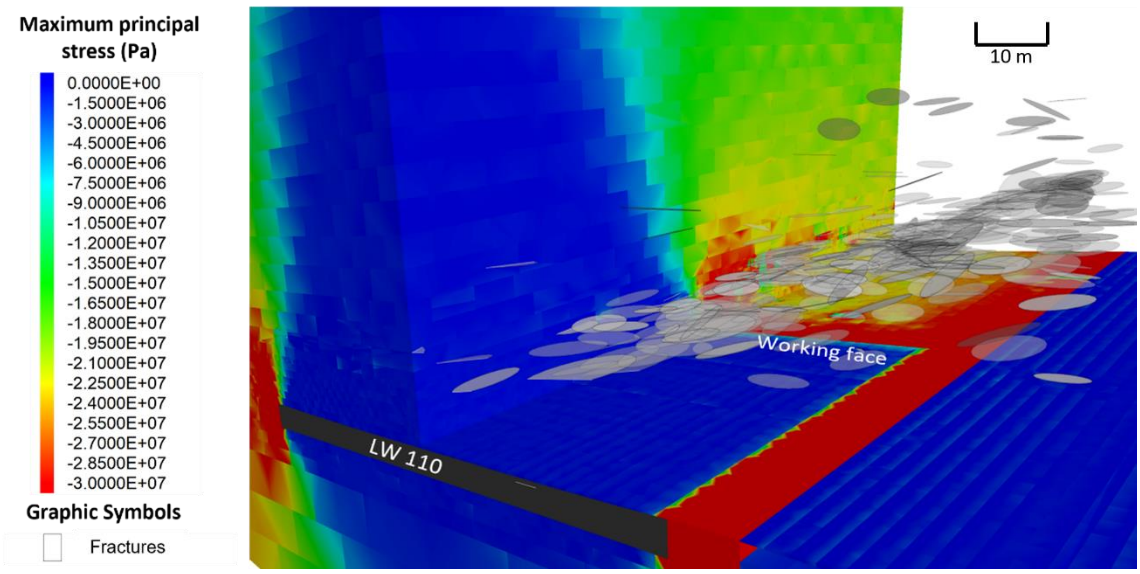

Figure 5-26 The equilibrium state of the maximum principal stress contour with the seismic-derived fractures

The modelling of seismic-derived fractures shows that the fracture geometry control stress regimes and failure responses, and then affects the damage zone development. In the meantime, the fracture responses from the simulation results can also be compared with the seismic monitoring results. Figure 5-27 presents the box plot of normal and shear displacement of seismic-derived fractures, which can be related to Figure 5-6. Again, the X represents the width of the longwall face, and the two red dashed line shows the edge of the longwall panel. The fractures are mainly recorded within the excavated zone. The shear and normal displacement within this area has a similar magnitude, while the mean value of normal displacement is larger than the value of shear displacement in most of the area of the excavated zone. Comparing along the X axis direction, the displacement within the longwall panel is larger than the edge area (maingate and tailgate). However, the fractures within the not mined area shows fluctuation along the panel. The shear and normal displacement have similar trends with the radius and aperture of seismic-derived fractures. However, the magnitude has about 100 times difference, which is a result that the released energy from rock failure may be dissipated in many forms and the seismic wave energy only accounts for a small fraction (Venkataraman and Kanamori 2004)

It should be noted that in Figure 5-27b, only the seismic-derived fractures that are active are being counted. In other words, only the fractures involved within Cycle 2 are activated and counted in the simulation process. This might cause a limited number of fractures being counted in Figure 5-27b, but the trend remains relatively clear still.

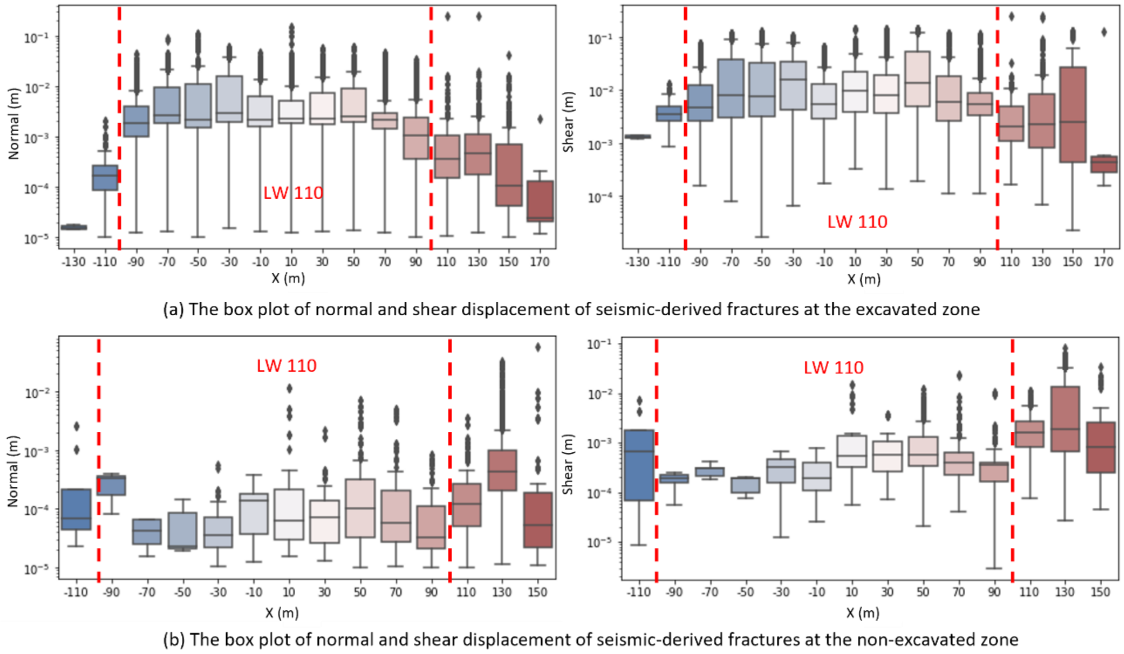

Figure 5-27 The box plot of normal and shear displacement of seismic-derived fractures at the (a) mined area and (b) solid coal

5.3.7. *Impact of fractures on the modelling results*

In Section 5.3.6 the fracture behaviours have been validated using results derived from seismic monitoring. Another significant aspect to consider is the impact of the originally inputted fracture model on the improvement and influence of the mining modeling process. In order to identify the impact of the fractures on the modelling, a similar model is run at the same condition following the same mining procedure but without considering the seismic-derived fractures. The in-situ stress, mechanical properties, and boundary conditions applied to the no-fracture models were the same as the models introduced above.

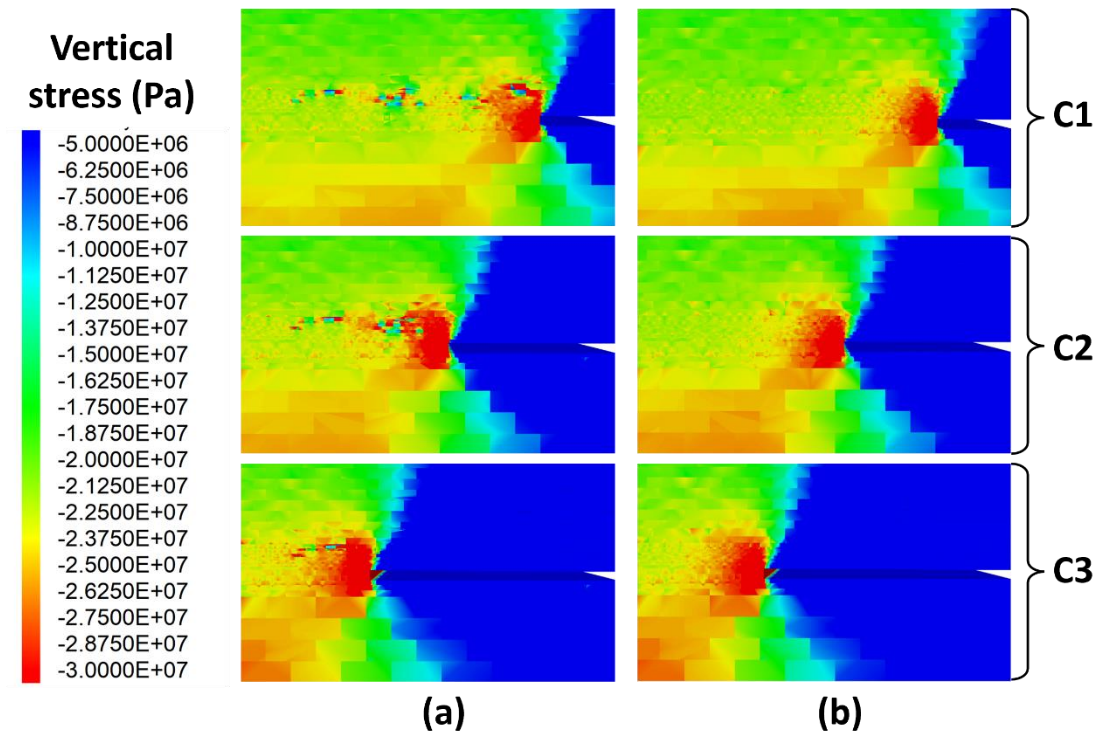

Figure 5-28 The vertical stress contour at the end of mining Cycles 1-3: (a) with seismic-derived fractures and (b) without seismic-derived fractures

The vertical stress contours at the end of mining Cycles 1-3 with considering seismic-derived fractures and without considering seismic-derived fractures are compared in Figure 5-28. The face advance is from the right side to the left. The comparison of Figure 5-28 (a) and (b) obviously shows the effect of seismic-derived fractures on the regional stress distribution, especially in the roof strata. The high-stress area caused by extraction is usually about 30-50 m ahead of the face. The fractures located within this area can generate a low stress zone. The fractures can release the accumulated stress caused by coal excavation and disperse the high-stress zones.

To further investigate the effects of seismic-derived fractures on the model results, Figure 5-29 presents the stress distribution around these fractures. Within the area above the goaf, a low-stress area has already been generated in an arched shape. The initial input fractures are hardly affecting the stress condition since plenty of fractures have been generated in this area with a large opening. The seismic-derived fractures are connected with each other above the goaf area. The stress is already released, so the fractures are dispersed and connected with the natural joints between the rock elements. It should be noted that since seismic sensors are frequently relocated when the working face moves during seismic monitoring, the fractures noted in the figure were generated before the working face arrived. After the coal extraction passes over this area, the fracture distribution is going to be close to homogeneous in the caved zones. However, when investigating the not mined area, the dense fracture zone shows a clear trend of stress release, and the range can be up to 20 m, which depends on fracture radii (the area that is affected by the seismic energy release). In addition, within the area that the seismic-derived fractures concentrate in and have a chance to be connected, the low-stress area may also connect and form a large stress relief zone. This can be observed in the top right region of Figure 5-29b. Although the volume of low-stress area around a single fracture is limited, a large low-stress layer is formed with the connected fractures along the orientation of most fracture planes.

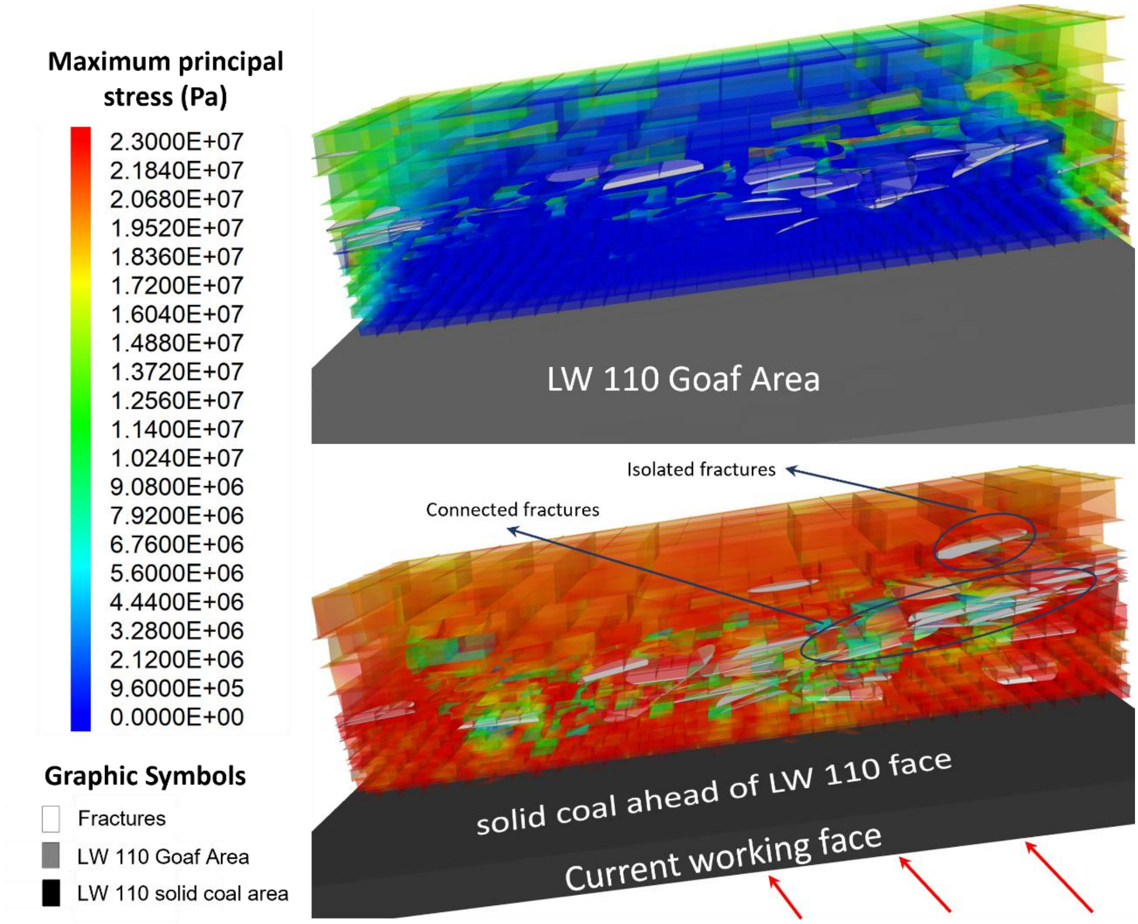

Figure 5-29 The clipped box of the excavated area and a solid coal area representing the contour of the maximum principal stress

Figure 5-30 shows the principal stress and the direction of the principal plane (i.e., the plane at which the maximum stress is induced) around the study panel at the end of Cycle 2 excavation. Figure 5-30a is at the roof of the coal layer, and Figure 5-30b is the plane that is 20-25 m above the coal layer, which is the layer where most of the seismic-derived fractures are located at. From the maximum principal figure, the stress is accumulated at the working face, and a large number of fractures occur within this area. Fractures affect more on the dip angle of the principal plane and maximum principal stress within this area. The dip angle of the principal plane is vertical but turns horizontal near the working face. The fractures cause the dip angle to turn horizontal as well. At the same time, the dip direction of the principal plane is more likely to be north-south but turns to the east-west near the working face. The influence of the seismic-derived fractures is uncertain since the fracture's dip direction has a wide distribution range, as Figure 5-9 shows.

These statistics also show that the direction of major principal stresses shifted from vertical to horizontal or near horizontal in the unmined coal seam upstream of the face line. Meanwhile, smaller principal stresses tend to shift from horizontal to vertical or inclined. These alterations are the result of horizontal stress concentration mixed with vertical stress release at this location. The orientations of principal stresses were progressively restored to their pre-mining status as one moved deeper into the unmined region. When the pre-mining major principal stress is horizontal, the direction shift may occur above and below the mined-out area.

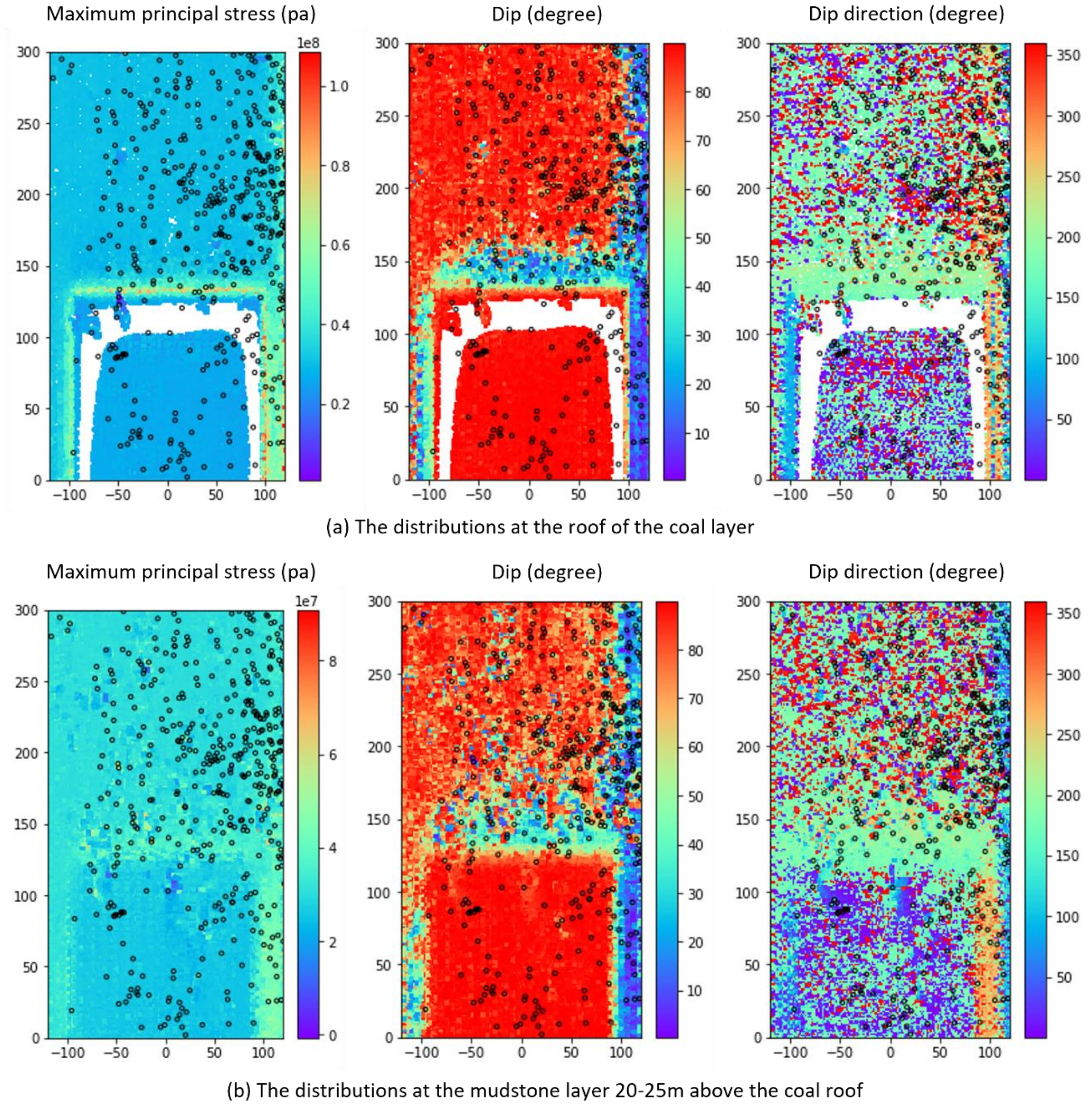

Figure 5-30 The principal stress and the direction of the principal plane at the end of Cycle 2 excavation at (a) the coal layer roof and (b) 20-25m above the coal layer

5.4. *Conclusions*

With the help of the synthetic triaxial signal, seismic source parameters of M_0, R and τ can be calculated. Taking the Yima coal mine as the case study site, the fracture network induced by longwall coal extraction was established using the proposed uniaxial seismic data analysis method. The seismic-induced fractures were classified by the types of failure mechanism, i.e., tensile and shear. The radius, aperture change, and orientation of each induced fracture were calculated. Most fractures are reported within the longwall panel and the mudstone strata above the panel. The fractures are more active on the goaf side compared with the solid coal side, and the magnitude of the fractures triggered by shear failure is affected by the F16 reverse fault near the panel. Most fracture orientations follow the orientation of the longwall panel, and the dip direction and dip angle have a variation within 50 degrees and 5 degrees, respectively.

With a comprehensive understanding of the spatial distribution of a mining-induced fracture network, the model of induced fracture map around the longwall panel was created and simulated with the working face advanced. Four cycles separate the total mining process to step the simulation process according to the b-value discussed in Chapter 3. The result apparently presents the stress condition along the face advance affected by seismic-derived fractures. And the mining induced fracture change in geometry matches the analysis of seismic signal processing.

The proposed methodology for characterising mining-induced fractures is clearly promising. However, additional validation is required to not only improve its reliability but also to acquire a fuller understanding of its strengths and limitations. One good approach to accomplish this is to perform further case studies in a variety of mining situations. These additional studies could be used to assess the applicability and generalizability of the proposed methodologies in the actual world. We can get useful information by evaluating how these strategies operate in diverse geological and operational circumstances. These findings may give information on the approaches' adaptability and robustness, as well as whether they can be depended on in a range of settings.

Furthermore, a comparison with existing fracture characterisation procedures could be quite valuable. This analysis would provide a fair assessment of the viability of the proposed methods. It would be especially valuable in cases when there are issues with data quality, resource accessibility, or computing needs. Such an analysis could aid in determining if the proposed methods offer any advantages over existing procedures and, if so, under what conditions these advantages may be most relevant. Furthermore, as described in Section 5.3, there is a need for a more complete investigation of roof falls during coal extraction. It is critical to comprehend the impact of these roof falls on fracture development and stress distribution. This greater comprehension could provide a more complete view of the processes at work in these complex systems. It may also lead to the creation of more effective ways for dealing with similar difficulties in the future, thereby boosting mining operations' safety and efficiency.

To sum up, the novel method introduced in this research helps to comprehensively understand the spatial distribution of a mining-induced fracture network using uniaxial seismic data. This analysis has the potential to not only dynamically update rock mass mechanical parameters but can also guide decision-makers to take preventive measures according to the dynamic development of mining-induced fractures.

Chapter 6. Conclusions and recommendations to the future research

A comprehensive literature review of applications of seismic monitoring revealed its benefits, limitations and future potential. Following the analysis of recent research outcomes and reports and documents from mine sites that applied seismic monitoring, the thesis narrowed down the problem into the mining-induced fractures assessment, which can be addressed by improving the analysis of the most applied type of seismic signals in the industry. Compared to numerous research of seismic monitoring in hydraulic fracturing, the review suggested that research is required in the seismic monitoring applied to the underground mining industry, such as correlation assessment and fracture distribution, due to the fact that mining-induced fractures are initiated by stress change and strata movement after mineral extraction instead of fluid injection. Since these applications are critical for monitoring rock behaviour and maintaining safe operating conditions, an effort was made to develop comprehensive seismic processing algorithms to achieve them. However, several tasks in achieving fracture monitoring using these algorithms still need to be solved in sequence.

The preliminary investigation of the seismic monitoring in underground mines exhibited a large limitation of the seismic-related parameters that could be calculated. The primary reason is that the uniaxial seismic sensors installed are widely used in underground mines as a result of low cost and high mobility is hard to receive complete signals from seismicity. An approach of artificial restoration of complete seismic information is required. Besides, seismic correlation is also a major problem for all the applications that rely on spatial-temporal seismic data. Thus, the assessment of spatial and temporal correlation was given equal importance, and an efficient approach was developed in this thesis to define the correlation period and range in temporal and spatial domains, respectively as well as the overall consideration of space and time. With the help of this research, the fracture distribution can be drawn and modelled with the effect of the site operation, and major decisions and plans can be made by synthesising research in this thesis suppose thesis methods are applied in ongoing underground longwall mining.

6.1. Contributions of the research

The conclusion of each chapter has been included by the end of each chapter. To give a comprehensive discussion of this project, this research aimed to advance the current methods of seismic monitoring at underground mine sites to provide comprehensive seismic-related induced fractures. Through this research, an effort was made to improve the mining-induced seismicity inverted in-situ fracture characteristic and provide reliable methods and data processing tools to support this assessment. The main contributions coming from the thesis are listed below.

- In Chapter 3, a novel approach using uniaxial seismic data to derive fracture network properties induced by mining has been developed. This is achieved by seismic moment tensor inversion, failure type analyses, source radiation pattern and the failure plane solution analysis in sequence. The Seismic monitoring data collected from the Yima underground coal mine in China was processed to verify the feasibility of the proposed method. The seismic signal processing, including pre-processing of filtering, frequency domain analysis, wave picks, event locations, and moment tensor inversion, are calculated in detail with the sample seismic waves and seismic events using the proposed uniaxial seismic data analysis method.
- In Chapter 4, quantitative approaches were applied for temporal, spatial and spatial-temporal correlation analysis of a set of seismic data in the longwall mining process. ACF was used to evaluate the correlation of evenly spaced seismic data in combination with semivariogram, whereby the temporal correlation of unevenly spaced seismic energy was also assessed. The SOF-time is applied to represent the period that a notable correlation of seismic data shows within. On the other hand, the spatial correlation of the seismic data was estimated using Moran's I. The spatial semivariogram assessment was applied to determine the radius of the correlative area (SOF-space). The spatial-temporal correlation has been assessed by investigating the distance and time difference with respect to three reference points. And clear clustering characteristics have been observed by investigating distance distribution to working face versus time distributions to assess the spatial and temporal correlation between different clusters at the last step of this research.

- In Chapter 5, With the help of the synthetic triaxial signal, seismic source parameters of M_0, R and τ can be calculated at the Yima coal mine. The seismic-induced fractures were classified by the types of failure mechanism, i.e., tensile and shear. Most fractures are reported within the longwall panel and the mudstone strata above the panel. With a comprehensive understanding of the spatial distribution of a mining-induced fracture network, the model of induced fracture map around the longwall panel was created and simulated with the working face advanced. The result apparently presents the stress condition along the face advance affected by seismic-derived fractures. And the mining induced fracture change in geometry matches the analysis of seismic signal processing.

6.2. *Scope of improvements and recommendations for future work*

Although this study has successfully delivered an improvement in the understanding of the fractures which caused by longwall mining, it has certain limitations. This section will discuss the potential improvement and scope for future work that can be built on this study.

- The uniaxial wave is synthesised to a triaxial wave if the number of uniaxial signals is sufficient. Despite a limit of the accuracy of triaxial as a result of only four sensors located in the maingate and tailgate at the same time, the synthetic triaxial wave can still provide abutment information that uniaxial wave can not provide, such as source vector, S-wave pick and rotate, corner frequency, ground motion, peak ground acceleration (PGA) and all the attributes already applied in this thesis. The significance of his novel method allows a bunch of analysed that requires a triaxial signal can be applied to the field, which installed mainly in uniaxial sensors. It significantly simplifies the planning of seismic monitoring system installation. On the other hand, the uniaxial sensor is cost friendly and easy to relocate. It provides a probability of using the lowest amount of triaxial sensors and the maximum number the uniaxial sensor to extend the wide range of recovered area so that the seismic signal can be detected with a friendly cost.
- The correlation assessment within this thesis mainly applied the seismic event temporal and spatial distribution as well as the energy of each seismic event. This can cover most conditions since most seismic attributes are related to the seismic event itself and energy. However, there are still correlations more reasonable to

use parameters other than those two in some situations. The significance of the correlation assessment algorism in Chapter 4 is that they are universally applicable and the only change in the current algorithm is to change the parameters.

- Beside the single parameter. With the wide range of attributes that uniaxial signals can calculate and the universally applicable correlation assessment algorism, multi-attributes assessment can be potentially conducted and improve the authenticity of the result. On the other hand, with enough type of attributes, the neural network can potentially help to predict the correlation spatially and temporally, even predict the occurrence of seismic in the time and space domain then. Moving forward, with a prediction of seismic event, the future activity of fractures can be detected with the method mentioned in Sections 5.1 and 5.2. The following research has a chance to predict the behaviour of fractures and the failure of rock within the longwall mining process.
- Despite being simplified, the numerical models proposed in Section 5.3 are subject to restricted computation in this work, particularly the true-dimensional models, surrendering some of their authenticity. As a result, several rock mass characteristics, such as joint set spacing and rock block size, could not be depicted as accurately or as detailed as in reality. Moreover. The material properties employed in the models were acquired mostly from the Yima Coalfield, and it appears that the fractures and stress distribution patterns may not be relevant to all other situations. It should also be remembered that knowledge of the properties of discontinuities inside the rock is always limited. Despite the fact that these model input parameters are appropriately and realistically approximated, the approximations of the rock mass material properties may still be a restriction. Future advances in understanding of mining-induced fracture behaviour could be made by taking into account: better time separation of the face advance; a better consideration of the failure mechanisms of the induced and natural fractures; and a better understanding of the aspect of a natural fault that disturbs the induced fracture behaviour.

6.3. Concluding remarks

With the mining sector focusing on safe and sustainable mining operations, seismic monitoring will play an important role due to its low cost, precision, wide monitoring range, mobility, and large-scale application. The outcomes of the major body chapters contribute to this purpose by refining the uniaxial seismic signal processing approach via synthetic triaxial waves, assessing the spatial and temporal correlation of seismic data, and detecting and processing fracture information for geotechnical applications. All of the suggested technologies have been tested using field data and can be easily implemented at mine sites to offer in-situ monitoring solutions as the longwall face advances. Furthermore, the study can be expanded to address and cover a broader range of application domains, such as comprehensive seismic-derived attribute analysis and density prediction from uniaxial data, multi-attribute correlation assessment, in-situ DFN mapping, predicting rock bursts, and assessing stability. More research is needed to enhance seismic processing algorithms in order to decrease inaccuracy and better comprehend mining-induced fractures around subterranean longwall panels.

References

Abbott D, Wilson L, Lakings J, et al (2007) Hydraulic Fracture Diagnostics In The Williams Fork Formation, Piceance Basin, Colorado Using Surface Microseismic Monitoring Technology. 1–10. https://doi.org/10.2523/108142-ms

Adhikary DP, Guo H (2014) Measurement of Longwall Mining Induced Strata Permeability. Geotechnical and Geological Engineering 32:617–626. https://doi.org/10.1007/s10706-014-9737-8

Aki K, Richards PG (1980) Quantitative seismology

Arabasz WJ, Nava SJ, McCarter MK, et al (2005) Coal-Mining Seismicity and Ground-Shaking Hazard: A Case Study in the Trail Mountain Area, Emery County, Utah. Bulletin of the Seismological Society of America 95:18–30. https://doi.org/10.1785/0120040045

Arabasz WJ, Nava SJ, Phelps WT (1997) Mining seismicity in the Wasatch Plateau and Book Cliffs coal mining districts, Utah, USA. Rockbursts And Seismicity In Mines 299–303

ASC (2022) InSite seismic processing software: User manual-Technical Appendices version 3.18.1

Baig A, Urbancic T (2010) Microseismic moment tensors: A path to understanding frac growth

Bandis SC, Lumsden AC, Barton NR (1983) Fundamentals of rock joint deformation. International Journal of Rock Mechanics and Mining Sciences & Geomechanics Abstracts 20:249–268. https://doi.org/10.1016/0148-9062(83)90595-8

Barker W (2009) Increased Production Through Microseismic Monitoring of Hydraulic Fracturing Over a Multiwell Program. 1–5. https://doi.org/10.2118/124877-ms

Bischoff M, Cete A, Fritschen R, Meier T (2010) Coal mining induced seismicity in the Ruhr area, Germany. Pure Appl Geophys 167:63–75. https://doi.org/10.1007/s00024-009-0001-8

Boore DM, Boatwright J (1984) Average body-wave radiation coefficients. Bulletin of the Seismological Society of America 74:1615–1621. https://doi.org/10.1785/BSSA0740051615

Bosch M, Mukerji T, Gonzalez EF (2010) Seismic inversion for reservoir properties combining statistical rock physics and geostatistics: A review. Geophysics 75:165–176. https://doi.org/10.1190/1.3478209

Brady BHG; ETB (1995) Rock mechanics

Brummer RK, Rorke AJ, Fairhurst C (1990) Case studies of large rockbursts in South African gold mines. Rockbursts and Seismicity in Mines 323–329

Brune JN (1970) Tectonic stress and the spectra of seismic shear waves from earthquakes. J Geophys Res 75:4997–5009. https://doi.org/10.1029/JB075I026P04997

Cai W, Bai X, Si G, et al (2020a) A Monitoring Investigation into Rock Burst Mechanism Based on the Coupled Theory of Static and Dynamic Stresses. Rock Mech Rock Eng 53:5451–5471. https://doi.org/10.1007/S00603-020-02237-6/FIGURES/15

Cai W, Dou L, Cao A, et al (2014) Application of seismic velocity tomography in underground coal mines: A case study of Yima mining area, Henan, China. J Appl Geophy 109:140–149. https://doi.org/10.1016/J.JAPPGEO.2014.07.021

Cai W, Dou L, Si G, et al (2019) A new seismic-based strain energy methodology for coal burst forecasting in underground coal mines. International Journal of Rock Mechanics and Mining Sciences 123:104086. https://doi.org/10.1016/j.ijrmms.2019.104086

Cai W, Dou L, Si G, Hu Y (2021a) Fault-Induced Coal Burst Mechanism under Mining-Induced Static and Dynamic Stresses. Engineering 7:687–700. https://doi.org/10.1016/J.ENG.2020.03.017

Cai W, Dou L, Zhang M, et al (2018) A fuzzy comprehensive evaluation methodology for rock burst forecasting using microseismic monitoring. Tunnelling and Underground Space Technology 80:232–245. https://doi.org/10.1016/j.tust.2018.06.029

Cai X, Zhou Z, Zang H, Song Z (2020b) Water saturation effects on dynamic behavior and microstructure damage of sandstone: Phenomena and mechanisms. Eng Geol 276:105760. https://doi.org/10.1016/J.ENGGEO.2020.105760

Cao W, Durucan S, Cai W, et al (2020) A physics-based probabilistic forecasting methodology for hazardous microseismicity associated with longwall coal mining. Int J Coal Geol 232:103627. https://doi.org/10.1016/j.coal.2020.103627

Cao W, Shi JQ, Si G, et al (2018a) Numerical modelling of microseismicity associated with longwall coal mining. Int J Coal Geol 193:30–45. https://doi.org/10.1016/j.coal.2018.04.010

Carpenter C (2017) Fracture Modeling Using a Constructed Discrete Fracture Network From Seismic Data. Journal of Petroleum Technology 69:75–77. https://doi.org/10.2118/0317-0075-JPT

Cesca S, Rohr A, Dahm T (2012) Discrimination of induced seismicity by full moment tensor inversion and decomposition. J Seismol 17:147–163. https://doi.org/10.1007/s10950-012-9305-8

Chaulya SK, Singh RS, Chakraborty MK, Dhar BB (1999) Numerical modelling of biostabilisation for a coal mine overburden dump slope. Ecol Modell 114:275–286. https://doi.org/10.1016/S0304-3800(98)00157-4

Chen Z, Shi L, Xiang D (2017) Mechanism of casing deformation in the Changning–Weiyuan national shale gas demonstration area and countermeasures. Natural Gas Industry B 4:1–6. https://doi.org/10.1016/J.NGIB.2017.07.001

Cipolla CL, Mack MG, Maxwell SC, Downie RC (2011) A Practical Guide to Interpreting Microseismic Measurements. North American Unconventional Gas Conference and Exhibition 14–16. https://doi.org/10.2118/144067-MS

Clark I (1979) Practical Geostatistics

Collins DS, Pettitt WS, Young RP (2002) High-resolution Mechanics of a Microearthquake Sequence. Pure Appl Geophys 159:197–219. https://doi.org/10.1007/pl00001251

de la Vergne J (2003) Hard rock miners handbook. McIntosh Engineering

de Natale G, Zollo A (1989) Earthquake Focal Mechanisms from Inversion of First P And S Wave Motions. Digital Seismology and Fine Modeling of the Lithosphere 399–419. https://doi.org/10.1007/978-1-4899-6759-6_18

Dershowitz WS, Cottrell MG, Lim DH, Doe TW (2010) A discrete fracture network approach for evaluation hydraulic fracture stimulation of naturally fractured reservoirs. 44th US Rock Mechanics Symposium - 5th US/Canada Rock Mechanics Symposium

Dmowska R, Saltzman B (2001) Advances in Geophysics

Donoho DL (1995) De-Noising by Soft-Thresholding. IEEE Trans Inf Theory 41:613–627. https://doi.org/10.1109/18.382009

Duncan PM, Eisner L (2010) Reservoir characterization using surface microseismic monitoring. 75:

Eyre TS, van der Baan M (2015) Overview of moment-tensor inversion of microseismic events. Leading Edge 34:882–888. https://doi.org/10.1190/tle34080882.1

Fehler M, House L, Kaieda H (1987) Determining planes along which earthquakes occur: Method and application to earthquakes accompanying hydraulic fracturing. J Geophys Res Solid Earth 92:9407–9414. https://doi.org/10.1029/JB092IB09P09407

Fletcher JB, Haar LC, Vernon FL, et al (2013) The Effects of Attenuation on the Scaling of Source Parameters for Earthquakes at Anza, California. pp 331–338

Fletcher JB, McGarr A (2005) Moment tensor inversion of ground motion from mining-induced earthquakes, Trail Mountain, Utah. Bulletin of the Seismological Society of America 95:48–57. https://doi.org/10.1785/0120040047

Fujii Y, Ishijima Y (1991) Numerical simulation of microseismicity induced by deep longwall coal mining. Mining Science and Technology 12:265–285. https://doi.org/10.1016/0167-9031(91)91193-L

Gao F, Stead D, Coggan J (2014) Evaluation of coal longwall caving characteristics using an innovative UDEC Trigon approach. Comput Geotech 55:448–460. https://doi.org/10.1016/J.COMPGEO.2013.09.020

Gao FQ, Stead D (2014) The application of a modified Voronoi logic to brittle fracture modelling at the laboratory and field scale. International Journal of Rock Mechanics and Mining Sciences 68:1–14. https://doi.org/10.1016/J.IJRMMS.2014.02.003

Gibowicz SJ (1986) Physics of fracturing and seismic energy release: A review. Pure Appl Geophys 124:611–658. https://doi.org/10.1007/BF00879602

Gibowicz SJ (2009) Seismicity Induced by Mining: Recent Research. Advances in Geophysics 51:1–53. https://doi.org/10.1016/S0065-2687(09)05106-1

Gibowicz SJ, Kijko A (1994) An Introduction to Mining Seismology. Warsaw, Poland

Gibowicz SJ, Lasocki S (2001) Seismicity induced by mining: Ten years later. Advances in Geophysics 44:39–181. https://doi.org/10.1016/S0065-2687(00)80007-2

Gill DE, Aubertin M, Simon R (1993) A practical engineering approach to the evaluation of rockburst potential. Rockburst and Seismicity in Mines Balkema, Rotterdam 63–68

Glazer SN (2016) Mine seismology: Data analysis and interpretation: Palabora mine caving process as revealed by induced seismicity

Glazer SN (2018) Mine Seismology: Seismic Warning Concept

Głowacka E, Kijko A (1989) Continuous Evaluation of Seismic Hazard Induced by the Deposit Extraction in Selected Coal Mines in Poland. Seismicity in Mines 523–533. https://doi.org/10.1007/978-3-0348-9270-4_15

González JA, Rodríguez-Cortés FJ, Cronie O, Mateu J (2016) Spatio-temporal point process statistics: A review. Spat Stat 18:505–544. https://doi.org/10.1016/j.spasta.2016.10.002

Guha SK (2000) Induced Earthquakes

Gutenberg B, Richter CF (1956) Earthquake magnitude, intensity, energy, and acceleration (Second Paper). Annals of Geophysics 9:1–15

Gutenberg B, Richter CF (2010) Magnitude and energy of earthquakes

Harthong B, Scholtès L, Donzé FV (2012) Strength characterization of rock masses, using a coupled DEM-DFN model. Geophys J Int 191:467–480. https://doi.org/10.1111/J.1365-246X.2012.05642.X/2/191-2-467-FIG018.GIF

Hazzard JF, Young RP (2004) Dynamic modelling of induced seismicity. International Journal of Rock Mechanics and Mining Sciences 41:1365–1376. https://doi.org/10.1016/j.ijrmms.2004.09.005

Huang NE, Wu Z (2008) A review on Hilbert-Huang transform: Method and its applications to geophysical studies. Reviews of Geophysics 46:. https://doi.org/10.1029/2007RG000228

Hudson JA (1984) Comprehensive Rock Engineering Principles, Practice & Projects. London

Jaeger C (1979) Rock Mechanics and Engineering. Rock Mechanics and Engineering. https://doi.org/10.1017/CBO9780511735349

Jaksa MB, Kaggwa WS, Brooker PI (1999) Experimental evaluation of the scale of fluctuation of a stiff clay. 8th International Conference on Applications of Statistics and Probability in Civil Engineering 415–422

Kaiser PK, Maloney SM (1997) Scaling Laws for the Design of Rock Support. Seismicity Associated with Mines, Reservoirs and Fluid Injections 150:415–434. https://doi.org/10.1007/978-3-0348-8814-1_4

Kelly M, Luo X, Craig S (2002) Integrating tools for longwall geomechanics assessment. International Journal of Rock Mechanics and Mining Sciences 39:661–676. https://doi.org/10.1016/S1365-1609(02)00063-1

Kijko A, Funk CW (1996) Space-time interaction amongst clusters of mining induced seismicity. Pure Appl Geophys 147:277–288. https://doi.org/10.1007/bf00877483

Kisilevich S, Mansmann F, Nanni M, Rinzivillo S (2010) Spatio-Temporal Clustering: a Survey. Data Mining and Knowledge Discovery Handbook 1–22

Kleczek Z, Zorychta A (2022) Coal bumps induced by mining tremors. In: Rockbursts and Seismicity in Mines 93: Proceedings of the 3rd international symposium, Kingston, Ontario, 16-18 August 1993. Routledge, p 87

Kwiatek G, Ben-Zion Y (2013) Assessment of P and S wave energy radiated from very small shear-tensile seismic events in a deep South African mine. J Geophys Res Solid Earth 118:3630–3641. https://doi.org/10.1002/jgrb.50274

Le TD, Oh J, Hebblewhite B, et al (2018) A discontinuum modelling approach for investigation of Longwall Top Coal Caving mechanisms. International Journal of Rock Mechanics and Mining Sciences 106:84–95. https://doi.org/10.1016/J.IJRMMS.2018.04.025

Lei Q, Gholizadeh Doonechaly N, Tsang CF (2021) Modelling fluid injection-induced fracture activation, damage growth, seismicity occurrence and connectivity change in naturally fractured rocks. International Journal of Rock Mechanics and Mining Sciences 138:104598. https://doi.org/10.1016/J.IJRMMS.2020.104598

Lei Q, Latham JP, Tsang CF (2017) The use of discrete fracture networks for modelling coupled geomechanical and hydrological behaviour of fractured rocks. Comput Geotech 85:151–176. https://doi.org/10.1016/J.COMPGEO.2016.12.024

Lei Q, Latham JP, Xiang J, et al (2014) Effects of geomechanical changes on the validity of a discrete fracture network representation of a realistic two-dimensional fractured rock. International Journal of Rock Mechanics and Mining Sciences 70:507–523. https://doi.org/10.1016/J.IJRMMS.2014.06.001

Leśniak A, Isakow Z (2009) Space-time clustering of seismic events and hazard assessment in the Zabrze-Bielszowice coal mine, Poland. International Journal of Rock Mechanics and Mining Sciences 46:918–928. https://doi.org/10.1016/j.ijrmms.2008.12.003

Li S, Gao M, Yang X, et al (2018) Numerical simulation of spatial distributions of mining-induced stress and fracture fields for three coal mining layouts. Journal of Rock Mechanics and Geotechnical Engineering 10:907–913. https://doi.org/10.1016/J.JRMGE.2018.02.008

Li T, Cai MF, Cai M (2007) A review of mining-induced seismicity in China. International Journal of Rock Mechanics and Mining Sciences 44:1149–1171. https://doi.org/10.1016/j.ijrmms.2007.06.002

Li X, Si G, Oh J, et al (2022) Effect of pretension on the performance of cable bolts and its optimisation in underground coal mines with various geological conditions. International Journal of Rock Mechanics and Mining Sciences 152:105076. https://doi.org/10.1016/J.IJRMMS.2022.105076

Linzer LM (2005) A relative moment tensor inversion technique applied to seismicity induced by mining. Rock Mech Rock Eng 38:81–104. https://doi.org/10.1007/s00603-004-0041-4

Lu Y, Wang L (2015) Numerical simulation of mining-induced fracture evolution and water flow in coal seam floor above a confined aquifer. Comput Geotech 67:157–171. https://doi.org/10.1016/J.COMPGEO.2015.03.007

Ma C, Li T, Zhang H, et al (2019) A method for numerical simulation based on microseismic information and the interpretation of hard rock fracture. J Appl Geophy 164:214–224. https://doi.org/10.1016/j.jappgeo.2019.03.014

Madariaga R (1976) Dynamics of an expanding circular fault. Bulletin of the Seismological Society of America 66:639–666. https://doi.org/10.1785/BSSA0660030639

Main IG, Meredith PG, Jones C (1989) A reinterpretation of the precursory seismic b-value anomaly from fracture mechanics. Geophys J Int 96:131–138. https://doi.org/10.1111/J.1365-246X.1989.TB05255.X

Maxwell S (2010) Microseismic: Growth born from success. The Leading Edge 29:338–343

Maxwell SC, Rutledge J, Jones R, Fehler M (2010) Petroleum reservoir characterization using downhole microseismic monitoring. Geophysics 75:75A129-75A137. https://doi.org/10.1190/1.3477966

McGarr A (1984) Scaling of Ground Motion Parameters, State of Stress, and Focal Depth. 84:5029–5033

McGillivray P (2005) Microseismic and time-lapse seismic monitoring of a heavy oil extraction process at Peace River, Canada. 74317663 5:

Mendecki AJ (1996) Seismic Monitoring in Mines

Mendecki AJ, Aswegen G van, Mountfort P (1999) A guide to routine seismic monitoring in mines

Mendecki AJ, Mountfort P, van Aswegen G (1997) Seismic monitoring for stability of underground mining operations. 613

Nelder JA, Mead R (1965) A Simplex Method for Function Minimization. Comput J 7:308–313. https://doi.org/10.1093/COMJNL/7.4.308

Nolen-Hoeksema R, Tectonophysics LR-, 2001 undefined Moment tensor inversion of microseisms from the B-sand propped hydrofracture, M-site, Colorado. Elsevier

Onyejekwe S, Kang X, Ge L (2016) Evaluation of the scale of fluctuation of geotechnical parameters by autocorrelation function and semivariogram function. Eng Geol 214:43–49. https://doi.org/10.1016/j.enggeo.2016.09.014

Ou G Bin (2008) Seismological studies for tensile faults. Terrestrial, Atmospheric and Oceanic Sciences 19:463–471. https://doi.org/10.3319/TAO.2008.19.5.463(T)

Pettitt WS (1998) in rock by Department of Earth Sciences these investigate the fundamental

Pine RJ, Coggan JS, Flynn ZN, Elmo D (2006) The development of a new numerical modelling approach for Naturally fractured rock masses. Rock Mech Rock Eng 39:395–419. https://doi.org/10.1007/S00603-006-0083-X/METRICS

Potvin Y, Jarufe J, Wesseloo J (2010) Interpretation of seismic data and numerical modelling of fault reactivation at El Teniente, Reservas Norte sector. In: Transactions of the Institutions of Mining and Metallurgy, Section A: Mining Technology. Maney Publishing, pp 175–181

Press F, Allen C (1995) Patterns of seismic release in the southern California region. J Geophys Res Solid Earth 100:6421–6430. https://doi.org/10.1029/95JB00316

Ranjith PG, Zhao J, Ju M, et al (2017) Opportunities and Challenges in Deep Mining: A Brief Review. Engineering 3:546–551. https://doi.org/10.1016/J.ENG.2017.04.024

Rogers S, Elmo D, Dunphy R, Bearinger D (2010) Understanding Hydraulic Fracture Geometry and Interactions in the Horn River Basin through DFN and Numerical Modeling. Society of Petroleum Engineers - Canadian Unconventional Resources and International Petroleum Conference 2010 2:1426–1437. https://doi.org/10.2118/137488-MS

Rutledge JT, Phillips WS (2003) Hydraulic stimulation of natural fractures as revealed by induced microearthquakes, Carthage Cotton Valley gas field, east Texas. Geophysics 68:441–452. https://doi.org/10.1190/1.1567214

Rydelek PA, Sacks IS (1989) Testing the completeness of earthquake catalogues and the hypothesis of self-similarity. Nature 337:251–253. https://doi.org/10.1038/337251a0

Sasaki S, Kaieda H (2002) Determination of stress state from focal mechanisms of microseismic events induced during hydraulic injection at the Hijiori hot dry rock site. Pure Appl Geophys 159:489–516. https://doi.org/10.1007/978-3-0348-8179-1_21/COVER

Sayers CM, den Boer LD (2012) Characterizing production-induced anisotropy of fractured reservoirs having multiple fracture sets. Geophys Prospect 60:919–939. https://doi.org/10.1111/j.1365-2478.2011.01030.x

Schultz R, Skoumal RJ, Brudzinski MR, et al (2020) Hydraulic fracturing-induced seismicity. Reviews of Geophysics 58:1–43. https://doi.org/10.1029/2019RG000695

Sellers EJ, Kataka MO, Linzer LM (2003) Source parameters of acoustic emission events and scaling with mining-induced seismicity. J Geophys Res Solid Earth 108:1–16. https://doi.org/10.1029/2001JB000670

Sen AT, Cesca S, Bischoff M, et al (2013) Automated full moment tensor inversion of coal mining-induced seismicity. Geophys J Int 195:1267–1281. https://doi.org/10.1093/gji/ggt300

Shearer P (1999) Introduction to Seismology. Cambridge University Press, Cambridge, England

Sheriff RE (1976) Inferring stratigraphy from seismic data. Am Assoc Pet Geol Bull 60:528–542

Si G, Cai W, Wang S, Li X (2020) Prediction of Relatively High-Energy Seismic Events Using Spatial–Temporal Parametrisation of Mining-Induced Seismicity. Rock Mech Rock Eng 53:5111–5132. https://doi.org/10.1007/s00603-020-02210-3

Si G, Durucan S, Jamnikar S, et al (2015) Seismic monitoring and analysis of excessive gas emissions in heterogeneous coal seams. Int J Coal Geol 149:41–54. https://doi.org/10.1016/j.coal.2015.06.016

Si G, Korre A, Jamnikar S, et al (2015) Monitoring and modelling of gas dynamics in multi-level longwall top coal caving of ultra-thick coal seams, part I: Borehole measurements and a conceptual model for gas emission zones. Int J Coal Geol 144–145:98–110. https://doi.org/10.1016/j.coal.2015.04.008

Si G, Shi JQ, Durucan S, et al (2015) Monitoring and modelling of gas dynamics in multi-level longwall top coal caving of ultra-thick coal seams, Part II: Numerical modelling. Int J Coal Geol 144–145:58–70. https://doi.org/10.1016/j.coal.2015.04.009

Stec K (2007) Characteristics of seismic activity of the Upper Silesian Coal Basin in Poland. Geophys J Int 168:757–768. https://doi.org/10.1111/j.1365-246X.2006.03227.x

Stump BW, Johnson LR (1977) The determination of source properties by the linear inversion of seismograms. Bulletin of the Seismological Society of America 67:1489–1502. https://doi.org/10.1785/BSSA0670061489

Tang C (2002) Numerical simulation of progressive rock failure and associated seismicity. International Journal of Rock Mechanics and Mining Sciences 34:249–261. https://doi.org/10.1016/s0148-9062(96)00039-3

Tiefelsdorf M, Boots B (1995) The exact distribution of Moran's I. Environ Plan A 27:985–999. https://doi.org/10.1068/a270985

Trifu CI, Shumila V (2002) The use of uniaxial recordings in moment tensor inversions for induced seismic sources. Tectonophysics 356:171–180. https://doi.org/10.1016/S0040-1951(02)00383-9

Udías A, Buforn E (2017) Principles of Seismology. Cambridge University Press

Vavryčuk V (2015) Moment tensor decompositions revisited. J Seismol 19:231–252. https://doi.org/10.1007/s10950-014-9463-y

Venkataraman A, Kanamori H (2004) Observational constraints on the fracture energy of subduction zone earthquakes. J Geophys Res Solid Earth 109:. https://doi.org/10.1029/2003JB002549

Wang H, Li M, Shang X (2016) Current developments on micro-seismic data processing. J Nat Gas Sci Eng 32:521–537. https://doi.org/10.1016/j.jngse.2016.02.058

Wang H, Shi R, Deng D, et al (2020) Characteristic of stress evolution on fault surface and coal bursts mechanism during the extraction of longwall face in Yima mining area, China. J Struct Geol 136:. https://doi.org/10.1016/J.JSG.2020.104071

Wang S, Elsworth D, Liu J (2013) Permeability evolution during progressive deformation of intact coal and implications for instability in underground coal seams. International Journal of Rock Mechanics and Mining Sciences 58:34–45. https://doi.org/10.1016/J.IJRMMS.2012.09.005

White D (2012) Monitoring CO2 storage during EOR at the Weyburn-Midale Field. https://doi.org/101190/13167786 28:838–842. https://doi.org/10.1190/1.3167786

Woessner J, Wiemer S (2005) Assessing the quality of earthquake catalogues: Estimating the magnitude of completeness and its uncertainty. Bulletin of the Seismological Society of America 95:684–698. https://doi.org/10.1785/0120040007

Woodward K, Wesseloo J, Potvin Y (2018) A spatially focused clustering methodology for mining seismicity. Eng Geol 232:104–113. https://doi.org/10.1016/j.enggeo.2017.11.015

Xiao YX, Feng XT, Li SJ, et al (2016) Rock mass failure mechanisms during the evolution process of rockbursts in tunnels. International Journal of Rock Mechanics and Mining Sciences 83:174–181. https://doi.org/10.1016/j.ijrmms.2016.01.008

Yasitli NE, Unver B (2005) 3D numerical modeling of longwall mining with top-coal caving. International Journal of Rock Mechanics and Mining Sciences 42:219–235. https://doi.org/10.1016/J.IJRMMS.2004.08.007

Yi X, Kaiser PK (1993) Mechanisms of rockmass failure and prevention strategies in rockburst conditions. In: Proceedings of the 3rd International Symposium on Rockbursts and Seismicity in Mines. pp 141–145

Young RP, Maxwell SC, Urbancic TI, Feignier B (1992) Mining-induced microseismicity: Monitoring and applications of imaging and source mechanism techniques. pure and applied geophysics 1992 139:3 139:697–719. https://doi.org/10.1007/BF00879959

Zerva A (1988) Seismic source mechanisms and ground motion models. Probabilistic Engineering Mechanics 3:64–74

Zhang F, Damjanac B, Maxwell S (2019) Investigating Hydraulic Fracturing Complexity in Naturally Fractured Rock Masses Using Fully Coupled Multiscale Numerical Modeling. Rock Mech Rock Eng 52:5137–5160. https://doi.org/10.1007/S00603-019-01851-3/FIGURES/25

Zhao Q, Lisjak A, Mahabadi O, et al (2014) Numerical simulation of hydraulic fracturing and associated microseismicity using finite-discrete element method. Journal of Rock Mechanics and Geotechnical Engineering 6:574–581. https://doi.org/10.1016/J.JRMGE.2014.10.003

Zhao Y, Yang T, Bohnhoff M, et al (2018) Study of the Rock Mass Failure Process and Mechanisms During the Transformation from Open-Pit to Underground Mining Based on Microseismic Monitoring. Rock Mech Rock Eng 51:1473–1493

Zhao Y, Yang T, Liu H, et al (2021) A path for evaluating the mechanical response of rock masses based on deep mining-induced microseismic data: A case study. Tunnelling and Underground Space Technology 115:104025. https://doi.org/10.1016/j.tust.2021.104025

Zhao Y, Yang T, Yu Q, Zhang P (2019a) Dynamic reduction of rock mass mechanical parameters based on numerical simulation and microseismic data – A case study. Tunnelling and Underground Space Technology 83:437–451. https://doi.org/10.1016/j.tust.2018.09.018

Zhao Y, Yang T, Zhang P, et al (2019b) Method for Generating a Discrete Fracture Network from Microseismic Data and its Application in Analyzing the Permeability of Rock Masses: a Case Study. Rock Mech Rock Eng 52:3133–3155. https://doi.org/10.1007/s00603-018-1712-x

Zhao Y, Yang T, Zhang P, et al (2017) The analysis of rock damage process based on the microseismic monitoring and numerical simulations. Tunnelling and Underground Space Technology 69:1–17. https://doi.org/10.1016/j.tust.2017.06.002

Zhu Q, Feng Y, Cai M, et al (2017) Interpretation of the extent of hydraulic fracturing for rockburst prevention using microseismic monitoring data. J Nat Gas Sci Eng 38:107–119. https://doi.org/10.1016/j.jngse.2016.12.034